DOCTORAL THESIS

Numerical Investigations of Shock Wave Boundary Layer Interaction in Hypersonic Flows

A thesis submitted in fulfilment of the requirements

for the Degree of

DOCTOR OF PHILOSOPHY

in the

Faculty of Engineering

by

Bibin John

DEPARTMENT OF MECHANICAL ENGINEERING

INDIAN INSTITUTE OF TECHNOLOGY GUWAHATI

GUWAHATI-781 039, INDIA

APRIL 2014

Declaration of Authorship

I, Bibin John, declare that this thesis titled, 'Numerical Investigations of Shock Wave Boundary Layer Interaction in Hypersonic Flows' and the work presented in it are my own. I confirm that, this work was done wholly while in candidature for a research degree at this institute and no part of this thesis has previously been submitted for a degree or any other qualification at this institute or any other institution.

Bibin John
Department of Mechanical engineering
Indian Institute of Technology Guwahati
Guwahati-781 039, Assam
INDIA.
April 2014.

Thesis Certificate

It is certified that the work contained in the thesis entitled **Numerical Investigations of Shock Wave Boundary Layer Interaction in Hypersonic Flows** by **Bibin John**, a student in the Department of Mechanical Engineering, Indian Institute of Technology Guwahati, India, for the award of the degree of **Doctor of Philosophy** has been carried out under my supervision and this work has not been submitted elsewhere for the degree.

Dr. Vinayak Kulkarni
Assistant Professor
Department of Mechanical engineering
Indian Institute of Technology Guwahati
Guwahati-781 039, Assam
INDIA.

“I have been impressed with the urgency of doing. Knowing is not enough; we must apply. Being willing is not enough; we must do."

Leonardo da Vinci

Abstract

Shock wave boundary layer interaction (SWBLI) is a classical example of viscous-inviscid interactions. Occurrence of SWBLI, in hypersonic flowfield, is extremely adverse for the space missions and needs thorough investigations. Enhanced surface heating, alteration in aerodynamic coefficients, vortex shedding etc. are the possible reasons for this consideration. In view of this numerical studies are planned to enhance the understanding about this interaction. However these investigations demand an efficient and accurate solver suitable for high speed flow analysis. Hence an in-house 2D-axisymmetric viscous compressible flow solver "USHAS" (Unstructured Solver for Hypersonic Aerothermodynamic Simulations) is developed to achieve the proposed goals. This solver is then validated and verified using the literature reported numerical or experimental test cases. During these studies, it has been noted that the AUSM family of schemes form a better compromise among convergence, stability and accuracy for hypersonic applications. Thus these schemes are preferred onwards for SWBLI studies.

The higher order accurate solver, USHAS, is then implemented for ramp induced SWBLI (R-SWBLI) studies. Initial efforts are invested to quantify the effect of various governing parameters such as ramp angle, freestream Mach number, freestream stagnation enthalpy, leading edge bluntness and wall temperature on the interaction. Results obtained from these simulations are compared with qualitative predictions in literature. It is shown that increase in Mach number as well as bluntness of the leading edge reduces the upstream influence resulting in a decrease in the extent of separation. Contrarily, increase in wall temperature and decrease in stagnation enthalpy enhance the separation size. Possibility of turbulent reattachment is also confirmed for leading edge bluntness case through the present simulations upon comparison of the results with the reported experimental data. Numerical studies also illustrate that the total to wall temperature ratio is a better indicator of SWBLI rather than the individual quantities themselves. Subsequently, using the same simulation data, various literature reported correlations to predict incipient separation condition, extent of upstream influence, separation bubble length, plateau pressure and separation pressure, have been critically reviewed and assessed. It has been noted that the correlation for incipient condition should only be used for ‘well separated flows’. Successful modifications are suggested in other correlations to widen their range of applicability.

The widely accepted control technique, provision of leading edge bluntness, is investigated to assess its capability to delay or avoid the separation. Various dependent parameters like sonic height, boundary layer edge Mach number, entropy layer, boundary layer thicknesses etc. are

considered for this evaluation. These studies revealed the existence of two critical radii of leading bluntness associated with R-SWBLI. The reference separation bubble size, corresponding to sharp leading edge plate, is seen to be widened with initial increase in leading edge radius, till the first critical radius. This critical radius is termed as inversion radius and it corresponds to maximum separation bubble size. Entropy layer swallowing has been accounted for this enhancement in separation bubble size. Increase in leading edge radius beyond the second critical radius is found to decrease the size of separation zone in comparison with sharp leading edge case. This second critical radius is termed as equivalent radius and it signifies the equal separation zone as that for reference sharp leading edge case. Extension of the over pressure region beyond the reference upstream influence location is credited for this separation zone decrement. In view of this, current studies are found to be very useful in selecting the leading edge bluntness radius for delaying the separation. Subsequently numerical studies are extended to analyse the parametric influence of freestream and geometric conditions on the critical radii of SWBLI. The critical radii of R-SWBLI are observed to be increasing with decrease in freestream Mach number and total enthalpy. However their magnitude increases with increase in wall temperature. Moreover the flowfield equivalence has been noticed for very small and large leading edge radii for two different total enthalpy streams, upon maintaining constant wall to freestream total temperature ratio (T_w/T_0). These studies are found very useful in devising mechanism for estimation of critical radii and as well for incorporating the amendment in the same due to change in governing parameters. Finally shock wave boundary layer interaction for axisymmetric configurations is also studied by considering its importance in space vehicle design. Influence of leading edge bluntness on two R-SWBLI parameters viz. separation bubble size and surface heatflux distribution are revealed through this study. Both the critical radii are observed during the two dimensional simulations while single critical radius has been observed for the axisymmetric computations for the range of radii under consideration. Lower entropy layer thickness due to decreased shock stand-off distance in the presence of three dimensional reliving effect is reasoned for this disparity.

Acknowledgements

First of all, thanks to God, the almighty who bring me to the level of writing this...

There are quite a lot of people who need to be acknowledged.

Foremost, I am deeply grateful to my supervisor, Dr. Vinayak Kulkarni who provided me the great opportunity of working in hypersonic aerodynamics. Without his guidance, support and extraordinary endurance, this work would not have been possible. Throughout this research phase, he has extended his supporting hands, which helped me a lot in surviving both academic and personal struggles.

I also want to thank Dr. Ganesh Natarajan for his kind and continuous support in the phase of development of present solver. Through friendly discussions he clarified most of my doubts and curiosities.

I am also grateful for having an encouraging doctoral committee. I would like to thank my doctoral committee members, Dr. Anoop K. Das, Dr. Niranjan Sahoo and Dr. Anugrah Singh for generously offering their valuable time, guidance and support throughout my doctoral studies. I am also grateful to departmental head, Dr. Pinakeswar Mahanta and other faculties in the department for their direct and indirect supports and guidance.

I want to thank all my colleagues and friends for their nice company during the stay in IIT Guwahati. Throughout the entire span of four years all of you have helped me in one way or other. Thanks for all of your nice company.

Above all, the support and encouragement received from my family members during the course of my stay at IIT is acknowledged with profound gratitude. Special thanks to my beloved wife Sreeja for her love, support and motivation. Sreeja, I am lucky to have you as my wife.

Contents

List of Figures

List of Tables

Abbreviations

BWT	Blast Wave Theory
CFD	Computational Fluid Dynamics
FVM	Finite Volume Method
SWBLI	Shock Wave Boundary Layer Interactions
R-SWBLI	Ramp induced Shock Wave Boundary Layer Interactions
USHAS	Unstructured Solver for Hypersonic Aerothermodynamic Simulations
2D	Two Dimensional
Quasi-**1D**	Quasi one dimensional

Symbols

C, C_w	Chapman-Rubesin parameter	
C_f	Skin friction coefficient	
Cp	Pressure coefficient	
C_p	specific heat at constant pressure	J/kgK
E_I	x-component of inviscid flux vector	
F_I	y-component of inviscid flux vector	
E_V	x-component of viscous flux vector	
F_V	y-component of viscous flux vector	
H	Total Enthalpy	
L_{ui}	Upstream influence extent	m
L_b	Separation bubble size	m
L	Length of flat plate section	m
M	Mach number	
p	Pressure in general	N/m^2
Pr	Prandtl number	
q	Heatflux	W/m^2
Re	Reynolds Number	
R_n	Leading edge radius	m
S	Source term	
St	Stanton number $(St = q/\rho_\infty U_\infty Cp_\infty (T_0 - T_w))$	
t	Time	sec
T	Temperature	K
T_0	Stagnation temperature	K

U	Conservative variable vector	
U_∞	Freestream velocity	m/s
u	Velocity in x-direction	m/s
v	Velocity in y-direction	m/s
x	x-coordinate/ distance in x-direction	m
y	y-coordinate/ distance in y-direction	m
x_0	Distance from leading edge to upstream influence starting location	m

Greek symbols

α_r	Relaxation parameter	
β^*	Temperature scaling term for upstream influence extent	
β_{lb}	Temperature scaling term for separation bubble size	
γ	Specific heat ratio	
δ	Boundary layer thickness	m
δ^*	Displacement thickness	m
θ	Flow deflection angle	degree
θ_c	Geometric angle	degree
θ_{is}	Incipient separation angle	degree
μ	Coefficient of dynamic viscosity	Ns/m^2
$\bar{\chi_L}$	Viscous interaction parameter	
ρ	Density	kg/m^3
τ	Shear stress	N/m^2
Ω	volume of cell (for 2D area of cell)	

Subscripts

0	Conditions immediately upstream of interaction location (ie, at x_0)
∞	Freestream conditions
w	Wall conditions
$incp$	Incipient separation condition
sep	Separation point condition
$plat$	Plateau value
$peak$	Peak value

e	Boundary layer edge condition

Superscripts

$*$	Reference temperature conditions

Dedicated to my family

Chapter 1

Introduction

Overview

Shock wave boundary layer interaction (SWBLI) is the topic for present investigations. In view of this, initial part of the chapter describes various terminologies and characteristic features of SWBLI. It is then followed by the experimental, theoretical and numerical contributions of several researchers in this field. Short comings or limitations of the literature reported finding are mentioned while defining the objectives of present studies. Structure of the thesis is finally discussed in this chapter.

1.1 Introduction

Bird flight has always provided inspiration to the mankind for possessing the desire of flying and designing associated objects. Therefore feather like structures were the outcome of the initial efforts based on this stimulus. However such failure attempts diverted the impetus towards lighter than air flight. As a result of which, first successful flight of a hot air balloon took off in 1783. Gliders were the successors of these balloons. Sir George Cayley was the brain behind the thought of connecting propulsive system to such fixed wing gliders. This perception about flying had sowed the invention of heavier than air flight. Consequently, world had experienced the first successful flight of Wright Brothers in December of 1903. Hereafter development of aeronautics and space flights took a leap and as an aftermath, first supersonic flight was possible in 1947 and destination moon was achieved in 1969.

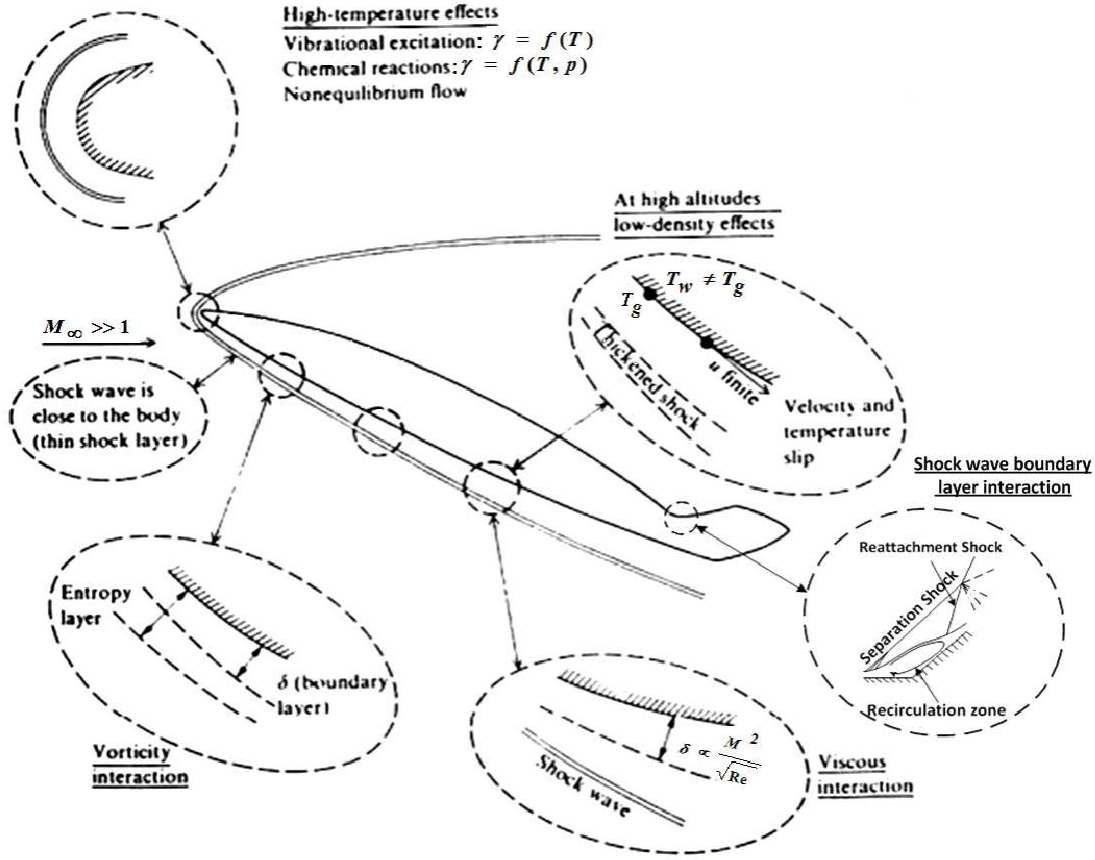

FIGURE 1.1: Important physical features of hypersonic flows.

Desire of flying faster and higher has disclosed various fluid flow regimes ahead the fluid dynamics research fraternity. Among those, hypersonic aerodynamics needs special attention for design of planetary space vehicles, satellite launch vehicles, intercontinental missiles etc. Fundamental understanding of the fluid flow is essential for designing these vehicles which would experience the hypersonic atmosphere. This flow regime is conventionally defined if the flow Mach number is greater than five or the flow velocity is more than five times of local speed of sound. However hypersonic flows are characterized by complex phenomenon as described in figure 1.1 (Anderson [1]). Presence of these special flow features constitutes the hypersonic flow. Deceleration of flow in the shock layer transforms the kinetic energy into heat energy which in turn triggers these distinct flow features. Among these special features, interaction of shock wave with thick boundary layer is of immense interest to the hypersonic community. In view of this, SWBLI is planned for investigations during present studies.

1.2 Shock wave boundary layer interaction

Shock wave is an inviscid flow feature which can be encountered whenever supersonic or hypersonic flow needs inward turning (figure 1.2). Shock waves provide discontinuity for most of the flow properties among which pressure, temperature and density increase across it. Strength of the shock or increase in these flow properties depends upon flow turning angle and freestream Mach number. Contrarily, boundary layer is invariantly present in the viscous flows, in the vicinity of the wall, for smoothening the velocity gradient between freestream and wall (figure 1.3). Importantly, some part of the boundary layer flow remains subsonic although freestream is supersonic or hypersonic. Streamwise growth of such boundary layer depends upon freestream Reynolds number, Mach number and the pressure gradient in the same direction. The interaction of shock wave and boundary layer is therefore a viscous-inviscid type. Such situations are prominent in external flows like flow over control surface and internal flows like scramjet intake flow. At lower strength of this interaction, flow retains stability but gets disturbed in the presence of interaction. However if the strength of the interaction increases then flow separation, turbulent transition, enhancement in wall heat transfer rates, vortex shedding etc., are expected. As a result of this, performance of control surface and engine gets affected. Thus it is essential to study the shock wave boundary layer interaction. This interaction can be broadly classified in two types as, oblique shock based interactions and normal shock based interactions. The oblique shock based interactions can be further classified as impingement based SWBLI (I-SWBLI) and ramp induced SWBLI (R-SWBLI).

1.2.1 Shock impingement based SWBLI (I-SWBLI)

This interaction takes place when an oblique shock penetrates through the boundary layer developing over the surface of space vehicle and reflects back from it as shown in figure 1.4(a). Here, the oncoming supersonic or hypersonic flow undergoes two successive deflections in the presence of primary and reflected shocks, depending on the approaching Mach number (M_1) of the flow. These deflections may lead to separation of the boundary layer in the vicinity of the shock impingement location. Such type of interaction is prominent in scramjet intakes.

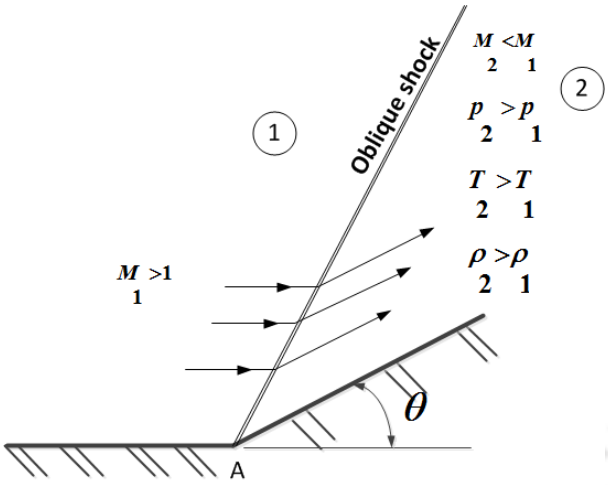

FIGURE 1.2: Inviscid shock generation in the presence of compression corner (picture from Anderson[1].

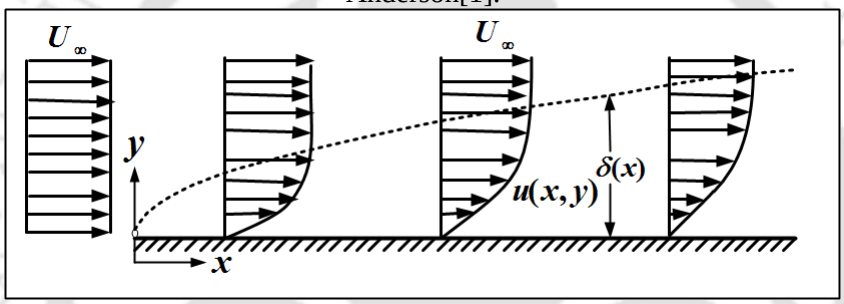

FIGURE 1.3: Boundary layer growth and associated velocity vectors (picture from Schlichting [2])

1.2.2 Ramp induced SWBLI (R-SWBLI)

This interaction generally occurs due to the presence of compression surfaces or discontinuous change in the surface inclination. Such compression corners root the oblique shock at the foot and provide adverse pressure gradient to the oncoming boundary layer. Therefore thickness of the boundary layer increases in the presence of imposed adverse pressure gradient which in turn may lead to flow separation at the ramp foot. Typical R-SWBLI is depicted in figure 1.4(b). Various space vehicle components or subsystems like wing body junctions, engine inlet, control surfaces etc., get affected by this type of shock wave boundary layer interactions.

1.2.3 Interaction of normal shock and boundary layer

Interaction between normal shock and boundary layer can be encountered in supersonic diffusers, wind tunnels, shock tubes, transonic aerofoils etc. The important feature of this SWBLI

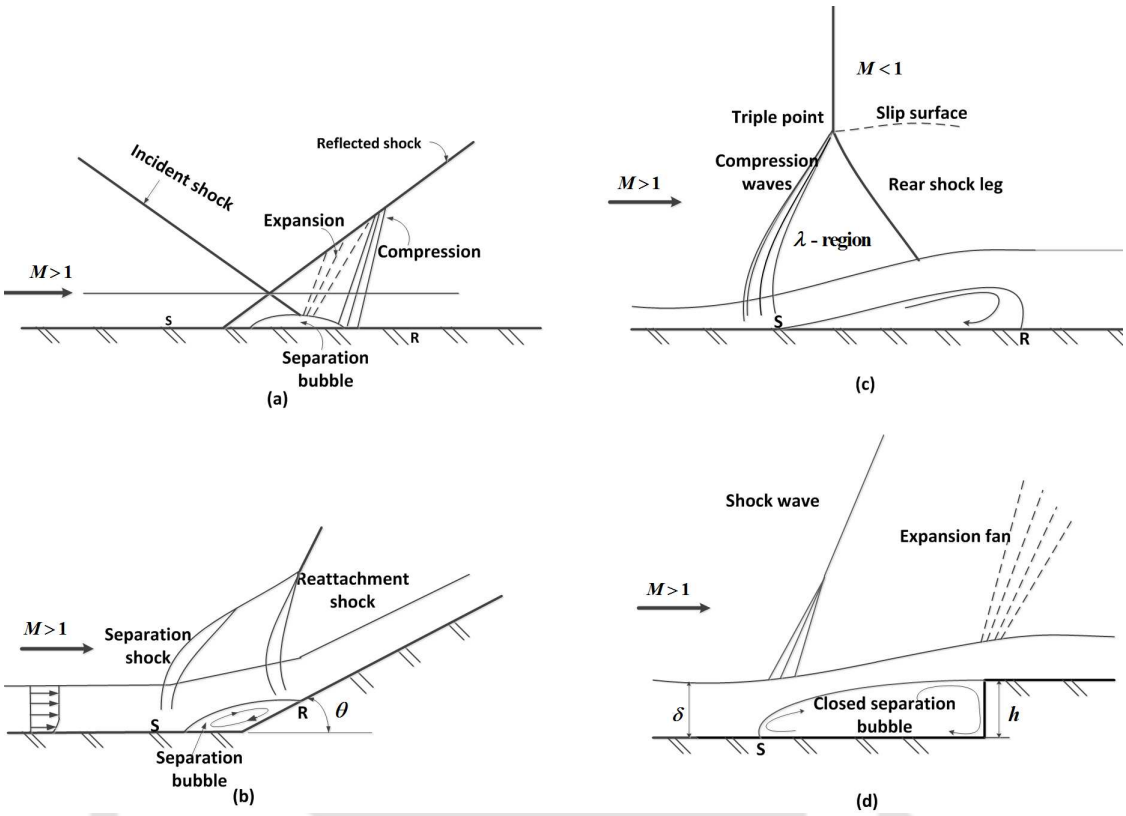

FIGURE 1.4: Important types of two dimensional shock wave boundary layer interactions.

is that the flow remains subsonic downstream of the interaction. Flow pattern near the wall for such interaction is given in figure 1.4(c). Since this type of interaction creates subsonic flow region behind the interaction, the downstream flow alterations may influence the interaction zone. Hence complex unsteady phenomenon can also be expected during this interaction. Presence of forward facing step in supersonic or hypersonic flowfield also induces interaction of this kind as shown in figure 1.4(d).

1.3 Flowfield in the presence of SWBLI

It had been observed that response of the SWBLI is independent of its type and remains almost similar in all those cases. Therefore typical flowfield in case of R-SWBLI is discussed herewith.

Ramp like shapes are very common in the design of space vehicles and engine inlets. Abrupt deflection of flow in the presence of ramp leads to the generation of shock wave emanating from the compression corner. Flow deceleration takes place across this shock wave as a result

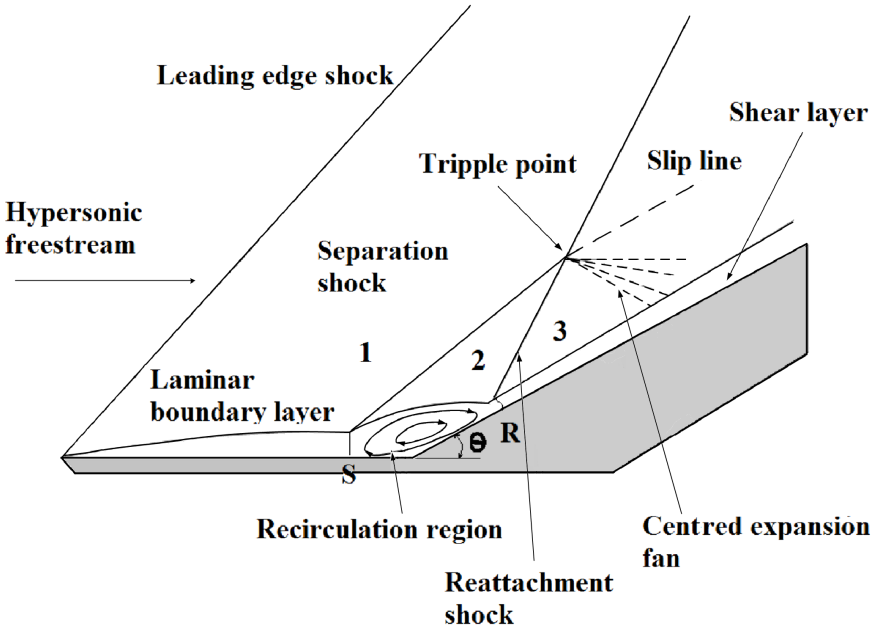

FIGURE 1.5: Schematic diagram representing, the 2D high speed flow over a compression corner with SWBLI.

of which pressure in the downstream region increases. Such disturbance propagates upstream of the compression corner through the subsonic part of the approaching boundary layer. This upstream propagation of disturbance leads to boundary layer thickening which in turn may end in separation.

Compression corner based adverse pressure gradient in the presence of oblique shock remains one of the driving parameters for the possible separation in case of R-SWBLI. However, such local flow separation is not always guaranteed. Separation of the flow in the presence of ramp induced adverse pressure gradient depends on many parameters like Mach number, Reynolds number, ramp angle, wall temperature, boundary layer stability etc. For a given freestream conditions the minimum ramp angle required to initiate the separation is known as incipient separation angle [3]. If the deflection angle is higher than the incipient separation angle, then boundary layer separation takes place at station 'S' (shown in figure 1.5), well ahead of the compression corner, depending on the viscous interaction parameter. In such a case, the thickened separated boundary layer locally deflects the inviscid freestream over the boundary layer. Deflection of inviscid flow forms an oblique shock wave known as the separation shock. Reattachment of the separated flow takes place at station 'R' downstream of the compression corner.

Such reattachment raises pressure and local heat flux. The closed separated region with subsonic recirculation remains isolated from the approximately inviscid supersonic flow above it by a thin mixing layer, called as shear layer. The supersonic flow above the shear layer and below the separation shock gets deflected by the reattachment shock. Therefore prediction of various features of SWBLI becomes a challenging task in the presence of such a complicated flowfield.

1.4 Shock wave boundary layer interaction terminologies

The intensity of SWBLI and its dependence on various parameters can be well understood using different SWBLI features. These characteristic features of SWBLI are clearly shown in figure 1.6. Prior quantification of these SWBLI parameters is extremely necessary for the successful design of hypersonic systems involving shock wave boundary layer interactions. Therefore definitions of important SWBLI parameters are discussed here under.

1.4.1 Upstream influence

Presence of ramp can leads to considerable flow alterations, even without separation, in the region, upstream of the interaction. Such upstream flow alteration is generally termed as upstream influence. In case of R-SWBLI, extent/length of upstream influence is defined as the distance from the ramp-foot to the most upstream location, which experiences the influence of ramp based disturbance. Higher the value of extent of upstream influence, higher is the intensity of SWBLI.

1.4.2 Separation bubble size

Separation bubble size is another important terminology. It needs consideration only when flow is separated due to R-SWBLI. However, separation depends on ramp angle, freestream conditions and wall specifications. Therefore separation bubble size is also function of these parameters. Here, separation bubble size is defined as the linear or streamwise distance between the separation and reattachment points for the well separated flow. Higher value of separation bubble size indicates high intensity of shock-boundary layer interaction.

1.4.3 Separation and Plateau pressure

Separation and plateau pressures are important SWBLI parameters, obtained from wall pressure distribution. As their names represent, these two are the pressure values corresponding to separation point and plateau region of a typical wall pressure distribution in the presence of SWBLI. Here, plateau pressure is the nearly constant pressure in the separation zone. This pressure remains a clear indicator of separated flowfield.

1.4.4 Peak Stanton number

Peak Stanton number is the non-dimensional value of maximum heatflux on the ramp surface. Here peak Stanton number is expressed as,

$$St_{peak} = \frac{q_{max}}{\rho_\infty U_\infty C_{p_\infty}(T_0 - T_w)}$$

This parameter is important for R-SWBLI with separation. In such cases, the reattached boundary layer attains minimum thickness downstream of the reattachment point which leads to maximum local surface heatflux. Beyond this location the Stanton number decreases due to further thickening of the boundary layer. Hence, this parameter helps to quantify the strength of the interaction.

1.5 Literature review

In the past, SWBLI has been investigated by several researchers owing to its growing significance. Research in this field has been started early in 1950. From this time, many investigations and parametric studies are reported for high speed laminar and turbulent flows. Some of these studies are related to understanding of the SWBLI and its dependence on various influencing parameters. Few researchers have also concentrated on development of correlations for prediction of characteristic features of interaction using freestream and geometry conditions. Some findings are related with the control of SWBLI. Experimental, computational and theoretical efforts in this field are summarised in following subsections.

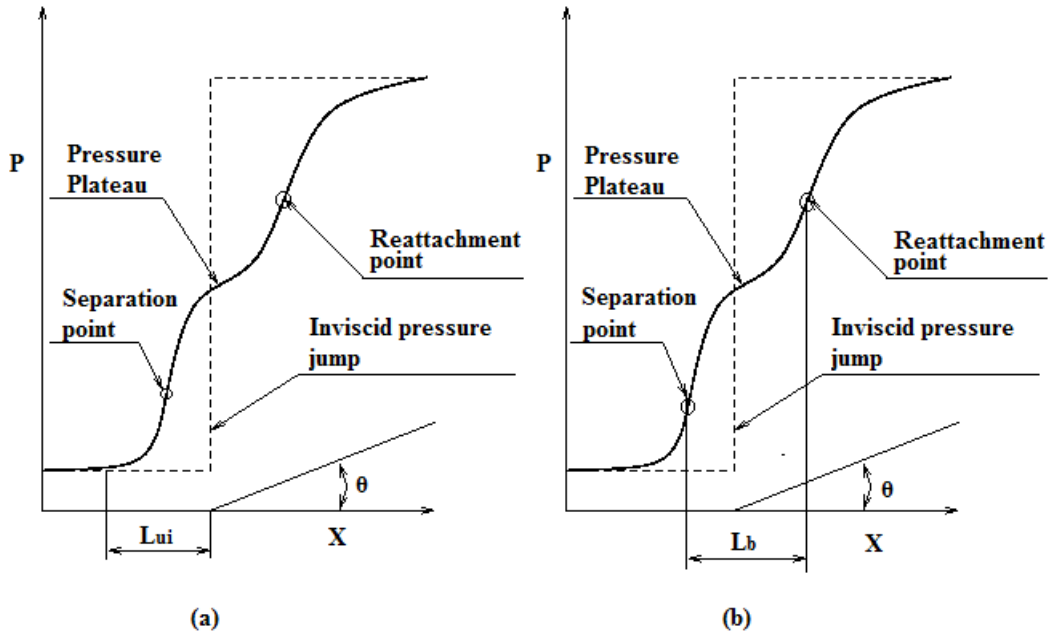

FIGURE 1.6: Typical pressure distribution along the wall for ramp based SWBLI.

1.5.1 Experimental studies

The studies of Chapman et al. [4] can be considered as the oldest one among the available studies related to SWBLIs in high speed flows. Chapman et al. first proposed the free-interaction theory through experimental and theoretical studies. His free-interaction concept is worth noticeable due to its prime importance in explaining the basic physics of SWBLI. This theory has showed the independency of separation point pressure, plateau pressure and extent of first part of separation on downstream parameters. Subsequently Kuehn [5] continued the shock wave boundary layer interaction studies and focused on identification of incipient separation condition. Here, incipient separation condition was defined as a situation where some portion of the surface skin friction distribution becomes exactly zero. However by considering the difficulty involved in experimental measurement of skin friction distribution, Kuehn proposed an alternative method to predict incipient separation from surface pressure measurements. According to this revised proposition, incipient separation should coincide with the first appearance of three inflection points in the surface pressure distribution. Followed by Kuehn, Needham [6] proposed another methodology to estimate the incipient separation. This criterion was based on the heat transfer measurements, which identifies incipient separation from a rounded minimum heatflux near the interaction region. However both Kuehn's and Needham's methods were observed to be failing

in predicting very small separation bubble sizes. Later, Needam and stollery [3] established a correlation to predict incipient separation angle based on their experimental pressure measurements. An elaborated review of most of the such investigations about SWBLIs is summarized by Green [7].

Research in the field of both laminar and turbulent SWBLI was continued in the next decade where focus was mainly on the identification of parametric influence of various freestream and geometric conditions on intensity of SWBLI. The experimental studies of Holden [8] and Hankey and Holden [9] were most appreciated on such aspects of the SWBLIs. In those studies, interaction of shock wave with both laminar and turbulent boundary layers were investigated in high speed flows ranging from supersonic to hypersonic flow regime. Parametric influence of various flow and geometric quantities like, Mach number, Reynolds numbers, wedge angle and the leading edge bluntness on the interaction were investigated. Those studies were especially conclusive in strong as well as weak interaction flows about the effects of governing parameters on the upstream influence, separation extent and peak heating. Finally authors reported that, upstream influence increases with ramp angle and decreases with Mach number while it gets weakly affected by the Reynolds number in case of turbulent interaction. The increasing nature of upstream influence and separation bubble size with enhancement of ramp angle had been confirmed experimentally by Bloy and Georgeff [10]. Few researchers [11, 12] investigated the effect of wall temperatures on SWBLI phenomenon. Back and Cuffel [11] presented the experimental studies about effect of surface cooling and surface heating on the impingement kind interaction for an impinging shock of 8.4^0 shock angle. Two wall conditions viz. a cooled wall with total temperature ratio (T_w/T_0) of 0.44 and heated wall corresponding to T_w/T_0 of 1.1, were considered during those experiments. Significant variation in the shock interaction structure and size of the separation bubble were observed for those wall conditions. The size of the separation region was found to be decreased with surface cooling and thereby steeper pressure rise in the interaction region was noticed as compared to the heated wall condition. Coet and Chanetz [12] conducted experiments for understanding the influence of wall temperature on the SWBLI, especially for the separation zone. These studies when conducted for R-SWBLI, authors noticed that, the wall to interaction zone-upstream temperature ratio (T_w/T_1) has significant effect

on R-SWBLI and the intensity of interaction increases with increase in this temperature ratio. Hayakawa and Squire [13] experimentally investigated supersonic SWBLI for compression corners and focused on the effect of upstream boundary layer on downstream interaction region. The verification of earlier reported correlations for upstream influence and incipient separation was also carried out in that reporting. Dependency of upstream influence on ramp angle was observed in this study. It had also been shown that the non-dimensionalized extent of upstream influence varies linearly with the inviscid pressure jump. Here boundary layer thickness at a location, immediately upstream of interaction station, was considered as the reference length scale for non-dimensionalization. Additionally, inverse proportionality of the non-dimensional extent of upstream influence with the local skin-friction coefficient was also confirmed.

The shock wave boundary layer interaction in case of non-sharp or blunt leading edge configurations had also been experimentally studied by many researchers. Townsend [14] investigated bluntness effect on two dimensional flowfields, while Gray [15] carried out studies for the similar objective for axisymmetric flowfields. Townsend observed decrease in separation bubble size with increase in leading edge bluntness, while Gray noticed opposite trend of increase in separation zone with increase in bluntness. Later studies of Holden [8] revealed the existence of a critical leading edge bluntness beyond which separation zone shrinks for R-SWBLIs. During these experimental studies, it was observed that initial increase in leading edge bluntness led to increased separation zone and a decrease of the same would be expected beyond a critical radius. The later was referred here as the bluntness dominated zone while the former was called as the displacement dominated zone. Decrease in boundary layer edge Mach number has been accounted for separation zone widening while bluntness induced favourable pressure gradient has been attributed for decrease in separation zone size. Coet et al. [16], during their studies, also focused on the effect of leading edge bluntness and associated entropy layer on the ramp induced shock wave boundary layer interaction. Conclusions of these studies were also in-line with Townsend's observation. Among the limited investigations in laminar region, recent shock tunnel based studies of Neuenhahn and Olivier [17] on R-SWBLI for scramjet intake flow with leading edge bluntness portrayed that relative thickness of boundary layer and entropy layer is

responsible for variation in separation bubble size. The investigation of combined effect of leading edge bluntness and real gas behaviour on R-SWBLIs was also discussed through rigorous experimentation by Mallinson et al. [18]. Similar to the perfect gas studies, the intensity of SWBLI was observed to be reducing with increase in leading edge bluntness for high enthalpy reacting flows as well. However the difference between the sharp and blunt leading edge flowfields was observed to be less pronounced for high enthalpy flows as compared perfect gas flows. Reduction in shock stand-off distance in the presence of reactions in the flow was reasoned for this observation.

Besides the above discussed SWBLI studies, there are few more literature that presented experimental measurements of shock wave boundary interactions in laminar high speed flows. Investigations of Hakkinen et al. [19], Needham [20], Kaufman and Johnson [21], Holden [22], Marrini [23] are also part of experimental studies in the field of 2D laminar SWBLI. Most of such earlier experimental studies are reviewed by Dolling [24]. Apart from these, Chanetz [25], Holden [26] and Dieudonne et al. [27] conducted experiments in case of SWBLI for axisymmetric flows to validate the computational results. These experimental measurements are useful to other researchers as well for the same purpose. Findings of Tutty et al. [28] is the latest one which dealt with SWBLI. Hypersonic flow of freestream Mach number 6.7 over a fin-body junction was considered in this study. Almost ten times increase in surface heating was observed in the presence of SWBLI as compared to undisturbed boundary layer. In addition to this, Borovoy et al. [29] recently conducted experiments with blunt flat plates to investigate the effect of leading edge bluntness on the surface heating due to the interaction of an impinging shock with boundary layer. It was concluded that the plate bluntness significantly reduces the heat transfer in the shock interference region. The enhancement of separation zone size and the reduction of gas density in the high-entropy layer were pointed out as the possible reasons for such heatflux reduction in the presence of bluntness. These studies also explored the existence of a threshold leading edge radius for heat transfer reduction.

1.5.2 Theoretical studies

The theoretical treatment for SWBLI was initially started from inviscid perspective with the assumption that the prorogation of the disturbance based on shock wave interaction in the

boundary layer is governed by inviscid flow governing equations. On this ground, Howarth [30] had first theoretically explained the shock wave boundary layer interaction. It was argued that, SWBLI based flowfield changes are so rapid that the viscosity is of secondary importance for this phenomenon. However, later Lighthil [31], discarded this pure inviscid theory using the strong justification of inadequacy of this theory in explaining complete phenomenon. Therefore subsequent studies were carried out by various researchers using the integral form of the boundary-layer equations to explain the interaction. The theoretical study of Crocco and Lees [32] is found to be the first of such kind that provided agreement with the experimental measurements. Through their studies they showed that upstream propagation of disturbances is possible if an inviscid outer stream is coupled to the displacement upstream of separation. Subsequently, Lighthill [33] introduced an inner boundary layer to his earlier study and produced a coherent self-consistent theory. However this theory was incapable to account for boundary layer separation. But through this theory Lighthill could hint about the possibility of separation. Based on the Lighthill's theory, Stewartson and Williams [34] and Neiland [35] later introduced supersonic triple-deck theory which included nonlinear effects and provided a theoretical explanation for the upstream influence, as well as for self-induced separation of a boundary layer in supersonic flow. These investigations were useful to present the effective use of triple-deck theory for laminar SWBLI. Further extension of triple-deck theory to supersonic and hypersonic flowfields can be seen through the explorations of Neiland [36], Stewartson [37, 38] and Messiter[39]. Rizetta et al. [40] applied triple-deck theory specifically to compression and expansion corner based boundary layer interactions using the idea of applicability of triple deck solution to entire shock interaction region in case of small disturbances of the order Re^{-4}. Comparison of theoretical results with experimental measurements for wide range of corner angles was also discussed to show the accuracy of the theoretical model. Later Katzer [41] carried out numerical investigations of I-SWBLI in supersonic laminar flowfield to verify the triple deck predictions and also to analyse the length scales involved in the SWBLI. Katzer noticed an encouraging match in the numerically predicted separation and plateau pressures by comparing with theoretical scaling laws of Chapman et al. [4], and Stewartson [37]. Among the two length parameters of SWBLI, the non-dimensional free interaction length scale with reference boundary layer displacement thickness was found to be independent of shock strength; while, size of separation zone showed

linearity with shock strength. Katzer proposed a new scaling law for SWBLI based separation bubble size based on the understanding of numerical data in comparison with triple deck theory. Theoretical studies of SWBLI involving blunt leading edge was carried out by Holden [42] using solutions of integral form of boundary layer equations governing both attached and separated flows near the compression ramps with highly cooled walls. The requirement of a jump condition to join the supercritical boundary layer at the beginning of the interaction to the subcritical boundary layer at separation was noticed through this study. Besides, Sobey [43], Dechaume et al.[44] and Inger [45] presented their recent theoretical studies related to SWBLI.

1.5.3 Numerical studies

The history of numerical studies for SWBLI dates back to late 1970. The work of Carter [46] can be considered as the earliest numerical studies of laminar SWBLI phenomenon. Finite difference technique was used in this study to obtain steady state solution. In 1975, Maccormack and Baldwin [47] presented an article describing the methodology of solving unsteady Navier-Stokes equation to obtain solution for strong shock wave boundary layer interaction phenomenon. As its extension, Hung and Maccormack [48] investigated both supersonic and hypersonic compression corner flows. Three wedge angles, viz. $15^0, 18^0$ and 24^0 were considered in this study. Reasonably good agreement, among numerical and experimental measurements, was observed. A correlation between the leading edge shock strength and peak in heatflux and peak wall pressure was also noticed through this study. Later Balleur et al. [49] presented two numerical approaches to analyse supersonic high Reynolds number flows with SWBLI. These techniques were named as global approach and coupling approach. In global approach, complete Navier-Stokes equations were solved in the physical domain without differentiating the inviscid and viscous portion of the flowfield. Whereas in coupling approach, solutions to the inviscid and viscous portion of the flowfield were obtained simultaneously by solving Euler and Navier-Stokes equations in the respective domains. Both R-SWBLI and I-SWBLI were analysed by employing these numerical techniques. Subsequent numerical investigations of compression corner induced SWBLI in laminar high speed flows were carried out by Fay and Sambamurthi [50], Rudy et al. [51], Garsso et al. [52], Grasso and Marini [53] and Layland [54]. Comparison of accuracy of four different Navier-Stokes solvers, in simulating the two dimensional R-SWBLI in hypersonic flowfield,

was presented by Rudy et al. [51]. In this study three dimensional effects of the flowfield were also accounted. Grasso et al. [52] discussed extensive validation procedure for hypersonic flow solvers by studying compression corner flows. Through this study, authors also extended Eckert's results [55] to determine the skin-friction and Stanton number distributions in the region upstream of the interaction zone. Such analytical values of skin friction and Stanton number at the reference upstream influence starting location can be considered in proposing or modifying the scaling laws for laminar SWBLI. Following to it, Grasso and Marrini [53] later performed computations employing various experimental freestream conditions. Influence of flow deflection angle, leading edge state, viscous interaction parameter etc., was critically assessed in this study. Based on the numerical understanding and theoretical considerations, Grasso and Marrini proposed simple scaling laws for upstream influence extent and aerodynamic coefficients. Further by using the peak heating correlation of Hung and Barnett [56], it was also showed that the peak heating can be correlated to length of upstream influence. Katzer [41] conducted simulations for two dimensional I-SWBLI and associated scaling laws. Lately Marini [57] consolidated the ramp induced SWBLI interaction in the laminar hypersonic flow regime. In this review, the effects of different freestream and wall conditions on the SWBLI based flow separation were discussed. Comparison of numerical data, in the light of earlier reported scaling laws for SWBLI, was also summarised. Inconsistency of scaling laws in scaling SWBLI parameters for different wall and freestream conditions (especially wall temperature) was noticed through this work. Effect of high enthalpy non-equilibrium flow on SWBLI had also been accounted by Davis and Sturtevant [58]. During these studies, computations were carried out for high enthalpy flowfield over two dimensional double ramp model. A new scaling law for separation bubble size of R-SWBLI was proposed. It was also conclusively pointed that the proposed scaling law can be extended for varying wall temperature conditions. Numerical studies of SWBLI in the presence of leading edge bluntness was reported by Neuenhahn and Olivier [59]. Combined effect of leading edge bluntness and wall temperatures was explored in this study. On similar line, Savino and Paterna [60] presented the wall temperature effect on blunted double cone model. Apart from these studies, SWBLI on axisymmetric double cone and/or hollow cylinder fare was numerically investigated by many researchers [61, 62, 63, 64, 65, 66]. These computational studies include both Direct Simulation Monte Carlo (DSMC) [61, 62] solver and Navier

Stokes solver [63, 64, 65, 66]. Most of these findings focused mainly on the code validation. Detailed review, discussing the capability of CFD technique in predicting such complex hypersonic SWBLI on axisymmetric models, can be found in the recent published article by Knight et al. [67]

Numerous reporting about SWBLI in turbulent flowfields are available in open literature. In summary, such studies employed different turbulent simulation techniques, such as direct numerical simulation (DNS), large-eddy simulation (LES), and hybrid large-eddy simulation/ Reynolds-averaged Navier-Stokes (LES-RANS) methods. Recently, Knight [68] and Edwards [69] reviewed such findings. Present studies are planned for laminar flows; therefore SWBLI studies in only laminar hypersonic flows has been presented in detail. Based on this literature review following objectives are set for current investigations.

1.6 Objectives of present research

Shock wave boundary layer interaction has attracted various researchers to contribute in terms of experimental, computational and theoretical studies. These investigations are very much useful for prediction of SWBLI parameters like upstream influence location, separation bubble size, separation and reattachment locations, wall parameters etc. Thus the information about the control surface performance, scramjet intake efficiency, possibility of transition, vortex shedding and noise remains with the hypersonic system designer. This database helps for optimizing the performance of associated object through aerodynamic alterations and for silent operation of systems and subsystems through separation and noise control. In view of this, there exists lot of scope for further studies in the area of SWBLI. Some of the major topics undertaken as objectives for present studies are discussed in this section.

Current investigations are planned through computational means. Hence, there is an immediate need of development of higher order accurate viscous compressible flow solver. Validation and verification of this solver using the literature reported test cases is the prime requirement before employing this solver to study the sensitive topics like SWBLI. The proposed finite volume

solver needs to be equipped with various flux computing schemes to broaden its range of applications. Studies for the best suited scheme for hypersonic flow regime are extremely essential so as to implement the same for SWBLI explorations. Computational simulations are planned to compliment the experimental results and also to extract the data which is difficult to measure during experiments. Measurement of wall shear stress in high-speed facilities is a prominent example for this. Apart from this, arriving at the field information is costly through the well-established flow visualization techniques. However extraction of data about entropy layer and boundary layer is also difficult from such experiments. Hence the higher order accurate solver provides a robust means to get the wall parameters and field data essential to study the SWBLI phenomenon.

In view of the literature reported studies about interaction of shock wave and laminar boundary layer, limited number of findings [8, 23] are available which deal with the effect of freestream Mach number and stagnation enthalpy. Most of these theoretical and empirical methodologies, about finding the incipient separation condition, were observed to be derived out of pressure measurements. Moreover it is highly essential to get the wall friction coefficient data to precisely predict the separation and reattachment location and hence the separation bubble size. Thus applicability of such methods needs to be assessed through computational studies. Therefore this goal demands to revisit the results of separation length from pressure measurements in order to quantify these qualitative observations through high-resolution computations. Such simulations would then also be useful to resolve qualm from experimental outcome.

It has been noticed that, limited number of findings, which offer quantitative measure of separation bubble size and extent of upstream influence, in terms of geometrical and freestream parameters, provide correlations to predict these characteristic features of the SWBLI. The prime advantage of such simple correlations lies in the ease of their applicability in understanding the basics of R-SWBLI, without costly experimental investigations or complex computational simulations. The correlations proposed by Needam and Stollery [3] and Katzer [41] are important in such aspects. Recently Davis and Sturtevant [58] have also proposed a new correlation for separation bubble size based on the classical triple-deck formulation of Stewartson and Williams

[34]. However it has been observed that the scaling laws proposed by various researchers are not unique in nature. Hence it is extremely important to assess these correlations to check their suitability for various wall and freestream conditions. Efforts are also required to extend the envelop of the widely accepted correlations by suggesting suitable scaling parameters.

Provision of leading edge bluntness has been considered for separation control in some of the reported studies [14, 16]. However some researchers [8, 17] provide cautious remark about the same since it does not always decrease the separation bubble length. Among those limited studies as well, diversity has been noticed for reasoning the anomaly of this control technique [8, 17]. It has also been noticed that, all those findings focus on relative change in separation bubble size with increase in leading edge radius. Therefore emphasis of their studies has been limited to only one critical radius after which separation bubble size decreases. However, such relative decrement should not just be accounted since decrease in separation bubble size in comparison with the sharp leading edge case is essential for implementation of this technique as the separation control technique. Hence, this fact portrays the existence of second critical radius beyond which separation control can be guaranteed. Thus the investigations for R-SWBLI, in the presence of leading edge bluntness, are required to inspect the flowfield and to analyse the wall data to understand the flow physics near the critical radii. In addition to this, the parametric influence of freestream and surface conditions on these critical radii for R-SWBLI also needs to be visited. Another important observation from the literature is the opposing effect of leading edge bluntness on two dimensional and axisymmetric configurations [15]. Thus, reasoning for the same and understanding the flow physics for such anomalous behaviour remains as the goal of current investigations.

Thus the major objectives of present studies are,

1. Development of 2D-axisymmetric unstructured finite volume compressible flow Navier-Stokes solver for investigations of SWBLI.
2. Validation of Euler part of the solver and investigation for suitability of various upwind schemes for different high speed flow applications
3. Validation of complete Navier-Stokes solver for both 2D and axisymmetric simulations

4. Shock wave boundary Layer Interaction studies to understand the effect of Mach number, wall temperature, ramp angle and total temperature on upstream influence, boundary layer separation and wall heat transfer rate.
5. Quantitative prediction of various SWBLI parameters, reported in the literature, from the qualitative examination using pressure measurements
6. Assessment of the literature reported correlations for prediction of extent of upstream influence, separation bubble size, peak heating and plateau and separation point pressure.
7. Suggestion of suitable modifications in these correlations to extend their envelop of application.
8. Investigations for blunt leading edge based SWBLI control to identify the critical radii of bluntness and understand flow physics around them.
9. Studies on effect of various freestream and wall conditions on critical radii of R-SWBLI.
10. Examine the leading edge effect on axisymmetric shock wave boundary layer interactions in comparison with the two dimensional counterpart of the same.

1.7 Structure of the Thesis

This section is devoted to outline of the present thesis. Chapter-2 presents the detailed numerical frame work of the in-house developed solver, 'USHAS'. Therefore governing equations, boundary conditions, flux splitting schemes, gradient calculation strategy, implementation of higher order spatial and temporal accuracy, convergence acceleration through implicitization etc., are explained in detail over there. In Chapter-3, extensive validation studies of different aspects of the in-house developed solver are described. Validation studies employing both inviscid and viscous flow test cases are discussed in this chapter. Verification and validation of higher order spatial accuracy and equilibrium chemistry model are also covered there. Investigations about applicability of different convective flux splitting schemes for hypersonic flow simulations are discussed in Chapter-4. Important conclusions about efficient use of different convective flux schemes are summarized in this chapter. Effects of various freestream and geometric parameters on R-SWBLI are presented in Chapter-5. Multiple experimental conditions are employed

in the numerical studies discussed there. Numerical confirmation of experimental observation about SWBLI of blunt leading edge domain can also be found in this chapter. Numerical assessment of correlations for SWBLI is the topic of discussion of Chapter-6. Useful modifications in existing correlations to extend their applicability for various flowfield situations are explained in this Chapter. Chapter-7 is devoted to the explorations of leading edge bluntness effect on R-SWBLI. Existence of two critical radii, and the prediction strategy of those radii are explained in detail in this chapter. Effect of freestream and geometric parameters on the critical radii of R-SWBLI is discussed in Chpater-8. Influence of bluntness on axisymmetric flowfield is investigated in Chapter-9. Finally the present research work is summarized in chapter-10 by pointing out various important findings of present work and hinting about the scope of future work.

Chapter 2

Numerical formulation of "USHAS"

Overview

This chapter initially deals with the discussion about governing equations for the compressible flow. Detailed information about the cell centered finite volume formaulation adopted for the present solver is also provided herein. The various inviscid flux computation schemes and implementation of higher order accuracy for the same is part of this chapter. Implementation of equilibrium gas model along with the perfect gas one is also presented. Viscous flux calculation and various time integration techniques are also discussed.

2.1 Governing equations

The overwhelming growth of computer technology has placed computational fluid dynamics in such a position to use it as an effective tool for the design of civil aircrafts and hypersonic airplanes. In this scenario, the physical and numerical problems to be solved cover a wide range of the fluid flow regimes. Essentially CFD is a numerical method which seeks the solution of complex flows using corresponding governing equations. Since this method solves complete set of governing equations with the assistance of advanced computer technology, it provides solution for complex flows at relatively less cost in comparison with experiments. In the hypersonic continuum flow regime, Euler and Navier-Stokes (N-S) equations are the governing equations. These equations are based on the principles of conservation of mass (continuity), momentum (Newton's law of motion) and energy (first law of thermodynamics). Detailed understanding of viscous effects necessitate complete solution of N-S equations with proper implementation of physical boundary conditions.

Here in the present research, investigation of both planar 2D and axisymmetric flowfields are planned. Hence the 2D-axisymmetric compressible flow governing N-S equations are considered for solver development. The vector form of 2D-axisymmetric N-S equation can be expressed as,

$$\frac{\partial U}{\partial t} + \frac{\partial E_I}{\partial x} + \frac{\partial F_I}{\partial y} + \alpha S_I = \frac{\partial E_V}{\partial x} + \frac{\partial F_V}{\partial y} + \alpha S_V \tag{2.1}$$

where U is the conservative variable vector, E_I and F_I are convective fluxes in x and y directions respectively, while S_I represents inviscid axisymmetric source term. Similarly E_v and F_v are the viscous fluxes in x and y directions, where as S_v is the axisymmetric viscous source term. Additionally $\alpha = 0$ presents two dimensional planar flow governing equations and $\alpha = 1$ represents two dimensional axisymmetric flow governing equations. These flux vectors are given as,

$$U = \begin{bmatrix} \rho \\ \rho u \\ \rho v \\ \rho E \end{bmatrix} \tag{2.2}$$

$$E_I = \begin{bmatrix} \rho u \\ \rho u^2 + p \\ \rho uv \\ \rho u(E + \frac{p}{\rho}) \end{bmatrix} \tag{2.3}$$

$$F_I = \begin{bmatrix} \rho v \\ \rho uv \\ \rho v^2 + p \\ \rho v(E + \frac{p}{\rho}) \end{bmatrix} \tag{2.4}$$

$$S_I = \frac{1}{y} \begin{bmatrix} \rho v \\ \rho uv \\ \rho v^2 \\ \rho v(E + \frac{p}{\rho}) \end{bmatrix} \tag{2.5}$$

$$E_V = \begin{bmatrix} 0 \\ \tau_{xx} \\ \tau_{xy} \\ u\tau_{xx} + v\tau_{xy} - q_x \end{bmatrix} \tag{2.6}$$

$$F_V = \begin{bmatrix} 0 \\ \tau_{xy} \\ \tau_{yy} \\ u\tau_{xy} + v\tau_{yy} - q_y \end{bmatrix} \tag{2.7}$$

$$S_V = \begin{bmatrix} 0 \\ \tau_{xy} - \frac{2}{3} y \frac{\partial}{\partial x}(\mu v/y) \\ \tau_{yy} - \tau_{\theta\theta} - \frac{2}{3}\mu(\frac{v}{y}) - \frac{2}{3} y \frac{\partial}{\partial y}(\mu v/y) \\ u\tau_{xy} + v\tau_{yy} - q_y - \frac{2}{3}\frac{\mu v^2}{y} - \frac{2}{3} y \frac{\partial}{\partial y}(\mu v^2/y) - \frac{2}{3} y \frac{\partial}{\partial x}(\mu uv/y) \end{bmatrix} \tag{2.8}$$

The shear stress and heatflux components in the above vectors can be written as,

$$\tau_{xx} = \mu \left(\frac{4}{3}\frac{\partial u}{\partial x} - \frac{2}{3}\frac{\partial v}{\partial y} \right) \tag{2.9}$$

$$\tau_{yy} = \mu \left(\frac{4}{3}\frac{\partial v}{\partial y} - \frac{2}{3}\frac{\partial u}{\partial x} \right) \tag{2.10}$$

$$\tau_{xy} = \mu \left(\frac{\partial u}{\partial y} + \frac{\partial v}{\partial x} \right) \tag{2.11}$$

$$\tau_{\theta\theta} = \mu \left(-\frac{2}{3}\left(\frac{\partial u}{\partial y} + \frac{\partial v}{\partial x} \right) + \frac{4v}{3y} \right) \tag{2.12}$$

$$q_x = -k\frac{\partial T}{\partial x}, q_x = -k\frac{\partial T}{\partial y} \tag{2.13}$$

Sl.No.	Variable	Reference scale	Normalized variable
1	Length (x_i)	L_{ref}	${x_i}^* = x_i/L_{ref}$
2	Velocity (u_i)	U_∞	${u_i}^* = u_i/U_\infty$
3	Time (t)	L_{ref}/U_∞	$t^* = (tU_\infty)/L_{ref}$
4	Density (ρ)	ρ_∞	$\rho^* = \rho/\rho_\infty$
5	Dynamic viscosity (μ)	μ_∞	$\mu^* = \mu/\mu_\infty$
6	Pressure (p)	$\rho_\infty {U_\infty}^2$	$p^* = p/\rho_\infty {U_\infty}^2$
7	Temperature(T)	T_∞	$T^* = T/T_\infty$
8	Total specific Energy (E)	U_∞^2	$E^* = E/U_\infty^2$

TABLE 2.1: Normalization scales and the normalized variables

2.1.1 Normalized (non-dimensional) form of the governing equations

Non-dimensional form of governing equations are used to develop the present solver. In view of this development the non-dimensional variables are defined with reference to freestream values. The typical non-dimensionalisation strategy of present solver is given in table 2.1.

Thus obtained non-dimensional N-S equations are again identical to their dimensional form. However the elements of vector are non-dimensional parameters. Although the non-dimensional variables of modified N-S equations differ from earlier dimensional values, here onwards, while mentioning the governing equations the "$*$" distinguishing the non-dimensional variables are omitted, for the sake of clarity. The non-dimensionalisation mainly modifies the viscous source vector in equation (2.8) along with the definitions of shear stresses and heatflux components. Therefore only those modified terms are redefined bellow.

$$\tau_{xx} = \frac{\mu}{Re_\infty}\left(\frac{4}{3}\frac{\partial u}{\partial x} - \frac{2}{3}\frac{\partial v}{\partial y}\right) \tag{2.14}$$

$$\tau_{yy} = \frac{\mu}{Re_\infty}\left(\frac{4}{3}\frac{\partial v}{\partial y} - \frac{2}{3}\frac{\partial u}{\partial x}\right) \tag{2.15}$$

$$\tau_{xy} = \frac{\mu}{Re_\infty}\left(\frac{\partial u}{\partial y} + \frac{\partial v}{\partial x}\right) \tag{2.16}$$

$$\tau_{\theta\theta} = \frac{\mu}{Re_\infty}\left(-\frac{2}{3}\left(\frac{\partial u}{\partial y} + \frac{\partial v}{\partial x}\right) + \frac{4v}{3y}\right) \tag{2.17}$$

$$q_x = -\frac{\mu}{Re_\infty P_r(\gamma-1)M_\infty^2}\frac{\partial T}{\partial x}, q_x = -\frac{\mu}{Re_\infty P_r(\gamma-1)M_\infty^2}\frac{\partial T}{\partial y} \tag{2.18}$$

The modified viscous source vector is now defined as,

$$S_V = \begin{bmatrix} 0 \\ \tau_{xy} - \frac{2}{3}\frac{y}{Re_\infty}\frac{\partial}{\partial x}(\mu v/y) \\ \tau_{yy} - \tau_{\theta\theta} - \frac{2}{3}\frac{\mu}{Re_\infty}(\frac{v}{y}) - \frac{2}{3}\frac{y}{Re_\infty}\frac{\partial}{\partial y}(\mu v/y) \\ u\tau_{xy} + v\tau_{yy} - q_y - \frac{2}{3}\frac{\frac{\mu}{Re_\infty}v^2}{y} - \frac{2}{3}\frac{y}{Re_\infty}\frac{\partial}{\partial y}(\mu v^2/y) - \frac{2}{3}\frac{y}{Re_\infty}\frac{\partial}{\partial x}(\mu uv/y) \end{bmatrix} \tag{2.19}$$

where Re_∞ is Reynolds number ($Re_\infty = \rho_\infty U_\infty L_{ref}/\mu_\infty$), P_r is Prandtl number defined as, (P_r=$\mu_\infty Cp_\infty/k_\infty$) and M_∞ is the Mach number ($M_\infty = U_\infty/a_\infty$).

In order to close the N-S equations described above, it is necessary to construct the relationships between the thermodynamic variables (p, ρ, T) as well as to relate the transport properties (μ, k) to these thermodynamic variables. Since the present solver considers non-dimensional form of the equations, the Prandtl number value is necessary at each cell centroid instead of thermal conductivity k. Thus the requirement of closedness of N-S equations is achieved in the present solver by make use of two different gas models, the details of which would be discussed in later section of this chapter.

2.2 Finite volume method

Finite volume method (FVM) is the most versatile method among the standard techniques since it is highly successful in approximating the solution of wide variety systems. It is very much suitable for compressible flows since it is based on integration of conservation equations. It can also be easily implemented on structured as well as on unstructured grids and hence is

particularly suitable for treatment of flows in complex geometries. However, it is necessary to mesh the domain using non overlapping control volumes which permits the smooth integration of the conservation equations for each small control volume.

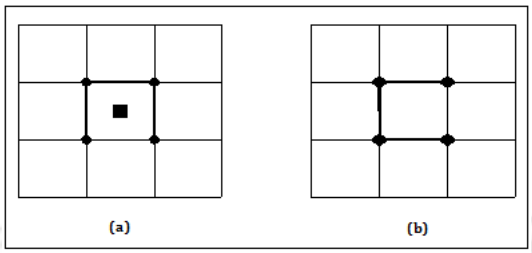

FIGURE 2.1: Representation of FVM approaches a) cell centered scheme b) cell vertex scheme

There are different frameworks established in FVM to arrange the finite control volumes in a given grid. The basic approaches among those are cell-centered and cell-vertex as shown in figure 2.1(a) and figure 2.1(b) respectively. In cell-centered approach, the flow quantities are stored at the centroid of the grid cells. Thus, the control volumes are identical to the grid cells. In this approach, we have to compute the fluxes at the cell faces. In cell-vertex scheme the flow variables are stored at the grid points. The control volume can either be the union of all cells sharing the grid point, or some volume centered around the grid point. The former case is referred as overlapping control volume, while the second case is termed as dual control volumes. Although the truncation error analysis has shown different behavior for the different arrangements of control volumes, sufficient accurate results were achieved with both the approaches. In present formulation, cell centered scheme is used because of its simplicity in formulation.

The present solver is written in unstructured data format. Therefore the solver can handle both structured and unstructured grids irrespective of its topology. Compared to structured grids unstructured grids are easier to generate for any complex geometry. Moreover in case of unstructured grids, grid cells and grid points have no particular ordering. Therefore neighbouring cells or grid points cannot be directly identified by their indices. However in the present solver, both structured and unstructured grid informations are treated in unstructured data format. In view of this grid connectivity information is the prime requirement for this solver. Face based algorithm is implemented in order to reduce the computational time and also for ease of future parallelization.

2.3 Theoretical formulation of cell centered FVM

The Integral form of the 2D- axisymmetric Navier-Stokes equations discussed in section 2.1 can be written as,

$$\int_{\Omega}\left(\frac{\partial U}{\partial t}+\frac{\partial(E_I-E_V)}{\partial x}+\frac{\partial(F_I-F_V)}{\partial y}+\alpha(S_I-S_V)\right)\mathrm{d}\Omega=0 \tag{2.20}$$

This equation can be rearranged as,

$$\int_{\Omega}\frac{\partial U}{\partial t}\mathrm{d}\Omega=-\int_{\Omega}\left(\frac{\partial(E_I-E_V)}{\partial x}+\frac{\partial(F_I-F_V)}{\partial y}+\alpha(S_I-S_V)\right)\mathrm{d}\Omega \tag{2.21}$$

Left hand side of equation (2.21) can be written as,

$$\begin{aligned}\int_{\Omega}\frac{\partial \mathrm{U}}{\partial \mathrm{t}}\,\mathrm{d}\Omega &= \frac{\partial}{\partial \mathrm{t}}\int_{\Omega}\mathrm{U}\,\mathrm{d}\Omega\\ &= \frac{\mathrm{d}}{\mathrm{dt}}(\overline{U}\Omega)\\ &= \Omega\frac{\mathrm{d}\overline{U}}{\mathrm{d}t}\end{aligned} \tag{2.22}$$

where

$$\overline{\mathrm{U}}=\frac{\int_{\Omega}\mathrm{U}\,\mathrm{d}\Omega}{\int_{\Omega}\mathrm{d}\Omega}$$

For the right hand side of equation (2.21) we have,

$$\begin{aligned}&\int_{\Omega}\left(\frac{\partial(E_I-E_V)}{\partial x}+\frac{\partial(F_I-F_V)}{\partial y}+\alpha(S_I-S_V)\right)\mathrm{d}\Omega\\ &\quad=\int_{\Omega}\left(\nabla.(H_I-H_V)+\alpha(S_I-S_V)\right)\mathrm{d}\Omega\end{aligned} \tag{2.23}$$

where,

$$H_I=\begin{bmatrix}E_I & F_I\end{bmatrix},H_V=\begin{bmatrix}E_V & F_V\end{bmatrix},\quad \nabla=\begin{bmatrix}\frac{\partial}{\partial x} & \frac{\partial}{\partial y}\end{bmatrix}$$

Let,

$$H = H_I - H_V \tag{2.24}$$

According to Gauss Divergence theorem,

$$\int_\Omega \nabla . H \, \mathrm{d}\Omega = \int_S H . \hat{n} \, \mathrm{d}S \tag{2.25}$$

where,

$$\hat{n} = \begin{bmatrix} n_x & n_y \end{bmatrix} \tag{2.26}$$

where, $\hat{n}$ unit normal pointing outward the control volume, n_x and n_y are the x and y component of the unit vector $\hat{n}$.

$$\int_S H . \hat{n} \, \mathrm{d}S = \sum_{J \epsilon \Omega} H_J . \hat{n}_J \, \Delta S_J = \sum_{J \epsilon \Omega} H_{\perp J} \, \Delta S_J \tag{2.27}$$

where Ω is the area of control volume in 2D and ΔS_J is the length of the face of a control volume. Whereas, $H_\perp$ is the total normal flux of a face, which include both viscous and inviscid contributions. Thus,

$$H_\perp = H_{I_\perp} - H_{V_\perp} \tag{2.28}$$

where,

$$\mathrm{H_{I_\perp}} = \begin{bmatrix} \rho u_\perp \\ \rho u u_\perp + p n_x \\ \rho v u_\perp + p n_y \\ (\rho e + p) u_\perp \end{bmatrix}$$

$$\mathrm{H_{V_\perp}} = \begin{bmatrix} 0 \\ n_x \tau_{xx} + n_y \tau_{xy} \\ n_x \tau_{yx} + n_y \tau_{yy} \\ n_x \Theta_x + n_y \Theta_y \end{bmatrix}$$

where the contravariant velocity $u_\perp$ given as,

$$u_\perp = u.n_x + v.n_y \tag{2.29}$$

In energy equation the terms dealing with work done by viscous force and heat transfer by heat conduction can be written as,

$$\begin{aligned} \Theta_x &= u\tau_{xx} + v\tau_{xy} - q_x \\ \Theta_y &= u\tau_{yx} + v\tau_{yy} - q_y \end{aligned} \tag{2.30}$$

Similar to equation (2.22),

$$\int_\Omega \alpha(S_I - S_V)\,\mathrm{d}\Omega = \alpha\Omega\overline{S} \tag{2.31}$$

where,

$$\overline{S} = \overline{S}_I - \overline{S}_V \tag{2.32}$$

Therefore from equation (2.22), (2.27) and (2.31) the integral form of the governing Equation (2.21) can be rewritten as,

$$\Omega_\mathrm{i}\frac{\mathrm{d}\overline{\mathrm{U}}_\mathrm{i}}{\mathrm{dt}} + \sum_{\mathrm{J}\epsilon\mathrm{i}} \mathrm{H}_{\perp_\mathrm{J}}\,\Delta\mathrm{S}_\mathrm{J} + \alpha\Omega_\mathrm{i}\overline{\mathrm{S}}_\mathrm{i} = 0$$

$$\frac{\mathrm{d}\overline{\mathrm{U}}_\mathrm{i}}{\mathrm{dt}} = -\frac{1}{\Omega_\mathrm{i}}\sum_{\mathrm{J}\epsilon\mathrm{i}} \mathrm{H}_{\perp_\mathrm{J}}\,\Delta\mathrm{S}_\mathrm{J} - \alpha\overline{\mathrm{S}}_\mathrm{i} = \mathrm{R}(\overline{\mathrm{U}}_\mathrm{i}) \tag{2.33}$$

This is the semi-discrete finite volume update. The conserved variable vector and source vector in the equations are derived out of cell-centered quantities.

2.4 Spatial discretization

Having written the semi-discrete form of the governing equations for each control volume as in equation (2.33), the residual $R(\overline{U}_i)$ needs to be evaluated to perform time marching. In finite volume method this cell centroid residual calculation requires evaluation of inviscid and viscous fluxes at each face of the control volume. Hence the solution methodology employed for the calculation of face fluxes has vital role in deciding the accuracy of the final result. The convective and viscous flux calculation methodologies adopted in the present solver are discussed below.

2.4.1 Calculation of convective fluxes

The unsteady compressible inviscid flow governing equations are hyperbolic in nature. The property of nonlinear hyperbolic system of equations allows discontinuities in the solution even if the initial condition is smooth. Therefore concerned numerical discretization schemes, based on the information propagation direction, are known as upwind schemes. Here in the present study seven different upwind schemes, which belong to either of the following two categories are considered.

- Flux-vector splitting
- Flux difference splitting

The flux-vector splitting methods can be viewed as the first level of upwind schemes, since they only account for the direction of wave propagation. The flux-vector splitting schemes decompose the vector of the convective fluxes into two parts according to the sign of characteristic variables. The second category, flux-difference splitting schemes is based on the solution of the local the Riemann (shock tube) problem. The upwind schemes that are incorporated in the present solver along with their references and flux formulations are given in Appendix A. Each of these schemes have advantages and limitations, which are explored through various numerical studies in next chapter.

2.4.2 Reconstruction and implementation of second order spatial accuracy

Upwind schemes require flow variables to be computed on the either sides of the faces of a control volume. These states can be assigned by extrapolating cell centroid values directly to the control volume faces, if only first order accuracy in spatial discretization is expected. But for enhancing the accuracy of results one should implement higher order extrapolation techniques in the solver. In the present solver second order accuracy in spatial discretization is achieved by implementing piecewise linear reconstruction method suggested by Barth and Jespersen [70]. In this reconstruction technique, it is assumed that solution is piecewise linearly distributed in the

control volume. For a cell-centered scheme, Barth and Jespersen calculated the left and right states for a control surface using the following relations,

$$\begin{aligned} U_L &= U_i + \varphi\left(\nabla U_i \cdot \vec{r_L}\right) \\ U_R &= U_i + \varphi\left(\nabla U_j \cdot \vec{r_R}\right) \end{aligned} \tag{2.34}$$

where ∇U_i is the gradient of any flow variable U at the cell center I , which is given by,

$$\nabla U_i = \left[\frac{\partial U}{\partial x}, \frac{\partial U}{\partial y}\right]^T \tag{2.35}$$

The term φ is the limiter function. Here, $\vec{r_L}$ and $\vec{r_R}$ are the vectors pointing from the cell-centroid to the face centroid as shown in the figure 2.2.

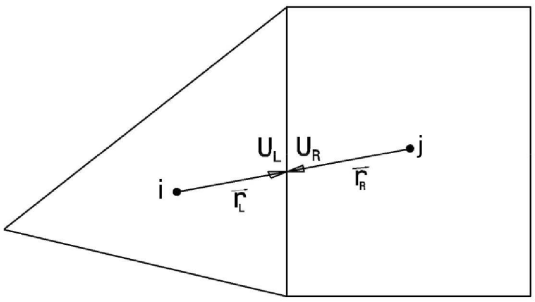

FIGURE 2.2: Linear reconstruction for the cell centered scheme

Another important fact in this contest is that without a flux limiter, solution of second or higher order schemes suffers from oscillations in the neighborhood of discontinuities. This situation is generally referred to as monotonicity lose. So care must be taken in the implementation of reconstruction to ensure the monotonicity while, reconstructing left and right variable values. This is achieved by the use of limiters. At strong discontinuities, limiter will reduce the slope to zero to prevent the generation of a new extremum, thus at the region of discontinuity, solution becomes first order accurate in order to ensure monotonicity. Therefore popular Venkatakrishnan limiter [71, 72] implementation is used in the present solver. Venkatakrishnan's limiter offers

monotonic solution as well as better convergence to steady state. According to this methodology the limiter function is calculated as follows.

$$\varphi = \left\{ \begin{array}{ll} \frac{1}{\Delta_2}\left[\frac{(\Delta_{1,max}{}^2+\varepsilon^2)\Delta_2 + 2\Delta_2{}^2\Delta_{1,max}}{\Delta_{1,max}^2 + 2\Delta_2{}^2 + \Delta_{1,max}\Delta_2 + \varepsilon^2}\right] & \text{if } \Delta_2 > 0 \\ \frac{1}{\Delta_2}\left[\frac{(\Delta_{1,min}{}^2+\varepsilon^2)\Delta_2 + 2\Delta_2{}^2\Delta_{1,max}}{\Delta_{1,max}^2 + 2\Delta_2{}^2 + \Delta_{1,max}\Delta_2 + \varepsilon^2}\right] & \text{if } \Delta_2 < 0 \\ 1 & \text{if } \Delta_2 = 0 \end{array} \right\} \tag{2.36}$$

where,

$$\begin{aligned} \Delta_{1,max} &= U_{max} - U_i \\ \Delta_{1,min} &= U_{min} - U_i \end{aligned} \tag{2.37}$$

where U_{max} and U_{min} are the maximum and minimum values of all surrounding cells j, including the cell i itself, and are given by;

$$\begin{aligned} U_{max} &= max\left(U_i, max_j U_j\right) \\ U_{min} &= min\left(U_i, min_j U_j\right) \end{aligned}$$

$$\Delta_2 = \nabla U_i \cdot \vec{r_L}$$

For avoiding the division by zero, Δ_2 is generally specified as,

$$\Delta_2 = |\Delta_2| + w$$

where, w is approximate machine accuracy, $\vec{r}$ denotes the vector from the cell centroid to the corresponding face centroid. The parameter ε^2 is evaluated as,

$$\varepsilon^2 = (K\Delta h)^3$$

where K is a constant of order one (generally taken as 2) and Δh is square root of area in 2D and cube root of volume in 3D. The solution accuracy and convergence obtained with Venkatakrishnan's limiter largely depends on the K value. Setting the value of $K = 0$, results in full limiting, which in turn leads to poor convergence. Whereas the use of large K values leads to no-limiting condition, thereby offers spurious solutions. So fine turning of the K is required to maintain optimum trade off between convergence and solution accuracy. Although the Venkatakrishanan's limiter offers substantial improvement in solution accuracy and convergence, the computational cost for the calculation of this limiter function is relatively high. The additional computations of the parameters involved in this limiter function necessitate additional time and storage. These pitfalls of the Venkatakrishnan's are tolerated to aim the solution accuracy and convergence.

2.5 Calculation of viscous fluxes

Evaluation of the viscous fluxes at the faces of the control volume requires flow quantities and their first derivatives at the faces. For the execution of it, the control volume definition considered for the viscous flux calculation is the same as that considered for inviscid flux computations. Such usage of unique control volume for both inviscid and viscous flux calculations helps in simplifying the data structure. Hence in the present cell-centered formulation, the values of a particular flow variable at the face is achieved by averaging the values of same quantity at the left and right cell of that particular face.

$$U_{i,j} = \frac{1}{2}\left(U_i + U_j\right) \tag{2.38}$$

where, $U_{i,j}$ represents the flow variable value at the face.

The next requirement is the evaluation of first derivatives of velocity components and temperature at the face centroids. Therefore the derivatives of primitive variables are first calculated at the cell centroid using discrete version of the Gauss theorem [73] given as,

$$\int_{\Omega} \nabla U \mathrm{d}\Omega = \int_{S} U \hat{n} \mathrm{d}S \tag{2.39}$$

where U is any scalar function, $\hat{n}$ is outward-pointing surface normal vector of control volume Ω. With the assumption of constant nature of ∇U over the control volume the Green-Gauss theorem can be rearranged as,

$$\nabla U\Omega = \int_S U\hat{n}\mathrm{d}S = \sum_J U_J \,.\vec{S_J} \tag{2.40}$$

here J represents the face index.

Therefore,

$$\nabla U = \frac{1}{\Omega}\sum_J U_J \,.\vec{S_J} \tag{2.41}$$

Thus evaluated gradients are used to calculate the same at nodes sharing the cell. Thus obtained nodal gradients are used to calculate the same at faces.

2.6 Implementation of boundary conditions

The imposition of precise boundary conditions is of extreme significance in obtaining an accurate numerical solution. In order to retain the generalization of present solver 'USHAS', various boundary conditions are employed and the formulation for them is discussed here.

2.6.1 Inviscid wall (free slip) or symmetry boundary condition

In case of inviscid flow, fluid is allowed to slip over the surface freely. That means the frictional forces at the inviscid wall are assumed to be zero. This allows the specification of non-zero tangential velocity at this boundary. However the inviscid wall must be treated as impermeable, therefore the normal component of velocity must be assigned as zero.i.e,

$$\vec{V}.\vec{n} = 0 \tag{2.42}$$

Further more if a flow is symmetric about any plane then net flux normal to the boundary is zero. Therefore, although the physics of inviscid wall and symmetry boundary conditions are

different, their implementation is same. The constraint of this boundary condition is that, the velocity must be tangent to this boundary and normal component of velocity must be zero. Numerical implementation of these boundary conditions is achieved by one of the following way.

1. **Mirror or Ghost cell approach:** In this approach velocity in ghost cell is taken as shown in figure 2.3

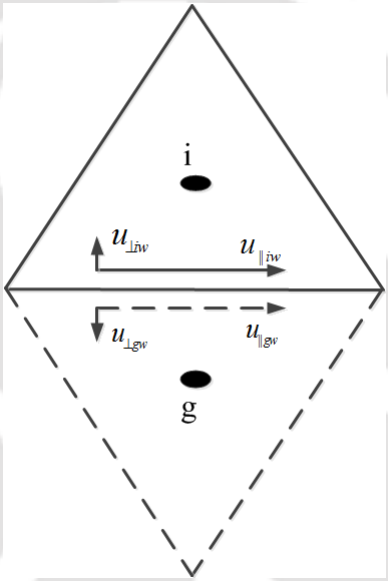

FIGURE 2.3: Mirror cell approach

$$\boldsymbol{u_{\perp_{gw}} = -u_{\perp_{iw}}, u_{\parallel_{gw}} = u_{\parallel_{iw}}, p_g = p_i, \rho_g = \rho_i}$$

where, 'g' and 'i' refer to ghost state and interior state respectively. The subscript, w represents the values on the boundary. The main advantage of mirror boundary-condition is that it permits the use of interior scheme on the wall boundary and thus it takes into account direction of propagation waves. The drawback is that, it does not take into account the effect of curvature and it is dissipative. The variables other than the normal velocity such as the tangential velocity and thermodynamic properties are to be obtained from the interior flow. Pressure at the boundary can be obtained by solving the momentum equation or by extrapolating from the interior points.

2. **Pressure extrapolation boundary condition:** This is an alternative way of assigning inviscid wall boundary condition using the fact that, there is no flow normal to the inviscid wall,

$$\vec{V}.\vec{n} = 0 \quad \text{at the surface,}$$

Hence the contravariant velocity is zero at the wall. Consequently, the elements of flux vector reduces to pressure term alone, i.e.,

$$H_{\perp_w} = p_w \begin{bmatrix} 0 \\ n_x \\ n_y \\ 0 \end{bmatrix}$$

Both the approaches are implemented in 'USHAS'. This solver is capable of switching between either of these two implementations

2.6.2 No slip boundary or viscous wall

No slip condition has been implemented for wall faces through mirror cell approach. Here this approach confirms zero value of tangential as well as normal velocity at the wall. The pressure values at the wall faces are extrapolated from the immediate interior cell. Temperature boundary conditions for the wall differ for isothermal and adiabatic cases. For isothermal boundary, the wall temperature is set with a known constant value, whereas for adiabatic condition, the gradients of temperature are set as zero.

Hence by referring to figure 2.3, for an adiabatic wall, the mirror cell approach gives,

$$\boldsymbol{u}_{\perp_{g_w}} = -\boldsymbol{u}_{\perp_{i_w}}, \boldsymbol{u}_{\parallel_{g_w}} = -\boldsymbol{u}_{\parallel_{i_w}}, \boldsymbol{p_g} = \boldsymbol{p_i}, \boldsymbol{\rho_g} = \boldsymbol{\rho_i}, \boldsymbol{E_g} = \boldsymbol{E_i}$$

For isothermal wall boundary,the velocity components are still reversed as in the case of adiabatic wall. Pressure is again calculated using the mirror wall approach with the consideration of zero pressure gradient normal to the wall boundary. The temperature at the boundary face is set with given constant value and the density and total energy are then evaluated using the known wall temperature and pressure.

2.6.3 Inflow/Outflow boundary conditions

The number of variables need to be imposed at the inflow or outflow boundary for a well-posed problem varies depending on whether the flow is locally subsonic or supersonic and is determined from the characteristic theory [74]. In this work mainly supersonic inflow and outflow conditions are considered.

1. **Supersonic inflow boundary**

   According to characteristic theory, for supersonic inflow, all eigenvalues values have the same sign. Therefore at the supersonic inflow boundary, all the flow variables are set to the freestream values corresponding to typical hypersonic flight conditions or ground test conditions.

2. **Supersonic outflow boundary**

   In this case most of the flowfield is assumed to be supersonic at the outflow boundary where it leaves the computational domain. Again this situation also gives all eigenvalues of same sign. Therefore with the consideration of zero upstream influence of supersonic flow, the flow variables at the supersonic outflow boundary are extrapolated from the interior cell. In the present study, a zeroth order extrapolation is used.

2.7 Gas models

It has been mention earlier in section 2.1 that, to ensure the closedness of compressible flow governing N-S equations, it is necessary to construct the relationships between the thermodynamic variables (p, ρ, T) as well as to relate the transport properties (μ, k) to these thermodynamic variables. This section deals with two different gas models through which these objectives are accomplished.

2.7.1 Perfect gas model

This gas model assumes thermally and calorically perfect nature of the flowfield, therfore the ideal gas equation of state can be used to correlate the thermodynamic properties as,

$$p = \rho RT \tag{2.43}$$

where R is the characteristic gas constant. Further the specific energy e, enthalpy h, and the speed of sound a can be correlated as,

$$e = \frac{RT}{(\gamma - 1)}, \quad h = \frac{\gamma RT}{(\gamma - 1)}, \quad a = \sqrt{\frac{\gamma p}{\rho}} \tag{2.44}$$

where γ is the specific heat ratio for the gas of interest, considered to be 7/5 = 1.4 for air.

After correlating the thermodynamic properties, now let us look in to the calculation of transport properties (k and μ) under this gas model. Since the equations are solved in non-dimensional format, it is not necessary to explicitly calculate the thermal conductivity of the fluid. Instead of that, the Prandtl number needs to be specified in the present solver frame work. For the perfect gas model the Prandtl number of the fluid is considered as constant. for air as working fluid it is used as 0.71.

Viscosity model

The present solver considers Sutherland's viscosity model [75] for calculation of coefficient of dynamic viscosity under perfect gas model. The fluid (air) is assumed to be an ideal gas. Therefore the Sutherland's model correlates the dynamic viscosity of air with temperature as,

$$\mu = \mu_{ref} \left(\frac{T}{T_{ref}} \right)^{3/2} \left(\frac{T_{ref} + S}{T + S} \right) \tag{2.45}$$

where, T_{ref} is the reference temperature, which is taken as 273.15 K for the present study, while μ_{ref} is the viscosity of air at reference temperature ($17.16 \times 10^{-6} Ns/m^2$). In equation (2.45), the Sutherland's constant S for air is taken as, 110.56.

2.7.2 Equilibrium flow model

At high speed flows, particularly at hypersonic high enthalpy flows, the perfect gas assumption may not be valid. Presence of dissociation or ionization reactions make this violation. Therefore the chemical reactions involved in the flow field must be modeled to get accurate results. Such high speed chemically reacting flows can be mainly classified into three.

1. **Frozen flow:** This is one of the extream conditions for the chemically reacting flows. Here the underlying assumption is that, the chemical reactions are exteamily slow so that the high speed flow passing the domain does not feel the effect of chemical reactions. Let T_f be the time required for a fluid particle to pass the specified domain at a specified velocity and let T_c be the time required for the chemical reaction. Then fluid flow will be in a state of frozen flow, if $T_f \gg T_c$.
2. **Equilibrium flow:** In the flowfield, if reactions rate are extreamly high, then chemical reactions take place instantaneously and the flow passing the domain will be in a state of chemical equilibrium. Thus in case of a equilibrium flow $T_f \ll T_c$. For a chemical equilibrium flow, the specific heats are the function of both pressure and temperature. The gas constant also vary because of the changes in molecular weight of the mixture.
3. **Non-equilibrium flow:** The above mentioned flow situations are two extream conditons of hypersonic flow. In reality both of them may not exist. That means the flow will be in a state of reaction. This situation is termed as non-equilibrium flow. For non-equilibrium flow, equation of state is valid, but the gas constant is a variable due to continuously changing molecular weight of the mixture. In order to analyse non-equilibrium reacting flows, one must take care of all the reactions involved in the flow and they are to be modeled accurately.

As an outcome of above discussions it should be noted that non-equilibrium reacting flow models are to be considered in real hypersonic flows. It has been observed that equilibrium flow model can also give accurate results in many hypersonic applications. The general approach to include equilibrium chemistry model needs to solve the governing eqution for the partial pressures of the species. If we restrict our studies to flow involving only air, then we can make

use of already developed various sets of tables and graphs for equilibrium flow modeling. These graphs and tables are based on the governing eqution for the partial pressures of air. One of such well known tabular approch (Tannehil Muge curve fit) [JC and PH] is utilized in this present solver to model equilibrium flows. The details of that implementation are discussed below.

2.7.2.1 Implementation of Tannehil Mugge curve fit

The thermodynamic properties of equilibrium air can be found out from two known thermodynamic variables. Here in this technique density and internal energy are taken as two input thermodynamic variables. Then the solution procedure is followed as below.

1. An effective γ denoted as $\bar{\gamma}$ is first calculated from following equation

$$\bar{\gamma} = a_1 + a_2 Y_1 + a_3 Z_1 + a_4 Y_1 Z_1 + a_5 Y_1^2 + a_6 Z_1^2 + a_7 Y_1 Z_1^2 + a_8 Z_1^3 + \frac{a_9 + a_{10} Y_1 + a_{11} Z_1 + a_{12} Y_1 Z_1}{1 + \exp\left[(a_{13} + a_{14} Y_1)(Z_1 + a_{15} Y_1 + a_{16})\right]} \tag{2.46}$$

where $Y_1 = \log(\rho/1.292)$ and $Z_1 = \log(\mathrm{e}/78408.4)$, ρ is the density in kg/m^3 and e is internal energy in m^2/s^2

2. Once $\bar{\gamma}$ is calculated, then the equation of state is used to find the pressure.

$$p = \rho e(\bar{\gamma} - 1), \tag{2.47}$$

where p is the pressure in N/m^2

3. Next the temperature is computed from the following relation

$$\log\left(\frac{T}{151.78}\right) = b_1 + b_2 Y_2 + b_3 Z_2 + b_4 Y_2 Z_2 + b_5 Y_2^2 + b_6 Z_2^2 + b_7 Y_2 Z_2^2 + b_8 Z_2^3 + \frac{b_9 + a_{10} Y_2 + b_{11} Z_2 + b_{12} Y_2 Z_2 + + b_{13} Z_2^2}{1 + \exp\left[(b_{14} Y_2 + b_{15})(Z_2 + b_{16})\right]} \tag{2.48}$$

where $Y_2 = \log(\rho/1.225)$, $X_2 = \log(p/1.0314 \times 10^5)$, $Z_2 = X_2 - Y_2$

4. Finally the exact expression for sound speed is calculated from

$$a = \left[e \left\{ k_1 + (\gamma - 1) \left[\bar{\gamma} + k_2 \left(\frac{\partial \bar{\gamma}}{\partial \log_e e} \right)_\rho \right] + k_3 \left(\frac{\partial \bar{\gamma}}{\partial \log_e \rho} \right)_e \right\} \right]^{1/2} \tag{2.49}$$

The coefficients used in above equations are taken from reference [JC and PH].

2.8 Temporal discretization

This section discusses about the time integaration methodologies for the attainment of steady state solution. Let us recall the semi-discrete form of the governing equations obtained in equation (2.33) and replace the $\bar{U}_i$, $\bar{S}_i$ with U_i, S_i. ,

$$\frac{\mathrm{d}U_i}{\mathrm{d}t} = -\frac{1}{\Omega_i} \sum_{J \epsilon i} H_{\perp_J} \Delta S_J - \alpha S_i = R(U_i) \tag{2.50}$$

The temporal discretization converts the ordinary differential equations obtained from the spatial discretization to a system of algebraic equations. There are mainly two types of time-marching methods, viz. explicit and implicit. Explicit methods are easy to implement, and their computational cost per time step are low. However the magnitude of the time step for an explicit method is restricted by the Courant-Friedrichs-Levy (CFL) condition to ensure the numerical stability. This stability issue leads to higher computational time especially in case of viscous flow simulations. For steady flow problems, where the higher time accuracy is not essential, much bigger time steps can be used with unconditionally stable implicit schemes. Although the conventional implicit formulations have increased computational cost per time step, they can reduce the entire computational time by order of magnitude through the use of higher time step as compared to explicit formulation. At the early stages of present solver development, explicit time marching strategy has been adapted. The implicitisation of the solver has been performed after successful implementation of explicit strategy.

In house solver ‘USHAS’ has two different explicit time integration provisions. First one is the simple explicit Euler scheme and second is the higher order accurate five stage Runge-Kutta method. The details of these two methods are discussed below.

2.8.1 Simple explicit Euler time stepping

The simple explicit Euler scheme for time integration of equation (2.50), leads to the fully discrete finite volume formulation for a i^{th} control volume as,

$$\frac{\Delta_t U_i}{\Delta t} = R(U_i^n) \tag{2.51}$$

where

$$\Delta_t U_i = U_i^{n+1} - U^n$$

Hence,

$$U_i^{n+1} = U^n + \Delta t R(U_i^n) \tag{2.52}$$

$$U_i^{n+1} = U^n - \frac{\Delta t}{\Omega_i} \sum_{J \epsilon i} H_{\perp_J} \Delta S_J - \alpha \Delta t S_i \tag{2.53}$$

So with the known values of variables at the n^{th} state, $(n+1)^{th}$, state can be explicitly calculated and subsequent time marching can be done. However this scheme is only first order accurate in time, therefore it is less preferable for unsteady time dependent simulations.

2.8.2 Five stage Runge-Kutta scheme

Higher order temporal accuracy is inevitable for unsteady time dependent simulations. One of the popular method of obtaining higher-order accuracy is to perform multiple computations per step using Runge-Kutta methods. Therefore in the present solver an explicit five stage Runge-Kutta scheme has been implemented to achieve higher order temporal accuracy. This scheme is a modified version of classical fourth order Runge-Kutta method [76]. The classical fourth order Runge-Kutta method requires large storage due to evaluation of convective and viscous fluxes for each stage (k=1, 2....no of stages). However the modified five stage Runge-Kutta scheme [77], considered in the present solver development, does not have this limitation, since its calculation for a i^{th} control volume follows the strategy given as,

$$U_i^{(0)} = U_i^n$$

$$U_i^{(m)} = U_i^{(0)} - \alpha_m \left\{ \frac{\Delta t}{\Omega_i} \sum_{J \epsilon i} H_{\perp_J} \Delta S_J - \alpha \Delta t S_i \right\} \quad \text{(m=1,2, ...5)} \tag{2.54}$$

$$U_i^{(n+1)} = U_i^{(5)}.$$

The stage coefficients α_m are tuned to improve stability and damping properties. For an efficient five stage scheme these stage coefficients are given as,

$$\alpha_1 = 1/4,\ \alpha_2 = 1/6,\ \alpha_3 = 3/8,\ \alpha_4 = 1/2,\ \alpha_5 = 1$$

2.8.3 Implicit time stepping

A matrix free implicit method is implemented in the in-house developed solver using Symmetric Gauss-Seidel relaxation procedures in a finite volume framework to accelerate the convergence rate to obtain steady state solution. This time marching strategy follows the implicit formulation given by Ganesh et al. [78] on the basis of implementation of LU-SGS by Luo et al.[79]. Recalling the semi-discrete form of the governing equation given in equation (2.50) and considering solution vector update, we can write,

$$\frac{\mathrm{d}\overline{\mathrm{U}}_\mathrm{i}}{\mathrm{dt}} = \mathrm{R}(\overline{\mathrm{U}}_\mathrm{i}^{\mathrm{n}+1})$$

$$\frac{\Delta_\mathrm{t}\overline{\mathrm{U}}_\mathrm{i}}{\Delta \mathrm{t}} = \mathrm{R}(\overline{\mathrm{U}}_\mathrm{i}^{\mathrm{n}+1}) \tag{2.55}$$

$$\frac{\Delta_\mathrm{t}\overline{\mathrm{U}}_\mathrm{i}}{\Delta \mathrm{t}} = \mathrm{R}(\overline{\mathrm{U}}_\mathrm{i}^{\mathrm{n}} + \frac{\mathrm{d}\overline{\mathrm{U}}_\mathrm{i}}{\mathrm{dt}} \Delta \mathrm{t} + \mathrm{h.o.t}) \tag{2.56}$$

where

$$\Delta_\mathrm{t}\overline{\mathrm{U}}_\mathrm{i} = \overline{\mathrm{U}}_\mathrm{i}^{\mathrm{n}+1} - \overline{\mathrm{U}}^{\mathrm{n}}$$

Neglecting the higher order terms and dropping the overbar representing the cell averaged quantity, this equation reduces to,

$$\frac{\Delta_t U_i}{\Delta t} = R(U_i^n + \Delta_t U_i) \tag{2.57}$$

On expanding the right hand side of equation (2.57) employing Taylor series,

$$\frac{\Delta_t U_i}{\Delta t} = R(U_i^n) + \Delta_t U_i \frac{\partial R}{\partial U} \tag{2.58}$$

Rearranging the above equation,

$$\left[\frac{I}{\Delta t} - \frac{\partial R}{\partial U}\right] \Delta_t U_i = R(U_i^n) \tag{2.59}$$

The implicit residual can be written as,

$$R(U_i^{n+1}) = -\frac{1}{\Omega_i} \sum_{J \epsilon i} H_{\perp J}(U_i^{n+1}, U_j^{n+1})\, \Delta S_J \tag{2.60}$$

Treating the residual term implicitly will reduce it to merely normal flux contributions of faces bounding the control volume. Hence using the flux vector splitting method , the normal flux for any interface J with in-cell i and out-cell j can be written as

$$H_{\perp J}(U_i^{n+1}, U_j^{n+1}) = H_{\perp J}^{+}(U_i^{n+1}) + H_{\perp J}^{-}(U_j^{n+1}) \tag{2.61}$$

Linearising the split normal fluxes,

$$H_{\perp J}^{+}(U_i^{n+1}) = H_{\perp J}^{+}(U_i^{n}) + A_i^{+}(U_i^{n}, \hat{n}_J)\Delta_t U_i \tag{2.62}$$

$$H_{\perp J}^{-}(U_i^{n+1}) = H_{\perp J}^{-}(U_i^{n}) + A_j^{-}(U_j^{n}, \hat{n}_J)\Delta_t U_j \tag{2.63}$$

where,

$$A_i^{+} = \frac{\partial H_{\perp J}^{+}}{\partial U_i} \tag{2.64}$$

$$A_j^{-} = \frac{\partial H_{\perp J}^{-}}{\partial U_j} \tag{2.65}$$

On applying equations (2.62) and (2.63) in equation (2.61) and then substituting in equation

(2.60),

$$\mathrm{R}(\mathrm{U}_{\mathrm{i}}^{\mathrm{n}+1}) = -\frac{1}{\Omega_{\mathrm{i}}}\sum_{\mathrm{J}\epsilon\mathrm{i}} \mathrm{H}_{\perp\mathrm{J}}(\mathrm{U}_{\mathrm{i}}^{\mathrm{n}}, \mathrm{U}_{\mathrm{j}}^{\mathrm{n}})\Delta\mathrm{S}_{\mathrm{J}} - \frac{1}{\Omega_{\mathrm{i}}}\sum_{\mathrm{J}\epsilon\mathrm{i}} \left[\mathrm{A}_{\mathrm{i}}^{+}(\mathrm{U}_{\mathrm{i}}^{\mathrm{n}})\Delta_{\mathrm{t}}\mathrm{U}_{\mathrm{i}} + \mathrm{A}_{\mathrm{j}}^{-}(\mathrm{U}_{\mathrm{j}}^{\mathrm{n}})\Delta_{\mathrm{t}}\mathrm{U}_{\mathrm{j}}\right]\Delta\mathrm{S}_{\mathrm{J}} \quad (2.66)$$

From equation (2.55) we have,

$$\frac{\Delta_{\mathrm{t}}\mathrm{U}_{\mathrm{i}}}{\Delta\mathrm{t}} = \mathrm{R}(\mathrm{U}_{\mathrm{i}}^{\mathrm{n}}) - \frac{1}{\Omega_{\mathrm{i}}}\sum_{\mathrm{J}\epsilon\mathrm{i}} \mathrm{A}_{\mathrm{i}}^{+}(\mathrm{U}_{\mathrm{i}}^{\mathrm{n}})\Delta_{\mathrm{t}}\mathrm{U}_{\mathrm{i}}\,\Delta\mathrm{S}_{\mathrm{J}} - \frac{1}{\Omega_{\mathrm{i}}}\sum_{\mathrm{J}\epsilon\mathrm{i}} \mathrm{A}_{\mathrm{j}}^{-}(\mathrm{U}_{\mathrm{j}}^{\mathrm{n}})\Delta_{\mathrm{t}}\mathrm{U}_{\mathrm{j}}\,\Delta\mathrm{S}_{\mathrm{J}} \quad (2.67)$$

Rearranging the above equation we get,

$$\left[\frac{\mathrm{I}}{\Delta\mathrm{t}} + \frac{1}{\Omega_{\mathrm{i}}}\sum_{\mathrm{J}} \mathrm{A}_{\mathrm{i}}^{+}(\mathrm{U}_{\mathrm{i}}^{\mathrm{n}})\Delta\mathrm{S}_{\mathrm{J}}\right]\Delta_{\mathrm{t}}\mathrm{U}_{\mathrm{i}} + \frac{1}{\Omega_{\mathrm{i}}}\sum_{\mathrm{J}} \mathrm{A}_{\mathrm{j}}^{-}(\mathrm{U}_{\mathrm{j}}^{\mathrm{n}})\Delta\mathrm{S}_{\mathrm{J}}\Delta_{\mathrm{t}}\mathrm{U}_{\mathrm{j}} = \mathrm{R}(\mathrm{U}_{\mathrm{i}}^{\mathrm{n}}) \quad (2.68)$$

Here it is to be noted that, the summation over 'J' implies the summation of flux contribution of all 'J' faces of a control volume 'i'. Therefore, the equation (2.68) can be written for all the finite volumes in the matrix form as,

$$\mathrm{M}\;\Delta_{\mathrm{t}}\mathrm{U} = \mathrm{R}^{\mathrm{n}} \quad (2.69)$$

with F_i as a set of face sharing neighbors of cell i,

$$\begin{aligned}
\mathrm{M}_{\mathrm{ij}} &= \frac{1}{\Omega_{\mathrm{i}}}\mathrm{A}_{\mathrm{j}}^{-}\Delta\mathrm{S}_{\mathrm{J}} \;\ldots \text{for } \mathrm{j} \in \mathrm{F}_{\mathrm{i}} \\
&= 0 \;\ldots \text{for } \mathrm{j} \notin \mathrm{F}_{\mathrm{i}} \\
\mathrm{M}_{\mathrm{ii}} &= \frac{\mathrm{I}}{\Delta\mathrm{t}} + \frac{1}{\Omega_{\mathrm{i}}}\sum_{\mathrm{J}} \mathrm{A}_{\mathrm{i}}^{+}\Delta\mathrm{S}_{\mathrm{J}}
\end{aligned}$$

where M_{ii} and M_{ij} denote the diagonal and off-diagonal elements of matrix M respectively.

Following expression was adopted by Yoon and Jameson [80] for the split normal flux Jacobian,

$$\mathrm{A}^{\pm} = \frac{1}{2}\left[\mathrm{A} \;\pm\; \rho_{\mathrm{A}}\mathrm{I}\right] \quad (2.70)$$

where ρ_A represents the spectral radius of the normal flux jacobian A.

$$\therefore \quad M_{ij} = \frac{1}{2\Omega_i}(A_j - \rho_{A_j} I)\Delta S_J \ ... \text{ for } j \in F_i$$
$$= 0 \ ... \text{ for } j \notin F_i$$
$$M_{ii} = \left[\frac{I}{\Delta t} + \frac{1}{2\Omega_i}\sum_J (A_i + \rho_{A_i} I)\Delta S_J\right]$$

The matrix M is decomposed into three parts, a diagonal part 'D', an upper triangular part 'C 'and a lower triangular part 'E 'such that M = C + D + E where,

$$C_{ij} = \left\{\begin{matrix} M_{ij}, & \text{for } i < j \\ 0, & \text{for } i \geq j \end{matrix}\right\} \tag{2.71}$$

$$D_{ij} = \left\{\begin{matrix} M_{ij}, & \text{for } i = j \\ 0, & \text{for } i \neq j \end{matrix}\right\} \tag{2.72}$$

$$E_{ij} = \left\{\begin{matrix} M_{ij}, & \text{for } i > j \\ 0, & \text{for } i \leq j \end{matrix}\right\} \tag{2.73}$$

So, equation (2.69) can be written as,

$$(C + D + E)\ \Delta_t U = R^n \tag{2.74}$$

$$\left[\frac{I}{\Delta t} + \frac{1}{2\Omega_i}\sum_J \rho_{A_i}\Delta S_J\right]\Delta_t U_i + \frac{1}{2\Omega_i}\sum_{J\notin B}(\Delta_t H_{\perp J} - \rho_{A_j}\Delta_t U_j)\Delta S_J + \frac{1}{2\Omega_i}\sum_{J\in B}(\Delta_t H_{\perp f} - \rho_{A_f}\Delta_t U_f)\Delta S_J = R_i^n \tag{2.75}$$

Source term appearing in the governing equations (particularly for axisymmetric studies in this thesis) are treated explicitly and absorbed in to the explicit residue term (R^n) of equation (2.75). Hence,

$$\mathrm{R_i^n} = -\frac{1}{\Omega_i}\sum_{J} \mathrm{H_{\perp J}}(\mathrm{U_i^n}, \mathrm{U_j^n})\Delta \mathrm{S_J} - \alpha \mathrm{S_i} \tag{2.76}$$

where, B represents boundary faces. The vector $\mathrm{R^n}$ is calculated by explicit procedure. The implicit formulation is extended to viscous flows by modifying the spectral radius by addition of a viscous velocity scale [73],

$$\sigma = \frac{1}{\mathrm{Re}_\infty}\frac{\mu}{\rho l} \tag{2.77}$$

where μ is the viscosity, Re_∞ is the Reynolds number, and l is the viscous length.

2.8.4 Relaxation procedure

Symmetric Gauss Seidel (SGS) relaxation procedure solves the equation (2.74) is in the following way:

$$\begin{aligned} \text{Forward sweep} : (\mathrm{E}+\mathrm{D})\Delta_t \mathrm{U}^* &= \mathrm{R^n} - \mathrm{C}\ \Delta_t \mathrm{U}^{(k-1)} \\ \text{Reverse sweep} : (\mathrm{D}+\mathrm{C})\Delta_t \mathrm{U}^k &= \mathrm{R^n} - \mathrm{E}\ \Delta_t \mathrm{U}^* \\ \text{with} : \Delta_t \mathrm{U}^0 &= 0 \end{aligned} \tag{2.78}$$

The forward and reverse sweeps are used to cancel the accumulated numerical errors of an iterative procedure. Therefore the equation solved,
In the forward sweep,

$$\begin{aligned} \left[\frac{\mathrm{I}}{\Delta t} + \frac{\mathrm{I}}{2\Omega_i}\sum_{J}\rho_{A_i}\Delta \mathrm{S_J}\right]\Delta_t \mathrm{U_i^*} = \mathrm{R_i^n} &- \frac{1}{2\Omega_i}\sum_{J_{j<i}}(\Delta_t \mathrm{H^*_{\perp J}} - \rho_{A_j}\Delta_t \mathrm{U_j^*})\Delta \mathrm{S_J} \\ &- \frac{1}{2\Omega_i}\sum_{J_{j>i}}(\Delta_t \mathrm{H^{(k-1)}_{\perp J}} - \rho_{A_j}\Delta_t \mathrm{U_j^{(k-1)}})\Delta \mathrm{S_J} \end{aligned} \tag{2.79}$$

In the reverse sweep we have,

$$\begin{aligned} \left[\frac{\mathrm{I}}{\Delta t} + \frac{\mathrm{I}}{2\Omega_i}\sum_{J}\rho_{A_i}\Delta \mathrm{S_J}\right]\Delta_t \mathrm{U_i^k} = \mathrm{R_i^n} &- \frac{1}{2\Omega_i}\sum_{J_{j<i}}(\Delta_t \mathrm{H^*_{\perp J}} - \rho_{A_j}\Delta_t \mathrm{U_j^*})\Delta \mathrm{S_J} \\ &- \frac{1}{2\Omega_i}\sum_{J_{j>i}}(\Delta_t \mathrm{H^k_{\perp J}} - \rho_{A_j}\Delta_t \mathrm{U_j^k})\Delta \mathrm{S_J} \end{aligned} \tag{2.80}$$

No matrix inversion's are involved for above equations. The conserved variables at the next time level are obtained from,

$$\mathrm{U_i}^{\mathrm{n+1}} = \mathrm{U_i^n} + \alpha_\mathrm{r}\ \Delta_\mathrm{t}\mathrm{U_i^{k_{max}}} \tag{2.81}$$

where α_r is the relaxation parameter whose value lies in the range 0 to 1 and $\mathrm{k_{max}}$ is the maximum number of sweeps involved.

2.8.5 Calculation of time step

The stability of explicit time marching scheme depends on the appropriate selection of time step Δt, that satisfies the Courant-Friedrichs-Lewy (CFL) criteria. For the present solver, CFL-limited appropriate time step is calculated at each control volume as, .

$$\Delta t_i = \frac{\lambda\sqrt{\Omega_i}}{|V_i| + a_i} \tag{2.82}$$

where, λ is the Courant-Friedrichs-Lewy number, V and a are the flow velocity and sonic velocity at the cell centroid respectively. It should be further noted that, for better stability of time-dependent simulations, the time-step should be chosen by calculating the time-step in each computational cell, and further using the smallest of all (global minimum). The value of CFL number is considered to be less than unity for all the explicit runs using present solver.

2.9 Summary

Conservative form of the N-S equations has been used for developing the algorithm for the present solver. This algorithm adopts cell centered finite volume formulation and has provision of seven inviscid flux computation schemes. Perfect gas model and equilibrium flow models are also available for choice. This solver is equipped with higher order time and spatial accuracy along with explicit and implicit time integration strategies.

Chapter 3

Validation and verification of in-house developed solver, “USHAS”

Overview

This chapter presents the detailed validation and verification of in-house developed solver ‘USHAS’. Validation for higher order spatial accuracy of the solver is essential to ensure the accuracy of simulation results obtained with present solver. Therefore the order of accuracy of the spatial discretization is initially validated by solving supersonic vortex flow test case. Subsequently the accuracy and applicability of equilibrium flow gas model of the solver is verified through the simulation of high Mach number flows through an axisymmetric diverging nozzle. The validation and verification of Euler sub-part and complete Navier-Stokes solver follows the gas model comparison study. Hypersonic flow over a hemisphere is considered for inviscid validation, while supersonic flow over flat plate involving I-SWBLI is presented as viscous part validation study. The efficiency and computational advantage of implicit time marching scheme over explicit time marching strategy for steady state simulations are also narrated in both inviscid and viscous validation studies. The presented validation studies clearly show the accuracy and correctness of in-house developed solver.

3.1 Background

An essential step in the CFD solver development is the verification and validation process. In this chapter, a qualitative and quantitative validation as well as verification of the in-house developed solver against experimental and analytical results are presented. Both inviscid and viscous

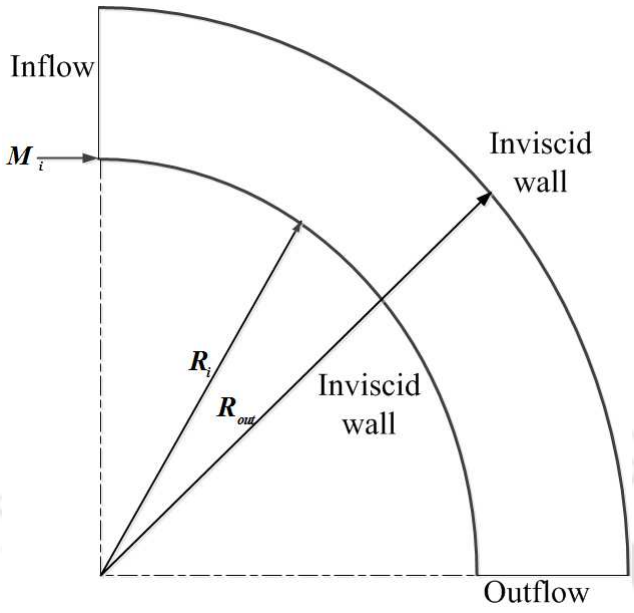

FIGURE 3.1: Supersonic vortex flow domain

validation studies are separately carried out to ensure the independent accuracy of Euler sub-part and complete N-S solver.

3.2 Supersonic vortex flow test case

For steady flow problems such as those considered in this study, it is well known that at least second order spatial accuracy is necessary for sharp resolution of flow features. The second order spatial accuracy of the unstructured solver has been assessed using the supersonic vortex flow test case [81]. This is a non-trivial problem governed by steady compressible Euler equations for which a smooth analytical solution is known. The geometry used for this test case is shown in figure 3.1.

The inviscid supersonic flow between concentric circular arcs presents a flow where the velocity varies inversely with radius. For the present test case the inner radius is chosen as unity, while the outer radius is taken as 1.384. This domain is meshed using both triangular and quadrilateral meshes. In either case, a sequence of uniformly refined grids starting from an initial grid of 31×6 in case of the quadrilateral meshes and 430 triangles in case of unstructured meshes are employed for the study (figure 3.2). The reference inlet Mach number, set at inner radius

(R_i), is 2.25. The exact solution of this problem can be found from suitable isentropic relations as,

$$
\begin{aligned}
&R_i = 1,\ M_i = 2.25, \rho_i = 1 \quad p_i = \frac{1}{\gamma {M_i}^2}, \quad R = \sqrt{x^2 + y^2} \\
&\rho = \rho_i \left[1 + \frac{\gamma - 1}{2} \left(1 - \frac{R_i^2}{R^2} \right) {M_i}^2 \right]^{1/(\gamma - 1)} \\
&p = p_i \left[1 + \frac{\gamma - 1}{2} \left(1 - \frac{R_i^2}{R^2} \right) {M_i}^2 \right]^{\gamma/(\gamma - 1)} \\
&U_{R_i} = M_i a_i, \quad a_i = \sqrt{\frac{\gamma p_i}{\rho_i}} \\
&U_{R_i} \propto \frac{1}{R_i}, \quad U_R \propto \frac{1}{R}, \quad U_R = U_{R_i} \frac{R_i}{R} \\
&u = \frac{y U_R}{R} = U_{R_i} \frac{y R_i}{R^2}, \quad v = -\frac{x U_R}{R} = -U_{R_i} \frac{x R_i}{R^2}
\end{aligned}
\tag{3.1}
$$

This exact solution is used as the initial condition for the present analysis and steady state solutions are obtained on all grids using the AUSM scheme. The error in density is measured in L_2 norm as,

$$
\|\varepsilon_\rho\|_2 = \sqrt{\frac{\sum_{i=1}^{nc} (\rho_{i,exact} - \rho_{i,Num})^2}{nc}} \tag{3.2}
$$

where nc is the number of finite volumes of given domain. In the expression above, $\rho_{i,exact}$ and $\rho_{i,Num}$ are the exact (analytical) and numerical values of density in the i^{th} cell. The variation of error with the characteristic length scale (h), defined as $h = \frac{1}{\sqrt{nc}}$, is shown in figure 3.3 for the cases with and without limiting on both grid topologies. It is observed that the error decreases with grid refinement at a rate around 2 in all cases. It demonstrates the nominal second order

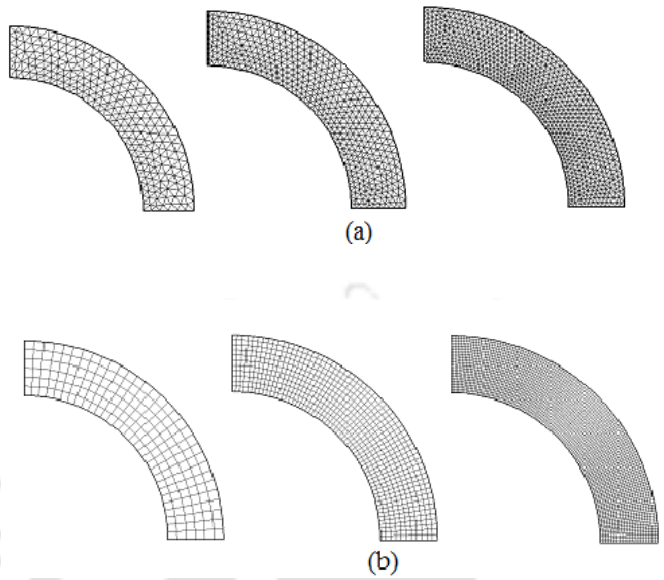

FIGURE 3.2: (a) Three mesh levels of triangular grid for supersonic vortex studies (b) Three mesh levels of quadrilateral grid for supersonic vortex studies

accuracy of the solver. It must be emphasized that the limiter indeed leads to higher error levels but does not drastically change the order of accuracy of the solver. All other numerical schemes discussed in this work have also result in error decay at a similar rate close to 2, although the magnitude of errors would be expectedly larger for more dissipative schemes.

3.3 Validation of the high temperature equilibrium flow model

The equilibrium flow gas model of present solver has been validated by solving quasi-one dimensional nozzle flow test case recommended by Hoffman and Chiang [82]. The quasi-1D solver has same temporal and spatial discretization methodology as considered for earlier test case. The details about governing equations for the quasi-1D case are given in Appendix B. A diverging nozzle is considered in this test case, for which area variation given by,

$$S(x) = 1.398 + 0.347 \tanh(0.8x - 4) \tag{3.3}$$

The nozzle inlet is situated at x =1.2 cm and exit location is at x =8.0 cm. Thus it provides an inlet to exit area ratio of 1.65. The domain is meshed with 69 equally spaced grid points. The physical shape of the domain is shown in figure 3.4. The inlet is considered as supersonic inlet

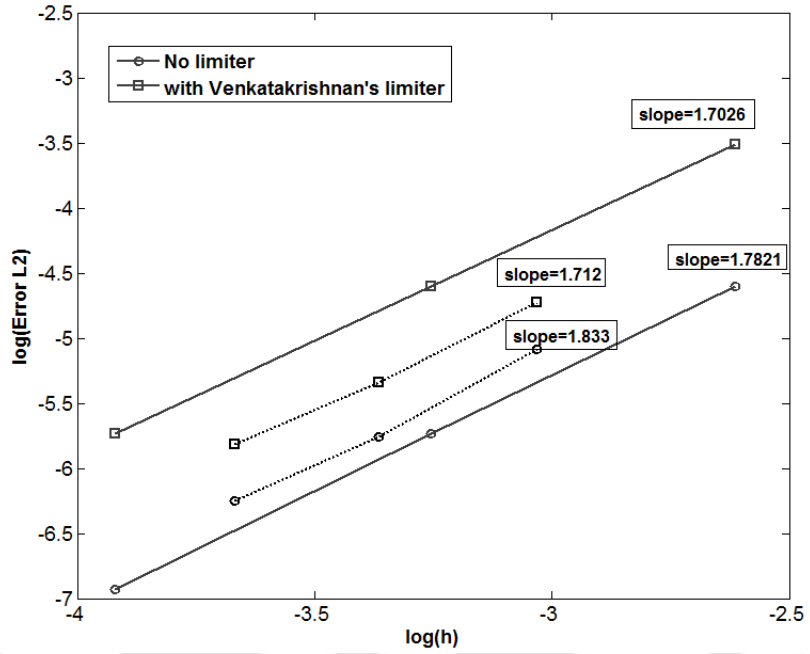

FIGURE 3.3: Order of accuracy with and without limiters on quadrilateral grid (solid line) and triangular grid (dashed line)

with freestream conditions. The outlet boundary condition is set by imposing a back pressure value, so as to get shock at x =4.0 mm. Two different cases are studied in order to analyze the difference in prediction of perfect gas model and equilibrium flow model. The inlet parameters for both the conditions are given in table 3.1. AUSM upwind scheme has been employed for the convective flux calculation.

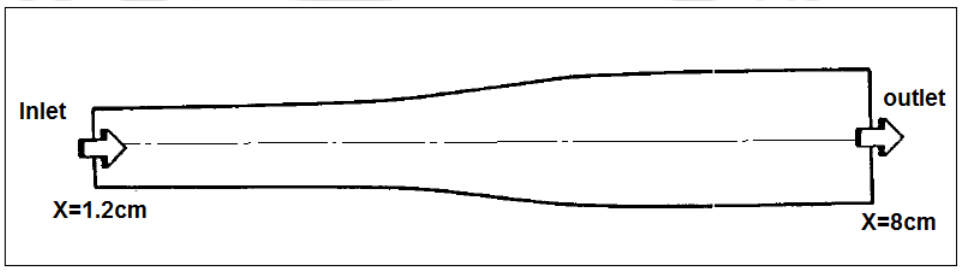

FIGURE 3.4: Physical shape of nozzle considered for equilibrium flow gas model validation

The temperature distributions of Mach 4 and Mach 20 cases obtained with two different gas models of present solver are shown in figure 3.5 and figure 3.6 respectively. Solver results are compared with the corresponding predictions of Hoffman and Chiang [82]. From the comparison, it has been observed that present solver results are in close match with reported results. It is

Case	P (Pa)	T K	M
1	26500	230.44	4
1	26500	230.44	20

TABLE 3.1: Inlet conditions for equilibrium flow model validation

also evident from figure 3.5 that temperature predictions by perfect gas model and equilibrium models are almost close. It is due to the fact that, static temperature rise across the shock is less at low Mach number condition, which does not trigger the chemical reactions in the shock layer. In this case the perfect gas assumption predicts maximum temperature rise within the domain close to 950 K, consequently the chemistry effects are minimal. In second case inlet Mach number is so high that the post shock temperature increases to higher values which ensures chemical reactions. Since the ideal gas model of the solver does not consider any chemistry effects, it predicts around 18500 K behind the shock (figure 3.6). However, the endothermic reactions tend to reduce the temperature in comparison with perfect gas case. Therefore the post shock temperature in this case is around 8200 K. Thus present test case validates the implementation of different gas models in 'USHAS'.

3.4 Hypersonic flow over hemisphere: an inviscid validation study

Simulations are carried out for the hypersonic flow over hemisphere to validate the axisymmetric Euler sub-part of 'USHAS'. In this test case, flow past a unit diameter sphere has been considered with input Mach number (M_∞) of 8.0. The computational domain used for the present investigation marked with boundary conditions is shown in figure 3.7 (a). This domain has been meshed with 40000 unstructured triangular cells. Free stream pressure of 89 Pa, and free stream temperature of 113 K are used for this study. These freestream parameters correspond to typical shock tunnel test conditions. Since it is a cold hypersonic flow, perfect gas model of the solver is employed for this simulation. Van-Leer convective flux scheme along with second order spatial accuracy is used in the simulation. Initially simple explicit time marching is employed to

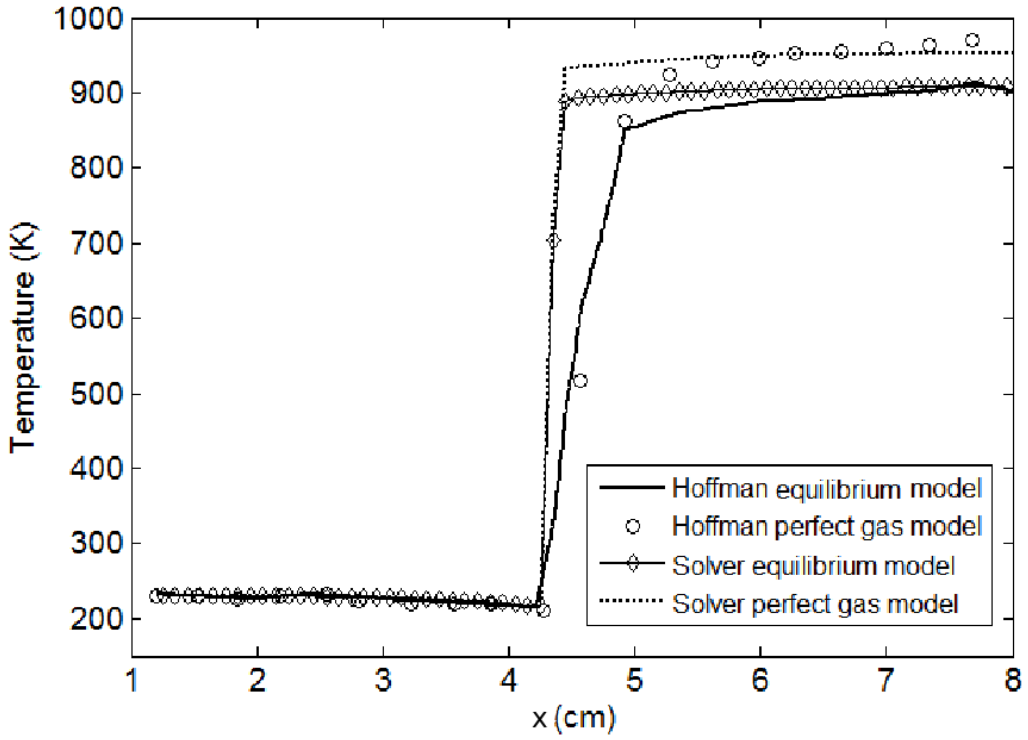

FIGURE 3.5: Temperature distribution along the axis of nozzle for Mach number 4 case

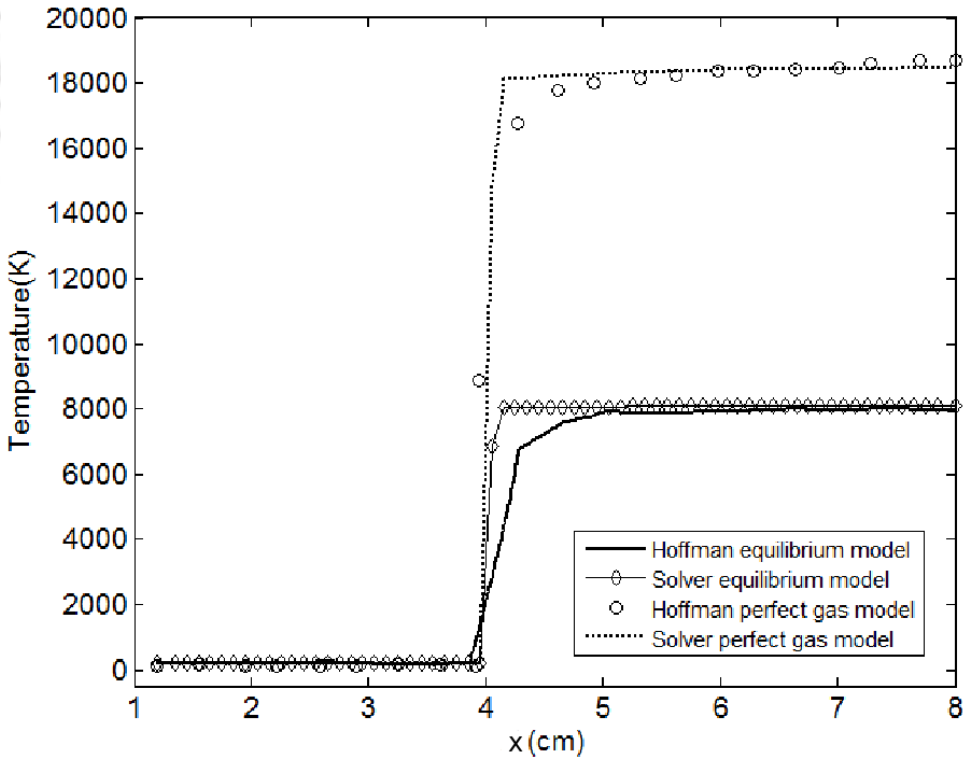

FIGURE 3.6: Temperature distribution along the axis of nozzle for Mach number 20 case

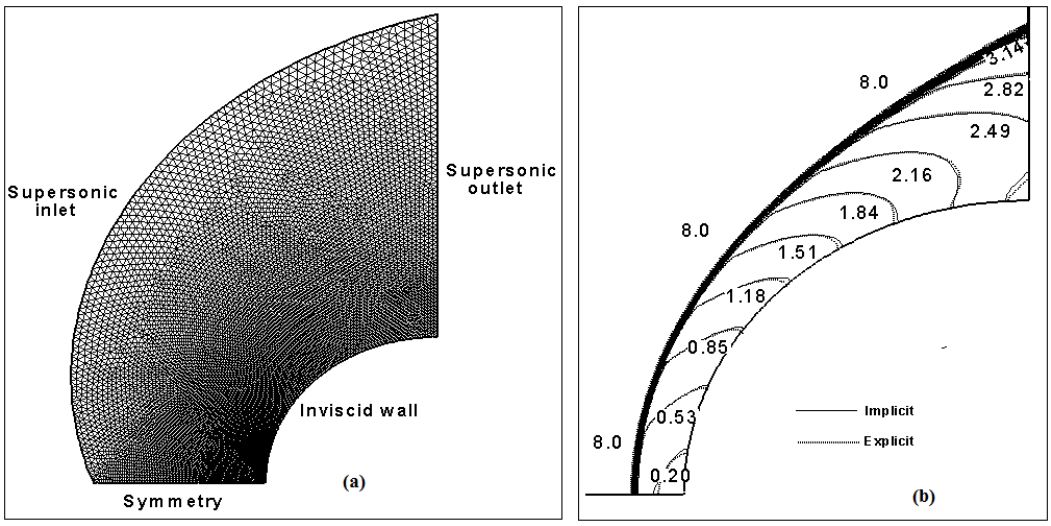

FIGURE 3.7: (a) Computational domain for hemisphere with boundary conditions (b) Mach contours of hypersonic (M_∞=8) flow over hemisphere

achieve steady state. Later simulation is repeated with implicit time marching strategy to compare the computational cost of two time marching schemes. For the implicit time marching, a starting CFL number of 5 is considered. Further this CFL is linearly ramped with iteration till convergence criterion is achieved. The relaxation parameter of 0.8 along with 16 inner sweeps is employed in the implicit run. The steady state results are then used to validate the prediction accuracy of present solver.

The Mach contours of hypersonic flow past hemisphere are shown in figure 3.7 (b). The contours obtained with both time marching schemes are overlapped in the same figure to represent their equivalent prediction accuracy. Prominent flow feature of this test case is presence of bow shock ahead the hemisphere. The maximum property jumps are observed along the stagnation stream line, which are equivalent to jump across a normal shock wave. The solver results are initially validated by comparing the pressure distribution over the surface of the hemisphere with the Newtonian theory [1] and Modified Newtonian theory [1]. According to Newtonian theory the pressure coefficient (C_p) distribution over the sphere surface can be obtained as,

$$Cp = 2Sin^2\theta \tag{3.4}$$

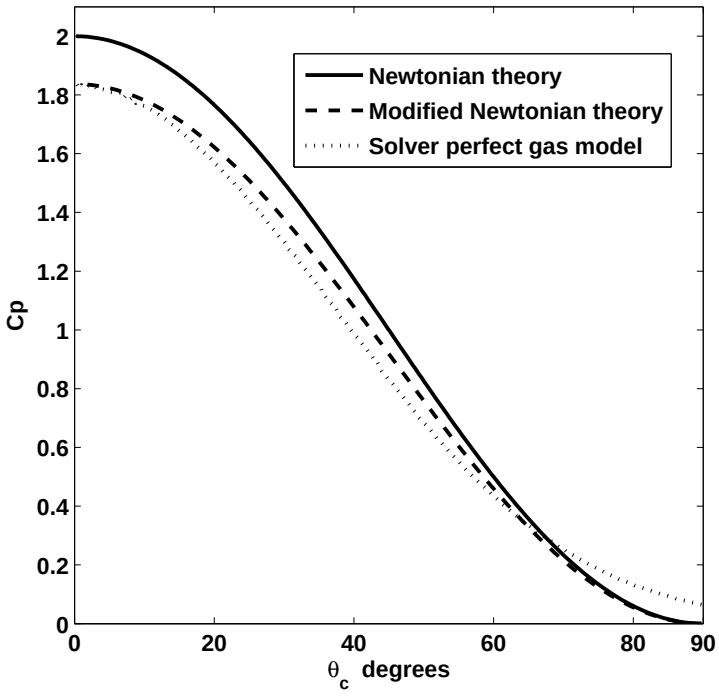

FIGURE 3.8: Comparison of Cp vs θ_c for hemisphere

As per the modified Newtonian theory, same is,

$$Cp = Cp_{max} Sin^2\theta \tag{3.5}$$

where, Cp_{max} is the value of C_p at the stagnation point, which is given by,

$$Cp_{max} = \frac{p_{02} - p_\infty}{\frac{1}{2}\rho_\infty U_\infty^2} \tag{3.6}$$

Where, p_{02} is the total pressure behind a normal shock wave at a given freestream Mach number.

From figure 3.8, it is clear that the solver results are in good agreement with the modified Newtonian theory. Further to demonstrate the computational advantage of implicit time marching over simple explicit scheme, the residual fall of these two time marching strategies are compared in figure 3.9(a). This figure shows that, the implicit formulation achieves convergence just after 398 iterations, whereas the explicit time marching takes 5900 iterations to reach steady

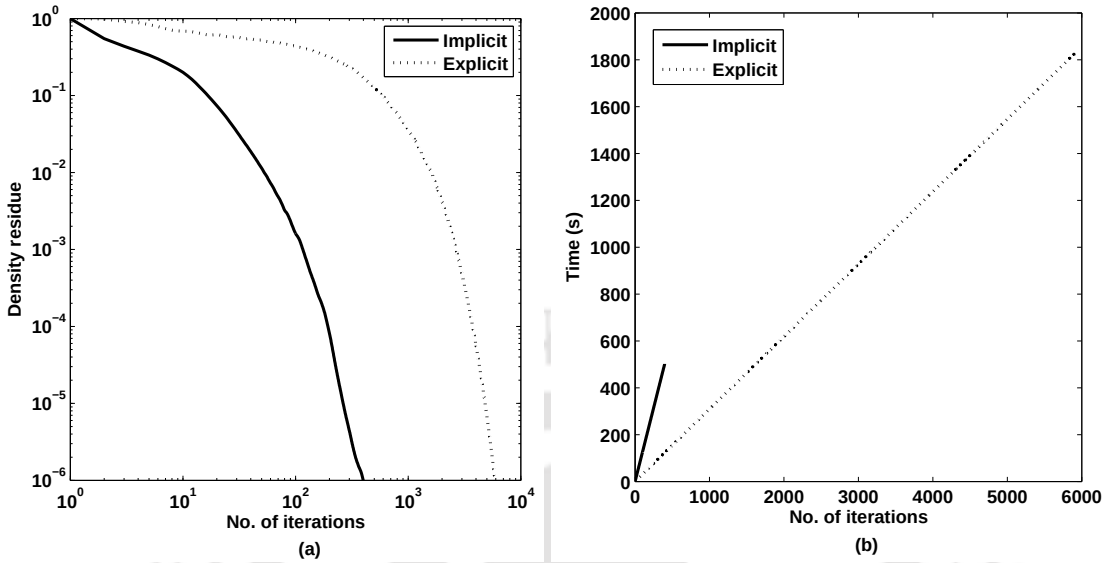

FIGURE 3.9: (a) Comparison of convergence histories of two time marching schemes (b) Comparison of simulation time of different schemes

state. Clock time and iteration comparison for both cases is shown in figure 3.9(b). This comparison clearly depicts that, the total computational time taken by implicit scheme (502 sec) is much less as compared to the time taken by explicit formulation (1825 sec). However the time per iteration can be observed to be large for implicit formulation. But, the implicit time marching should be considered to reduce both computational time and cost involved in steady flow simulations. The efficiency of implicit formulation can be further improved by fine tuning the initial CFL value, CFL ramping strategy, relaxation parameter and number of sweeps.

The studies are further extended to predict the variation of shock stand-off distance with Mach number. The shock detachment distance obtained from the solver has been compared with Billig correlation [83] for shock detachment distance given by,

$$\frac{\delta}{R} = 0.143 \exp\left(3.24/{M_\infty}^2\right) \tag{3.7}$$

For this study the freestream Mach number is varied from 2-10 in an interval of 1. The same computational domain employed for Mach 8 study is considered for all these investigations. The steady state results showed that, due to increase in freestream Mach number, the density behind the shock also increases which in turn leads to decrease in volume of the shock layer. The clear

evidence of this can be obtained from the comparison of non-dimensional density distribution along the stagnation streamline given in figure 3.10. This figure also displays the change in density across normal shock for Mach number 4 case. The density jump is observed to be the same for both numerical and theoretical predictions immediately downstream of the shock. Moreover the numerically obtained density ratio behind the shock is seen to be further rising towards the stagnation point. Apparently the distance between this property jump location and stagnation point can be treated as the shock detachment or shock stand-off distance. Hence the shock stand-off distances obtained from the steady state results are compared in figure 3.11. This comparison shows an encouraging agreement between numerical prediction and Billig correlation [83] for the range of Mach numbers considered in this study.

In addition to the correlation for shock stand-off distance, Billig has also proposed an empirical correlation for shock shape [83]. Therefore the numerically obtained shock shape can be compared with the correlation based shock shape. For a blunt sphere-cone model Billig's hyperbolic shock shape correlation [83] yields,

$$x = R + \delta - R_c \cot^2 \beta \left[1 + \frac{y^2 \tan^2 \beta}{{R_c}^2} - 1 \right] \tag{3.8}$$

where, R is the nose radius of the sphere, R_c is the radius of curvature of shock wave centered on the vertex of the hyperbola, which is given by [83],

$$\frac{R_c}{R} = 1.143 exp\left[0.54/(M_\infty - 1)^{1.2}\right] \tag{3.9}$$

The term δ in equation (3.8) stands for shock stand-off distance, whereas x and y are cartesian coordinates with origin at centre of sphere. The angle β is the shock wave angle at an infinite distance away from the stagnation point of the sphere. Assumption of β value as Mach angle ($\phi = \sin^{-1}(1/M_\infty)$) of a given freestream can give reasonably good estimate of shock shape in case of hypersonic flow over sphere. Thus obtained shock shape for Mach number 8.0 flowfield is compared with corresponding numerical prediction in figure 3.12. Excellent agreement between two predictions can be evidenced from figure 3.12, which in turn underline the accuracy of present solver.

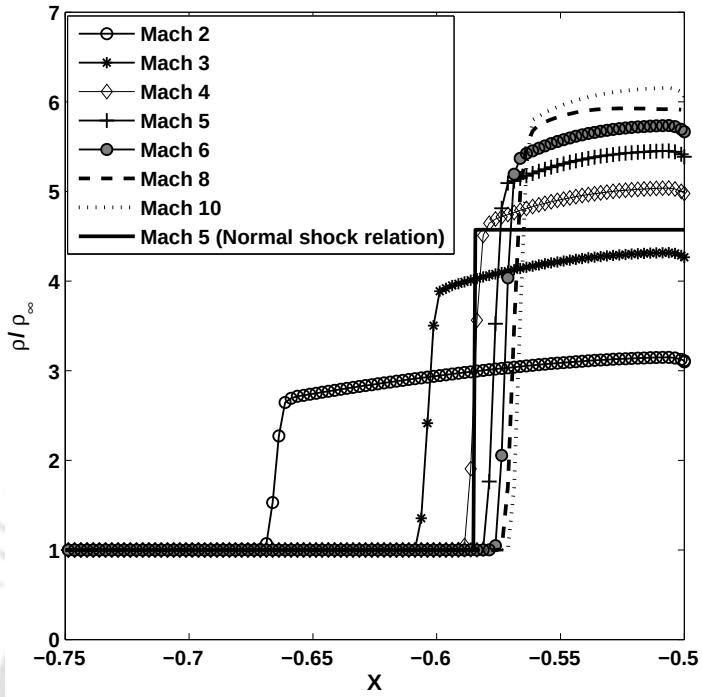

FIGURE 3.10: Comparison of density variation along the stagnation streamline

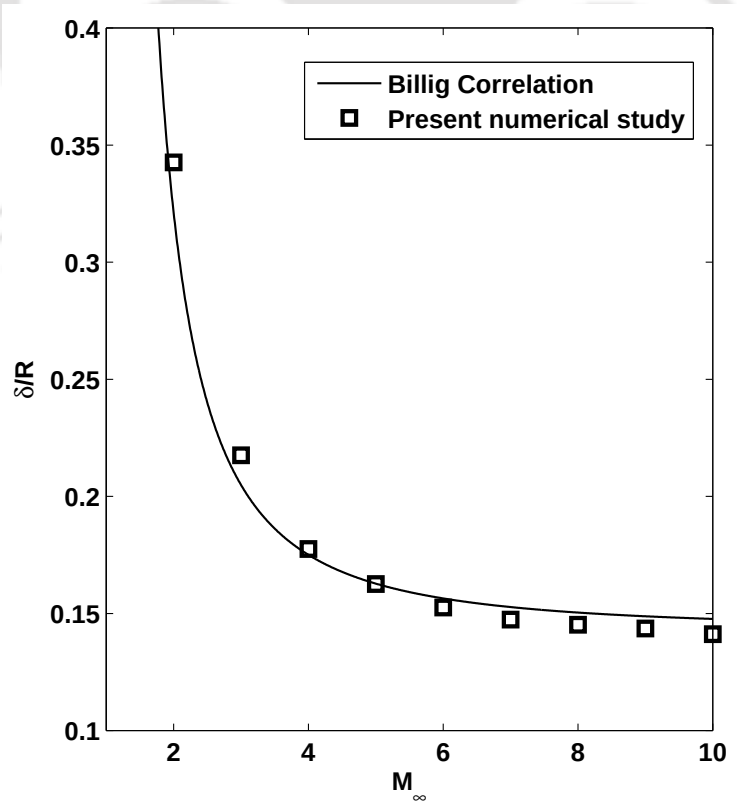

FIGURE 3.11: Variation of shock stand-off distance with Mach number

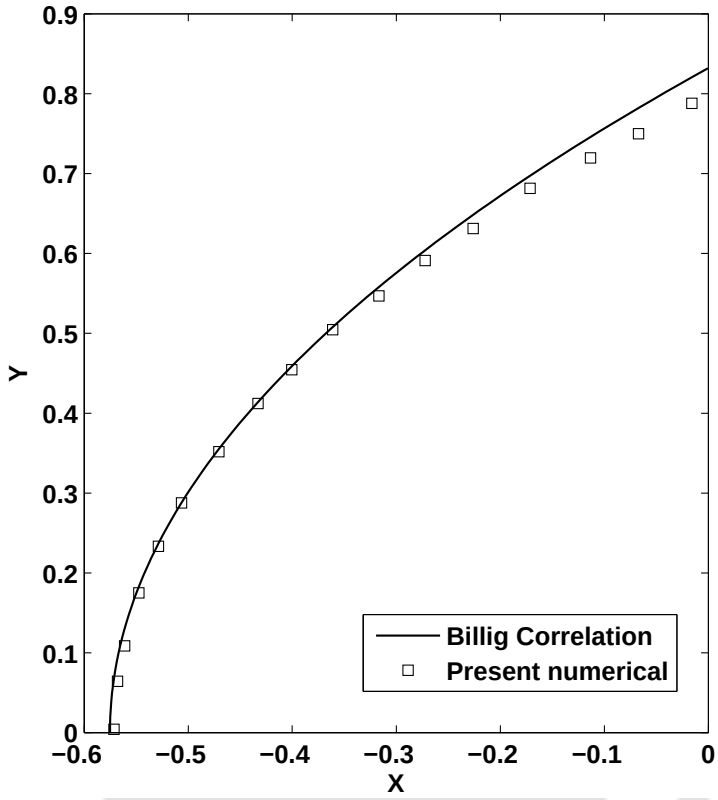

FIGURE 3.12: Comparison of shock shape for freestream Mach number 8

3.5 Laminar supersonic flow with I-SWBLI

Importance of SWBLI has already been discussed in Chapter 1. Therefore the experimental investigation of Hakkinen et al. [19] for I-SWBLI in a supersonic flowfield ($M_\infty = 2$) is considered here as the validation case for 'USHAS'. In the experimental study, Hakkinen et al. considered a situation of impingement of an oblique shock of strength (p_3/p_1) 1.4 into the laminar boundary layer over a flat plate. The same experimental conditions are considered in the present study to assess the numerical prediction on the light of available experimental data.

The schematic of the physical situation of I-SWBLI is shown in figure 3.13. A flat plate of length 88.9 mm with its leading edge at origin is considered for this study. The wedge which generates the shock has been set to establish an oblique shock of shock angle (β) 32.58^0 to hit the bottom flat plate at x=49.6 mm. Care has been taken in the selection of computational domain to avoid the secondary interaction of reflected shock with the boundary layer. The computational domain considered in the present study is shown in figure 3.14. Here the domain dimensions

are scaled with flat plate length upstream of interaction location, ie. 49.6 mm. In the domain, the first $1/3^{rd}$ of the bottom wall is set as inviscid wall whereas rest $2/3^{rd}$ is set as viscous wall to represent the flat plate. The various boundary conditions of the computational domain are marked in figure 3.14. The top inclined wall of the computational domain represents the inviscid surface of the wedge (shock generator). The inclination of the top wall has been selected to match the flow deflection angle of a wedge that could generate a shock at an angle of 32.58^0. The domain is meshed with quadrilateral grids. Three meshes, viz. 240×80, 360×120 and 480×160 are used to obtain grid independent solution. Grid clustering is carried out near the bottom wall for capturing the boundary layer and other viscous wall parameters for all meshes. Grid points are again clustered along the span wise direction locally at leading edge region and interaction location for better prediction of flow features. Explicit time stepping has been chosen and CFL of 0.2 is selected for this case. Time marching is performed until the density residue falls to 10^{-6}, which is assumed as the steady state for this case. In addition to simple explicit scheme, implicit formulation has also been considered for simulation to compare its performance in viscous flow simulation. For implicit simulation under relaxation factor of 0.6 along with starting CFL of 0.2 and linear CFL ramping is used. The number of sweeps are kept as 16 for this viscous simulation. The residual falls of these two time marching schemes are therefore compared in figure 3.15. This comparison clearly portrays considerably large computational cost for explicit scheme based computations as compared to implicit formulation. Explicit formulation has taken more than 400000 iterations to reach steady state, whereas implicit formulation takes only 3350 iterations for steady state solution. For a grid level of 360×120, the implicit formulation took 1.45 sec per iteration, which results in total simulation time of 4865 sec (around 1 hr 21 min). On the other hand, explicit formulation took only 0.3534 sec per iteration. However with the rate of 0.3534 sec/iteration, the total simulation time extended to 39 hrs. This is the clear evidence of the computational efficiency of implicit scheme in steady flow simulations.

The pressure distributions obtained with three different grid levels are compared along with experimental measurements [19] in figure 3.16(a). The numerical predictions are in good agreement with experimental measurements. The present simulations could predict almost all the expected flow features of this particular case. Although the distributions of different grid levels

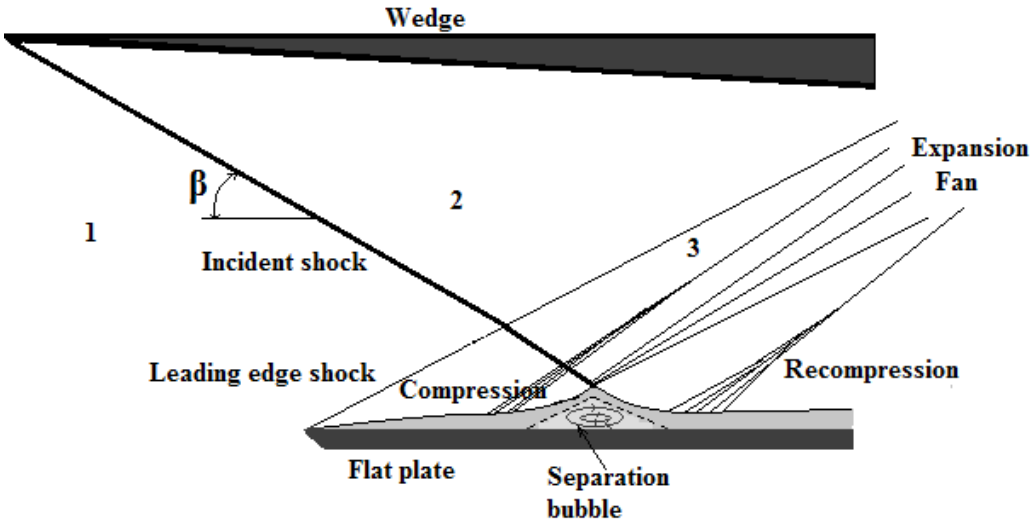

FIGURE 3.13: Schematic of physical situation of shock impingement caused SWBLI

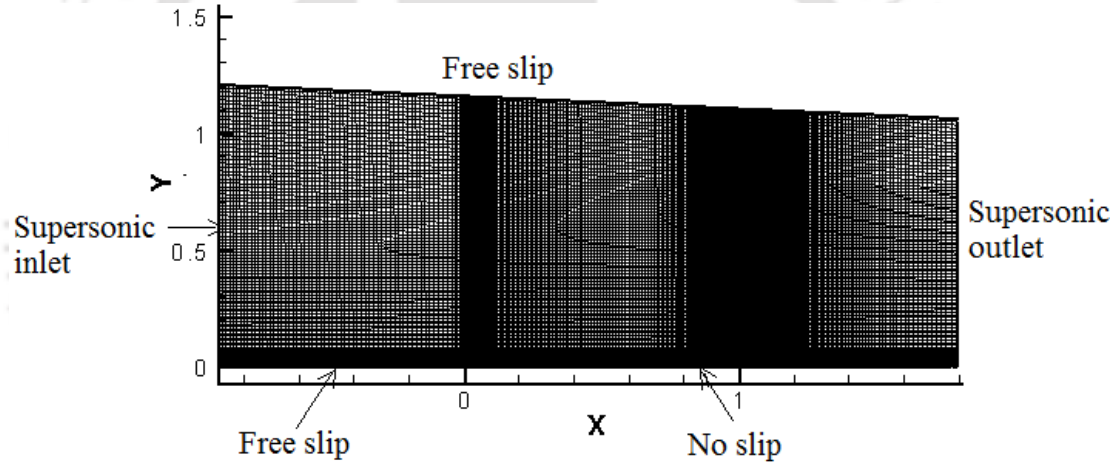

FIGURE 3.14: Meshed computational domain for shock impingement SWBLI study

have slight deviations, the difference between the distributions of 320×160 and 480×160 is very minor . Therefore results on 320×160 grid level is used for the further discussions. The Mach contours of the present study obtained with this grid is therefore shown in figure 3.18.

The Mach contours of implicit simulation were observed to be the same. Hence, for the sake of brevity, those contours are not merged with Mach contours of explicit scheme in this figure 3.18. Although the Mach contours show the interaction of oblique shock emerging from the compression corner with the lip shock before hitting the viscous wall, it is observed that this interaction does not alter the strength and angle of incident shock considerably. The comparison of predicted skin friction coefficient (C_f) distribution with reported experimental [19] as well as numerical results [41, 84], given in figure 3.17(a), confirm this argument. The skin friction

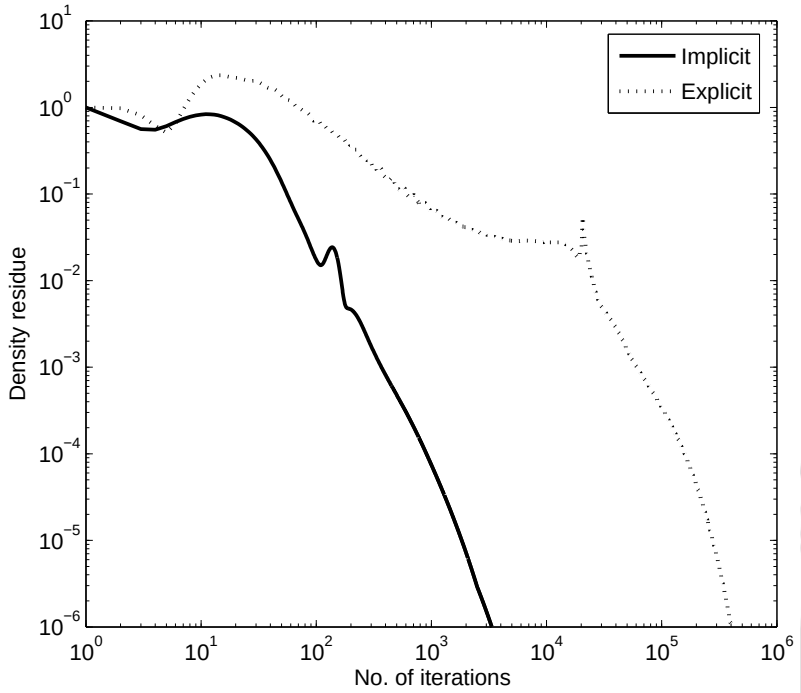

FIGURE 3.15: Comparison of residual fall of time marching schemes on 360×120 grid level

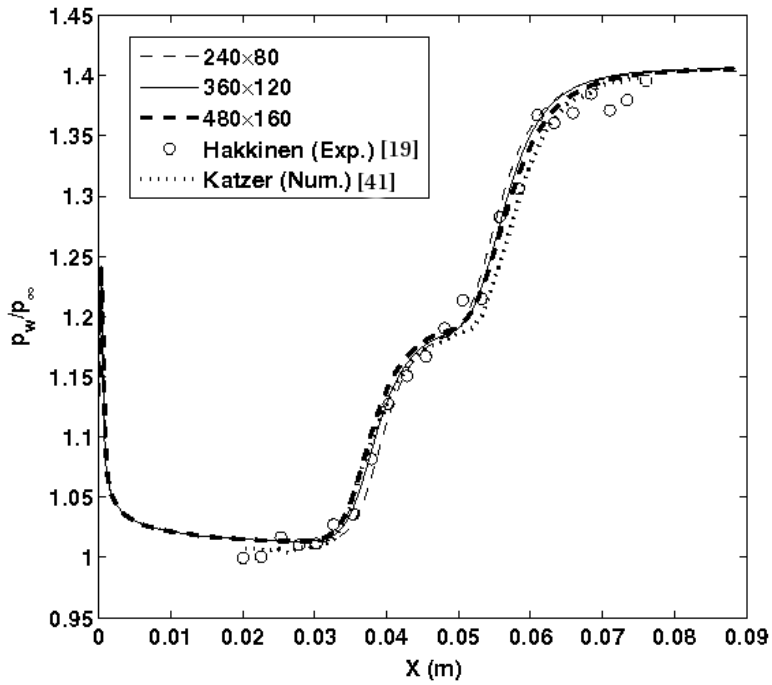

FIGURE 3.16: Comparison of surface pressure distributions of viscous flow test case

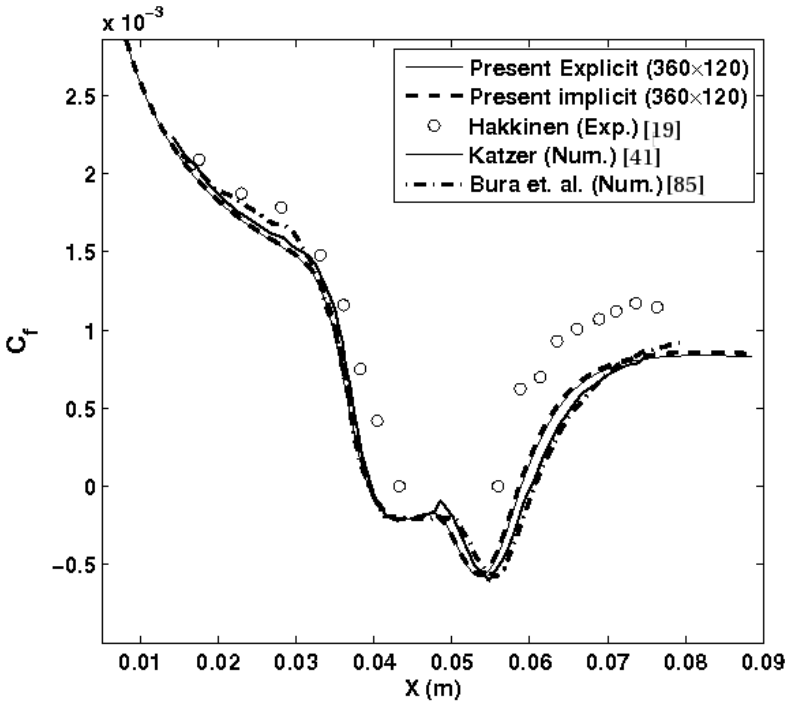

FIGURE 3.17: Comparison of skin friction distributions of viscous flow test case

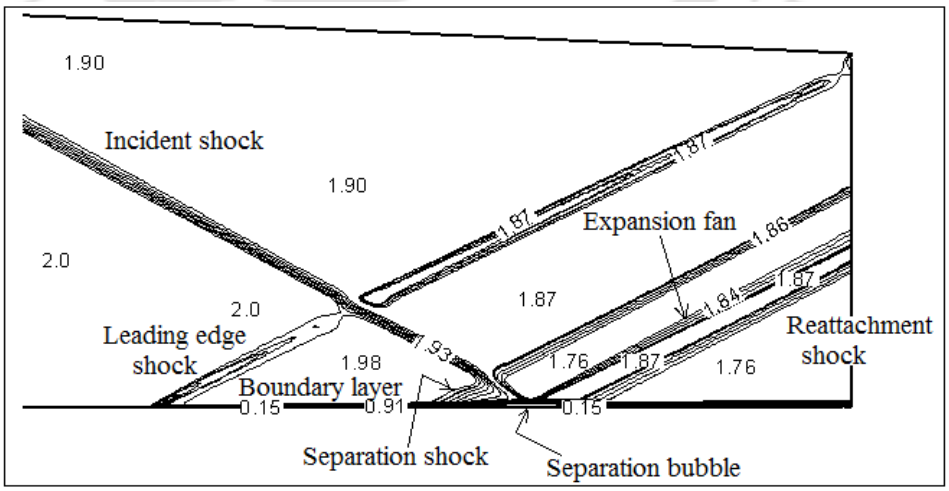

FIGURE 3.18: Mach contours of incident shock-boundary layer interaction study

distributions of both explicit and implicit simulations can be observed to be the same in figure 3.17(a). It shows that, the accuracy is same for both the formulations. Moreover, it is clear from the Mach contours and skin friction coefficient distribution that, the boundary layer thickens and separates due to the impingement of shock wave on the boundary layer. This flow separation leads to the formation of separation shock emanating from the separation point. The separated recirculating flow region extends from separation point to reattachment point. At the reattachment point a re-compression shock can be seen. The separation bubble size is thus the distance between separation point and reattachment point. Skin friction distribution is being utilized for this quantification. All numerical distributions are slightly over predicting the separation bubble size as compared to corresponding experimental value. This mismatch may be attributed to slight variation in assumed shock impingement location in the experimental study or the uncertainties in the skin friction measurements. The pressure distribution (figure 3.16(a)) have revealed that, in the region of separation, pressure rises and attains a plateau before the further increment associated with reattachment. On the other hand C_f is observed to be reducing and attaining negative values, which attribute to the flow separation and recirculation. Although numerically obtained C_f distributions has mismatch with experimental measurements in the separation region, the pressure distribution predictions of both experimental and numerical are closely matching each other. Since the present simulation results are observed to be falling very close to earlier numerical and experimental measurements, the solver accuracy in viscous flow simulations is also very clear.

3.6 Summary

An extensive validation of in-house developed solver has been carried out. The assessment of order of accuracy of present solver using supersonic vortex flow test case showed that, the present solver bears spatial accuracy of around 2. The investigation focused on the validation of gas models of present solver ensured the correct implementation of two gas models. This study also revealed the inaccuracy of perfect gas model for high Mach number high enthalpy flow simulations. The applicability of equilibrium flow model for such flow conditions is also verified. Euler sub-part of the solver is validated through the simulation of a range of high

speed flows over a hemisphere. The close agreement of numerical predictions with literature reported analytical correlations for surface pressure distribution, shock stand-off distance and shock shape confirmed the accuracy of Euler solver. Finally the complete Navier-Stokes solver is validated through the simulation for I-SWBLI in supersonic flow. The solver results are in good agreement with experimental as well as earlier reported numerical results for this test case. Hence this study evidences the applicability of present solver in viscous flow simulations. Additionally, the relative advantage of explicit and implicit time marching strategies of present solver is presented through the simulation of both inviscid and viscous flow test cases. It has been noticed that, although the implicit scheme require higher time per iteration, the use of this scheme ensures significant saving in total simulation time.

Chapter 4

Performance comparison of flux schemes for numerical simulation of high-speed inviscid flows

Overview

Numerical investigations are carried out to assess the performance of different inviscid flux computations schemes for the spatial discretisation of the Euler equations. Since the present solver is equipped with flux vector splitting, flux difference splitting and hybrid schemes, it is essential to identify the applicability of a particular scheme for a particular situation. In view of this, the solver is exposed to solve the problems ranging from lower supersonic to moderate hypersonic speeds. These problems involve various flow patterns like shock reflection, shock-shock interaction and interaction of shock with expansion fan and slip line. As a result of these studies, AUSM family of schemes are found to be the most accurate while the Rusanov scheme is observed to be the most robust for the range of Mach numbers considered in the study.

4.1 Background

Design and development of aircrafts for civil or military applications and space capsules for space missions require detailed knowledge of flow features of the flow regimes encountered by these vehicles. The relevant flow features provide the necessary inputs needed for efficient

aerodynamic design of these flight vehicles. In the high speed compressible flow regime, precise prediction of the flow features and its effect on aerodynamic coefficients has been one of the prominent issues faced by aerodynamicists. Preliminary information about this design data can be achieved using the Euler solver for which considerable advancement in development of schemes for computation of the inviscid fluxes has been done. Most of those well established schemes are part of the present solver. Although such convective flux schemes were developed for compressible flows with subsonic, transonic speeds or lower supersonic speeds, some of these schemes have been sparingly used in problems involving higher supersonic flows or even in hypersonic flow regime. There has been very limited concerted effort to analyse the suitability and applicability of these schemes for such high-speed flows. Supersonic and hypersonic flows often involve several complex flow phenomena such as strong shocks and expansions, regular or Mach reflections, shock-shock interactions and shock-expansion interactions. A recent study by Druguet et al. [85] demonstrated the effects of numerics on computations in hypersonic flows. Hence the focus of the present chapter is to evaluate the performance of several numerical flux computation schemes in predicting the complex physics associated with high Mach number inviscid flows. Therefore the effect of numerical fluxes obtained using Van-Leer scheme (FVS)[86], Roe scheme [87], Rusanov scheme [88], HLLE scheme [89] (FDS), AUSM [90] and AUSM+ [91] (Hybrid) schemes on the solution will be analyzed for various flow problems with Mach numbers varying from 1 to 8. These studies would be beneficial to decide about the best suited scheme for SWBLI studies. A comparative study of two different variants of the AUSM family viz. AUSM+ [91] and a latter variant AUSMPW [92] are also performed on two selected test cases.

4.2 Numerical investigations

The efficiency of standard flux computation schemes for high Mach number predictions is investigated in this section by considering four test problems. In all the cases described below, a constant Courant number of 0.5 is employed, unless otherwise specified

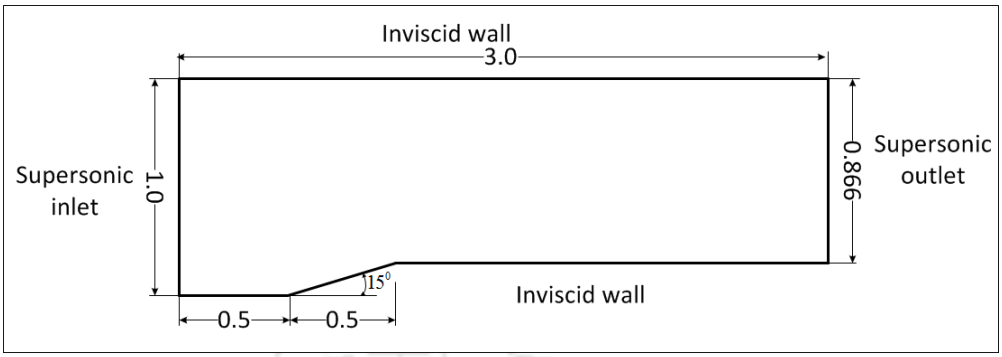

FIGURE 4.1: Domain and boundary conditions used for supersonic flow past ramp in a channel

4.2.1 Test case 1: Supersonic flow through a ramp in a channel

The suitability of different upwind schemes to capture the discontinuities present in the flow field is investigated using the Mach 2 flow past a ramp in a channel (Darren and Powell [93]). In the presence of the supersonic flow and the ramp, an attached shock is formed at the compression corner and reflects from the top wall, forming a small Mach stem. The reflected shock then further reflects from the bottom wall before exiting the channel. A weak slip line emanating from the triple point near the upper wall is also an integral part of the flowfield. The dimensions and boundary conditions for this test case are shown in figure 4.1. A 180×90 structured mesh is considered for the study.

This test case is simulated with all the seven schemes and steady state results are obtained for all simulations. Figure 4.2 and 4.3 show the pressure and Mach number contours while the surface pressure distribution is shown in figure 4.4, obtained using the Roe scheme. The surface pressure distribution is in good agreement with the results of Ganesh et al. [78] where unstructured adaptive meshing strategy was employed. Contours of flow quantities obtained using other schemes are similar and are not shown here for brevity. It was observed that while Roe and AUSM family of schemes indicate a crisp shock, the Rusanov scheme resulted in a more dissipative shock structure.

A comparison of the seven numerical schemes has been carried out for the pressure rise across the Mach stem. Figure 4.5 shows the pressure rise across the Mach stem computed with five different schemes. The AUSM family of schemes predict similar flow structure. Predictions from

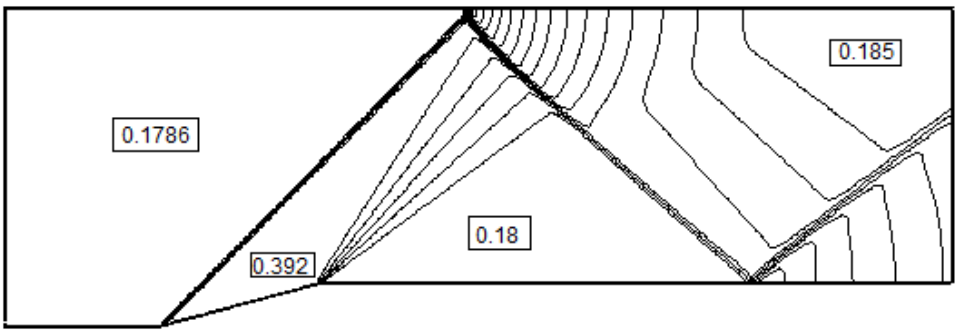

FIGURE 4.2: Non-dimensional pressure contours of supersonic flow past ramp in a channel

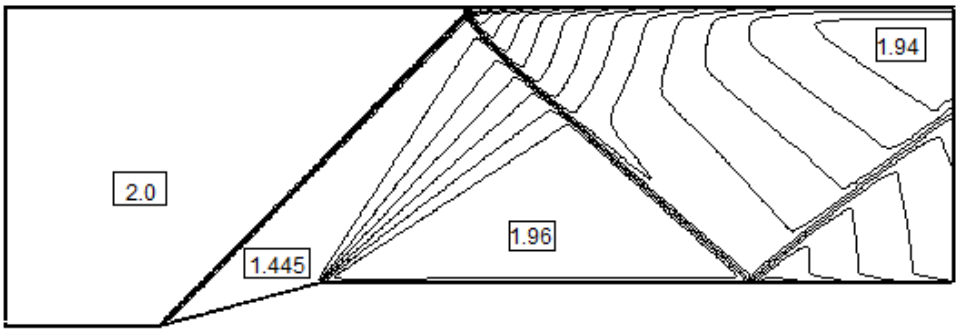

FIGURE 4.3: Mach contours of supersonic flow past ramp in a channel

the Van Leer scheme are not different from those using HLLE. Hence Van-Leer scheme and AUSM scheme are not included in this figure. It is evident from this comparison that the Roe and HLLE schemes are quite accurate and show comparative performance. The AUSM family of schemes are as accurate as the Roe scheme, but the AUSM+ scheme introduces overshoots and undershoots and this numerical behavior has been reported by other researchers as well. On the other hand, the fluxes computed using the AUSMPW scheme shows a smooth pressure rise similar to the Roe scheme. The Rusanov scheme predicts a much lower pressure rise as compared to all other schemes. The convergence history is shown in figure 4.6 and it indicates that there is little to separate between the seven schemes in terms of the computational cost, measured as time per iteration, although the Rusanov scheme converges marginally earlier compared to the remaining schemes.

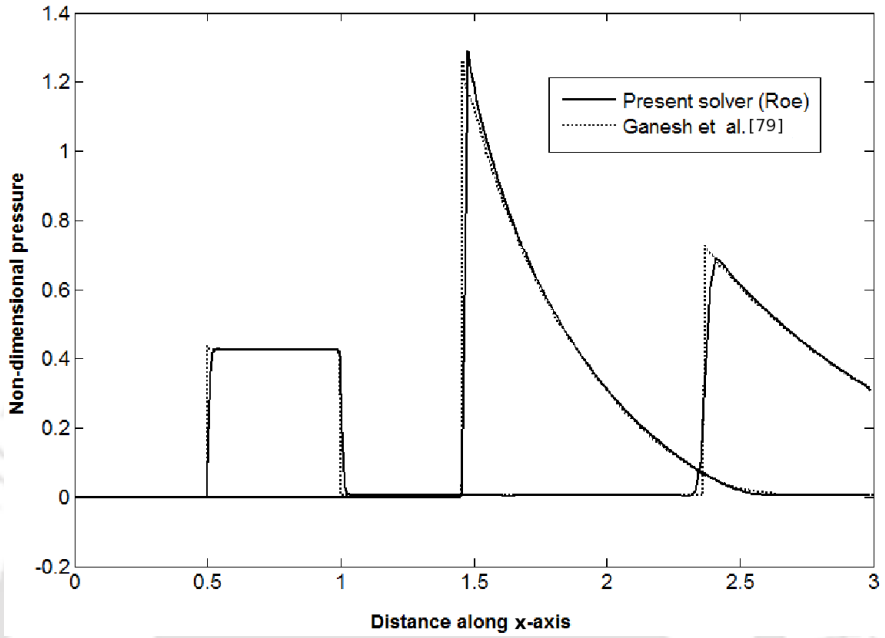

FIGURE 4.4: Wall pressure distribution for supersonic flow past ramp in a channel

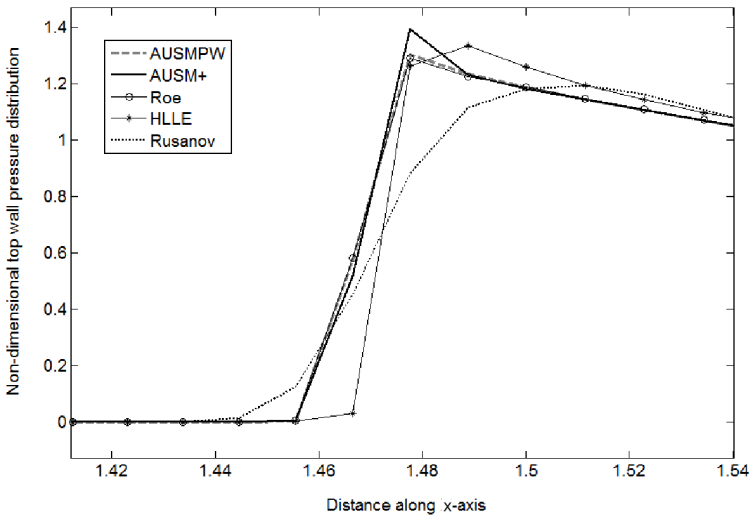

FIGURE 4.5: Comparison of pressure rise across Mach stem predicted by five different schemes for test case 1 (enlarged view)

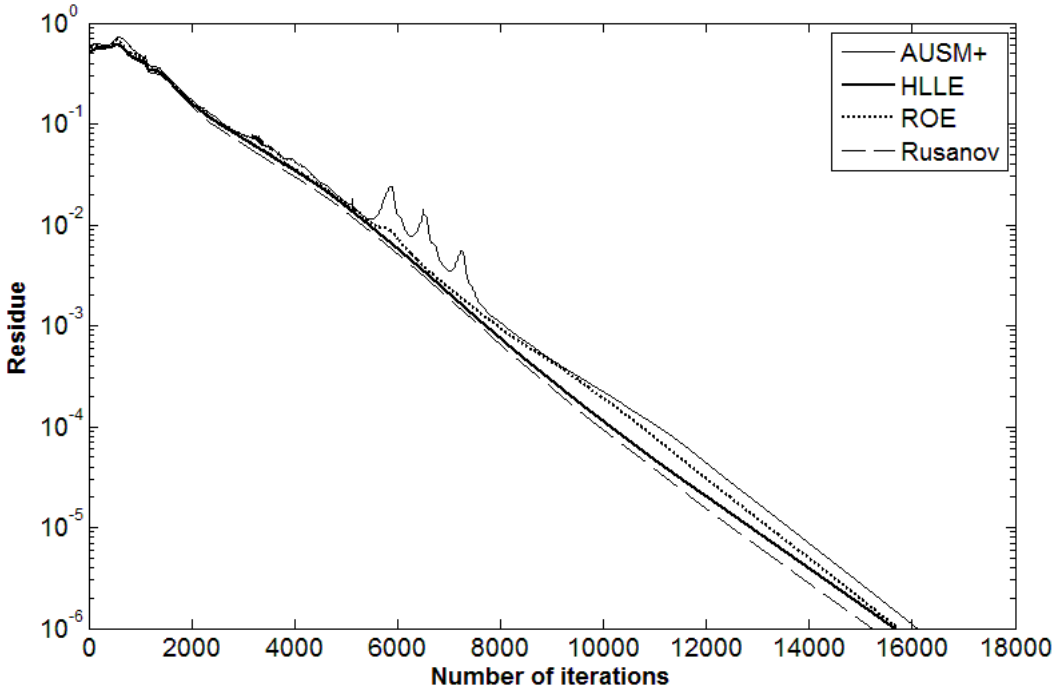

FIGURE 4.6: Residual fall comparison for test case 1

4.2.2 Test case 2: Mach reflection

Shock reflection has been a subject of intense research over the years because of its importance in high-speed flows. This test case deals with the shock reflection as Mach reflection from the solid wall. As shown in figure 4.7, there exists a triple point (T) at some distance away from the wall where the incident and reflected shocks intersect to form a normal shock which anchors itself to the wall. In the presence of three shock waves at point T, a slip line (SS) emanates to separate the streams of different entropies. The occurrence of Mach reflection and the resulting Mach stem height (Hm) are strong functions of the freestream Mach number and the wedge length (l_w).

The configuration considered by Hornung and Robinson [94] and Ben-Dor [95] has been used in the present study with an incident shock wave angle of 40.7^0 ($\beta \approx 40.7^0$). The domain and associated boundary conditions are shown in figure 4.8. A structured mesh having 20,000 cells is employed for this simulation. Here, freestream Mach number is 2.84 while wedge length is unity and throat height is 0.37. Such configuration has been considered by Azevedo and Liu [96] during their experiments.

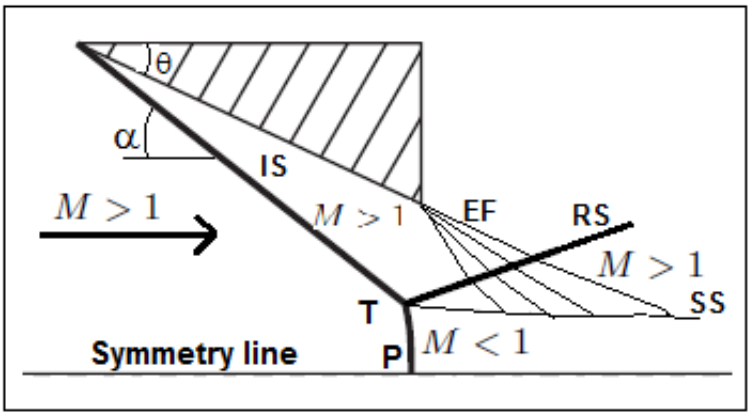

FIGURE 4.7: Schematic diagram of Mach reflection

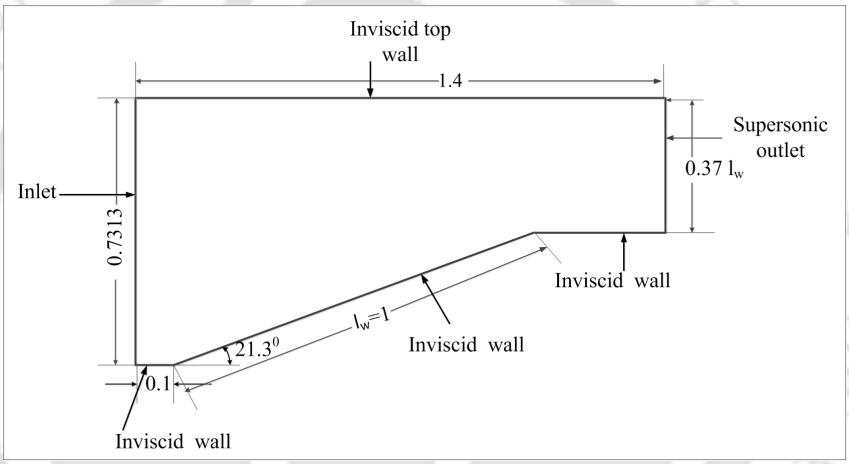

FIGURE 4.8: Domain and boundary conditions used for Mach reflection test case

All the numerical schemes except AUSMPW are employed to predict the flowfield. A representative density contour obtained using the Roe scheme is shown in figure 4.9. The incident and reflected shocks as well as Mach stem and the slip line are crisply captured. The remaining flux schemes also capture these flow features but their qualitative behaviour is similar to the earlier test case, with the Rusanov scheme being more dissipative in comparison with the Roe and AUSM family of schemes. The comparison of the Mach stem height of these studies is shown in figure 4.10. It is observed that all numerical schemes over predict the height of the Mach stem as compared to the analytical and experimental values. Such an over prediction has been reported earlier by Vuillon et al.[97]. As in the previous test case, there is little evidence for choice of a preferred scheme for the inviscid computations in this test case as well, on a sufficiently fine mesh.

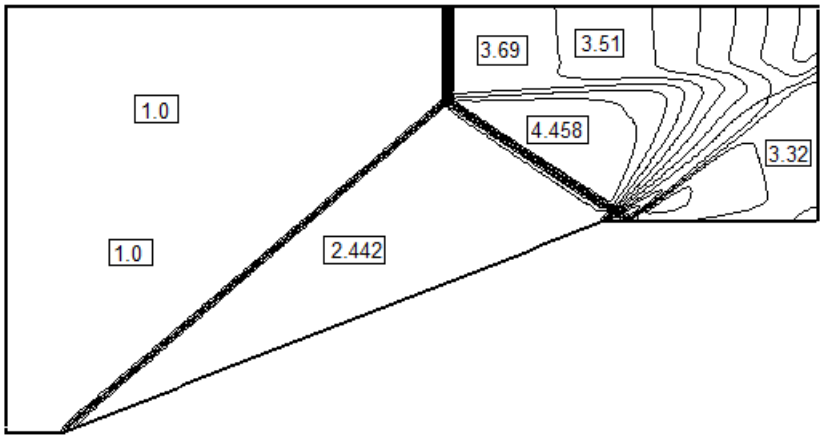

FIGURE 4.9: Non-dimensional density contours of Mach reflection test case

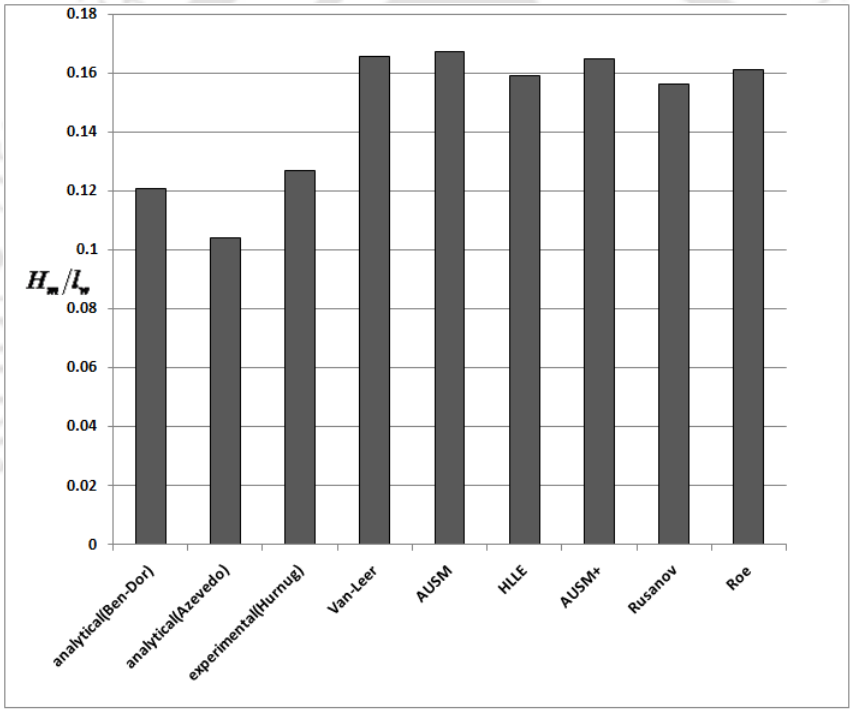

FIGURE 4.10: Comparison of Mach-stem height predicted by different methods for $M_\infty = 2.84, Ht/lw = 0.37, \beta \approx 40.7$

4.2.3 Test case 3: Hypersonic flow through SCRAMJET intake

In order to evaluate the feasibility of flux schemes for practical configurations encountered in high-speed flows, Mach 5 flow through a SCRAMJET (Supersonic Sombustion RAMjet) intake has been considered here. The configuration for this test problem is same as that proposed by Kumar [98] and is shown in figure 4.11. This test case provides a unique platform to evaluate the capabilities of different schemes to capture the complex internal flow hypersonic aerodynamics.

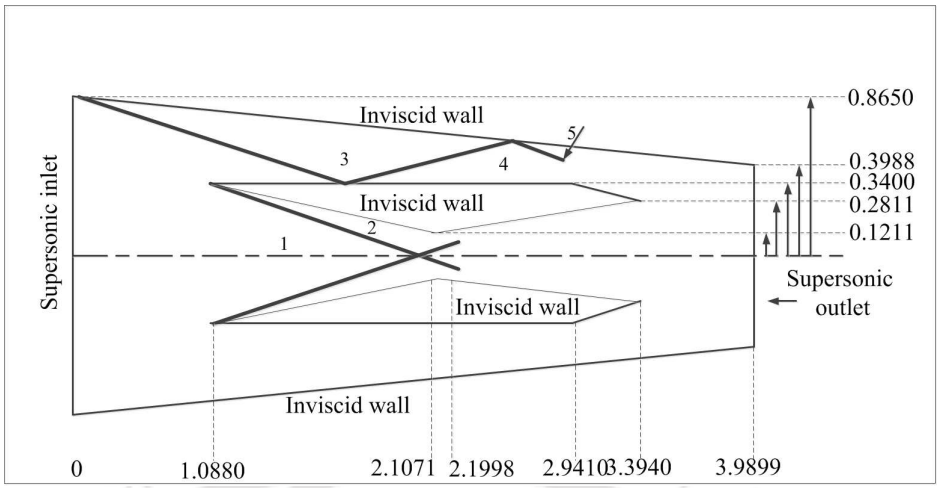

FIGURE 4.11: Geometry of the two dimensional SCRAMJET intake

This test case involves several complex flow features that include oblique shocks emerging from various compression corners of domain, expansion fans from different expansion corners, interaction of shocks at the symmetry line, reflection of shocks from walls, interaction of shocks and expansion waves and slip streams that separate different entropy layers.

A quadrilateral mesh having 18,900 cells is employed for simulation of this test case where all schemes excluding AUSMPW have been studied. It has been observed that the Roe scheme is unstable and no steady-state solution could be obtained, which is attributed to the lack of sufficient numerical dissipation. The convergence histories of five other schemes are similar and only those corresponding to AUSM+ and Rusanov have been plotted in figure 4.12. table 4.1 compares the jump in fluid properties across the cowl shock obtained using the AUSM+ scheme with the analytical oblique shock relations. A good agreement is seen which is testimonial to the performance of the AUSM+ scheme for this test problem. All other schemes also predict these jumps with comparable accuracy on this mesh, while the resolution of shocks and expansions by the schemes are qualitatively similar. It is evident from figures 4.13 and 4.14 that, the dissipative Rusanov scheme smears the weak slip streams as opposed to a sharp resolution of these slip lines by the AUSM+ and HLLE schemes. A similar observation may also be made from the centreline density variation obtained with one of the less dissipative scheme, AUSM+, and the highly dissipative scheme Rusanov as shown in figure 4.15.

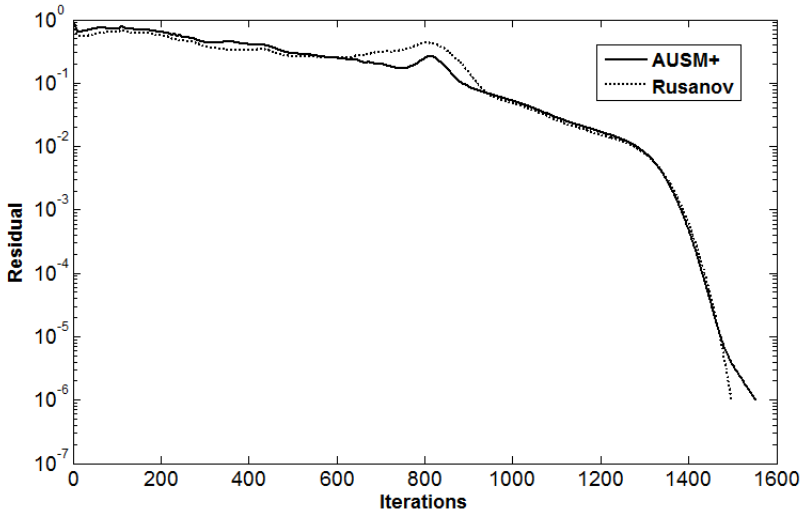

FIGURE 4.12: Residual fall comparison for test case 3

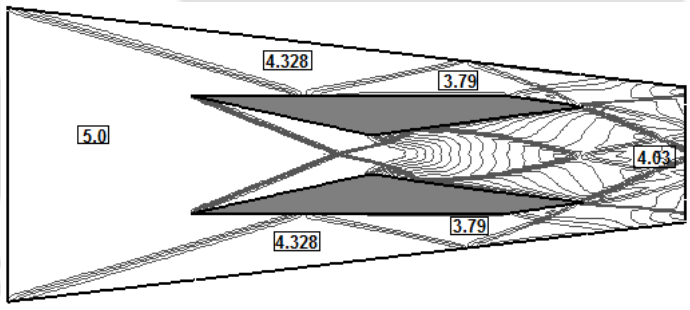

FIGURE 4.13: Mach contours using AUSM+ for test case 3

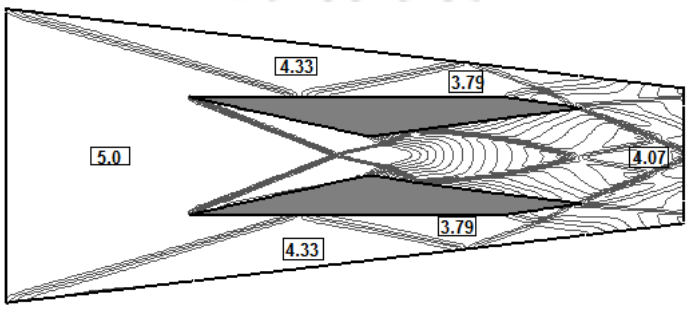

FIGURE 4.14: Mach contours using Rusanov scheme for test case 3

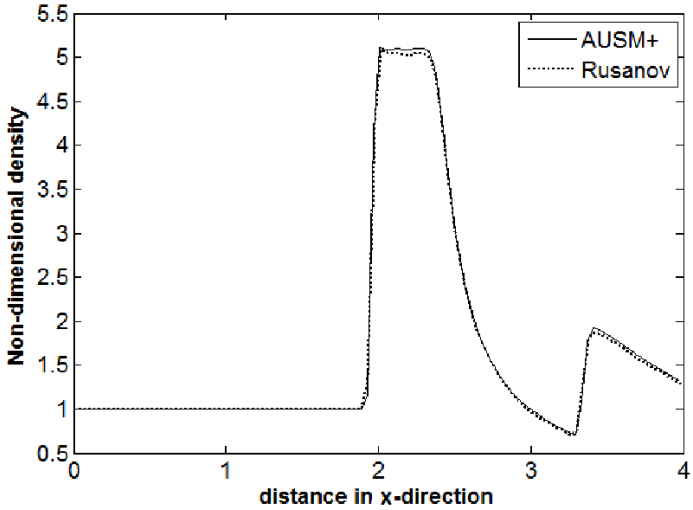

FIGURE 4.15: Comparison of centreline density variation obtained with AUSM+ and Rusanov schemes

	M_2	β	p_2/p_1	ρ_2/ρ_1	T_2/T_1
Present solver result	3.75	21.51	3.825	2.43	1.571
Oblique shock relations	3.76	21.72	3.828	2.44	1.569

TABLE 4.1: comparison of property jumps across oblique cowl shock

4.2.4 Test case 4: Hypersonic flow over double ellipse configuration

A good test problem to study the applicability of numerical flux schemes for high-speed external aerodynamics is the flow over a double ellipse configuration. This configuration represents the nose portion of space capsules and is a very relevant test problem in hypersonic aerodynamics. The suitability of the numerical schemes is studied for the Mach 8.15 flow past the double ellipse configuration. This test problem and associated boundary conditions are shown in figure 4.16. The proposed hypersonic stream is considered at 30^0 angle of incidence for the test configuration.

Unstructured mesh having 17,362 cells with sufficient clustering in the shock location (figure 4.17) has been employed for the simulation to illustrate the generic nature of the solver. All schemes except the Roe scheme are able to obtain converged solutions to steady-state. It can be

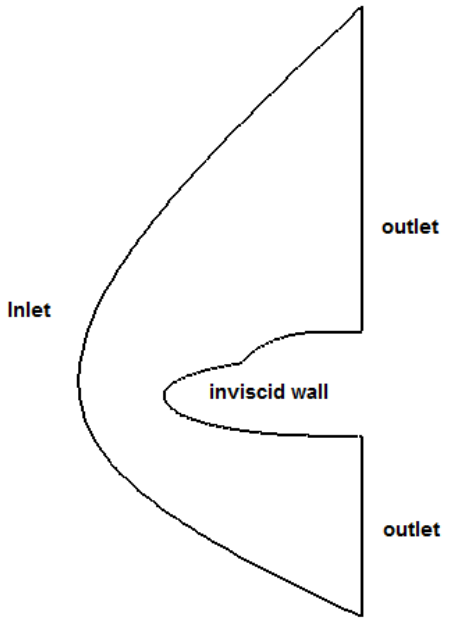

FIGURE 4.16: Geometry for hypersonic flow over double ellipse

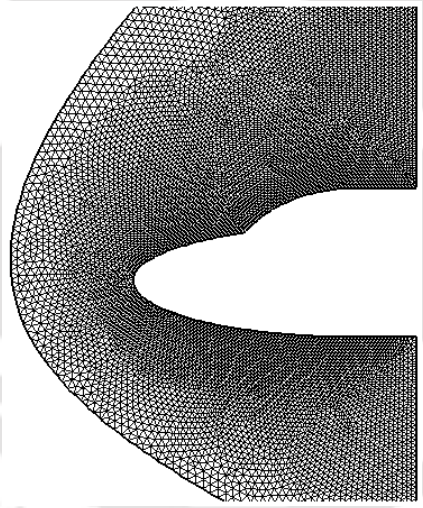

FIGURE 4.17: Enlarged view of mesh used for hypersonic flow over double ellipse

seen from the pressure and Mach contours obtained with the AUSM+ scheme (figures 4.18(a) and 4.18(b)) that the detached bow shock and the weak canopy shock are well resolved. All schemes are found to behave in a qualitative similar manner in resolving the flowfield. It is however reasonable, in the light of earlier investigations to assume that the Rusanov scheme would lead to a poorer resolution of the weaker canopy shock as compared to the AUSM and HLLE schemes. The surface pressure distributions from AUSM+ and AUSMPW schemes are seen to agree well with each other as well as the numerical results of Gustafsson et al. [99] and

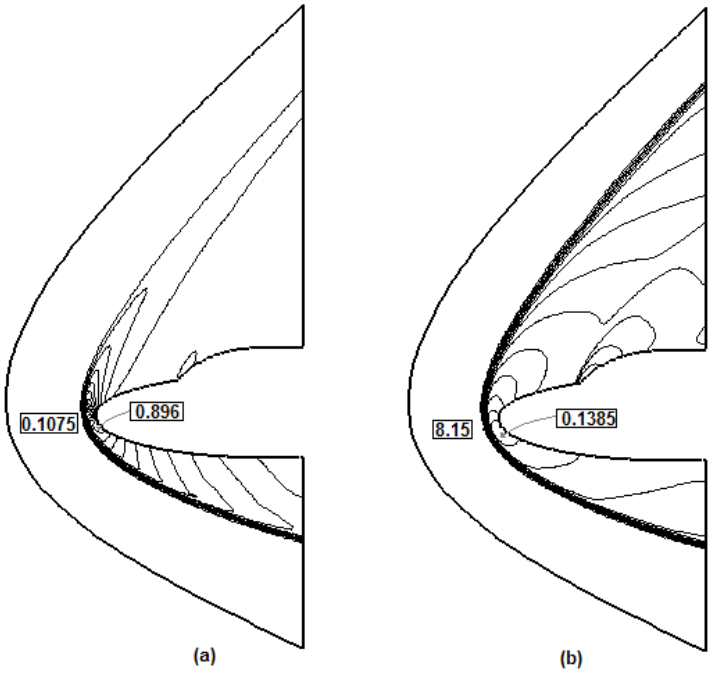

FIGURE 4.18: Contours of (a) pressure and (b) Mach number for hypersonic flow over a double ellipse

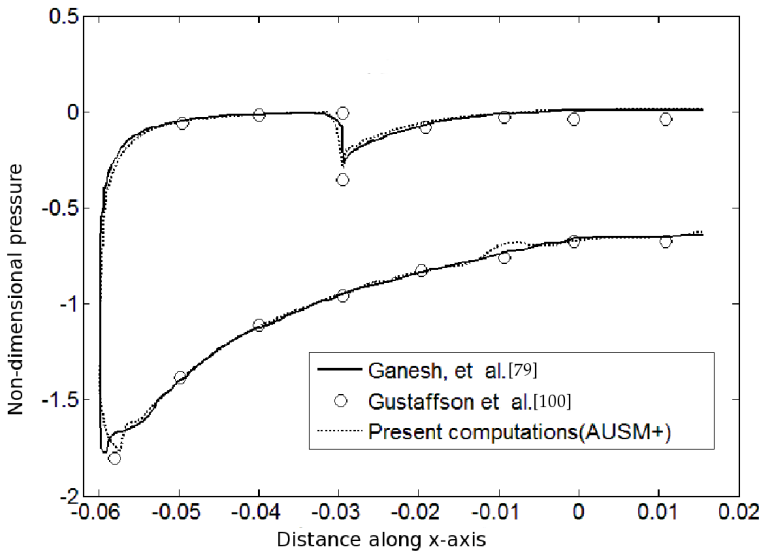

FIGURE 4.19: Comparison of surface pressure predicted using AUSM+ with reported numerical results for the hypersonic flow over a double ellipse case

Ganesh et al. [78], as shown in figure 4.19. The pressure distributions at the nose and canopy shock regions are enlarged (figure 4.20) to clearly distinguish the salient differences in surface pressure predictions of different schemes. As expected, predictions of HLLE and AUSM family of schemes are less dissipative when compared to the Rusanov scheme.

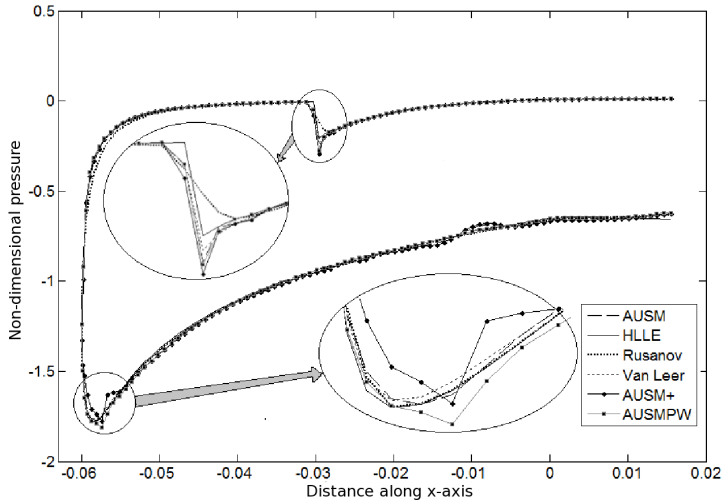

FIGURE 4.20: Comparison of surface pressure predicted by six different schemes for the hypersonic flow over a double ellipse case

4.3 Summary

The performance of different numerical flux schemes has been analysed for two dimensional inviscid flows in supersonic and hypersonic regimes. These studies have been performed on internal and external flow problems using structured and unstructured meshes in order to comprehensively assess the schemes for their ability to resolve the flow physics. The Roe scheme is found to work well for supersonic flows but fails for hypersonic flows, which is attributed to its low dissipation. On the contrary, the Rusanov scheme is noted to be the most dissipative scheme but relaible for convergence to the steady solution for all test problems. While the high numerical dissipation lends to a robust scheme, it also smears flow features such as shocks and slip lines. The Van Leer scheme behaves similar to the Rusanov scheme, but offeres lesser dissipation in comparison. The HLLE and AUSM family of schemes offer the best tradeoff between accuracy and dissipation. While some variants of the AUSM family of schemes, such as the AUSM+ scheme, show overshoots in pressure jumps. The HLLE scheme and latter variants of the AUSM family (such as AUSMPW as well as AUSMPW+) are as accurate and produce no overshoots or undershoots. In summary, while all schemes perform equally well for supersonic flows, the best schemes for hypersonic applications are the AUSM family and HLLE schemes. This study also points to the fact that there is a need to balance accuracy and dissipation to achieve robust and accurate solutions and therefore the necessity for the development of flux blended schemes for high speed fluid flow applications.

Chapter 5

Numerical investigations of ramp induced shock wave boundary layer interaction

Overview

The detailed numerical investigations about the physics of R-SWBLI is discussed in this chapter. Initially mesh independence study is presented for the literature reported configuration and test conditions. It is followed by the discussions on the numerical simulations of SWBLI about the effect of various parameters such as ramp angle, freestream Mach number, freestream stagnation enthalpy, wall temperature and leading edge radius on the separation bubble dynamics in hypersonic flows. Therefore the major thrust of present SWBLI studies is to understand the boundary layer separation due to the adverse pressure gradient offered by ramp induced shock wave. Quantification and qualitative judgement of this effect requires an analysis of quantities such as wall heat transfer, wall skin friction coefficient and wall pressure.

5.1 Background

It had been reported in the literature that the ramp induced separation of laminar boundary layer depends on several parameters like Mach number, Reynolds number, wall temperature, ramp angle, etc. Amongst them incipient separation angle, which is the minimum required flow deflection angle to ensure flow separation can be estimated using the relation given by Needham and Stollery [3].

$$M_\infty \theta_{is} = 80\sqrt{\bar{\chi_L}} \tag{5.1}$$

where χ_L is the viscous interaction parameter at the flat plate-ramp junction, and is given by,

$$\bar{\chi_L} = M_\infty^3 \sqrt{C}/\sqrt{Re_L} \tag{5.2}$$

Where,

$$C = \frac{\mu_W T_\infty}{\mu_\infty T_W}$$

If the deflection angle is higher than the incipient separation angle, then boundary layer separation takes place. Such ramp induced boundary layer separation may lead to significant deterioration of intended performance of various space vehicle components. Therefore present chapter deals with the effect of various governing parameters on the dynamics of SWBLI. Literature reported configurations and test conditions are chosen for these studies. Such computational simulations for the experimentally studied configurations and freestream conditions will also demonstrate the capability of present solver to handle and resolve the particular flow features. These efforts would also compliment the experimental results by providing specific information about separation point, reattachment point, separation bubble size and extent of upstream influence. Therefore such investigations are extremely essential to justify the conclusions drawn from experimental measurements which have constraint on resolution due to sensor size, therefore may lack in providing specific information. Some experimental studies are based on pressure measurement which as well bear same limitation. Thus quantification of the experimental qualitative observations can be achieved using such simulations.

5.2 Configurations, test conditions and solver settings

Numerical investigations of R-SWBLI phenomenon are carried out by employing in-house developed flow solver, 'USHAS'. Prominent experimental findings are considered to get the necessary input for configuration and test conditions. These cases are listed in table 5.1, while the figure 5.1 demonstrates the necessary terminologies using the computational domain and associated boundary conditions.

Case	Reference	T_0 K	T_w K	M_∞	Re_∞/m	θ degree
Case A	Holden [22]	1880.84	294.38	11.63	552116	15
Case B(1)	Marini [23]	1080	300,400,500	6 (5,7 and 8)	8×10^5	10,12.5,15
Case B(2)	Marini [23]	1800	300,400,500	6 (5,7 and 8)	8×10^5	10,12.5,15
Case C	Grasso et al.[52]	1102.5	290	10	1.65×10^5	15,20,25

TABLE 5.1: Details of investigated cases

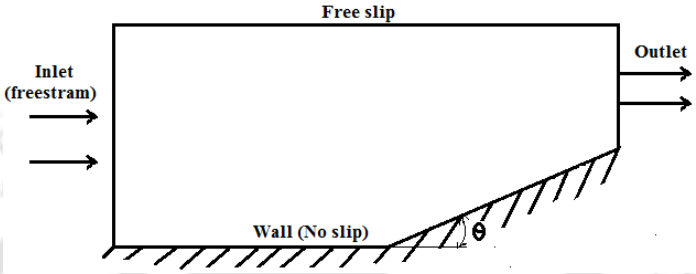

FIGURE 5.1: Schematic of computational domain

All of the above mentioned conditions belong to laminar flow. Therefore incipient condition analysis given by Needham and Stollery [3] can be performed for these cases to analyse the possibility of flow separation. Such incipient analysis has shown that, some of the cases are in separated region while others are in attached flow regime. This can be well understood from figure 5.2. Moreover the total temperature of all of the above mentioned conditions are sufficiently low to consider the flowfield as ideal gas flow. Hence the perfect gas model of the 'USHAS' is preferred for all the simulations. Inviscid fluxes are computed using second order AUSM scheme. The time integration for the present simulations is achieved by employing explicit Euler scheme.

5.3 Grid independence studies

This section deals with the methodology of grid independence test followed in present studies. Two such tests, "Case A" and "Case B", are chosen for this discussion due to large difference in their freestream Mach numbers.

5.3.1 Grid independence study for Case A

The grid independence study for the present case has been carried out by employing three different grid levels viz. $120 \times 60, 190 \times 80$ and 230×120, with sufficient clustering near the walls to

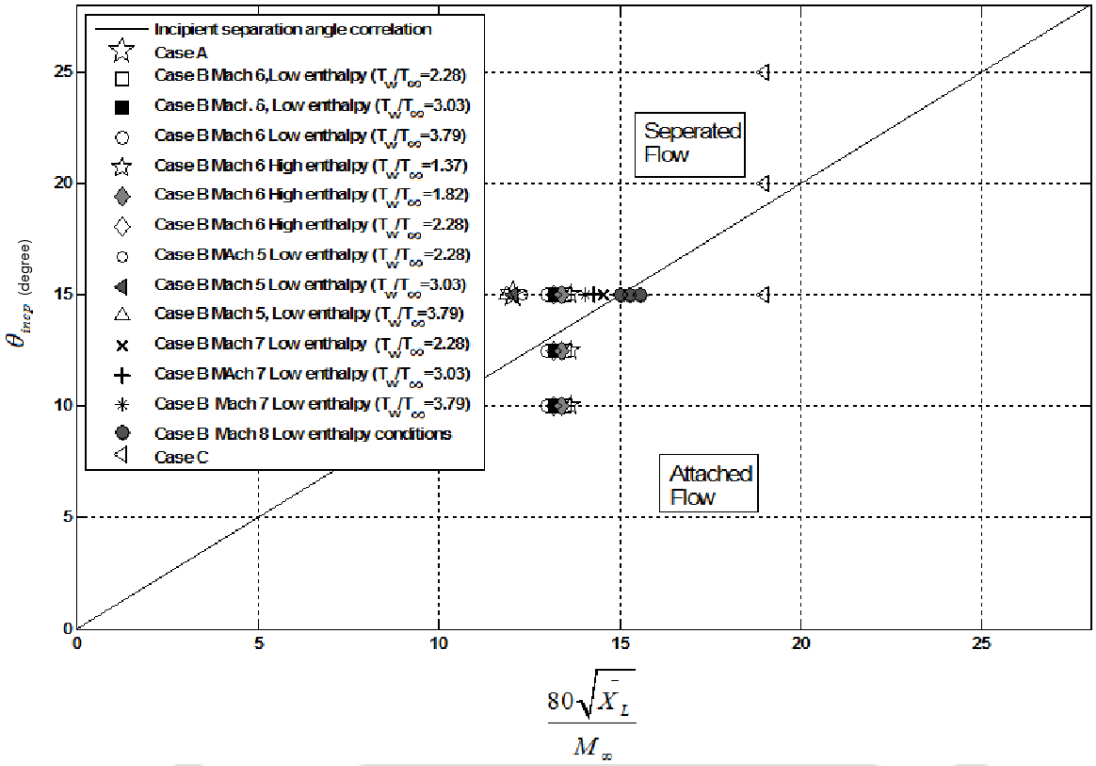

FIGURE 5.2: Incipient separation condition analysis

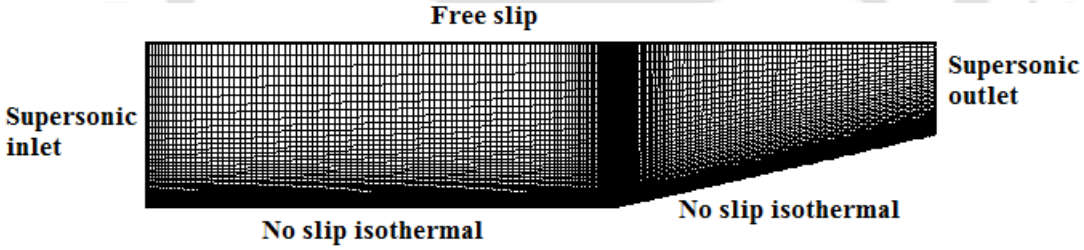

FIGURE 5.3: Sample mesh used for the simulation of Case A

resolve the boundary layer. Grid points are also clustered at the leading edge and ramp-flat plate junction for accurate prediction of flow features. Such grid used for the present study, marked with boundary conditions, is shown in figure 5.3.

The steady state results in terms of surface pressure, Stanton number and skin friction co-efficient distribution are shown in figure 5.4 and 5.5 respectively. It is clear from the surface parameter distribution comparison that, a grid size of 190×80 is sufficient enough to reproduce experimental measurements. Comparison of numerical results with experimental measurements shows a good agreement, which confirms the accuracy of present solver in the prediction of such complex flowfields. Thus all the flow features related to SWBLI are seen to be captured. Ramp

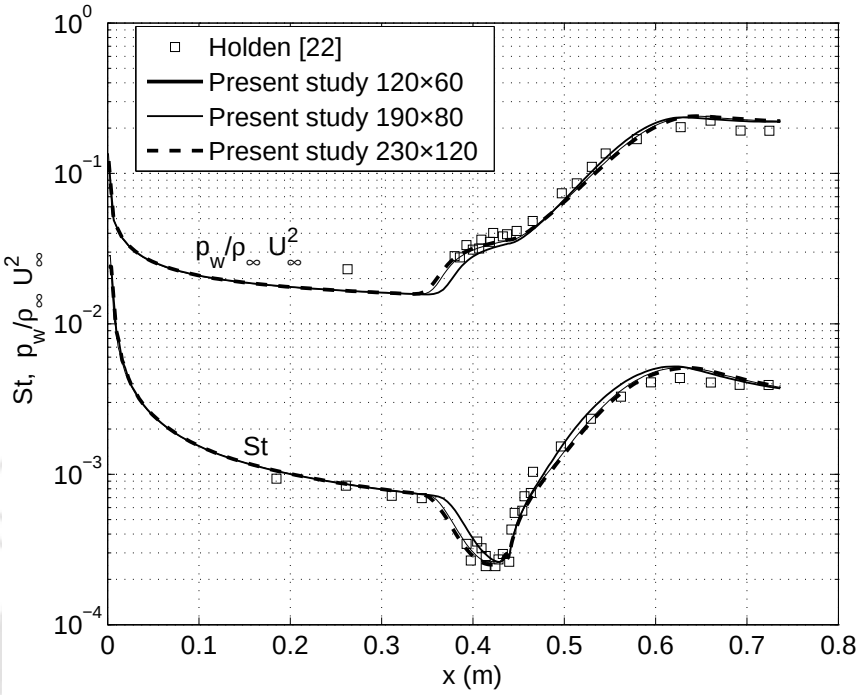

FIGURE 5.4: Stanton number and wall pressure distribution for Case A

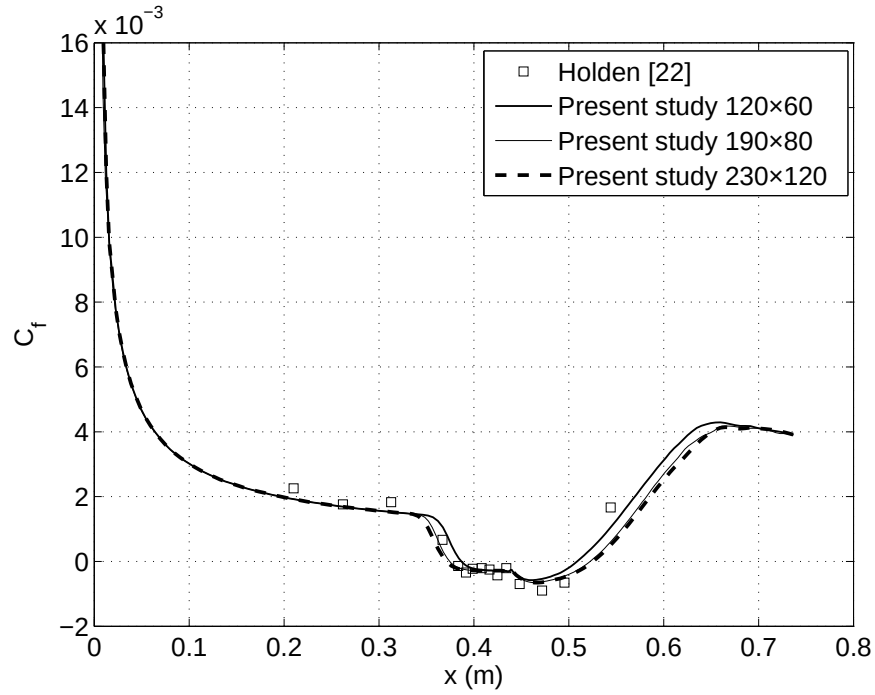

FIGURE 5.5: Skin friction distribution for Case A

angle of 15^0 is sufficiently above the incipient separation angle for the chosen freestream conditions. Therefore the flow separates well ahead of the ramp foot. The plateau pressure region of surface pressure distribution and negative values in the skin friction distribution are accounted for separation. From the Stanton number distribution analysis it is observed that the heat flux tends to reduce and reach a minimum value as the laminar boundary layer on the flat plate separates well ahead of the ramp foot. Further reattachment of the flow at the ramp surface, across the strong reattachment, shock terminates the separated region. The heat flux and skin friction coefficient are observed to be increasing rapidly beyond the reattachment point due to the recompression of boundary layer. This increasing nature of heat flux and skin friction coefficient reach a peak value at a location where, the boundary layer thickness reaches minimum, followed by gradual decrease due to boundary layer thickening and flow acceleration.

5.3.2 Grid independence study for Case B

The present investigations are centered on the experimental conditions of Marini [23] (Case B). Therefore grid independence studies are presented in this section for those experimental test conditions. These experimental freestream conditions are later varied to understand the parametric influence. Such variations are mentioned in table 5.1. Typical mesh independence test discussed herewith is performed for a flat plate of length 0.05 m attached with 15^0 ramp and exposed to freestream conditions of M_∞ = 6.0 and $Re_\infty = 8 \times 10^5 m^{-1}$. Four different meshes, viz. 180×60, 180×90, 240×120 and 360×180, with sufficient clustering near the wall to resolve the boundary layers, are employed for the computations. Alike Case A, here as well grid points are clustered at the leading edge of flat plate and ramp-flat plate junction. Details of the grids employed for the present study are given in table 5.2.

The convergence histories of all four grid levels are also given in figure 5.6. It is clear from this figure that, the cost involved in the computation enhances with increase in number of cells. Here figure 5.7 shows the variation of skin friction coefficient (C_f) along the wall, obtained using four grid levels. The skin friction coefficient value at a particular, location 0.035 m away from the leading edge, and separation bubble size (L_b) obtained with different grid levels are also compared in figure 5.8. It is evident from figures 5.7 and 5.8 that the 180×90 mesh

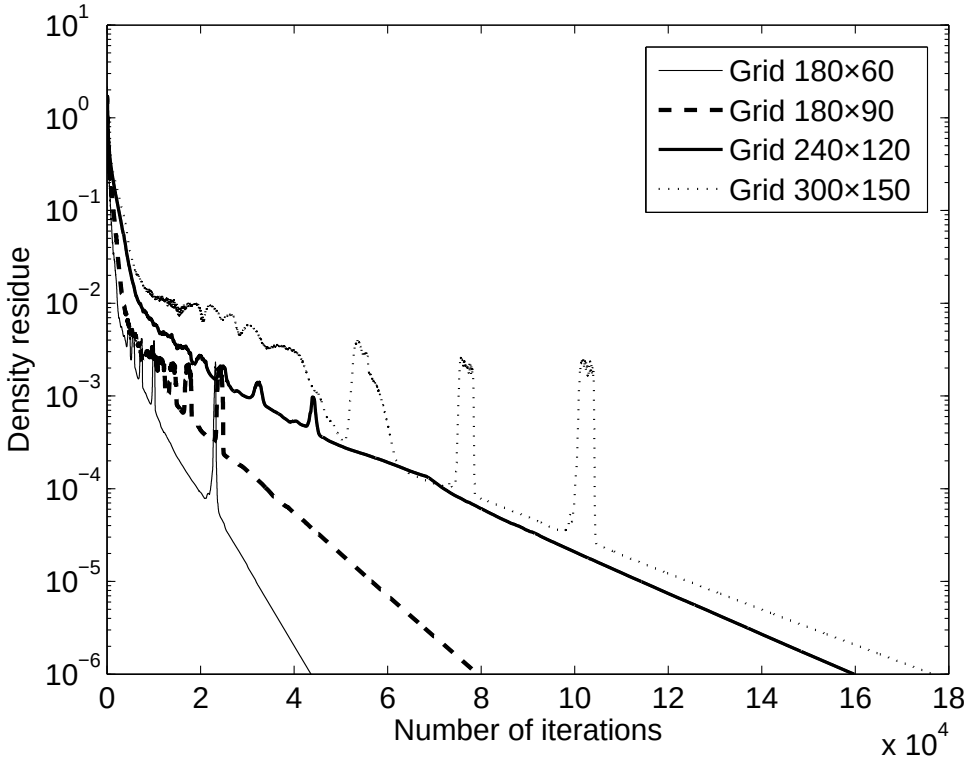

FIGURE 5.6: Convergence histories of different grid levels

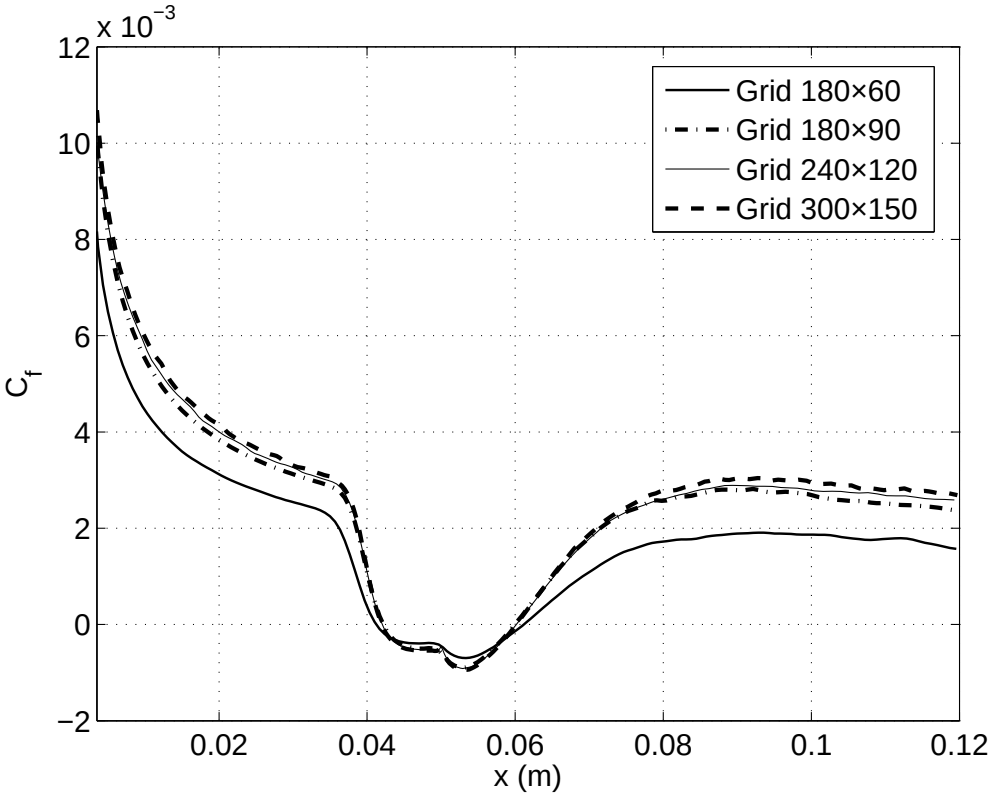

FIGURE 5.7: Grid independence study for a ramp based boundary layer separation (Case B)

Overall grid size	Maximum boundary layer thickness	No. of grid points in the boundary layer	Minimum element size near the wall (Δy_{min})	Minimum element size at the leading edge (Δx_{min})	Minimum element size at the flat plate -ramp junction ($\Delta x_{min,junc}$)
180×60	0.003	15	9×10^{-5}	7×10^{-4}	6×10^{-4}
180×90	0.003	20	5×10^{-5}	5×10^{-4}	4×10^{-4}
240×120	0.003	25	3×10^{-5}	3×10^{-4}	2×10^{-4}
360×180	0.003	35	1×10^{-5}	9×10^{-5}	8×10^{-5}

TABLE 5.2: Details of grids used for parametric studies of Marini's test case (Case B), where all dimensions are in m

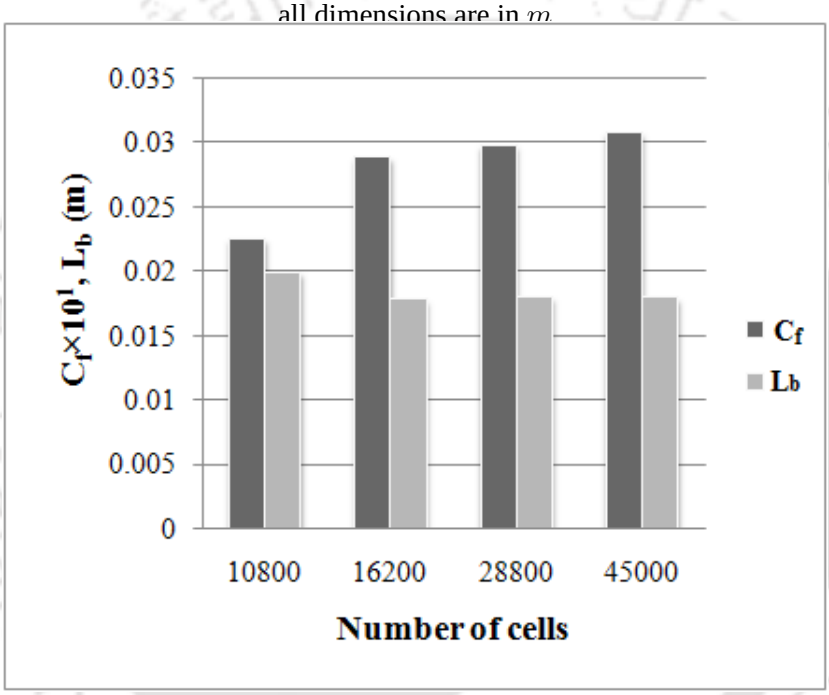

FIGURE 5.8: Comparison of C_f value at x = 0.035 m and separation bubble size (L_b) obtained with different grid levels

gives almost grid-independent solution with lesser computational cost. Such mesh independence studies are performed for all the test cases to arrive at an appropriate mesh size. Thus obtained mesh independent results are considered for understanding of SWBLI.

5.4 Effect of governing parameters on dynamics of SWBLI

5.4.1 Effect of ramp angle

Studies for the effect of ramp angle on SWBLI separation are carried out to verify the incipient separation condition [3] and also to enumerate the observations of Marini [23] from the pressure

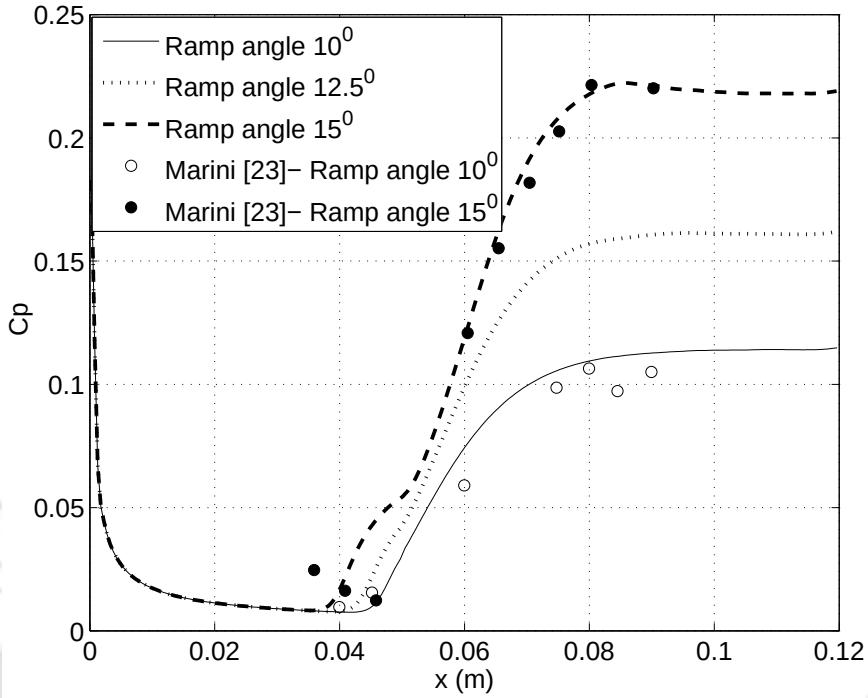

FIGURE 5.9: Effect of ramp angle on pressure distribution

measurement experiments. The freestream conditions considered for these simulations are Mach number 6, Reynolds number $8 \times 10^5\ m^{-1}$, wall temperature 300 K and freestream stagnation temperature 1080 K. These test conditions are same as in the experiments of Marini [23] on two test models. These configurations had same initial plate length (L) of 0.05 m but different angles viz. $\theta = 10^0$ and $\theta = 15^0$ respectively (figure 1.5). In addition, a model with ramp angle of 12.5^0 has been considered to verify the effect of numerics on the incipient separation angle (θ_{is}), which is 13.5^0 for the chosen test conditions. The surface pressure distribution from the present computations is compared with the experimental results of Marini [23] in figure 5.9. Encouraging agreement between the experimental and computational results can be noticed in this figure. Pressure distribution for the ramp angles 10^0 and 12.5^0 exhibit same trend unlike for the ramp angle 15^0 where marginal constant pressure region, upstream of the ramp, indicates the presence of a separation bubble.

The variation of heatflux along the plate and ramp for all the three cases is as shown in figure 5.10. This distribution is seen to follow the typical V-shaped curve in the vicinity of the ramp for the two lower angled test models, whereas the heat flux distribution of ramp angle 15^0 follows a

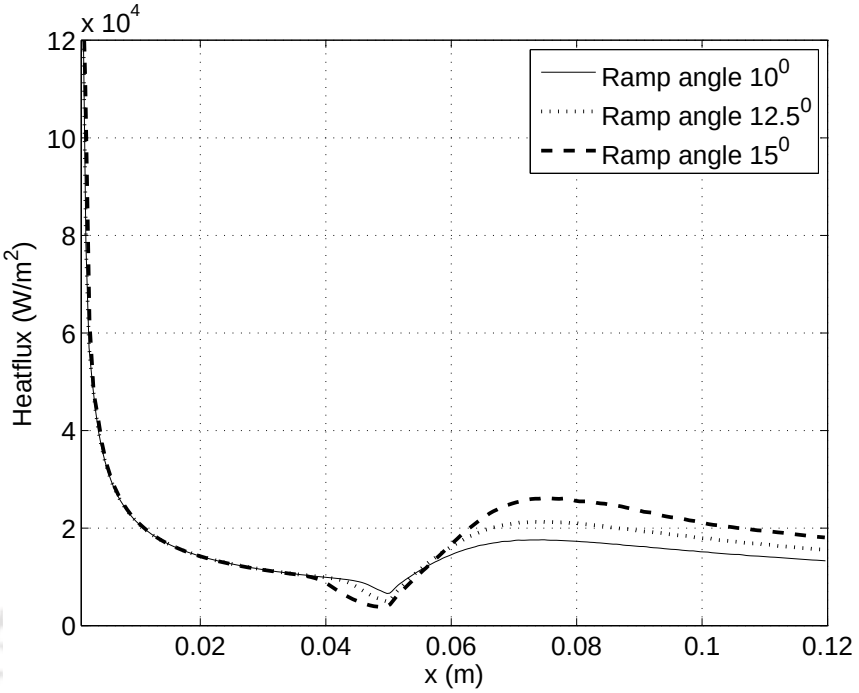

FIGURE 5.10: Effect of ramp angle on heatflux distribution

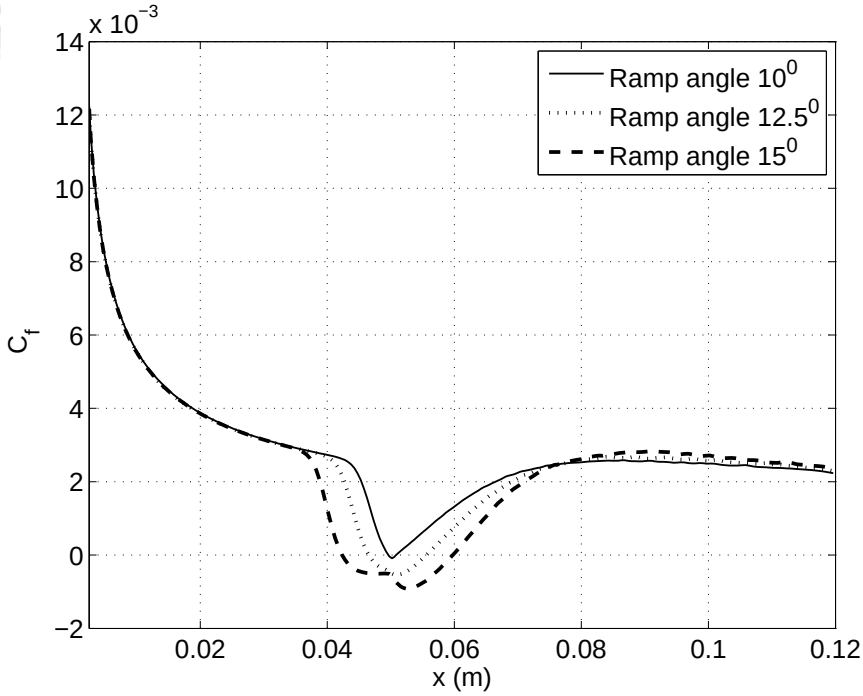

FIGURE 5.11: Effect of ramp angle on skin friction distribution

diffused V or U shaped curve at the same location. Increase in upstream influence, noted from early rise in pressure and drop in heatflux values ahead of the ramp, with increase in ramp angle can be depicted from both figures 5.9 and 5.10. However it is not possible to obtain further information with regard to separation from these data which otherwise is evident from the skin friction distribution on the wall (figure 5.11) obtained from computations. The points at which the skin friction curve crosses the zero line give the locations of separation and reattachment points. Details of numerical results obtained for ramp angle variations are given in table 5.3. From the present simulations, it is seen that the 10^0 ramp does not lead to separation while separation bubble of length 17.75 mm is observed for the ramp angle of 15^0. Interestingly, a separation zone of length 9.2 mm is observed for the 12.5^0 ramp, in contrast to Needham and Stollery's correlation which predicts no separation for ramp angles below 13.5^0. Therefore this correlation must be alluded to only for cases that are "well-separated," since the numerical solutions are grid-independent and high-resolution. The latter flows are those for which there exists a discernible plateau in the pressure measurements. In other words, for ramp angles within the range of incipient separation predicted by the correlation, numerical studies are necessary to reveal the physics of the actual flow.

5.4.2 Effect of wall temperature

Numerical simulations are also carried out to understand the effect of wall temperature on SWBLI. A 15^0 ramp has been considered for this study as it has the maximum separation length among configurations considered herein. The freestream conditions are chosen as M_∞ = 6.0, Re_∞ = $8 \times 10^5\ m^{-1}$ and T_0 = 1080 K along with two different wall temperatures viz. 300 K and 500 K. In addition, the effect of an adiabatic wall as opposed to an isothermal wall is also investigated. Surface variation of pressure coefficient, heatflux and skin friction coefficient are shown in figures 5.12- 5.14 respectively.

Numerical results for wall temperature variations are also summarized in table 5.3. From the present studies, it is clear that the upstream influence increases with increase in wall temperature. Hence the adiabatic wall boundary condition has the largest upstream influence. Wall heatflux is seen to be decreased at all the locations for increased wall temperature case. The reason for

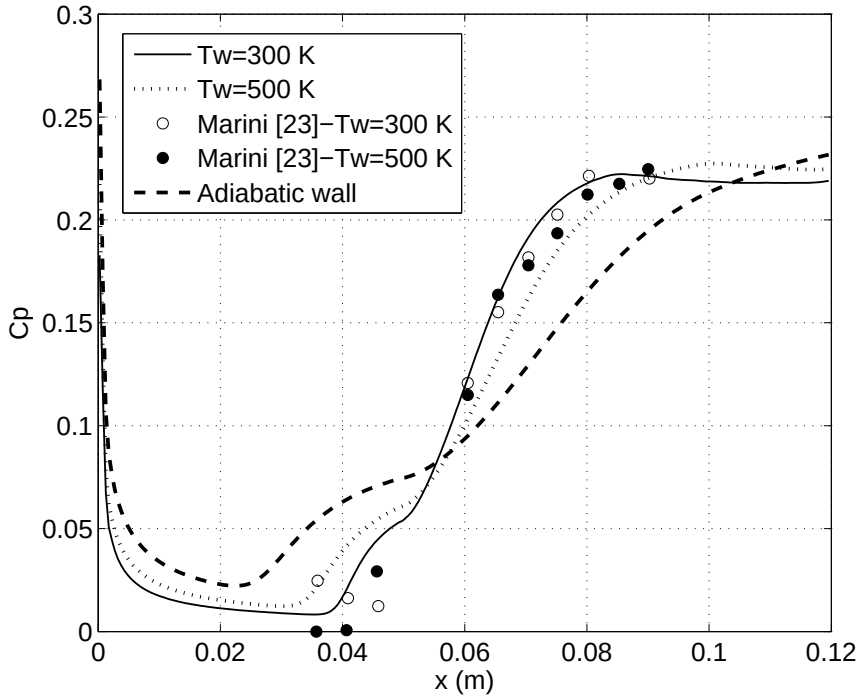

FIGURE 5.12: Effect of wall temperature on pressure distribution

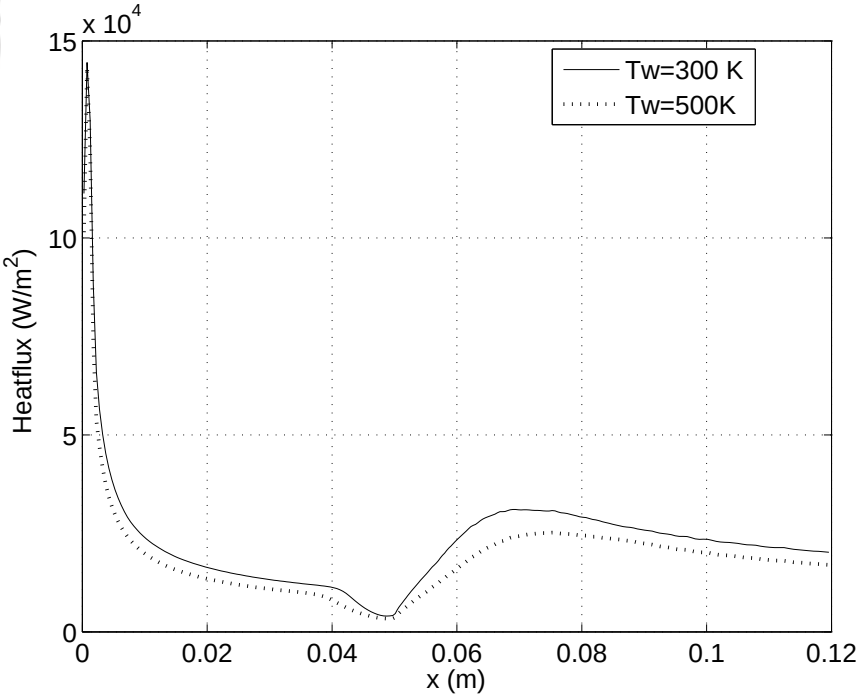

FIGURE 5.13: Effect of wall temperature on surface heat flux distribution

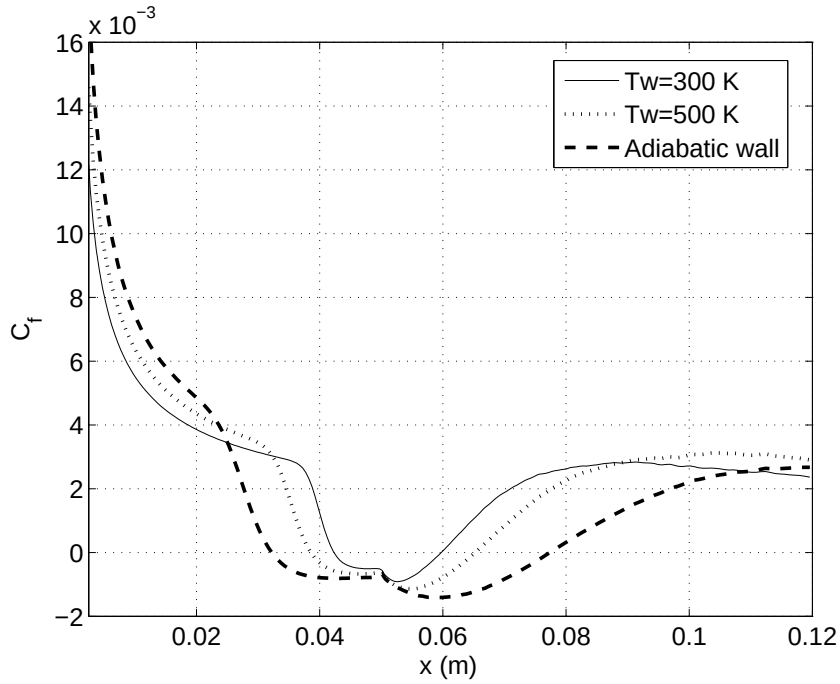

FIGURE 5.14: Effect of wall temperature on skin friction distribution

decrease in these wall properties lies in the fact that the increased wall temperature increases the viscosity which in turn increases the hydrodynamic and thermal boundary layer thicknesses. Hence, decrease in near wall gradients leads to decrease in heatflux. However, thicker boundary layer is more susceptible for separation, therefore early separation at x = 0.03825 m can be noticed for the increased wall temperature (500 K) case. Most upstream separation can be seen for adiabatic wall condition at x = 0.03225 m. Point of reattachment exhibits a trend of downstream shift with increase in wall temperature. Hence the separation bubble length is seen to be increased from 17.75 mm for 300 K case to 27 mm for 500 K wall temperature while the same for the adiabatic wall case is 46.25 mm. Therefore, the longest separation bubble among the three cases is for the adiabatic wall which is consistent with the results on upstream influence as well.

5.4.3 Effect of variation of freestream total enthalpy

Investigations have been performed with flows having two total temperatures to explore the effect of freestream total enthalpy (or total temperature). The conditions corresponding to total temperature 1080 K are referred here as low enthalpy test conditions while conditions corresponding to total temperature 1800 K are referred here as high enthalpy test conditions (table

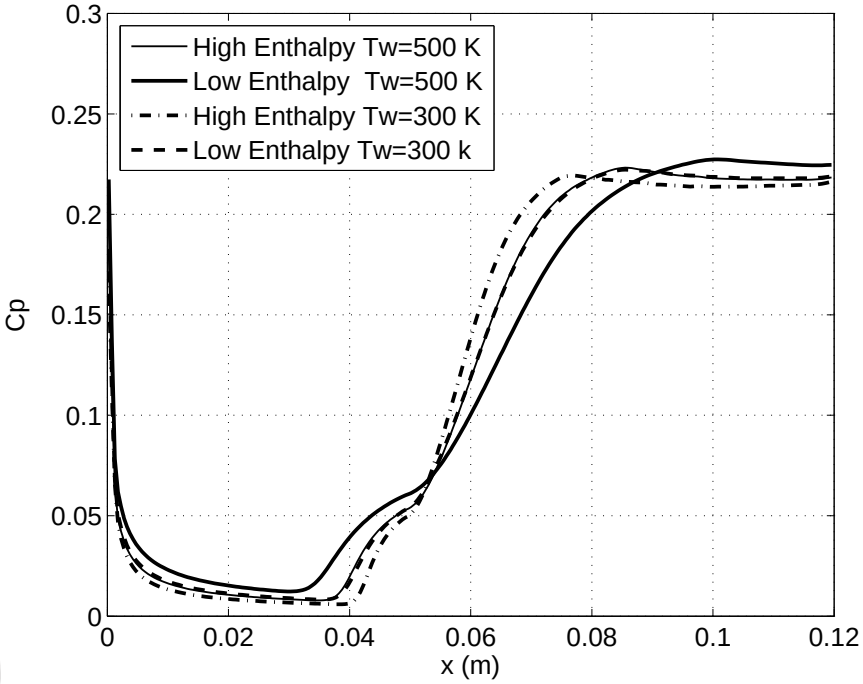

FIGURE 5.15: Effect of freestream enthalpy on pressure distribution

5.1). For these simulations, freestream Mach number and unit Reynolds number are 6 and $8 \times 10^5\ m^{-1}$ respectively. Computations are carried out with two different wall temperatures, viz. 300 K and 500 K. The variation in freestream total temperature affects the properties at the edge of the boundary layer, while wall temperature controls the temperature distribution within the boundary layer. Therefore the focus herein is also to study the combined effect of these quantities on SWBLI. The surface variation of pressure coefficient, skin friction coefficient and non-dimensional heatflux are shown in figures. 5.15-5.17 respectively. Here, non-dimensional heat flux at a location has been obtained using reference maximum surface heat flux. For a given wall temperature, increase in freestream stagnation enthalpy is seen to decrease upstream influence and consequently the extent of separation. For instance, the separation length for 300 K wall temperature reduces from 17.75 mm at low enthalpy conditions to 13.2 mm for high enthalpy conditions. The main reason for this observation is that, the increased stagnation enthalpy increases the kinetic energy of the fluid and provides greater resistance to the adverse pressure gradient. Similar observation can also be made for wall temperature of 500 K and is evident in figure 5.16.

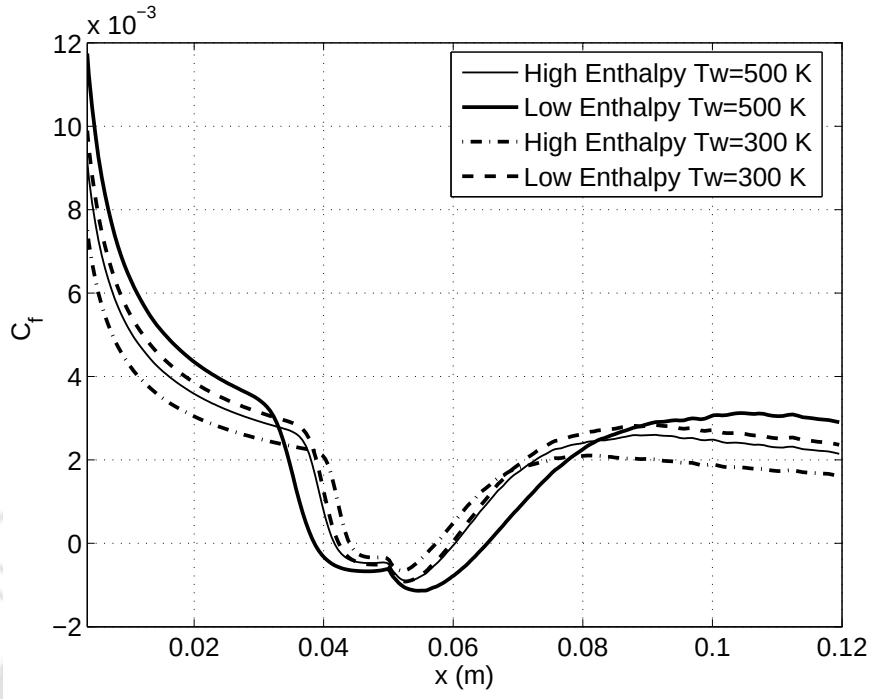

FIGURE 5.16: Effect of freestream enthalpy on skin friction distribution

An interesting observation in this study is that the non-dimensional heat flux distribution, surface pressure distribution as well as the skin friction distribution are nearly identical for the conditions of low stagnation enthalpy with low wall temperature as well as high stagnation enthalpy with high wall temperature. It follows that in either cases, the ratio of wall-to-total temperature is the same and therefore this non-dimensional ratio can be considered as an important indicator of SWBLI rather than the stagnation and/or the wall temperature themselves. Hence, from the present limited investigations, it is hypothesized that the parameter T_w/T_0 is the best indicator to make a meaningful comparison of SWBLI. Summary of these results is also provided in table 5.3.

5.4.4 Effect of variation of freestream Mach number

Four Mach numbers viz. 5, 6, 7 and 8 have been used in the present study to explore the Mach number effect on SWBLI. In this case, a fixed value of Reynolds number $8 \times 10^5\ m^{-1}$ has been used along with constant freestream temperature of 131.7 K and wall temperature of 300 K. The incipient separation condition analysis shows that, the critical angle is a direct function of freestream Mach number and also it decreases with increase in Mach number. However the

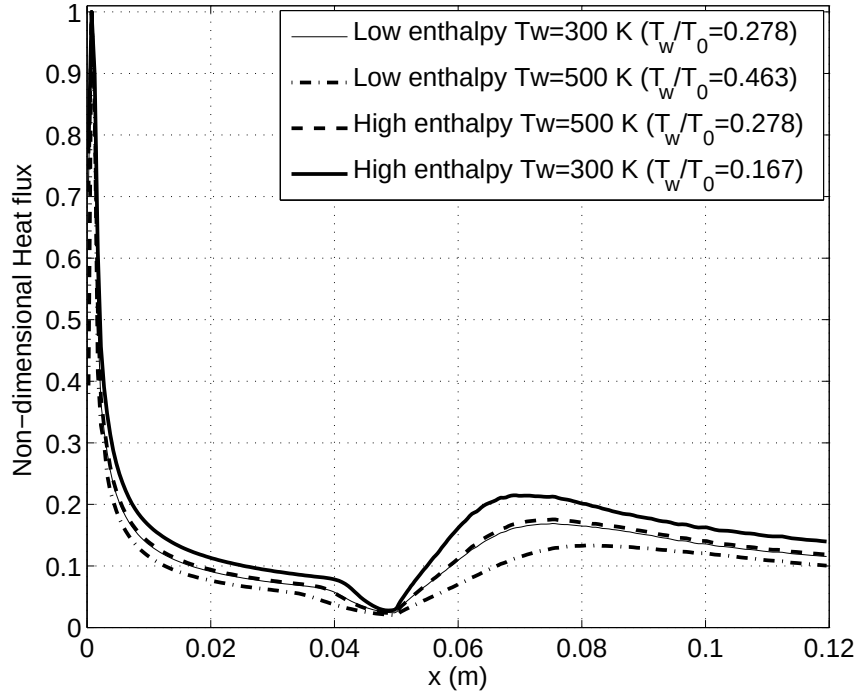

FIGURE 5.17: Effect of freestream enthalpy on non-dimensional heatflux distribution

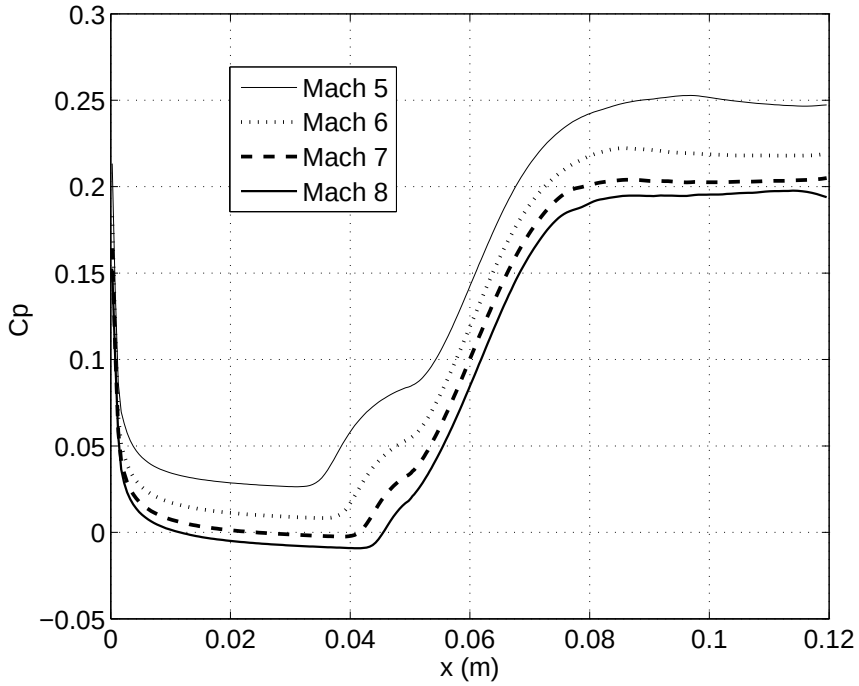

FIGURE 5.18: Effect of freestream Mach number on Cp distribution

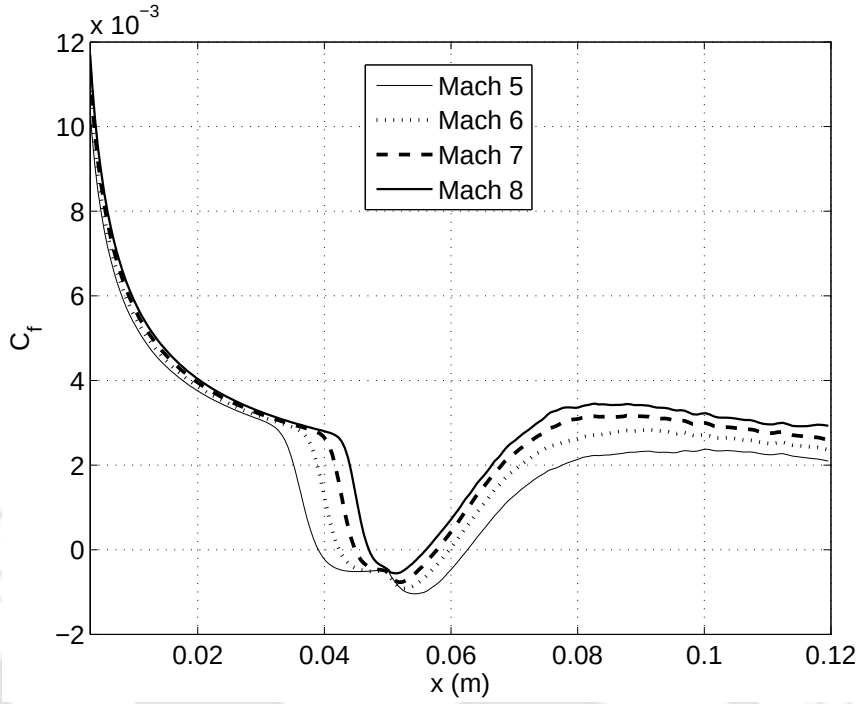

FIGURE 5.19: Effect of freestream Mach number on C_f distribution

ramp angle under consideration (15^0) is sufficiently above the incipient separation angle for the lowest Mach number considered for present studies. This is easily identified from the plateau in the pressure plot (figure 5.18) as well as the skin friction distribution (figure 5.19). Effect of freestream Mach number variation on the interaction is given in table 5.3. The points of separation and reattachment show that the longest separation bubble occurs at Mach number 5 while at Mach number 8 the flow cannot be considered as "well-separated". This observation is along expected lines because a higher freestream Mach number in the present case means higher kinetic energy of the flow for same internal energy which in turn leads to a smaller separation bubble.

5.4.5 Effect of ramp angle variation (Case C)

An additional investigation of Case C has been performed to confirm the ramp angle effect that has been observed with Case B. In addition to two ramp angles (15^0 and 25^0) considered for the experimental studies, an intermediate ramp angle of 20^0 is also considered in the present numerical studies. The ramp length has been taken according to ramp angle. That is for 15^0 and 25^0 ramp angle, similar to experimental cases, the total length of the model is 235 mm

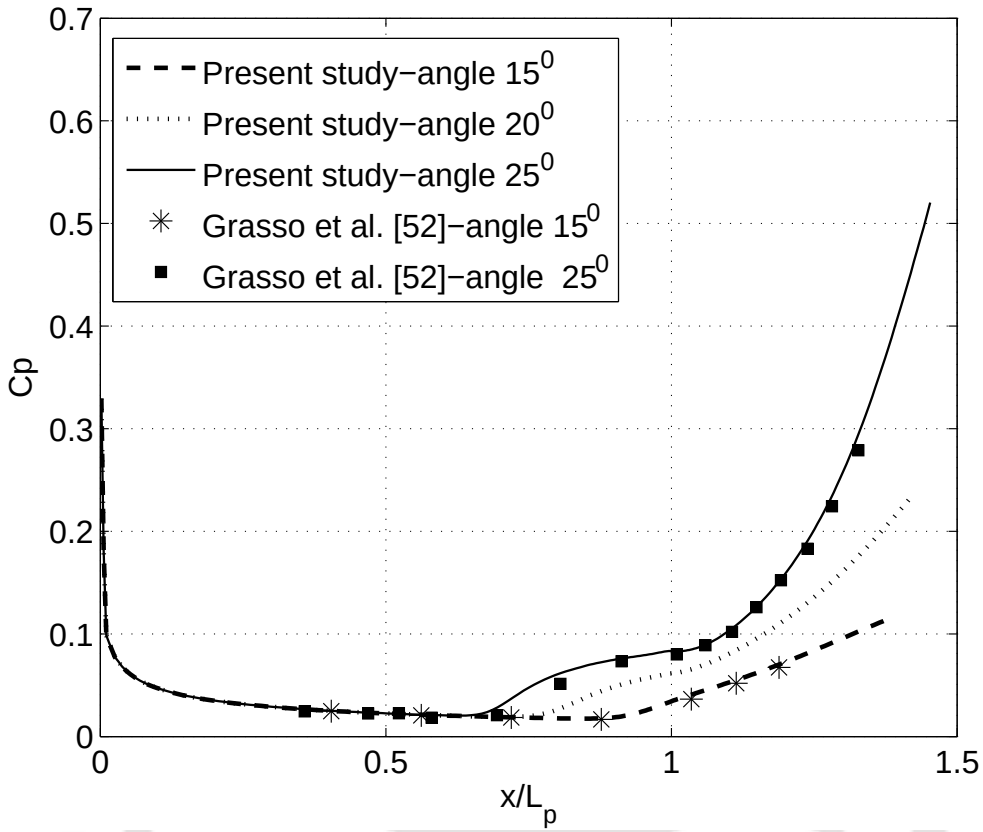

FIGURE 5.20: Surface pressure (Cp) distribution (Case C)

and 269 mm respectively. An intermediate length of 250 mm is taken for 20^0 ramp angle case. Quadrilateral grids of sizes 220×70, 225×70, and 230×70 are used for the simulation of ramp angle 15^0, 20^0 and 25^0 respectively.

The simulation results plotted in terms of surface pressure, skin friction coefficient and Stanton number distributions are shown in figure 5.20, 5.21 and 5.22 respectively. The wall pressure distributions obtained with present simulations are closely matching with experimental results. However the Stanton number distributions (figure 5.22) show slight under prediction in the reattachment region. Apart from this the results obtained with present case also show a very similar trend of increasing separation zone with increase in ramp angle. Among the three ramp angles considered in this study, two higher angles forced the flow to separate near the ramp junction. This separated nature of flow can be recognized from the corresponding plateau in the pressure distribution and negative values in the skin friction distributions.

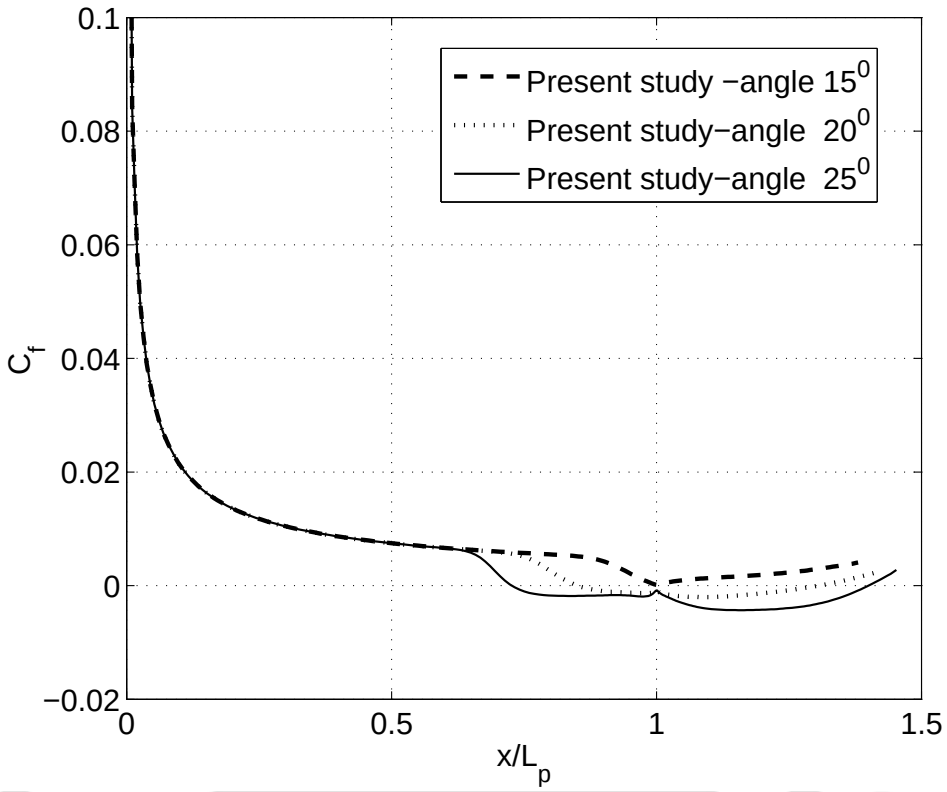

FIGURE 5.21: Skin friction coefficient distribution (Case C)

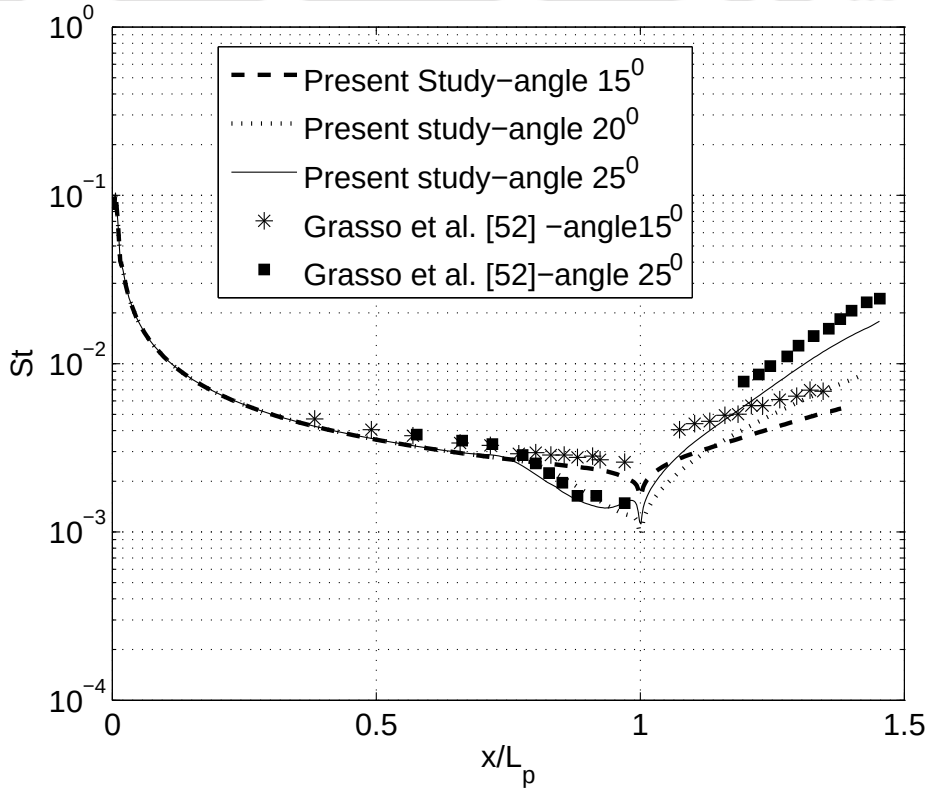

FIGURE 5.22: Stanton number distribution (Case C)

5.4.6 Effect of Leading edge bluntness

Hypersonic vehicles have blunt nosed configuration to reduce the surface heating rate. From a practical viewpoint, it is imperative to understand how leading edge bluntness may affect the SWBLI. Moreover, the entropy layer formation associated with detached bow shock in the presence of blunt leading edge has significant effect on shock boundary layer interaction. Hence exploration of the same is the objective of present study. Experimental studies were performed by Coet et al. [16] to investigate this effect through the pressure and heat flux measurements for Mach 10 flow over 15^0 ramps attached with flat plate having three leading edge curvatures viz. sharp, R_n=2.5 mm and R_n=5 mm. In the present study, computations are carried out to reveal the effect of leading edge bluntness for the same configurations that were experimentally investigated by Coet et al. The computational domain for the cases of leading edge radius zero, 2.5 mm and 5mm are meshed with quadrilaterals and have sizes 510×90, 480×90 and 470×90 respectively. The numerical investigations showed that the leading edge shock is a detached bow shock in case of blunted leading edge, where as it is an attached oblique shock in case of sharp leading edge. It should also be noticed here that, for the same freestream Mach number, the ramp-approach Mach number reduces in the presence of bow shock. Studies in section 5.4.4 have shown that SWBLI would be prominent at lower Mach numbers. However, the presence of the bow shock for a blunted leading-edge ramp creates an entropy gradient normal to the flow behind the shock. This entropy gradient generates a strong vortical activity just outside of the boundary layer and provides a stabilizing effect which counters the destabilizing effect of reduced Mach number. This explains the reduction in the intensity of SWBLI with increased leading edge bluntness. The skin friction distribution shown in figure 5.23 illustrates a reduction in separation bubble with increase in bluntness and supports this conclusion (table 5.3). investigation is necessary to conclusively establish the nature of reattachment.

The surface pressure distributions predicted from computations are shown in figure 5.24 which agree well with experimental results. Interestingly, it can be noticed that the peak pressure downstream of the reattachment point, in the case of the blunt leading edge ramp, is nearly half of its value as compared to a sharp leading edge ramp. This may be attributed to the stronger separation shock in the latter case. Numerical predictions of the Stanton number (figure 5.25)

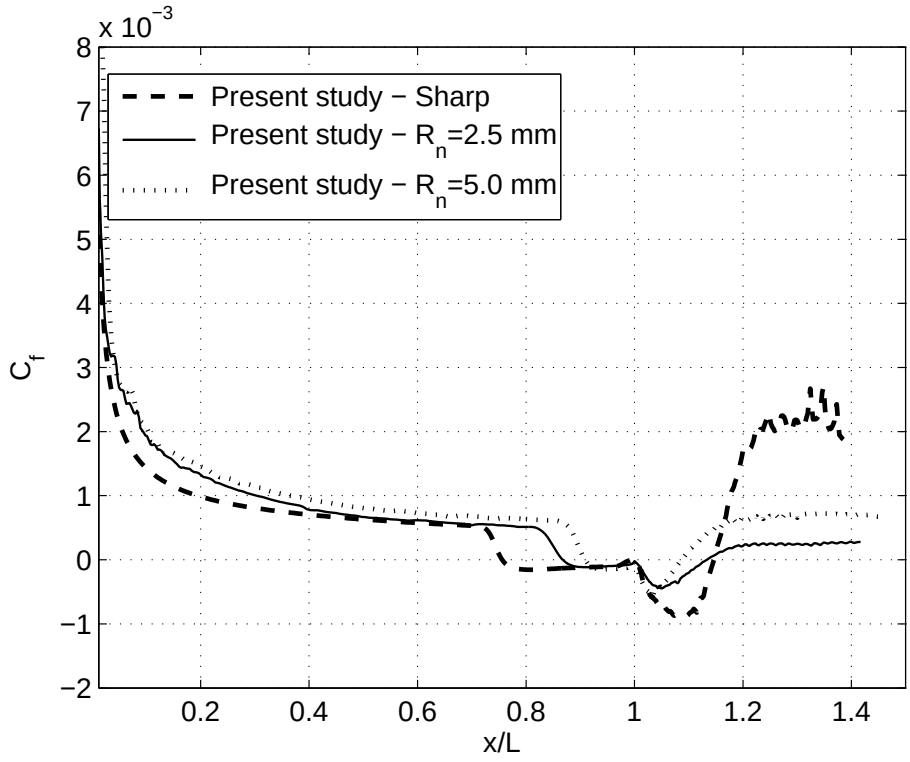

FIGURE 5.23: Effect of leading edge bluntness on C_f

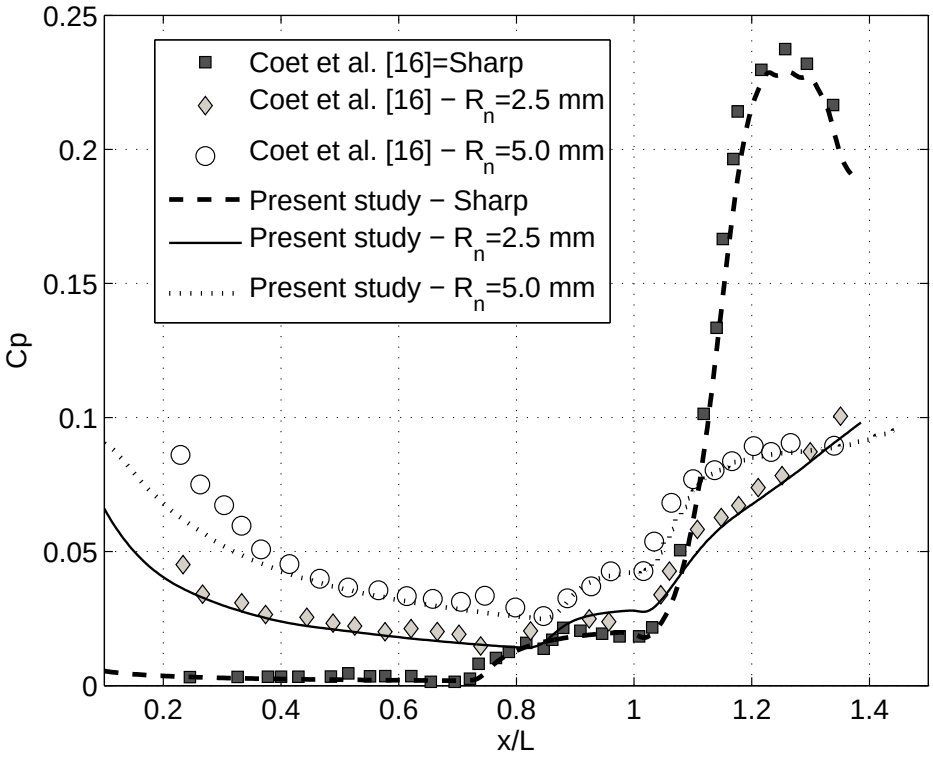

FIGURE 5.24: Effect of leading edge bluntness on Cp

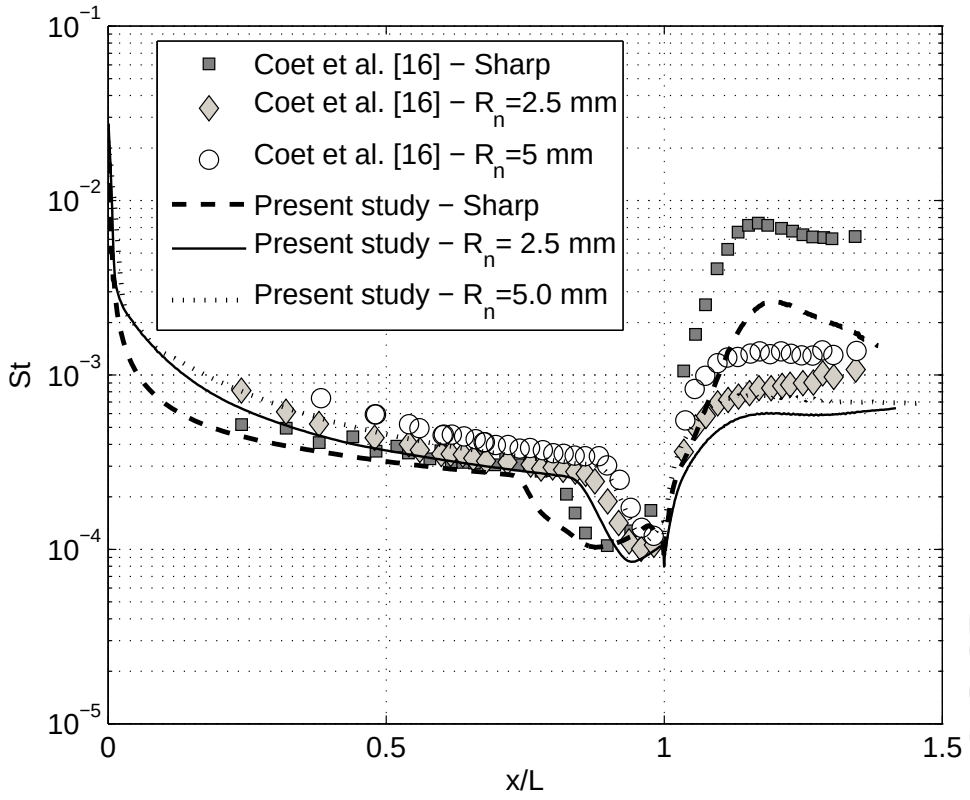

FIGURE 5.25: Effect of leading edge bluntness on St

are similar to the skin friction coefficient and show excellent agreement with the results of Coet et al. for all cases except in the post-reattachment regions. The computations consistently under predict the heat transfer rate downstream of the reattachment point and this discrepancy between the numerical and experimental results is more prominent for the sharp leading edge ramp as compared to the blunted leading edge ramps. This points to the fact that the assumption of laminar flow considered in the computations is not valid in the post-reattachment regions and is consistent with the experimental observations of Coet et al. who have hinted at the possibility of a turbulent reattachment. Furthermore, the heat transfer rates from experimental measurements are higher than those from numerical predictions, which also add credence to the theory of possible turbulent reattachment in the case of sharp leading edge ramp. The reattachment in the case of blunted leading edge ramps could also be turbulent or even transitional and a closer investigation is necessary to conclusively establish the nature of reattachment.

Parameter	M_∞	$Re_\infty(m^{-1})$	$T_0(K)$	$T_w(K)$	$\theta(^0)$	$R_n(mm)$	$L_b(mm)$	Inference
Ramp angle	6	8×10^5	1080	300	10	0.0	0.0	
	6	8×10^5	1080	300	12.5	0.0	9.2	$\theta \uparrow L_b \uparrow$
	6	8×10^5	1080	300	15	0.0	17.75	
Wall	6	8×10^5	1080	300	15	0.0	17.75	
temperature	6	8×10^5	1080	500	15	0.0	27.0	$T_w \uparrow L_b \uparrow$
	6	8×10^5	1080	adiabatic	15	0.0	46.25	
Freestream	6	8×10^5	1800	300	15	0.0	13.2	
enthalpy	6	8×10^5	1080	300	15	0.0	17.75	$\frac{T_w}{T_0} \uparrow L_b \uparrow$
	6	8×10^5	1800	500	15	0.0	18.2	
	6	8×10^5	1080	500	15	0.0	27.0	
Mach	5	8×10^5	790.2	300	15	0.0	23.0	
number	6	8×10^5	1080	300	15	0.0	17.75	$M_\infty \uparrow L_b \downarrow$
	7	8×10^5	1422.4	300	15	0.0	13.25	
	8	8×10^5	1817.5	300	15	0.0	17.75	
Leading	10	8.36×10^6	1100	300	15	0.0	97.2	$R_n \uparrow L_b \downarrow$
edge radius	10	8.36×10^6	1100	300	15	2.5	55.5	
	10	8.36×10^6	1100	300	15	5.0	38.3	

TABLE 5.3: Summary of parametric studies of SWBLI

5.5 Summary

The effect of various flow and geometric parameters on the R-SWBLI in laminar hypersonic flows have been investigated using a high-resolution viscous flow solver. It has been shown that pressure measurements only provide a qualitative picture of flow separation and reattachment. Therefore wall shear stress distribution is necessary to provide quantitative estimates of separation bubble length and upstream influence. The use of correlations to predict the separation is also critically analysed. Thus the numerical studies demonstrate that the correlation may be effectively employed only for "well-separated" flows. The extent of separation is shown to decrease with increased freestream stagnation enthalpy and Mach number while it increases with increase in wall temperature and ramp angle. It is observed that the wall-to-total temperature ratio is the correct indicator to compare the effect of SWBLI for variable wall temperature and stagnation enthalpies. The effect of leading edge bluntness on SWBLI has also been numerically studied. Computational results for the limited range of radii indicate that bluntness reduces the extent of separation but may lead to transitional or turbulent reattachment. However detailed study about the effect of leading edge radius is discussed in later chapters.

Chapter 6

Assessment of correlations of shock wave boundary layer interactions

Overview

Shock wave boundary layer interaction is most attended research theme in the high speed flow regime for effective design of various parts of space vehicles. Hence, investigations in this field are invariantly carried out to estimate the extent of upstream influence, length of separation bubble, separation point pressure, plateau pressure and peak heatflux or Stanton number. Literature reported correlations, for prediction of these features of the interaction, are explored herewith using the in-house solver. However, results of present simulations for various freestream and wall conditions portrayed their inabilities to incorporate the variations of influencing parameters while retaining the linearity. In view of this, efforts are extended either to modify these widely appreciated correlations or to suggest a better among the reported ones to improve the estimates. The modifications suggested for prediction of extent of upstream influence, separation bubble size and peak Stanton number are seen to improve the applicability of the existing correlations.

6.1 Background

The topic of SWBLI has gained inevitable significance in the area of high speed aerodynamics. Hence it is essential to predict the features of this interaction during the design phase of

components or subcomponents. Simplest way of estimation is to device a correlation for the corresponding feature in terms of governing parameters like freestream and configuration details. Few researchers have established such correlations for prediction of separation bubble size, extent of upstream influence and peak heatflux. The basic advantage of such correlations lies in the ease of their applicability in understanding the fundamentals of ramp induced SWBLI, without costly experimental investigations or complex computational simulations. The correlations proposed by Needham and Stollery [3] and Katzer [41] are important in such aspects. Recently Davis and Sturtevant [58] have also proposed a new correlation for separation bubble size based on the classical triple-deck formulation of Stewartson and Williams [34]. However the choice of scales considered for developing these correlations has introduced limitations for their applicability which reduces their envelop size. Therefore present investigations focus on assessment for suitability of the literature reported and widely accepted correlations for quantitative prediction of SWBLI parameters. Efforts are also extended to modify these correlations to accommodate the available SWBLI data. Numerical data obtained from the studies presented in the previous chapter are employed in this analysis.

6.2 Review of supplementary correlations

Prior to the detailed assessment of various scaling laws for R-SWBLI parameters, it is very much important to have a brief discussion of empirical correlations applicable for the undisturbed compressible laminar boundary layer over the flat plate ahead of the interaction region. The importance of this discussion lies in the fact that, most of the correlations proposed for the extent of upstream influence or separation bubble size have considered the undisturbed upstream boundary layer thickness or its representatives as scaling parameters.

In case of hypersonic flowfield the leading edge shock and aligned strong viscous interaction cannot be neglected. Hence the effect of strong viscous interaction due to the formation of leading edge shock can be accounted by considering the hypersonic approximated equation for pressure rise [1] given by,

$$\frac{p_e}{p_\infty} = 1 + A\bar{\chi} \tag{6.1}$$

where $\bar{\chi}$ is the viscous interaction parameter given by $\bar{\chi} = \frac{M_\infty^3\sqrt{C}}{\sqrt{Re_x}}$, C is the Chapman-Rubesin parameter. The value of A depends on nature of interaction ($A \approx 0.5$ for Strong interaction, whereas $A \approx 0.078$ for weak interaction). In the present case for laminar flow over flat plate, the Blasius boundary layer solution, corrected for compressibility effect along with Eckert's reference temperature method [55], can be applied to find the skin friction and Stanton number distribution ahead of the interaction zone. Those correlations are given by,

$$C_f = \frac{0.664\sqrt{C^*}}{\sqrt{Re_x}}, \qquad St = \frac{1}{2}{P_r}^{-2/3}C_f \tag{6.2}$$

where C^* is the Chapman-Rubesin constant calculated based on reference temperature given by,

$$\frac{T^*}{T_e} = 1 + 0.032M_e^2 + 0.58\left(\frac{T_w}{T_e} - 1\right) \tag{6.3}$$

In addition to these parameters, the calculation of other boundary layer parameters like boundary layer thickness, momentum and displacement thicknesses etc., have been carried out using Eckert's reference temperature method as mentioned [52].

6.3 Analysis of extent of upstream influence

Extent of upstream influence is generally considered as the distance measured from the ramp foot to a location of flat plate where the usual pressure distribution of undisturbed flat plate start rising in the presence of downstream located ramp. During the numerical studies in last chapter, it has been noted that, the extent of upstream influence increases with increase in wall temperature and decreases with increase in freestream Mach number and freestream stagnation enthalpy or total temperature. These numerical investigations have also proved that, upstream influence is always present for any R-SWBLI case, irrespective of magnitude of ramp angle. Moreover, strength of interaction is found to increase with increase in ramp angle. The results of the simulations discussed in last chapter, for various cases, are analyzed using wall pressure distribution to evaluate the extent of upstream influence in that particular case. Thus obtained upstream influence distances are used to assess the various literature reported correlations.

The scaling law proposed by Needham and Stollery [3] correlates the upstream influence with the associated parameters as,

$$\frac{L_{ui}}{\delta_0} = F_{ui}\frac{M_\infty \theta^2}{\bar{\chi_0}} \tag{6.4}$$

Boundary layer thickness (δ_0) at the upstream influence location (x_0) is considered here as the length scale for non-dimensionalisation. For the present study, such boundary layer thickness has been calculated from the Blasius solution given by Mallinson et al.[18]. The parameter $\bar{\chi_0}$ in equation (6.4) is the viscous interaction parameter at that location x_0, which can be calculated based on reference temperature. The required function F_{ui} in equation (6.4) can be found out by fitting the above correlation for different experimental or numerical results.

Another important correlation for upstream influence, available in literature, is the one proposed by Grasso and Marini [53], through the findings of Hayakawa and Squire [13]. Here, the upstream influence is expressed as,

$$\frac{L_{ui}}{L}M_\infty^{1/2} = \frac{\delta_0}{L}\frac{2}{\gamma}\frac{1}{M_\infty^{3/2}}C_{f_0}\left(\frac{p_3}{p_1} - 1\right) \tag{6.5}$$

Plate length, L, is used here for non-dimensionalisation instead of the boundary layer thickness. The term $\left(\frac{p_3}{p_1} - 1\right)$ has been included to incorporate the effect of ramp angle. Introduction of this term was based on the Hayakawa and Squire's observation of dependency of upstream influence on pressure rise $(p_3 - p_1)$ at the compression corner [13]. The influence of Reynolds number, wall temperature and freestream temperature is introduced into the correlation in terms of skin friction coefficient (C_{f_0}) at a location (x_0) where upstream influence starts. Specific heat ratio (γ) is also considered in this correlation.

Outcome of the simulations discussed in last chapter are used to evaluate these two scaling laws as shown in figure 6.1 and figure 6.2 respectively. The present data points fitted according to Needham and Stollery's correlation [3] (equation (6.4)) and the correlation given by Grasso and Marini [53] (equation (6.5)) show that, these correlations relate the upstream influence linearly with ramp angle for constant freestream and wall parameters. According to these correlations, variation of wall to total temperature ratio is seen to shift the curves vertically. Both the

facts support the earlier observation of increase in extent of upstream influence with increase in wall temperature and ramp angle for given freestream conditions. Though both the prediction techniques support the inverse proportionality of upstream influence with the freestream Mach number, the strategy given by Needham Stollery [3] correlates it linearly with positive slope (figure 6.1) while the other technique [53] does the same with negative slope (figure 6.2). This disparity in slopes of the corresponding lines is due to the fitting functions given by equation (6.4) and equation (6.5). Lines corresponding to Mach number variation are also seen to shift vertically upwards with increase in wall to freestream temperature ratio in both the figures. Another important point noted about these correlations is that, the points corresponding to different wall to total temperature ratios obtained for a particular freestream stagnation enthalpy condition follow one path in vertical shift, whereas, the points for different wall to total temperature ratios, for another freestream stagnation enthalpy condition, follow different path in upward shifting. Figure 6.1 portrays prominence of this effect while it is minimal in figure 6.2. Hence the correlations given by equation (6.4) and equation (6.5) are found suitable for predicting upstream influence in case of ramp angle variation for a particular wall and freestream parameters. Therefore need of a parameter which mainly accounts for the wall to total temperature ratio is felt to modify these correlations to extend their applicability. In view of the above discussed limitation, efforts are made to modify the correlation given by Needham and Stollery [3] to improve the prediction strategy. Initial attempts are made to express the effect of ramp angle implicitly in terms of pressure rise across the oblique shock for hypersonic or high Mach number assumption [1], $M_\infty^2 \gg 1$. Hence the pressure ratio given by oblique shock theory is considered for the same,

$$\frac{p_3}{p_1} = \frac{2\gamma}{\gamma+1} M_0^2 sin^2\beta \tag{6.6}$$

Here $\frac{p_3}{p_1}$ stands for the inviscid pressure jump across the attached oblique shock. Since, $\theta \propto \beta$, we can replace the term β in above expression with θ to achieve the following proportionality, $\frac{p_3}{p_1} \propto M_0^2\theta^2$. This leads to the modified Needham and Stollery correlation as,

$$\frac{L_{ui}}{\delta_0} = F_{ui} \frac{\sqrt{Re_{x_0}}}{M_0^3\sqrt{C^*}} \frac{p_3}{p_1} \tag{6.7}$$

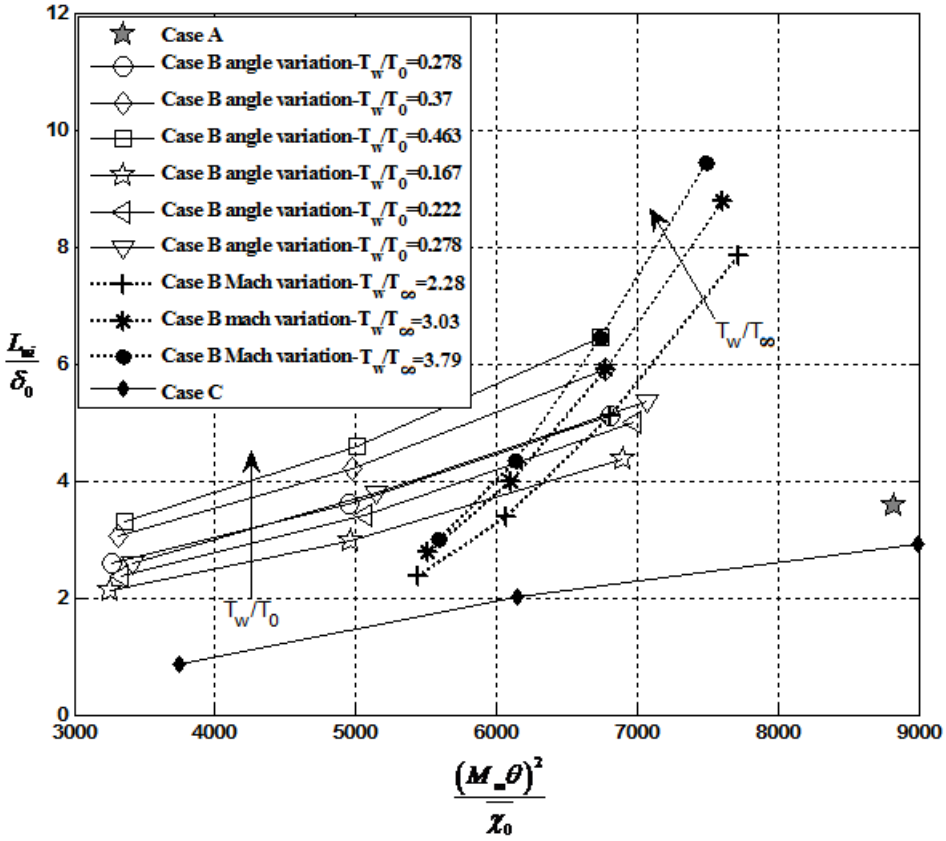

FIGURE 6.1: Data points fitted according to Needham and Stollery's correlation

The above equation can be re-written as follows to meet zero upstream influence in the absence of ramp,

$$\frac{L_{ui}}{\delta_0} = F_{ui}\frac{\sqrt{Re_{x_0}}}{M_0^3\sqrt{C^*}}\left(\frac{p_3}{p_1}-1\right) \tag{6.8}$$

Further modifications in the above expression are considered to incorporate the effect of wall temperature and freestream total temperature. Therefore a new term, β^*, has been introduced for the same. Hence the final version of modified Needham and Stollery correlation for upstream influence is as,

$$\frac{L_{ui}}{\delta_0} = F_{ui}\frac{\sqrt{Re_{x_0}}}{M_0^3\sqrt{C^*}}\left(\frac{p_3}{p_1}-1\right)\beta^* \tag{6.9}$$

where,

$$\beta^* = \left(\frac{T_w}{T_0}\right)^m\left(\frac{T_\infty}{T_0}\right)^n$$

The present data points are again considered using this final correlation for $m = 0.5$ and $n = 0.5$. Excellent prediction with linear fit, for all the data points with variations such as ramp angle, freestream total enthalpy, wall temperature etc., is seen in the figure 6.3. A proportionality

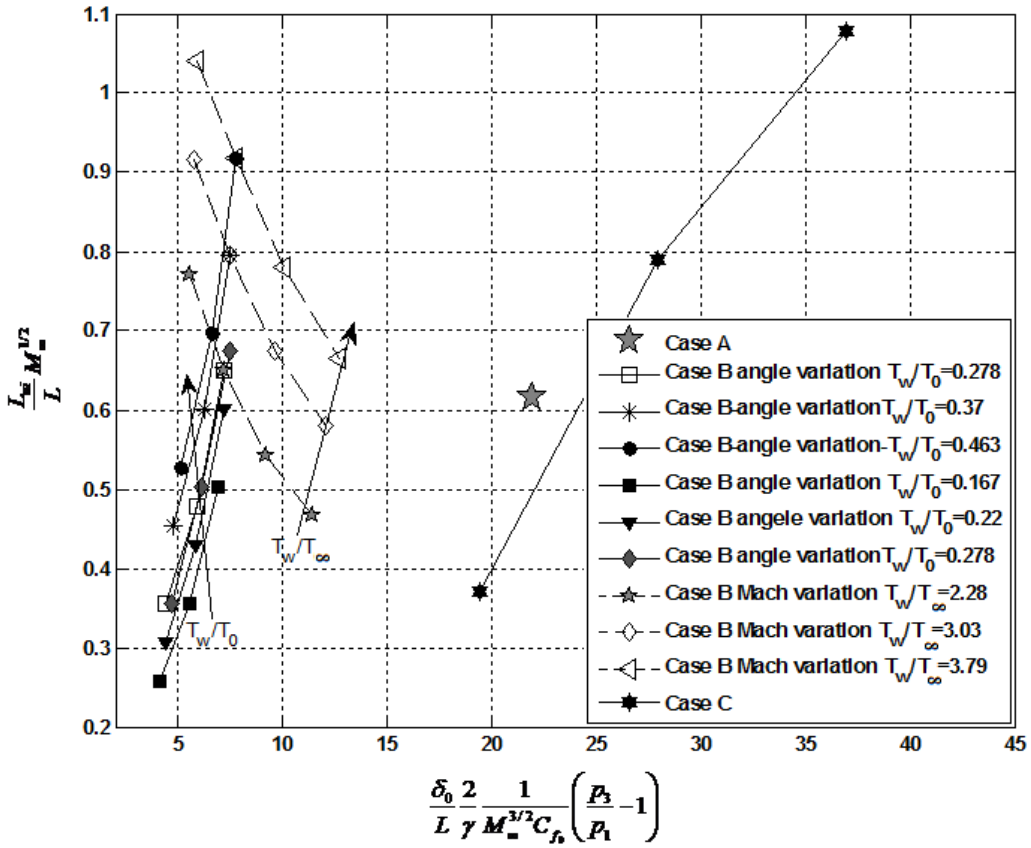

FIGURE 6.2: Data points fitted according to Grasso and Marini's correlation

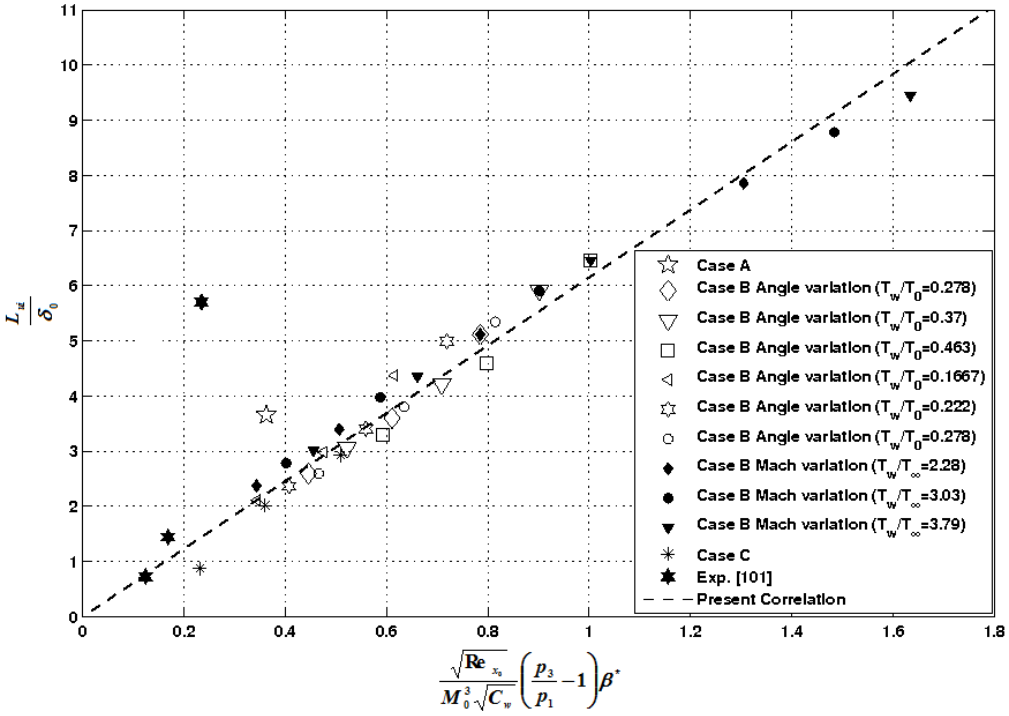

FIGURE 6.3: Data points fitted according to present modified correlation for extent of upstream influence

constant (F_{ui}) of 6.15 has been obtained for the present data set. The experimental result of Holden and Moselle [100], which was not considered earlier (figures 6.1 and 6.2), is also plotted in this figure to further evaluate the present correlation. Encouraging match can be experienced, in this figure, for this result as well. Hence the equation (6.9) can be treated as the generalized correlation for prediction of upstream influence.

6.4 Analysis of separation bubble size

Separation bubble size is an important terminology of R-SWBLI. However a specific combination of freestream and wall conditions which offer a considerable amount of upstream influence, does not always guarantee separation bubble. Hence the ramp angle should be more than the incipient separation angle (θ_{is}) given in equation (5.1). Present studies have reasserted the literature reporting that separation bubble length increases with increase in wall temperature and decreases with increase in freestream Mach number and freestream stagnation enthalpy or total temperature. Various correlations, widely admired for prediction of separation bubble size, are considered here with for their assessment.

There are four major correlations to predict the separation bubble size. The first one is proposed by Needham [20] through the experimental studies for hypersonic flows ($7 < M_\infty < 14$) over compression ramp. The expression for the same is,

$$\frac{L_b}{x_0} \propto \frac{\sqrt{Re_{x_0}}}{M_0^3} \left(\frac{p_3}{p_2}\right)^2 \tag{6.10}$$

For the present study p_2 in equation (6.10) is assumed to be equal to incipient pressure p_{incp} [58]. From this expression it is clear that, effect of wall temperature and freestream enthalpy on separation bubble length is not incorporated in it. Further, Needham along with Stollery [3] suggested that the correlation for extent of upstream influence (equation (6.4)) can also be used to correlate the separation bubble size.

Another important scaling law for separation bubble size is proposed by Katzer [41]. This correlation is as,

$$\frac{L_b}{\delta_0^*} \propto \frac{\sqrt{Re_{x_0}}}{M_0^3\sqrt{C}} \left(\frac{p_3 - p_{incp}}{p_1}\right) \tag{6.11}$$

Here, the required displacement thickness at location x_0 can be obtained through the correlation proposed by Bertram and Blackstock [101]. The above equation has also been expressed by the authors as,

$$\frac{L_b}{\delta_0^*} \frac{M_0^3\sqrt{C}}{\sqrt{Re_{x_0}}} \propto \left(\frac{p_3 - p_{incp}}{p_1}\right) \tag{6.12}$$

These (equations (6.11) and (6.12)) correlations have been originally developed for I-SWBLI in supersonic flow regime. Hence the applicability of the same correlation for R-SWBLI, needs thorough analysis.

Expression for the separation bubble size (equation (6.13)) has also been recently devised by Davis and Sturtevant [58] for which limited supporting investigations are available.

$$\frac{L_b}{x_0} \propto \frac{\Lambda_0}{\gamma^{3/2} M_0^3} \left(\frac{p_3 - p_{incp}}{p_1}\right)^{3/2} \tag{6.13}$$

In this correlation, dependency of Mach number is expressed in the same way as that in the previous correlations. Besides, the formulation of pressure term is seen to be altered. The new parameter, Λ_0 which appears in this correlation, stands for the effect of skin friction and wall to edge temperature ratio. This parameter is given by,

$$\Lambda = \frac{\mu_w}{\mu^*} \frac{T^*}{T_e} \left(\frac{T_w}{T_e}\right)^{1/2}$$

Here, the terms with $'*'$ are to be evaluated at reference temperature (equation (6.3)). This correlation has been proposed for high enthalpy hypersonic flows, hence its applicability for ideal gas flows needs to be evaluated. Apart from this, caution has also been reported by the authors that the correlation would have least quantitative prediction capacity.

Wall shear distribution obtained from the current numerical studies reported in Chapter-5 is used to measure the size of separation bubble. Hence, cases which fall in the "separated flow" region of figure 5.2 would only be useful. These cases include Case A, combination of Mach 5, 6, and 7 with ramp angle of 15^0 of Case B and ramp angle 20^0 and 25^0 of Case C (refer table 5.1). In addition to these, ramp angle 15^0 and Mach 6 combination of Case B has also been considered to reveal the effect of wall to total temperature ratio. For this study, simulations are repeated with all three wall temperatures and two enthalpy conditions of Case B, so as to get extra data points. Thus obtained separation bubble sizes for various freestream and wall conditions have been considered to assess the literature reported correlations.

In the present study, the incipient pressure rise (p_{incp}/p_1) has been calculated by making use of triple deck solution proposed by Inger [45]. Thus obtained data points fitted according to equations (6.10) and (6.4) are shown in figures 6.4 and 6.5 respectively. The points corresponding to ramp angle and Mach variations are seen to follow linear trend in both the cases with different slopes. These expressions are also seen to exhibit upward shifting of trend lines with increasing wall to freestream temperature ratio. Moreover, the upward shift which is consistent in figure 6.4 for variation of freestream stagnation enthalpy is unseen in figure 6.5. Hence these correlations are found suitable in predicting separation bubble size for the cases with variation in Mach number or ramp angle only.

Similar experience can be gained by fitting the data points using Katzer's correlation (equation (6.11)) as shown in figure 6.6. From the figure, the current form of the equation, proposed for prediction of separation bubble length in case of shock impingement separation, is examined to be unsuitable to use for ramp induced separation. However, the other form given by equation (6.12) is observed to offer improved trend, as shown in figure 6.7. Marginal deviation noticed for Mach number variation cases is the only limitation of this correlation. Hence, from the narrow envelop of the present data sets, the equation (6.12) is experienced to be a better prediction method for length of separation bubble in case of R-SWBLI case as well.

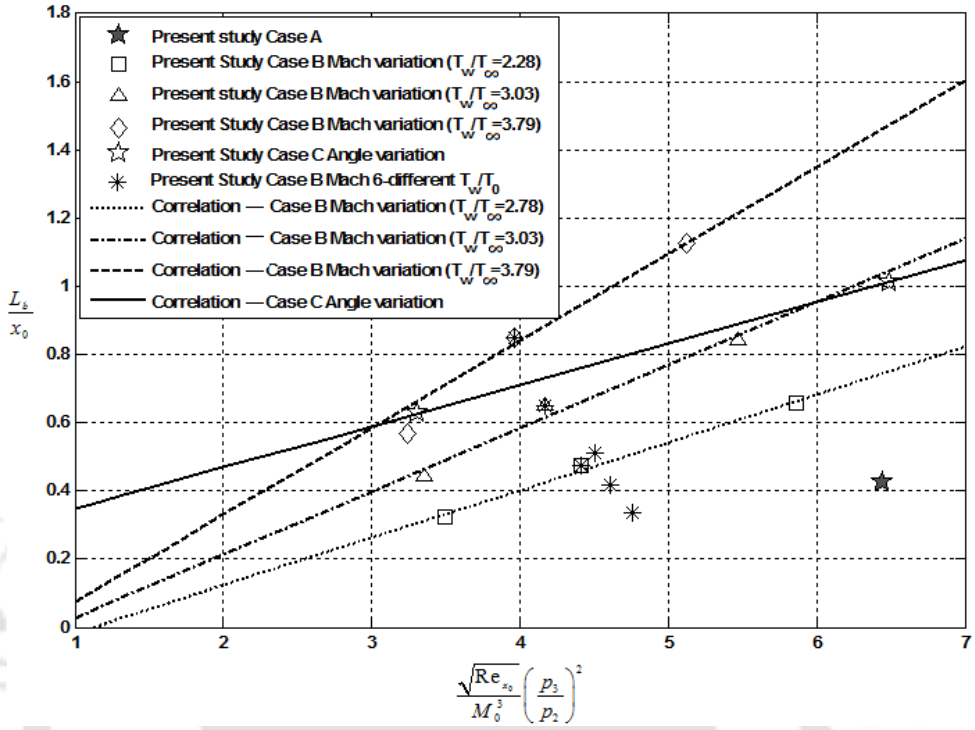

FIGURE 6.4: Present data points fitted according to Needham's correlation (equation (6.10))

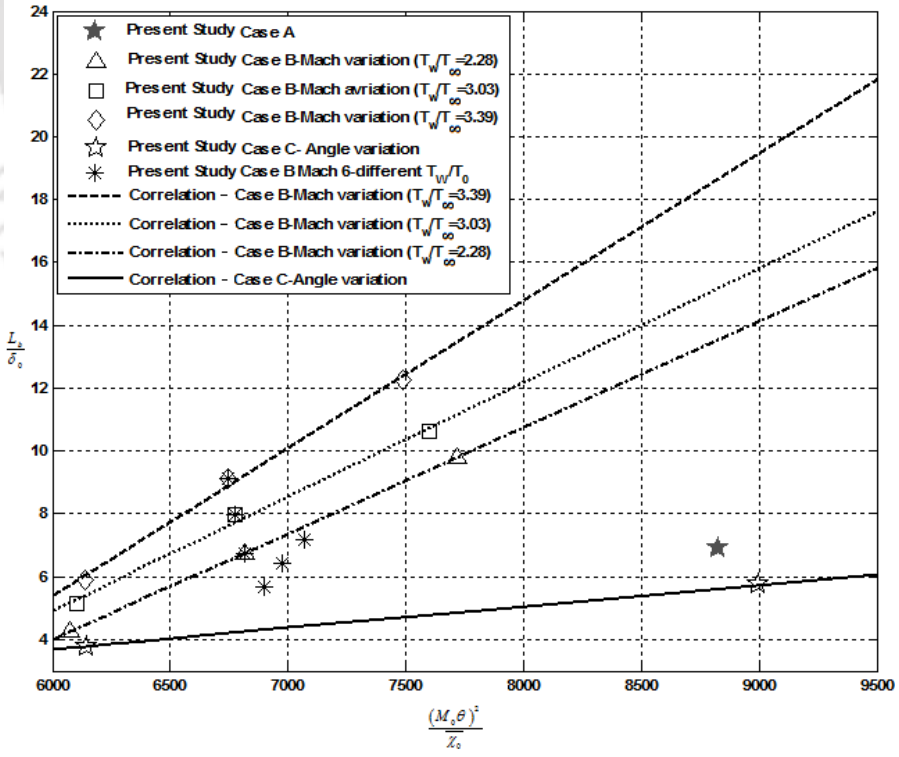

FIGURE 6.5: Present data points fitted according to Needham and Stollery's correlation (equation (6.4)).

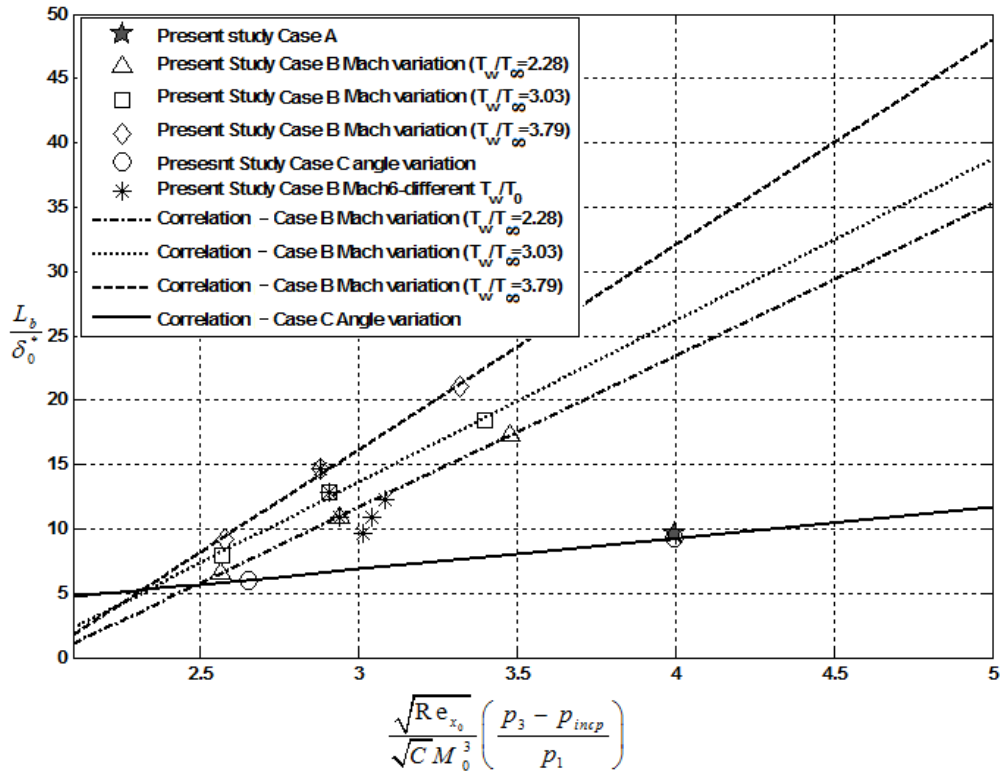

FIGURE 6.6: Present data points fitted according to Katzer's correlation (equation (6.11)).

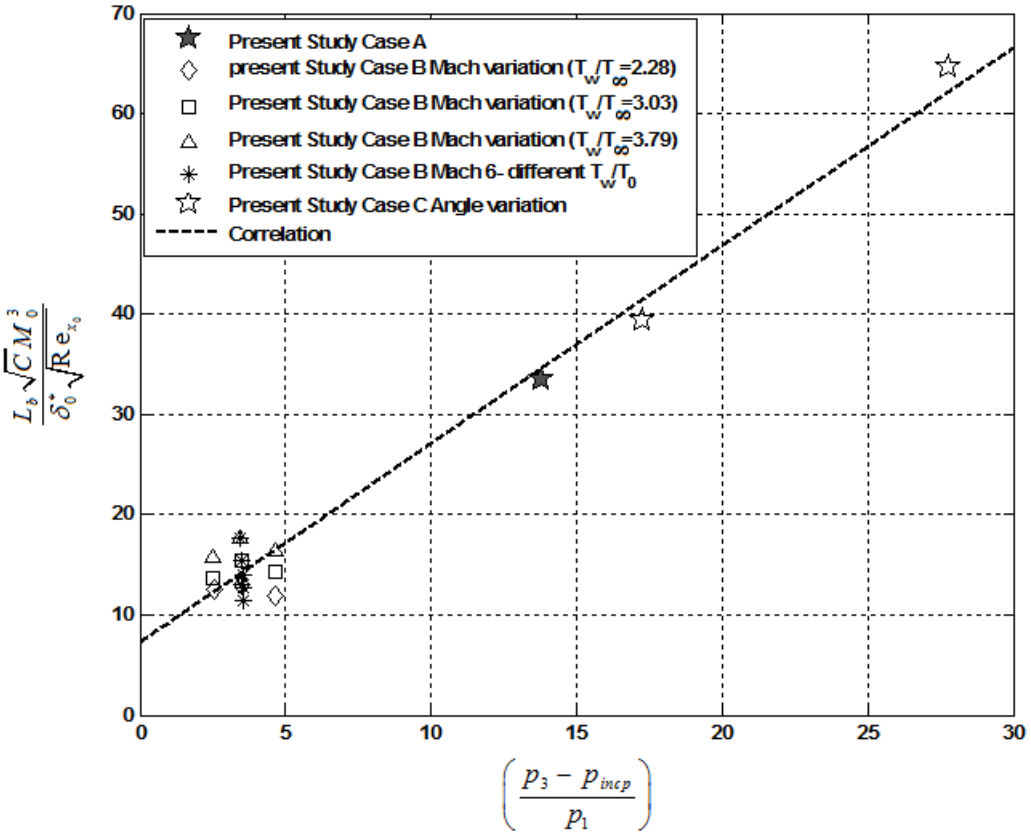

FIGURE 6.7: Present data points fitted according to Katzer's correlation (equation (6.12)).

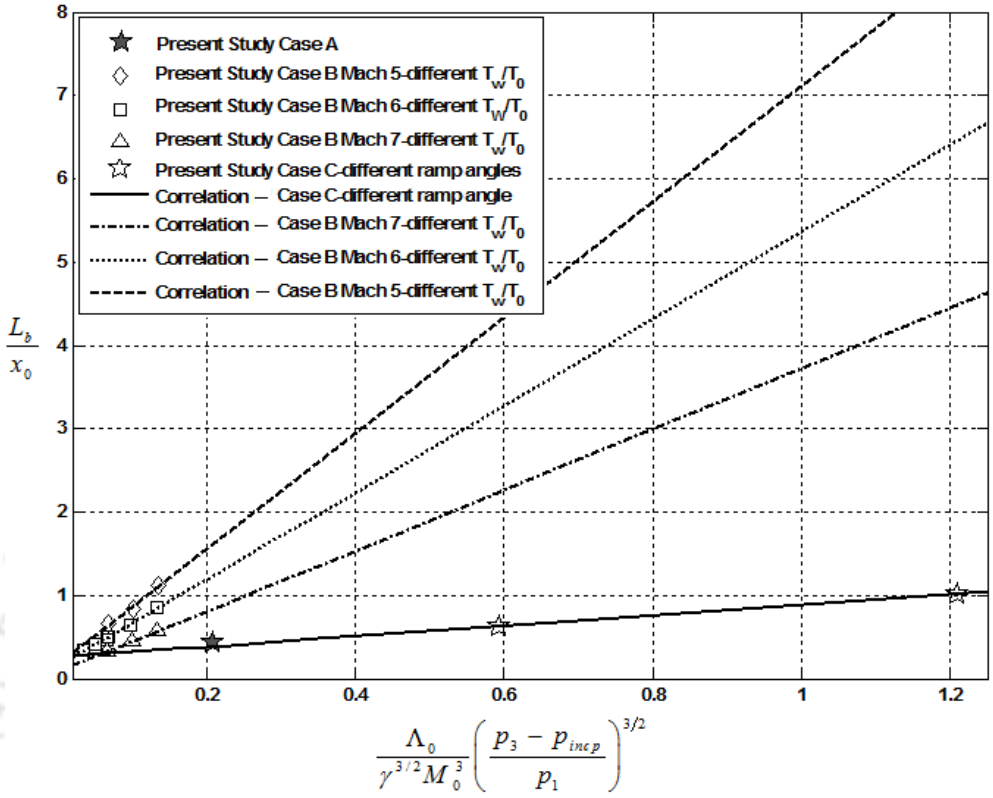

FIGURE 6.8: Present data points fitted according to Davis and Sturtevant's correlation(equation (6.13)).

The present data points are then fitted according to method proposed by Davis and Sturtevant (equation (6.13)). The trend lines fitted according to this correlation are shown in figure 6.8. The argued advantage of suitability of this correlation for different wall to total temperature ratio cases has been observed with present data points as well. Contrary to other three correlations of separation bubble size, this correlation offers linear trend for different wall to freestream total temperature ratios. This observation supports the excellent scaling of the wall temperature and freestream enthalpy, in this correlation, through the term Λ. The ramp angle variation is also experienced to follow linear trend in this strategy. However, it is evident from this figure that, the cases with Mach number variation deviate from linearity. As a part of this, the lines of different wall to temperature ratio are seen to shift upwards with decreasing Mach number.

The four reported correlations assessed herewith are lacking in offering uniqueness in the prediction of separation bubble size for various freestream and geometric conditions. The suitability of each of those correlations is restricted only to few parametric variation cases. Hence

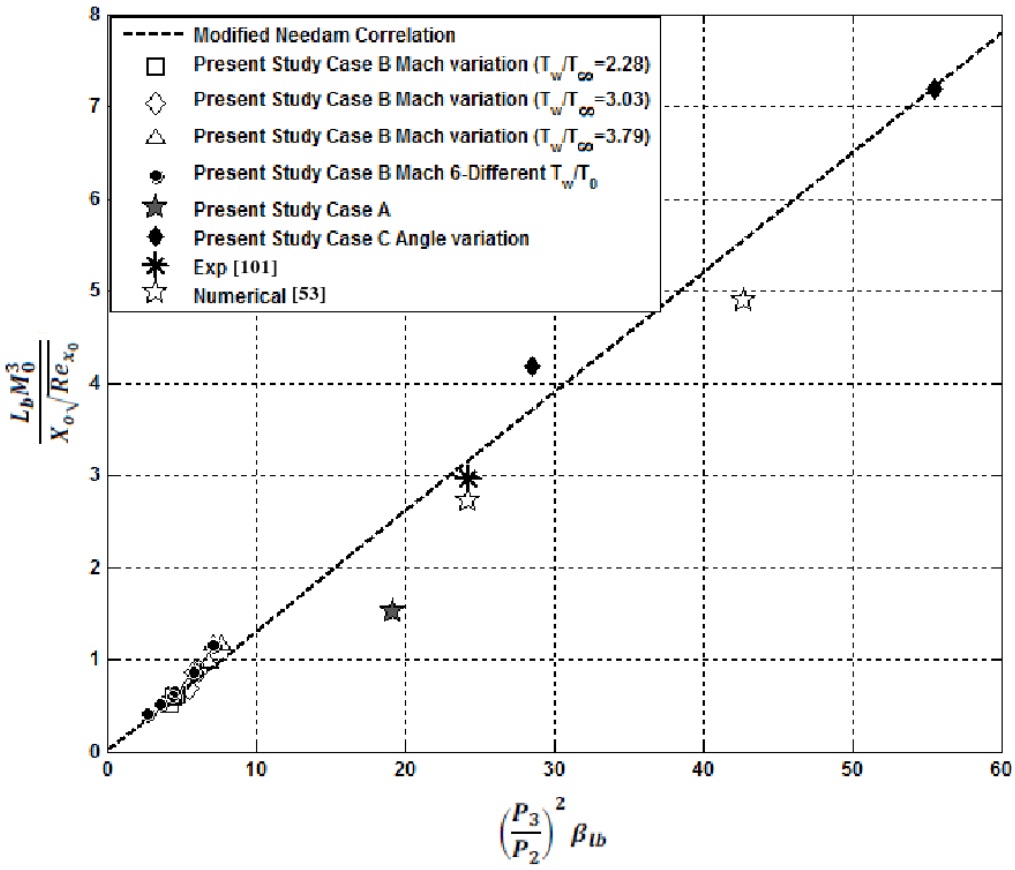

FIGURE 6.9: Present data points fitted according to modified Needham's correlation(equation (6.14)).

present efforts are extended to modify the Needham's correlation (equation 6.10) in order to fit the present data set into a narrow region. The main deficiency which was noticed with this correlation is its inaccuracy in scaling the wall and total temperature variation. Therefore an additional term has been introduced in equation 6.10 which leads to the modified Needham correlation as,

$$\frac{L_b}{x_0}\frac{M_0^3}{\sqrt{Re_{x_0}}} = F_{lb}\left(\frac{p_3}{p_2}\right)^2 \beta_{lb} \tag{6.14}$$

where F_{lb} is the proportionality constant and β_{lb} is the scaling parameter for wall to total temperature ratio and is given by,

$$\beta_{lb} = \left(\frac{T_w}{T_e}\right)\left(\frac{T_e}{T_0}\right)^{1/2}$$

The present data points fitted according the modified correlation are shown in figure 6.9. The rearrangement and introduction of an additional temperature scaling in the Needham's correlation is found to arrange the present data along a straight line. Additionally considered data

points corresponding to experimental studies of Holden and Mosselle [100] and numerical studies of Grasso and Marini [53] are also in agreement with the trend line obtained from modified Needham's correlation. The value of F_{lb} is observed as 0.13.

6.5 Studies for separation point pressure and plateau pressure

Studies are also carried out to assess the prediction capabilities of free interaction theory [4] based correlations for separation point pressure coefficient and plateau pressure coefficient using present data points. According to this theory, pressure coefficients at separation point (Cp_{sep}) and plateau region (Cp_{plat}) can be expressed as a function of flow conditions immediately upstream of the interaction location (x_0). The correlation for separation point and plateau pressure coefficient can be expressed as,

$$Cp_{sep/plat} = F_{sep/plat}\sqrt{2C_{f_0}/\left(M_0^2-1\right)^{1/2}} \tag{6.15}$$

The present data points fitted according to this correlation are shown in figure 6.10. In this figure, open bubbles and dashed lines refer to separation point pressure coefficient, while solid line and dark bubbles refer to plateau pressure coefficient. This figure portrays that the trend lines corresponding to separation and plateau pressures have different slopes. For a given wall to freestream temperature ratio, Mach number variations are found to be following the linear trend. Moreover these data points are observed to be deviating from the trend line with variation in wall to total temperature ratio. Hence this observation points the necessity of modification in this correlation to properly scale the wall and total temperature effect and ramp angle influence. The value of proportionality constants obtained for present data set are as, F_{sep} = 1.04 and F_{plat} = 1.84.

6.6 Correlation for peak heatflux

Peak heatflux, in the post reattachment region, is another important SWBLI parameter. Design of appropriate thermal protection system remains a task in the presence of such higher surface

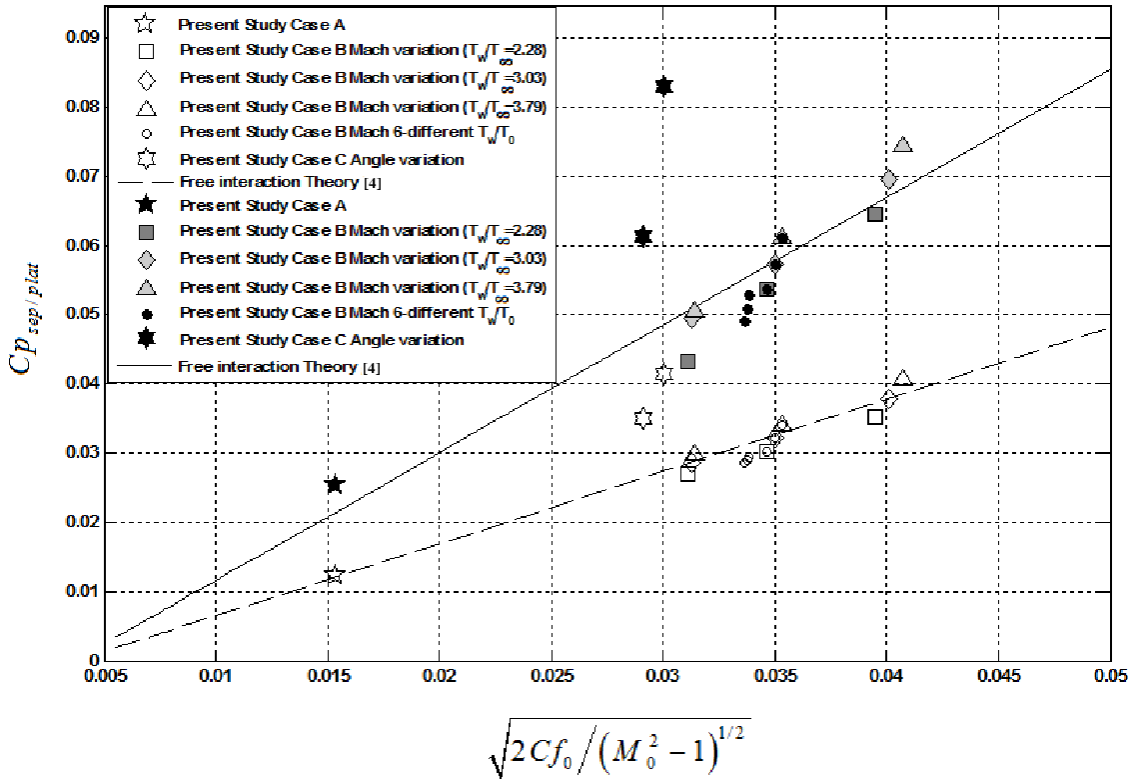

FIGURE 6.10: Data points fitted according to separation point and plateau pressure coefficient correlations.

heating rates due to SWBLI. Hence a simple relation is the prime requirement to correlate the peak heatflux with freestream or other SWBLI parameters. In the past, Hung and Barnett [56] proposed a correlation for the peak heating ($St_{peak}/St_0 \approx (P_3/P_0)^{1.13}$) for laminar case which has been later modified by Grasso and Marini [53] using extent of upstream influence as,

$$\frac{St_{peak}}{St_0} \propto \left(\frac{L_{ui}}{\delta_0}\frac{\gamma}{2}M_\infty^2 C_{f_0} + 1\right)^{1.13} \tag{6.16}$$

Here St_0 stands for reference undisturbed Stanton number at a station immediately before upstream influence start location. This parameter can be calculated using the methodology, mentioned by Grasso [52].

Efforts are initially extended to assess the applicability of this correlation for wide range of SWBLI conditions. Thus obtained trend lines are shown in figure 6.11. Clear evidence of limitation of this correlation in fitting different data points into a single trend line can be seen in this figure. As it has been observed in the case of extent of upstream influence, this

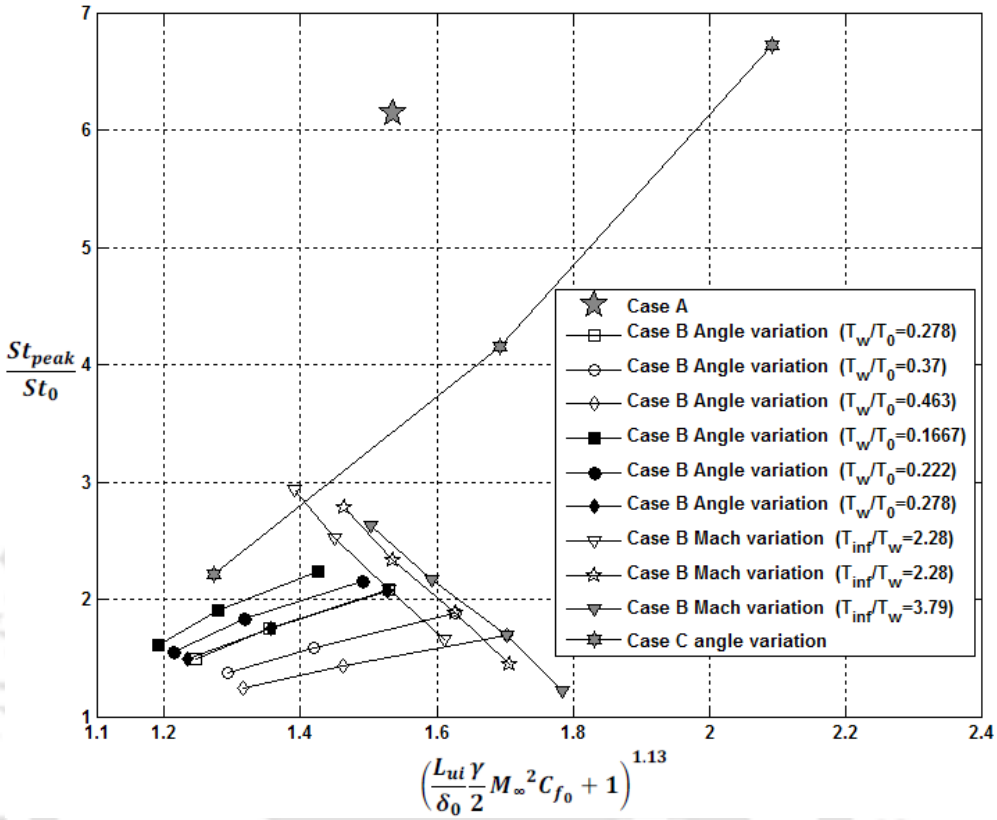

FIGURE 6.11: Present data points fitted according to Grasso and Marini's correlation for peak Stanton number.

correlation as well fits almost linear trend for ramp angle variation cases. However, the nature of trend is completely different in case of SWBLI with varying Mach numbers. Moreover both the ramp angle and Mach number variation trends are different for different freestream and wall temperatures. Hence the correlation for the peak Stanton number with upstream influence extent is modified for accommodating variations in dependent variables. For this modification, the presently proposed upstream influence correlation is considered instead of the one considered by Grasso and Marini. The step followed in the formulation of modfied correlation for peak heatflux is given under.

From equation (6.9), the $p_3/p_0 = p_3/p_1$ can be written as,

$$\frac{p_3}{p_1} \propto \left(\frac{L_{ui}}{\delta_0}\frac{M_0^3}{\beta^*}\sqrt{\frac{C_w}{Re_{x_0}}}+1\right)$$

Upon replacing the pressure ratio in Hung and Barnett's correlation from the above relation, the present correlation for peak Stanton number is obtained as,

$$\frac{St_{peak}}{St_0} \propto \left(\frac{L_{ui}}{\delta_0} \frac{M_0^3}{\beta^*} \sqrt{\frac{C_w}{Re_{x_0}}} + 1 \right)^{1.13} \tag{6.17}$$

Better accuracy in prediction is expected for this correlation, since it has wall and freestream temperature scaling terms as well. The present numerical data points are first plotted according to the proposed correlation, there after an average trend is fitted for these data points (figure 6.12). Thus obtained trend shows a linear variation of normalized peak Stanton number for different interaction cases. Here the nature of trend obtained for different ramp angle, Mach number and wall and freestream temperature conditions is almost same. Therefore almost all the present data points lie closer to the fitted line which confirms the enhanced prediction capability of present correlation. Further to ensure this observation, few additional experimental data points are also plotted in the same figure. This additional evidence supports the accuracy of present peak heatflux correlation.

6.7 Summary

Literature reported correlations for various SWBLI parameters are assessed in light of present numerical results. It has been noticed that, none of the reported correlations predict unique trend for different parametric variations. Needham and Stollery's correlation for upstream influence is found to provide better trend for different flow and geometric parameters as compared to Grasso and Marini's correlation. However both correlations fail in the prediction for different wall to freestream temperature ratios. Therefore modification has been suggested in the Needham and Stollery's correlation with sufficient theoretical support for prediction of extent of upstream influence. This strategy is seen to have improved quantitative prediction of upstream influence. Reported correlations for separation bubble size, except the Davis and Sturtevant's correlation, are found to fit linear trend for different Mach number and ramp angle cases. However, their prediction is seen to deviate from linearity for varying wall to total temperature cases. The exceptional correlation is found to be reliable for predicting separation bubble size for different wall to total temperature ratio cases but fail to correlate varying Mach number cases. Therefore modification has been proposed in Needham's correlation for the qualitative prediction of

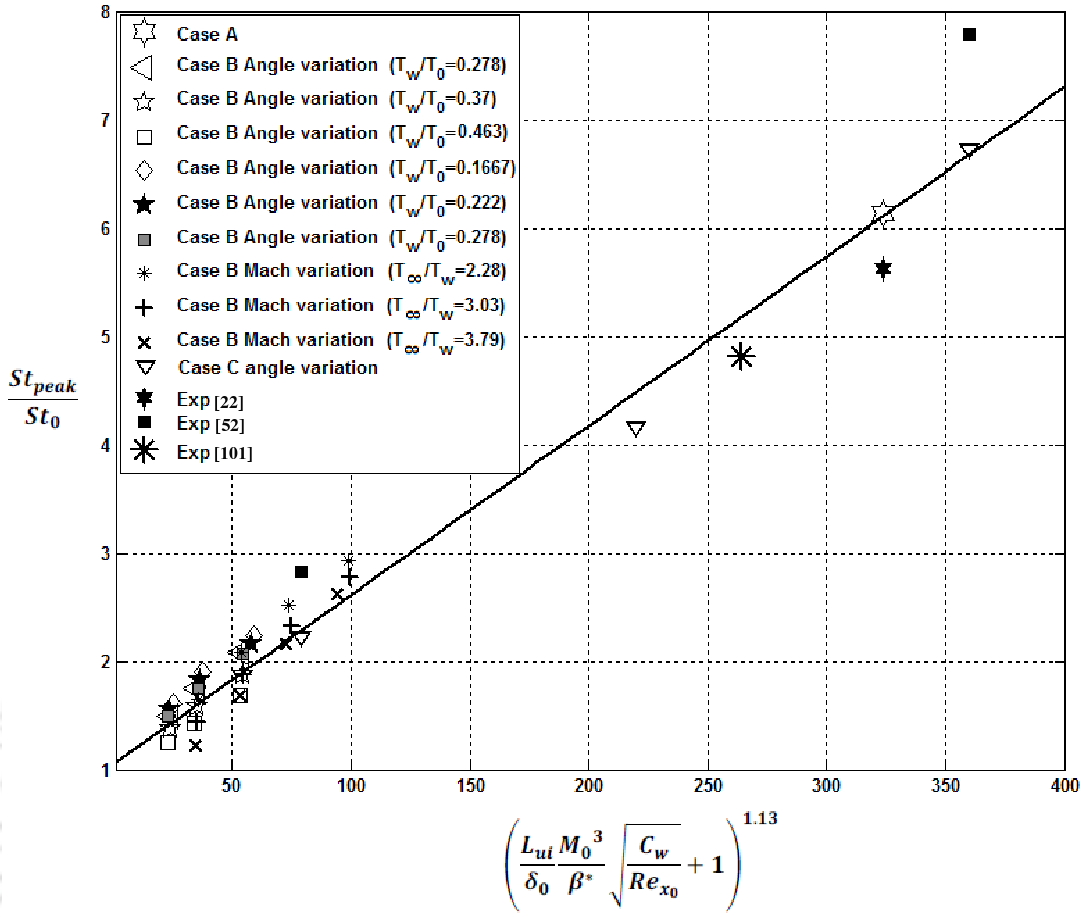

FIGURE 6.12: Data points fitted according to present correlation for peak Stanton number.

separation bubble size. Such modified correlation has been observed to improve the estimate and widen the range of applicability of the correlation. Accuracy of free interaction theory for the prediction of separation point and plateau pressure has also been analyzed. These studies portrayed the need for additional scaling parameters in the expression for ramp angle and wall temperature. Literature reported correlation, for peak Stanton number in the post reattachment region, has been observed to have limitations for accommodating variations in freestream, geometric and wall conditions. The prediction capability of the same correlation is seen to be improved by incorporating the presently proposed extent of upstream influence relation in the same.

Chapter 7

Effect of leading edge bluntness on ramp induced shock wave boundary layer interaction

Overview

This chapter deals with the studies related to R-SWBLI in the presence of leading edge bluntness. Boundary layer edge Mach number and temperature, sonic height, boundary layer thicknesses, skin friction coefficient and pressure difference are considered for the close inspection. Present studies revealed the existence of two critical radii of leading edge bluntness associated with R-SWBLI. Increase in separation bubble size has been observed with increase in leading edge radius until the first critical radius called as 'inversion radius' which corresponds to maximum extent of separation. Swallowing of the entropy layer by the boundary layer is seen to increase the separation zone size while the separation bubble length decreases when the boundary layer is covered by the entropy layer. The inversion radius is shown to be associated with equal thicknesses of the entropy and boundary layers. Increase in leading edge radius beyond the second critical radius, called as 'equivalent radius', is found to decrease the size of separation zone in comparison with that of the sharp leading edge case. This reduction is attributed mainly to the existence of a wide over pressure region. Physics-driven predictive strategies, to determine the critical radii for given geometry and freestream conditions, are derived successfully from the present numerical simulations. Current studies on a 50 mm long plate with 15^0 *compression*

ramp for Mach number 6 and wall temperature of 300 K show that the inversion radius lies between 0.3 and 0. 6 mm while the equivalent radius lies between 1 and 1.2 mm.

7.1 Background

Viscous-inviscid interaction is one of the characteristic features of supersonic or hypersonic flow regimes. Ramp induced shock wave and boundary layer interaction is the prominent example of the same for laminar as well as turbulent flows. This interaction may leads to boundary layer separation, turbulent transition and enhanced surface heating which in turn would affect the performance of associated components. Therefore, various control mechanisms are reported in the open literature to reduce the intensity of this interaction by delaying separation [8, 8, 16, 102, 103]. Provision of leading edge bluntness is the most widely considered separation control technique for R-SWBLI and I-SWBLI. Schematic of the flowfield for R-SWBLI with leading edge bluntness is as shown in figure 7.1. Dynamics of shock wave and boundary layer interaction completely changes in the presence of such leading edge bluntness. Primary reason for this change is the replacement of attached shock by a stronger detached bow shock. Formation of strong entropy layer in the presence of bow shock and interaction of the same with the boundary layer adds to the complexity for understanding of this interaction. Apart from detachment of the shock, leading edge bluntness induces a favorable pressure gradient which accelerates the flow passing over the object of interest. Therefore a high speed shear flow comprised of boundary layer and entropy layer approaches the ramp for sudden turning. Hence, the upstream influence location, separation location, separation bubble size, incipient separation angle and the re-attachment station change with respect to the corresponding reference values of sharp leading edge case. In view of this, it is inevitable to understand the effect of leading edge bluntness on these fundamental interaction parameters before implementing it for separation control.

Earlier studies [14, 16] reported that the leading edge bluntness can act as the effective technique for separation control. However, this technique does not guarantee separation control for all radii as observed by some researchers [17, 42]. But difference in opinion has been noticed

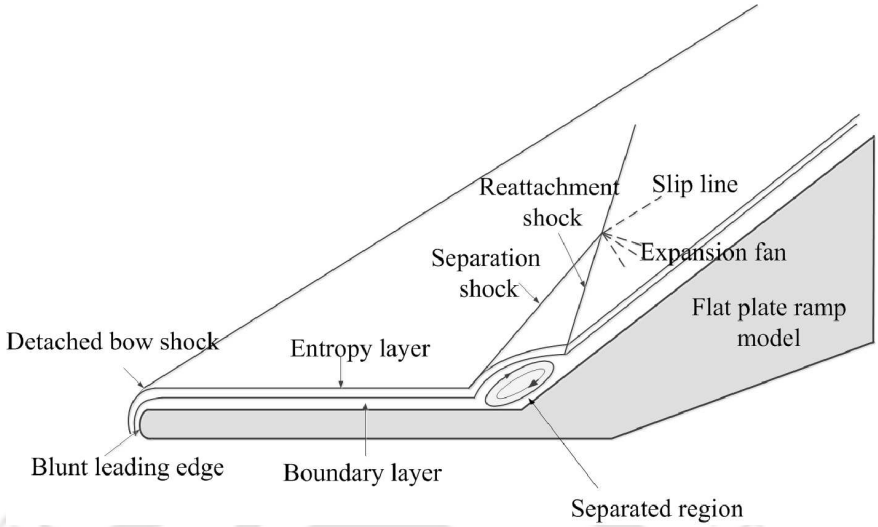

FIGURE 7.1: Schematic of R-SWBLI on a blunted leading edge flat plate-ramp model

among those particular studies [17, 42] for justifying the irregular behavior of this control technique. Hence it is essential to develop a unifying theory about effect of leading edge bluntness. Therefore understanding of the flowfield in the vicinity of critical radius is an immediate need. Apart from this, earlier reportings focus on only one critical radius at which separation bubble size is maximum. Moreover, control strategy demands for the separation size lower than the base or reference value corresponding to the sharp leading edge case. Thus decrement of separation size with increase in leading edge is important if and only if it is lower than that of sharp case in order to implement it as a control technique. Thus two important radii exist which correspond to maximum separation size and to the separation size equal to that of sharp leading edge case. Therefore present chapter initially deals with identification of the critical radii and proceeds further to reason for their identity using literature reported reference sharp leading edge case.

7.2 Solver settings

Numerical investigations of R-SWBLI, in case of sharp and blunted flat plate attached with a ramp, are carried out using 2D version of 'USHAS'. The steady state of the solution is assumed upon the density residual fall below 10^{-6}. Structured quadrilateral elements are used to mesh the computational domain. The details of the computational domains employed for the present study are discussed in the subsequent sections. Highly accurate AUSM+ [91] scheme has been employed for the convective flux calculation in the present study. By considering the steady flow

nature of present cases, time integration is achieved using simple Euler explicit scheme. The fluid (air) is assumed to as ideal gas. There fore Sutherlands viscosity model [75] is employed for the calculation of coefficient of dynamic viscosity in the present study. Additionally the Prandtl number of the fluid is considered as 0.71 for all simulations.

7.3 Numerical studies

7.3.1 Studies with sharp leading edge plate for R-SWBLI

The experimental conditions of Marini [23] are considered here in the present computational studies for sharp and blunt leading edge cases of R-SWBLI. These conditions in terms of freestream Mach number (M_∞), freestream static temperature (T_∞), freestream static pressure (p_∞), freestream unit Reynolds number (Re_∞/m) and wall temperature (T_w) are mentioned in table 7.1. This test case of sharp leading edge flat plate is referred herewith as the reference test case. Plate of 50 mm in length attached to a 15^0 ramp, employed by Marini [23], has been considered for all the simulations. The computational domain opted for the simulation of the same, marked with boundary conditions, is shown in figure 7.2. Quadrilateral elements are considered for meshing the computational domain. Three levels of meshes are employed for the simulation to ensure the grid independency of the solution. Details of these grids are provided in table 7.2.

M_∞	Re m^{-1}	T_∞ K	p_∞ N/m^2	T_w K	R_n mm
6	8×10^5	131.7	199.4345	300	0.1,0.3,0.5,0.6,0.8, 1.0,1.2,1.4,1.5,2.0

TABLE 7.1: Freestream and boundary conditions for the present simulations

Experimental pressure measurements are compared in figure 7.3 during the grid independence studies. Excellent agreement with the experimental measurements can be seen for the mesh size of 204×90 and above. Same fact can be revisited in figure 7.4 which compares surface variation of skin friction coefficient for different meshes along with the analytical skin friction variation for hypersonic flow over flat plate portion [104].

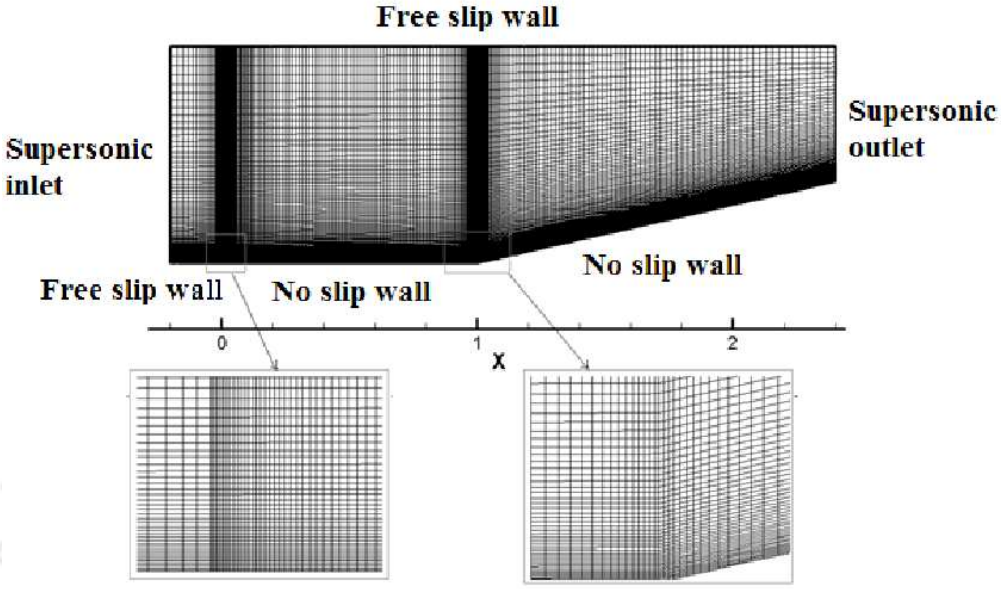

FIGURE 7.2: Computational domain of sharp leading edge case marked with boundary conditions

Case	Overall grid size	Minimum element size near the wall (Δy_{min})	Minimum element size at the leading edge ($\Delta x_{min_{le}}$)	Minimum element size at the flat plate-ramp junction ($\Delta x_{min_{junc}}$)
Sharp leading edge case	120×60	5×10^{-5}	5×10^{-4}	4×10^{-4}
	240×90	2.5×10^{-5}	2×10^{-4}	1×10^{-4}
	360×120	9×10^{-6}	8×10^{-5}	7×10^{-5}
0.5 mm blunt leading edge case	200×80	5×10^{-5}	9×10^{-5}	4×10^{-4}
	300×120	2.0×10^{-5}	2×10^{-5}	1×10^{-4}
	450×180	8×10^{-6}	1×10^{-5}	6×10^{-5}

TABLE 7.2: Details of grids used for the present simulations

Hence various R-SWBLI parameters viz. upstream influence location, separation region pressure, separation bubble size, separation location and reattachment location are seen to be correctly captured. These parameters of sharp leading edge flat plate are considered herewith as the reference parameters. Comparison of the numerically obtained surface pressure variation from weak and strong interaction theories [105] with the computationally obtained one for the flat plate portion of the present configuration is as shown in figure 7.5. This figure clearly depicts

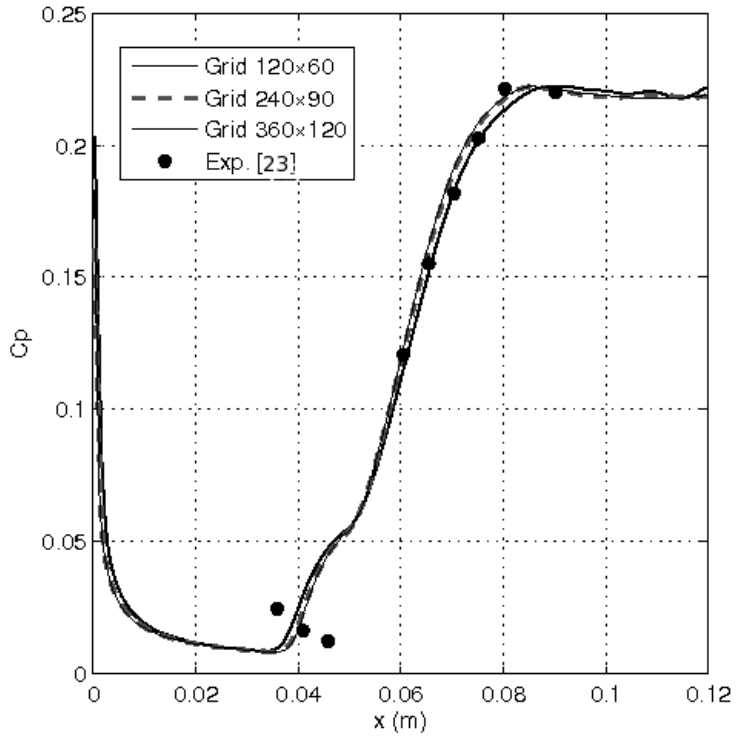

FIGURE 7.3: Surface pressure distribution for the reference case

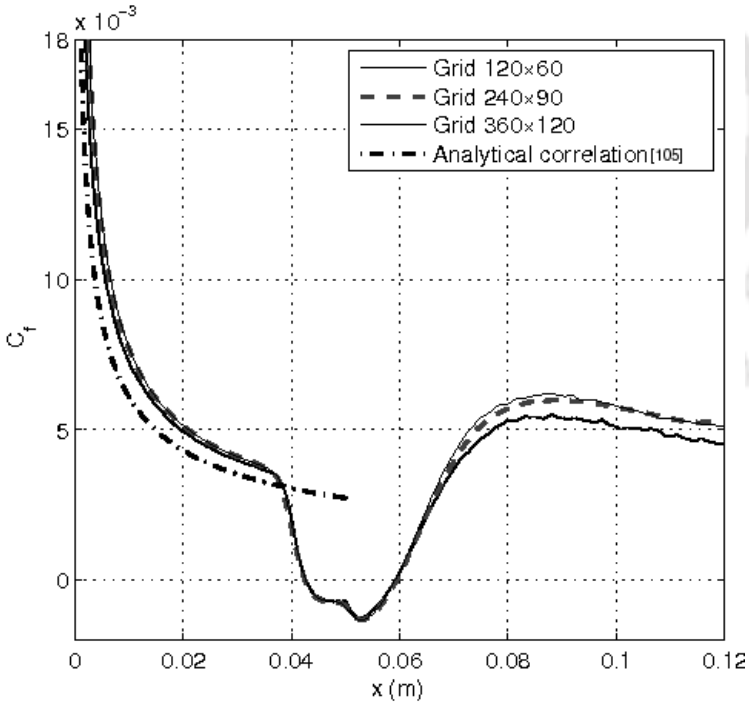

FIGURE 7.4: Skin friction distribution for the reference case

that the present studies belong to the strong interaction case.

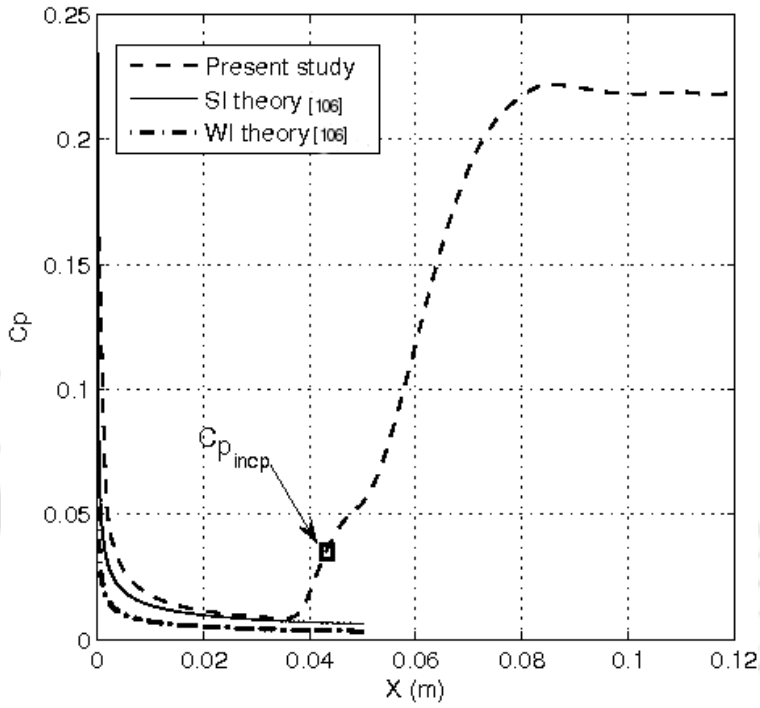

FIGURE 7.5: Comparison of wall pressure distribution on the plate portion of the model with viscous interaction theories

7.3.2 Studies with blunt leading edge plate for R-SWBLI

The same sharp leading edge plate and ramp combination, referred earlier, is chosen to study the effect of leading edge bluntness on R-SWBLI. Leading edge radii (R_n), considered for present studies, vary from 0.1 mm to 2 mm as mentioned in table 7.1. Computational domain selected for the blunt leading edge case differs from the same considered for sharp leading edge case. A representative computational domain of 0.5 mm leading edge bluntness case, marked with boundary conditions, is shown in figure 7.6. Typical variation of skin friction coefficient along the surface of this configuration, for different mesh sizes, is shown in figure 7.7 to demonstrate the grid independence test. Encouraging agreement can be noticed with increase in mesh size. Waviness has been observed in the post reattachment region for the skin friction distribution in case of finest mesh. These are however small frequency and do not significantly impact the physics of the problem. These oscillations may be attributed to the high aspect ratio of the element near the wall. Moreover, from this figure a grid level of 300×120 can be identified as

an optimum grid level that offer grid independent solution. Such mesh independent results are considered for analysis of R-SWBLI. Similar mesh refinement and mesh independence studies are carried out for all the radii under consideration. Different levels of quadrilateral meshes are employed for these studies as well. The details of the computational domains employed for blunt leading edge studies are also given in table7.2

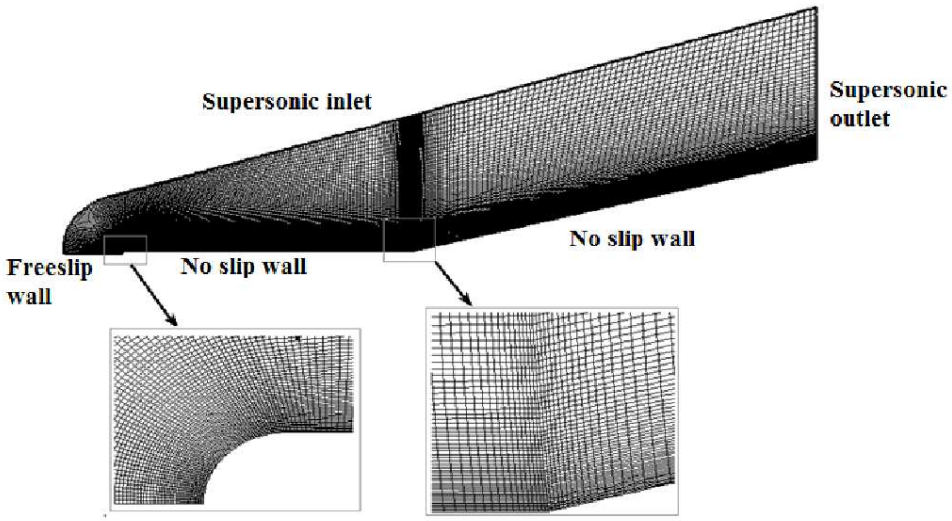

FIGURE 7.6: Computational domain of representative blunt leading edge (R_n=0.5 mm) case marked with boundary conditions

Grid independent Mach number contours for the reference case and leading edge bluntness of 0.5 mm are as shown in figure 7.8. Completely different aerodynamics can be noticed with leading edge radius, even at upstream of the ramp. The foremost change that can be evidenced is the replacement of attached weak leading edge shock for the reference test case by the strong detached bow shock ahead of the blunt plate. Such a shock pattern alters the flow properties where Mach number and flow velocity decrease while temperature and pressure increase in the shock layer. Presence of entropy layer is also inevitable for such blunted configurations. The characteristic features of the shock layer are thus largely dependent on interaction of boundary layer with this entropy layer. These changes affect the downstream viscous-inviscid interaction.

The variation of pressure along the wall, for different leading edge radii, is shown in figure 7.9. Increase in favorable pressure gradient along the plate, with increase in leading edge radius, is evident from this figure. Besides, increase in upstream influence pressure and decrease in peak

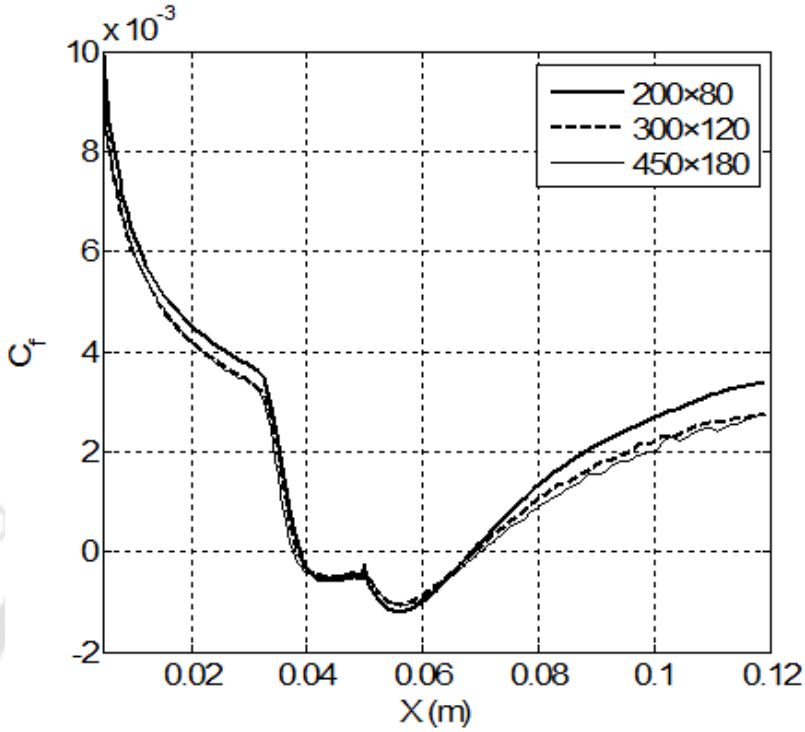

FIGURE 7.7: Skin friction distribution for various mesh sizes in case of R_n=0.5 mm

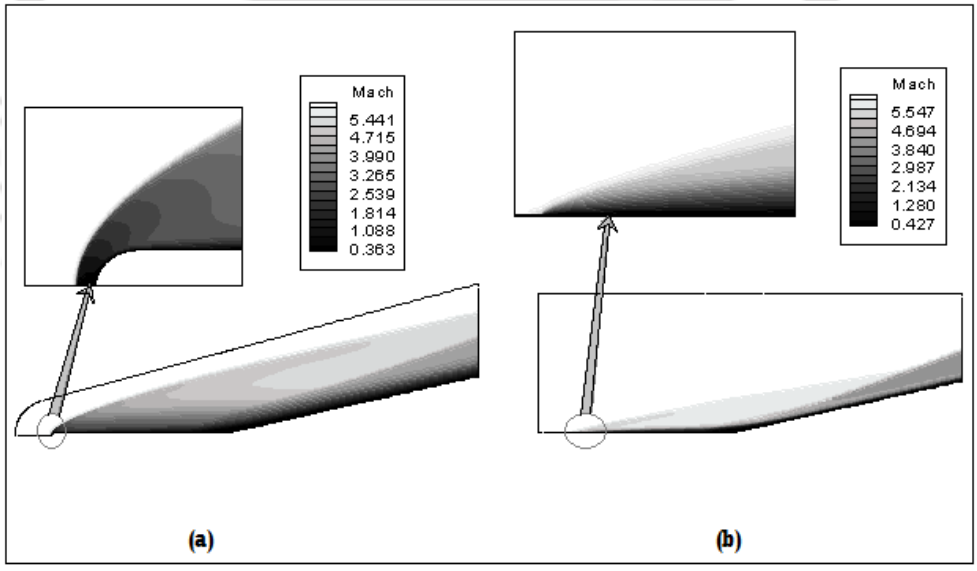

FIGURE 7.8: Comparison of Mach contours for (a) blunt leading edge case and (b) sharp leading edge reference case

pressure on the ramp, with increased leading edge bluntness, is also clear here. Distribution of skin friction coefficient (C_f) and Stanton number (St) along the wall, shown in figure 7.10 and figure 7.11 respectively, confirms the observations of pressure plot. Sudden decrease in surface heat flux beyond the upstream influence location is evident from figure 7.11 for all

bluntness radii. It can as well be observed that the reduction in peak heat flux on the ramp portion of the model exhibits same trend as that of the peak pressure with increase in leading edge radius. Furthermore, separation point and reattachment point can be located from figure 7.10 as the points where distribution of skin friction coefficient crosses zero line. Variation of these two locations for different leading edge radii is plotted in figure 7.12. It can be noticed here that, the separation point moves upstream with initially increase in leading edge radii, whereas reattachment point shifts downstream for the initial change in radius. However, this trend reverses between R_n=0.3 mm and 0.6 mm of leading edge bluntness. Length of separation bubble can be evaluated from these locations since it is defined as the stream-wise distance between separation and reattachment point. Thus obtained separation bubble size, for all the radii under consideration, is plotted in figure 7.13.

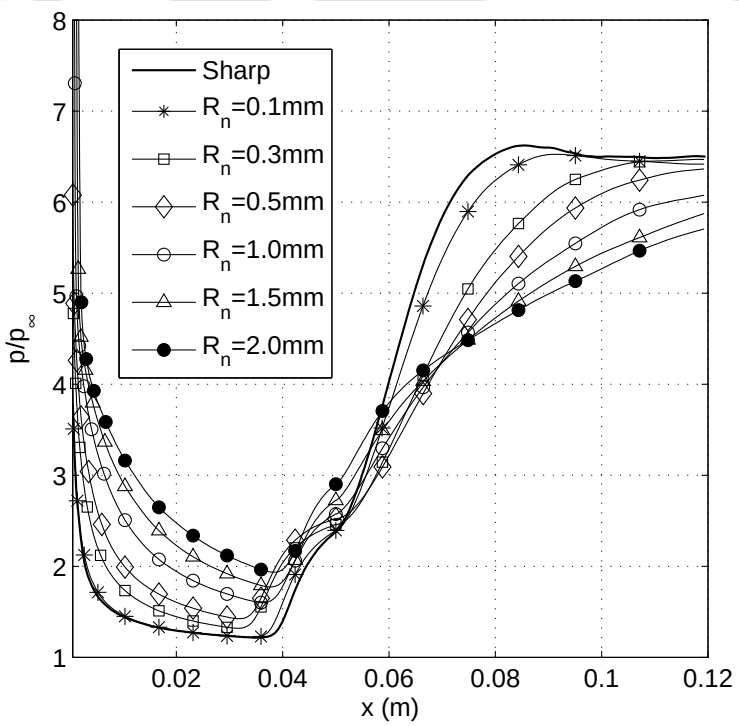

FIGURE 7.9: Comparison of surface pressure distributions for various leading edge radii

In this figure, separation bubble size is non-dimensionalised using the reference length scale as the distance between leading edge and upstream influence start location (x_0). Choice of this length scale is mainly due to its direct correlation with the boundary layer thickness at upstream influence location [20]. Here the separation bubble size is first seen to increase with increase in

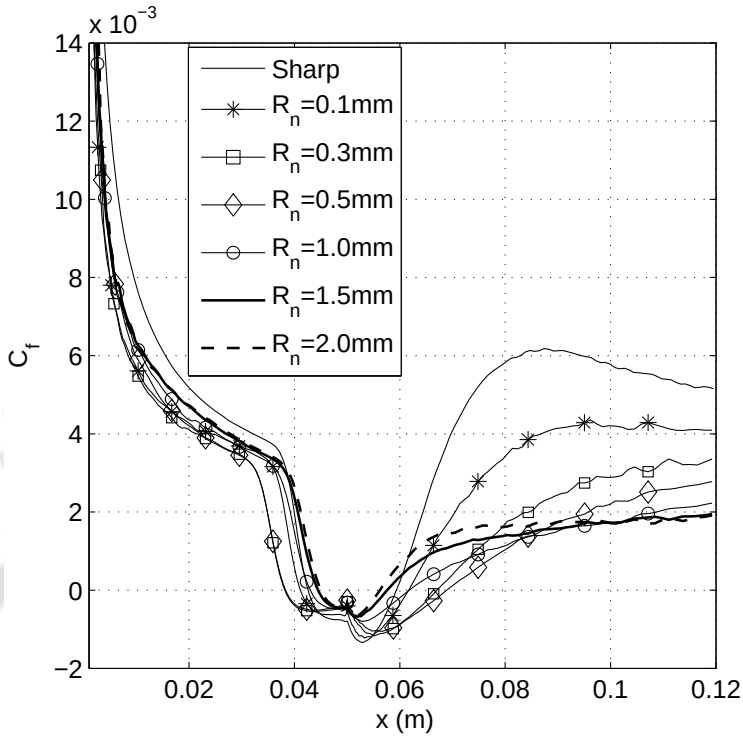

FIGURE 7.10: Comparison of skin friction distributions for various leading edge radii

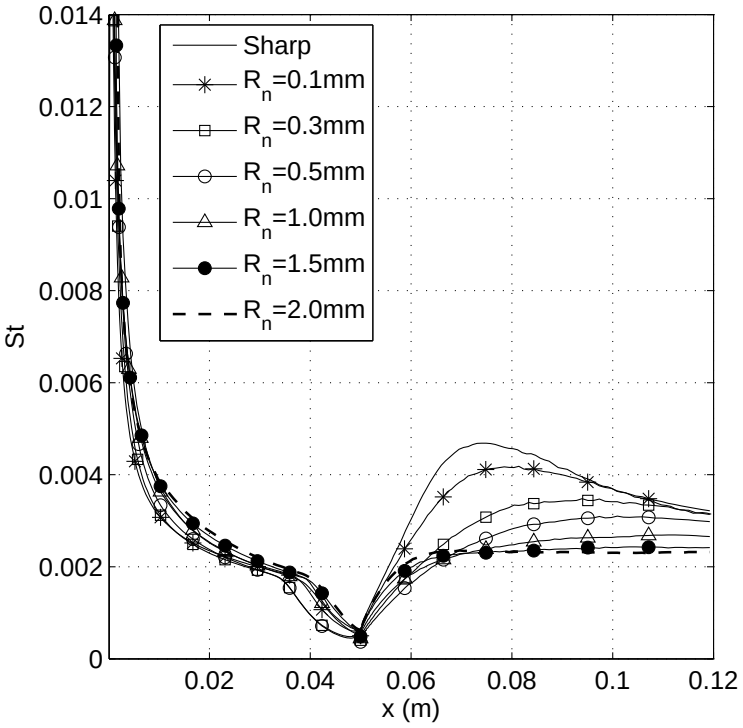

FIGURE 7.11: Comparison of Stanton number distributions for various leading edge radii

leading edge radius till the first critical radius. This radius can be termed as 'inversion radius', since it represents the maximum separation bubble size for given geometry and freestream conditions. Although separation bubble size decreases beyond the inversion radius, its magnitude is still greater than the reference separation bubble size till the leading edge radius reaches to a second critical value. This critical radius can be termed as 'equivalent radius' for which separation bubble size is same as that of the reference case of sharp leading edge plate. A smaller separation zone in comparison with the reference case is observed for leading edge radii greater than the equivalent radius and hence this range of radii must be chosen for implementation of separation control.

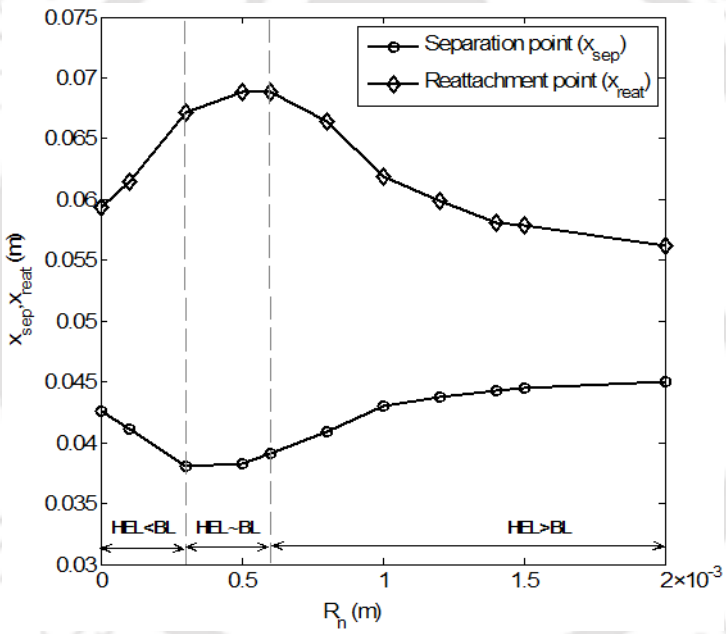

FIGURE 7.12: Variation of Separation and reattachment locations for various leading edge radii (BL is boundary layer and HEL is high entropy layer)

7.4 Effect of governing parameters on R-SWBLI

Katzer's functional relation [41] can be used to understand the behavior of separation bubble size with increase in leading edge radius. Such a relation can be expressed as,

$$L_b \propto \delta_0^* (\frac{Re_{x0}}{C})^{1/2} M_0^{-3} (\frac{p_3}{p_1} - \frac{p_{incp}}{p_1}) \tag{7.1}$$

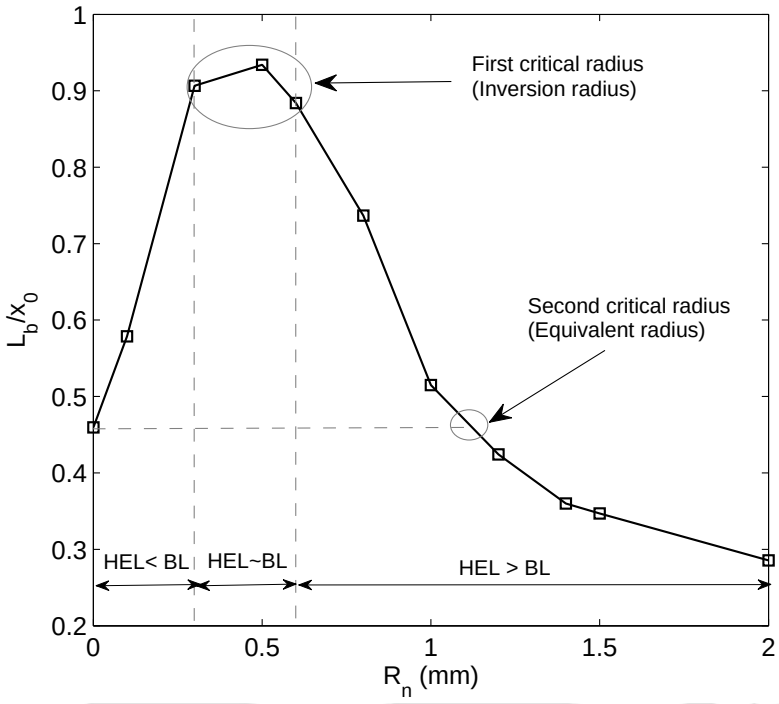

FIGURE 7.13: Variation of separation bubble size for various leading edge radii (BL is boundary layer and HEL is high entropy layer)

Here, L_b is the separation bubble length, δ^* is displacement thickness at x_0 which is upstream influence, Re_{x0} is the Reynolds number at x_0 , C is Chapman-Rubesin parameter, M_0 is Mach number at x_0, p_3 is pressure at the reattachment location, p_1 is pressure at x_0 and p_{incp} is the incipient pressure or pressure at separation location. This relationship can be rearranged and rewritten in terms of skin friction coefficient (C_{f_0}) and boundary layer thickness (δ_0) or sonic height at upstream influence start location. Introduction of these parameters in the expression is mainly due to the correlation among the existing independent variables of equation (7.1) in terms of above mentioned ones. In addition to these, dependence of wall temperature (T_w) and boundary layer edge temperature (T_e) can be incorporated in the same expression since this ratio also governs the separation bubble size [16, 17]. Therefore the functional relationship of separation bubble size with influencing parameters in most general form is,

$$L_b = f(\delta_0, \frac{1}{C_{f_0}}, \frac{T_w}{T_e}, M_0^{-3}, \frac{p_3}{p_1} - \frac{p_{incp}}{p_1}) \tag{7.2}$$

Detailed understanding about dependence of each term on separation bubble size would help in defining significance of the two critical radii discussed earlier.

7.4.1 Boundary layer thickness and sonic height

Boundary layer thickness or its subsonic counterpart, sonic height, has functional relation with the separation bubble size. Hence, boundary layer at a particular location should be selected to examine the effect of interaction in the presence of leading edge bluntness. Moreover, it can be seen from the surface pressure variation for different leading edge radii (figure 7.9) that the extent of upstream influence follows the same trend as that of the separation bubble size with increase in leading edge bluntness. Hence a representative location (x=32 mm) which is most upstream and undisturbed for all radii, is considered herewith to understand the effect of bluntness on boundary layer thickness.

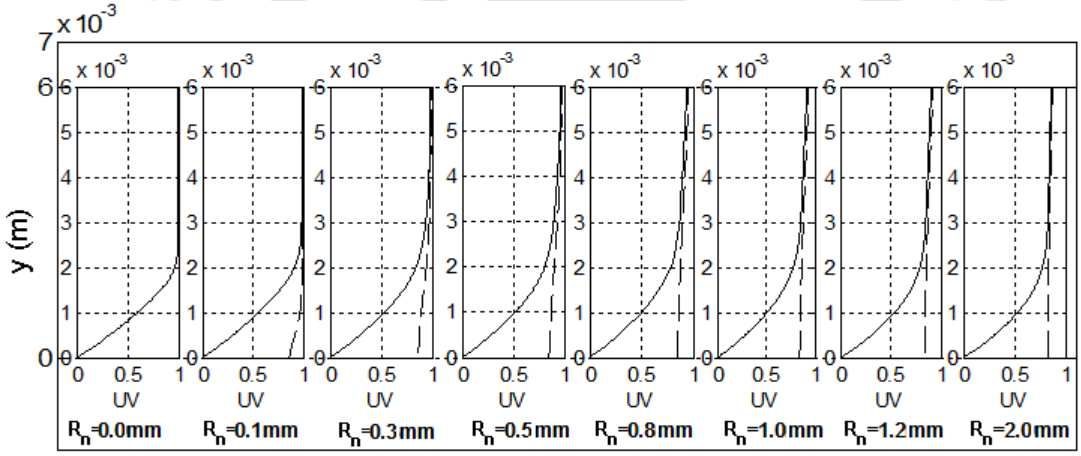

FIGURE 7.14: Velocity boundary layer at x=32 mm for different leading edge radii

Velocity profile in the boundary layer for few selected radii is compared in figure 7.14. Identification of the edge of this boundary layer is a challenging task in this case due to the non-uniform flow in the shock layer. Therefore velocity profiles obtained from viscous and inviscid simulations are simultaneously plotted in figure 7.14. The location where viscous velocity profile (solid lines) asymptotically approaches the inviscid velocity profile (dotted lines) is accounted here as the edge of the boundary layer. Thus evaluated boundary layer thickness can be seen to increase initially with increase in leading edge bluntness. This qualitative variation of boundary layer can be seen to decreases between 0.3 mm and 0.5 mm. Further increase in radius reduces the boundary layer thickness. Similar observation can be made from figure 7.15 which portrays the variation of subsonic part of boundary layer, called as 'sonic height', with

leading edge bluntness. Since higher sonic height is the sign of disturbed upstream boundary layer flow, it hints for early separation of the boundary layer. Besides, sonic height and boundary layer thickness remain thickened than the reference case for the highest bluntness radius (2 mm) under consideration.

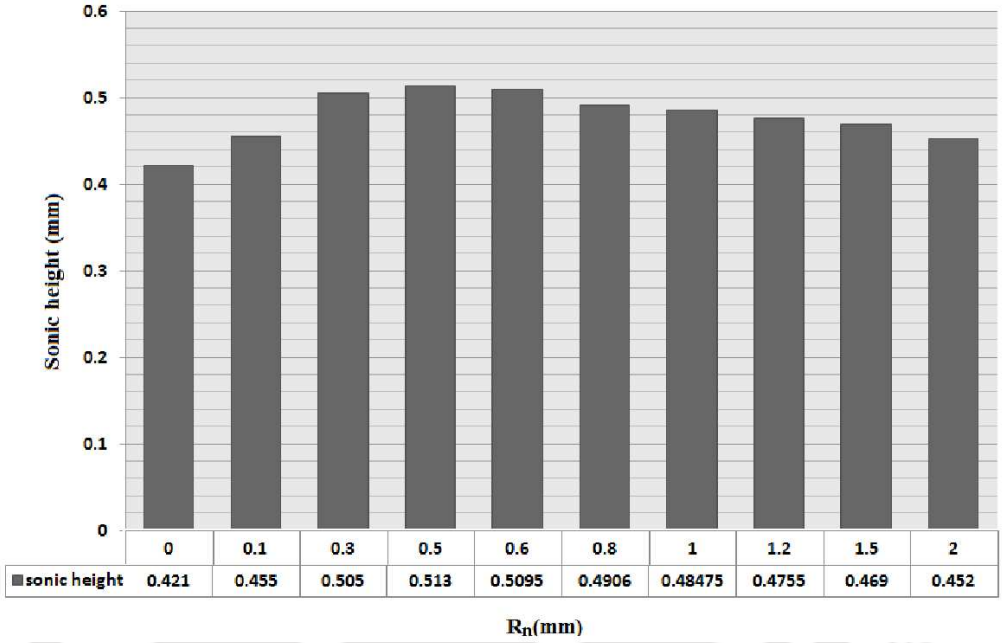

FIGURE 7.15: Sonic height at x=32 mm for different leading edge radii

7.4.2 Skin friction coefficient

In equation (7.2), skin friction coefficient exhibits inverse proportionality with separation bubble size. Hence after analyzing the velocity boundary layer thickness, this sub-section deals with the near wall velocity variation and in turn the local skin friction coefficient with leading edge bluntness. Same upstream location (32 mm) is considered here as well for discussing the effect of leading edge bluntness on local skin friction coefficient. Figure 7.16 re-confirms the inverse relationship of skin friction coefficient with separation bubble size. Hence initial decrease in magnitude of the skin friction coefficient with increase in leading edge radius can be correlated to thicker boundary layer which is susceptible for separation. Therefore the observation from figure 7.16 is consistent with that from figure7.15. Similar trend inversion can be noted herewith for skin friction coefficient between 0.3 mm and 0.5 mm of bluntness radius. Thus it can be clearly depicted from the boundary layer and near wall analysis that, the separation prone thicker

boundary layer with lower wall shear is the possible reason for early separation for all the leading edge radii till inversion radius. Moreover, skin friction coefficient at this station remains always lower than the reference value for all radii under consideration.

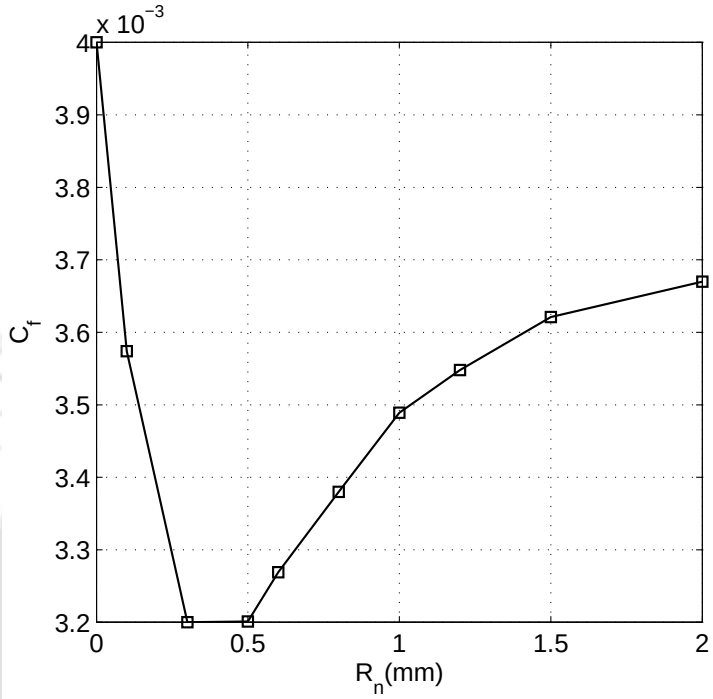

FIGURE 7.16: Variation of skin friction coefficient at x=32 mm with leading edge bluntness

7.4.3 Boundary layer edge Mach number

Shock wave boundary layer interaction largely depends on the freestream Mach number. However equation (7.2) correlates boundary layer edge Mach number as an influencing parameter for deciding the separation bubble size. Present case stands as a perfect example to justify this fact since here boundary layer edge Mach number changes with change in degree of bluntness for same freestream Mach number. In view of this, Mach number variation in the direction normal to the wall, at selected streamwise locations, for specific leading edge radii, is shown in figure 7.17. This figure clearly portrays the continuous reduction of edge Mach number with increase in leading edge radius. No trend reversal can be experienced for this parameter as it had been observed for boundary layer thickness or skin friction coefficient. Moreover, it has already been observed in Chapter-5 that the intensity of R-SWBLI decreases with increase in

freestream Mach number. In line with this, strength of the interaction should increase with increase in leading edge bluntness due to reduction in boundary layer edge Mach number for the given freestream Mach number. As a result of which increase in separation bubble length is expected for every incremental change in leading edge radius. However, such trend is prominent for initial increase in radius till inversion radius. Hence, only separation zone widening can be accounted by reduction in boundary layer edge Mach number as claimed by Holden [8, 42].

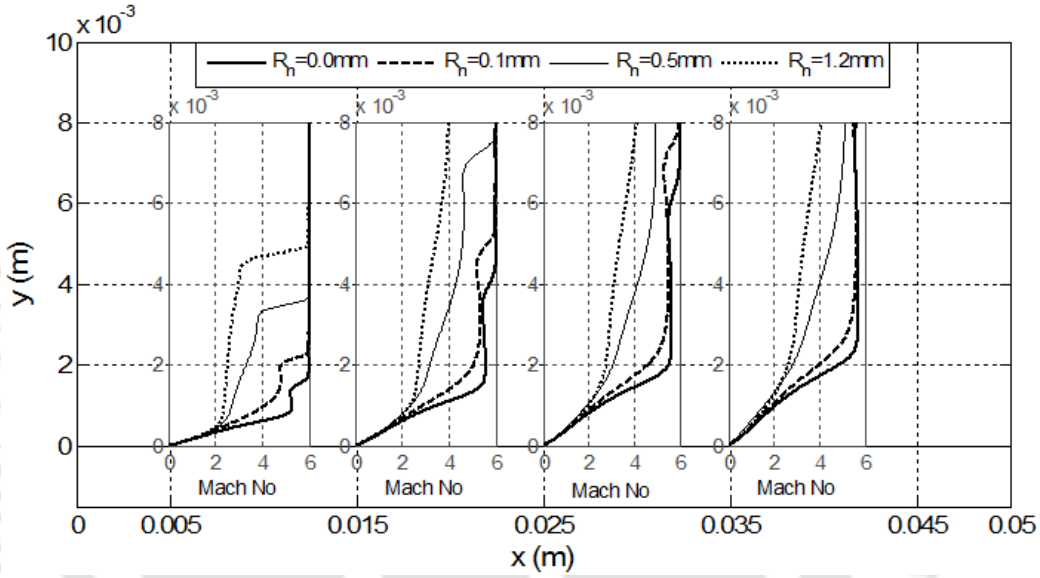

FIGURE 7.17: Mach number variation in the velocity boundary layer at different streamwise locations for different leading edge radii

7.4.4 Wall to boundary layer edge temperature ratio

Wall temperature and freestream temperature independently influence the R-SWBLI. Higher values of wall temperature alter the near wall properties of the hydrodynamic boundary layer. Among these alterations, vital one is the reduced density of the boundary layer flow which in turn inflates the same. Widened separated zone for adiabatic wall condition, in comparison with the isothermal wall, supports the fact of forming separation prone boundary layer with increase in wall temperature. Apart from this, change in boundary layer edge temperature can be associated to change in freestream temperature or freestream stagnation enthalpy of the flow for the same freestream Mach number. Therefore the elevated edge temperature offers more resistance against the separation for the reference test case. Hence the effects of wall and boundary layer

edge temperatures on the interaction counteract each other for the reference case of sharp leading edge plate. However, present studies are carried out for constant wall temperature where boundary layer edge temperature changes due to leading edge bluntness for the same freestream Mach number and stagnation enthalpy. Therefore, the ratio of these temperatures, which forms an independent variable in equation (7.2), helps to analyze the effect of leading edge bluntness on R-SWBLI. In view of this, it is essential to analyze the relation between the leading edge bluntness and boundary layer edge temperature.

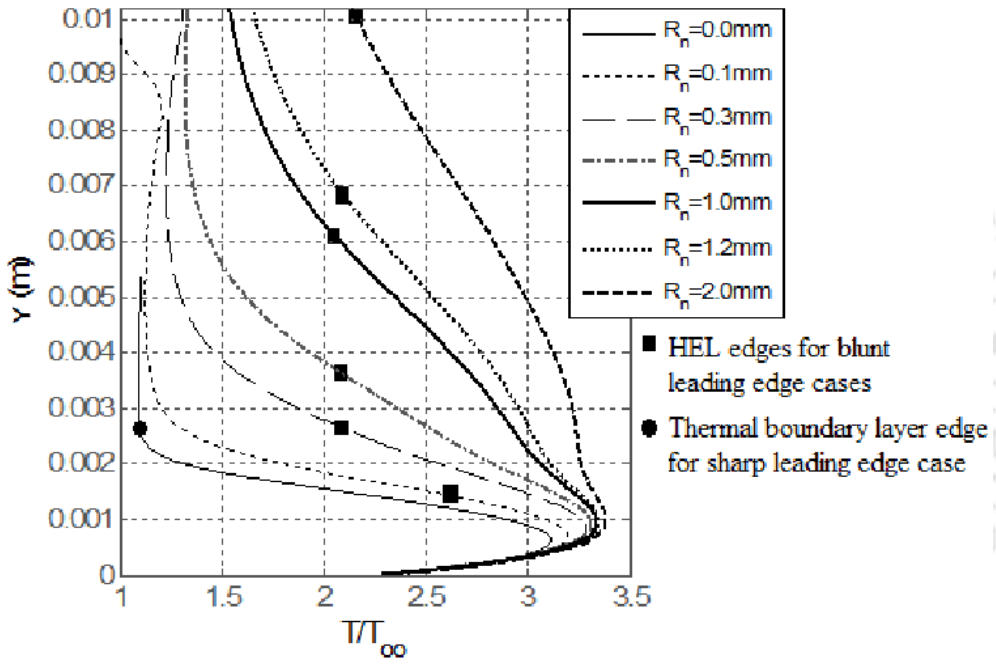

FIGURE 7.18: Thermal boundary layer at x=32 mm from leading edge for different leading edge radii

Temperature distribution normal to the wall is plotted for a specific streamwise location (x=32 mm) in figure 7.18 for different leading edge radii. It is evident from this figure that, the thermal boundary layer edge temperature increases with increase in leading edge radius. Thus, there exists no trend reversal for this parameter as well. Moreover, such variation of boundary layer edge temperature is complementary with the boundary layer edge Mach number. Consequently, the reduction in edge Mach number can be attributed to enhanced edge temperature. Hence, increased edge temperature can as well be accounted for only separation zone widening like edge Mach number. Therefore the static temperature boost, at the edge of the thermal boundary layer,

for the same stagnation enthalpy, is seen to hinder the resistance of the boundary layer against separation. This observation contradicts the effect of enhanced edge temperature, for reference test case, with increase in stagnation enthalpy. Besides, nature of variation of maximum temperature within the thermal boundary layer is also noticeable. Increase in leading edge radius, till the 'inversion radius', is seen to increase the maximum temperature rapidly; beyond which marginal enhancement in the same can be noticed.

7.4.5 Separation and reattachment pressures

The non-dimensional difference in reattachment and separation point pressures is a governing parameter for the separation bubble size (equation (7.2)). In case of the reference sharp leading case, this pressure difference depends only on the downstream ramp angle for given freestream conditions. Nonetheless, the effect of leading edge bluntness has been studied here for constant ramp angle at a given freestream conditions. Therefore, change in this independent variable for present studies should be accounted due to change in leading edge bluntness radius with unaltered freestream conditions and ramp angle. This fact justifies the importance of non-dimensional pressure difference to study the R-SWBLI in the presence of leading edge bluntness. Therefore, pressure at upstream influence point (p_1), incipient pressure (p_{incp}) and reattachment point pressure (p_3) are plotted in non-dimensional form against the leading edge radius in figure 7.19. Here, non-dimensionalization is done using freestream pressure as a reference pressure. Additionally, non-dimensionalization of these pressures using upstream influence pressure is also plotted in figure 7.19. Apart from these ratios, the non-dimensional pressure difference from equation (7.2) is also part of this figure. Hence this figure is useful to understand the variation of absolute values of these pressures and their required non-dimensional difference due to change in leading edge bluntness. It is very much evident from this figure that, the relative variation of the pressures with increase in radius provides marginal variation in the non-dimensional difference for smaller radii. However, this difference decreases for larger radii due to increase in upstream influence pressure and decrease in re-attachment pressure. Hence, it can be depicted from this figure that the governing non-dimensional pressure difference has marginal influence till the inversion radius. Moreover, decrease in this pressure difference beyond the inversion radius leads to lessen the adverse pressure gradient to the impending flow. This critical

analysis supports the observation of decrease in separation bubble size beyond the inversion radius. Therefore the decrements in non-dimensional pressure difference can be attributed for reduction in separation zone size.

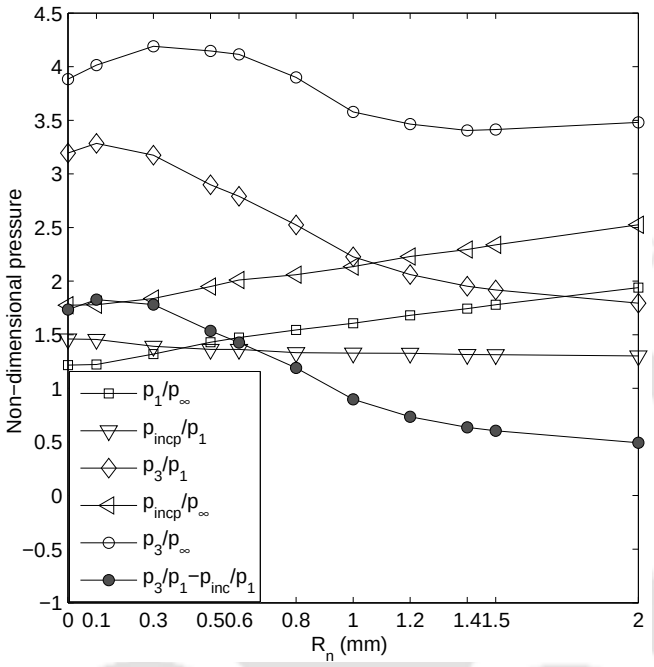

FIGURE 7.19: Variation of vital pressures and their difference with leading edge bluntness

7.5 Prediction methodology for "inversion radius"

Above discussed governing parameters exhibit certain changes with increase in leading edge bluntness, some of which can be reasoned for existence of the "inversion radius". But the underlying flow physics needs to be revealed for accountability of these ascribed changes in governing variables for prediction of the "inversion radius". Therefore, an attempt has been made herewith to sum up all these reasons in terms of interaction of the entropy layer with the boundary layer. Understanding of the proposed interaction of layers is mainly the quantification of relative thicknesses of these layers around the R-SWBLI station. If the entropy layer thickness is smaller as compared to the boundary layer thickness, then it is termed as 'entropy layer swallowing' by the boundary layer. Completely swallowed entropy layer mainly alters flow properties within the boundary layer. However, if the entropy layer thickness is sufficiently higher so as to cover the entire boundary layer, then the boundary layer grows within the entropy layer. Such thicker

entropy layer then alters the properties both at the edge and within the boundary layer. In order to understand such interaction, it is very much essential to evaluate the thickness of entropy layer for different leading edge radii.

By the definition, complete shock layer should be treated as entropy layer for hypersonic flow over blunted configuration. But the region of strong entropy gradient is only responsible for its interaction with the boundary layer. In view of this, interaction of boundary layer only with the high entropy layer (HEL) as described by Borovoi et al. [29], is considered in following discussion. Thickness of such HEL at the leading edge is almost equal to the leading edge bluntness radius [29]. This point essentially corresponds to the location on the bow shock beyond which change in shock angle is negligible. Such point divides the bow shock into two parts viz. highly curved and marginally curved or oblique shock. Downstream of the shock, HEL had been considered as the layer of constant thickness [17]. But such representation does not account for downstream alterations in the entropy layer thickness. Similar to the bow shock dividing point, HEL edge is responsible to segregate the uniform and non-uniform regions of entropy in the shock layer. Hence HEL edge downstream of detached shock is considered herein as the streamline passing through the point on the standing shock wave at height equal to the bluntness radius at the leading edge as shown in figures 7.20 and 7.21. Figure 7.20 strongly supports such representation by displaying high magnitude entropy beneath the separating streamline. Similarly, this HEL edge also divides the shock layer into a strongly non-uniform flow which has passed through the highly curved shock and weakly non-uniform flow which has passed through the marginally curved or oblique shock. Figure 7.21 demonstrates the HEL edge and variation of non-dimensional entropy normal to the wall at different streamwise locations for 1.5 mm leading edge radius case. This figure also shows that a major portion of the entropy, by magnitude and gradient at any streamwise location, is within the entropy layer which is consistent with the definition of the HEL as considered herein.

This strategy of HEL definition can be used to study its interaction with boundary layer. Velocity variation in the boundary layer at some selected streamwise locations and the edge of HEL are plotted in figure 7.22, figure 7.23 and figure 7.24 to demonstrate the relative thickness

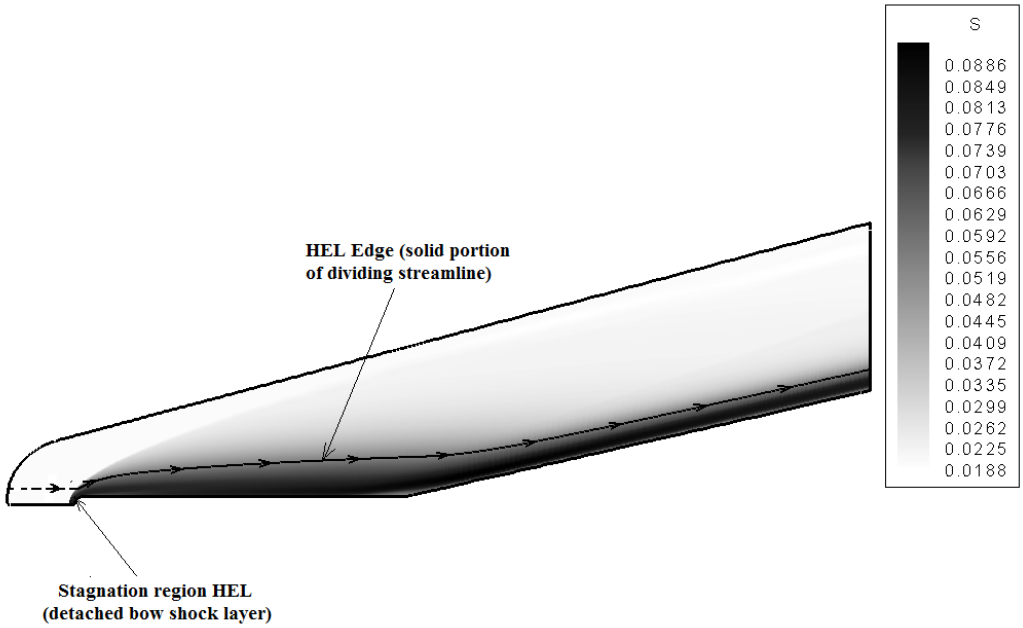

FIGURE 7.20: Representation of the HEL edge together with entropy contour for leading edge radius of 1.5 mm

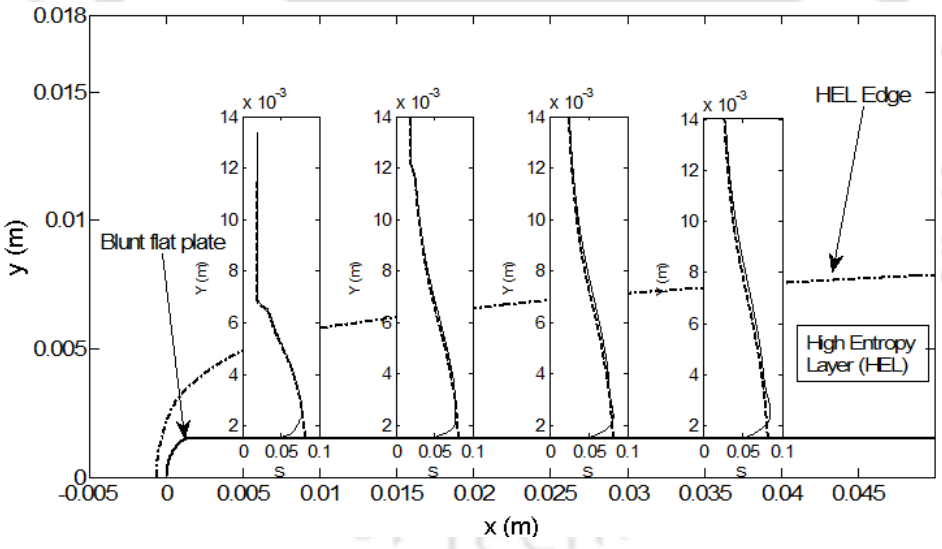

FIGURE 7.21: Representation of the HEL edge and non-dimensional variation of entropy in the shock layer at selected streamwise location for leading edge radius of 1.5 mm

of both the layers for leading edge radii 0.1 mm, 0.5 mm and 1.2 mm respectively. For leading edge radius of 0.1 mm, the entropy layer is very thin as compared to boundary layer at all representative locations. Therefore, entropy layer swallowing occurs quite close to the leading edge at this radius. However, in the case of leading edge radius of 0.5 mm, entropy layer is seen to be thicker than the boundary layer until 0.035 m from the leading edge. Entropy layer

swallowing station for this case is immediately upstream of the reference upstream influence location. Moreover, for leading edge radius of 1.2 mm, entropy layer is considerably thicker at all the locations in comparison with the boundary layer. Hence, boundary layer is completely immersed in the entropy layer for this case. This exercise hints for the conclusion that separation bubble size increases if the entropy layer gets swallowed ahead of the reference upstream influence location. The possible justification of this conclusion lies in the alterations caused by the near wall presence of fluid from HEL. Such high temperature fluid, which has passed across the stronger portion of the bow shock, increases the near wall viscosity and reduces the density. These effects result in thickening of the boundary layer and reduced wall shear. Such thickened boundary layer displaces the outer inviscid flow thereby increasing the strength of marginally curved portion of the standing shock. This in turn leads to decrease in the boundary layer edge Mach number and increase in the edge temperature. Such physical analysis thus accounts for the effects of all parameters, except the pressure difference, on the separation bubble size. This inclusive analysis is thus helpful in understanding the existence of 'inversion radius' in the presence of boundary layer and entropy layer interaction.

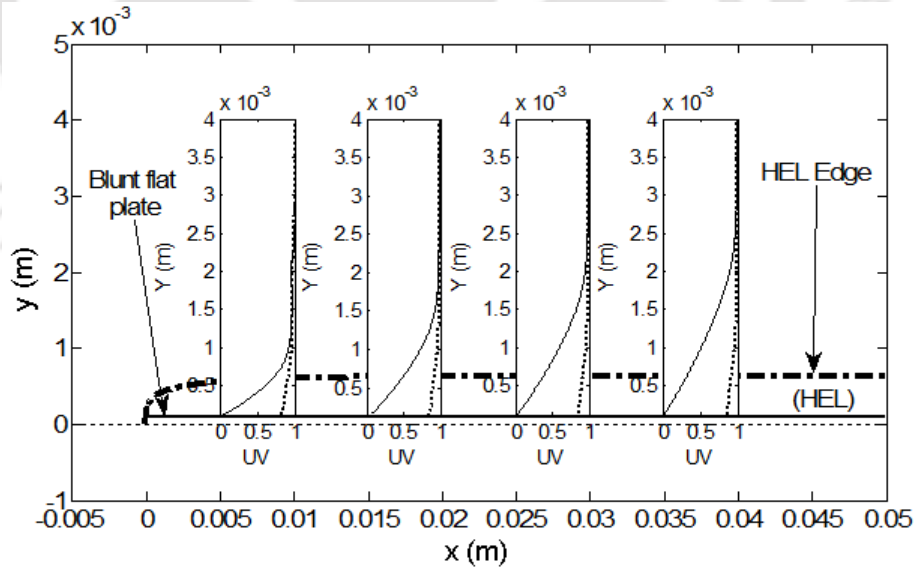

FIGURE 7.22: Interaction of boundary layer and entropy layer for R_n = 0.1 mm

It has been observed earlier that the boundary layer edge Mach number and temperature varied monotonically with increase in bluntness. Therefore, unlike other governing parameters, given in equation (7.2), inversion radius can't be evaluated from the trend of their variations. However,

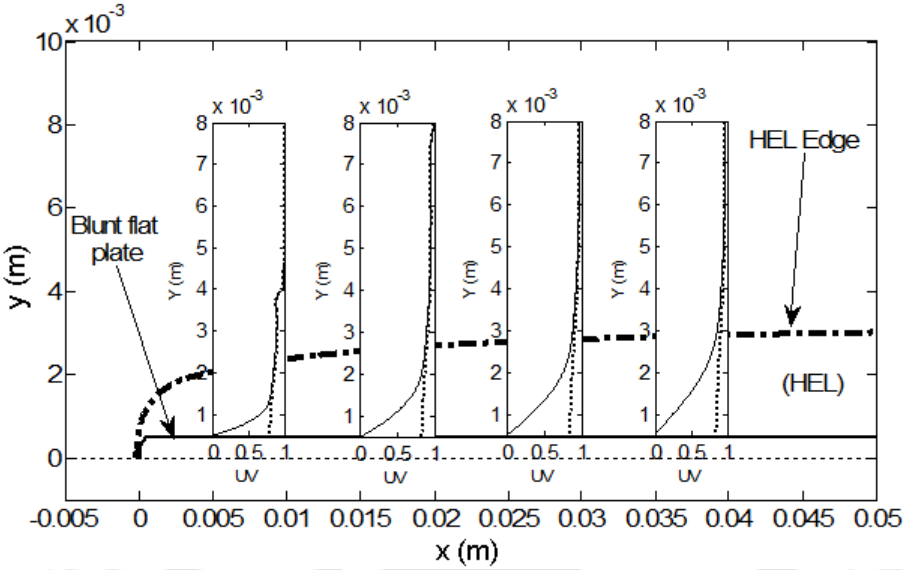

FIGURE 7.23: Interaction of boundary layer and entropy layer for R_n = 0.5 mm

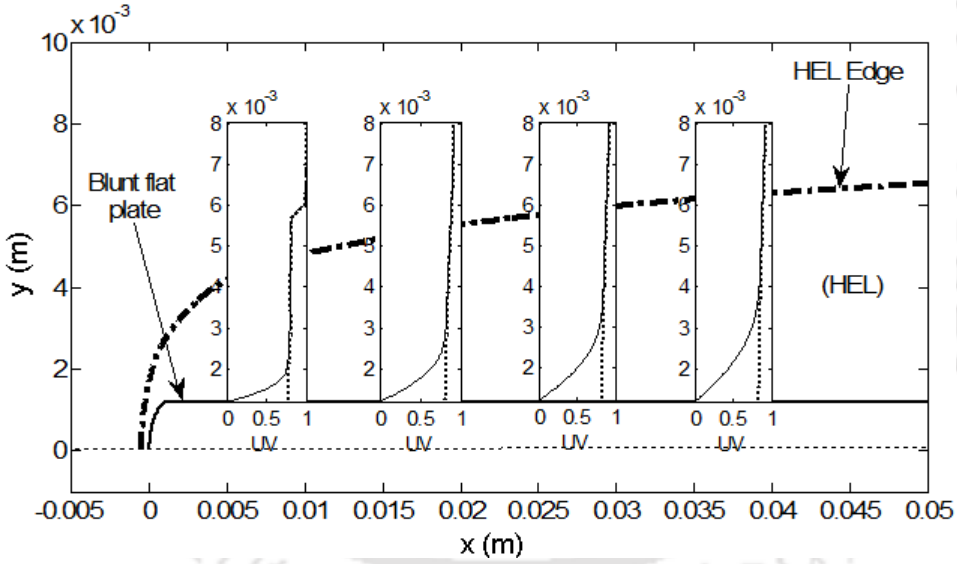

FIGURE 7.24: Interaction of boundary layer and entropy layer for R_n =1.2 mm

the reasons for this monotonic behavior, before and after the inversion radius, are completely different. The background flow structure which alters these motives for the monotonic change can also be explained from the entropy layer analysis. Entropy layer swallowing clearly suggests that there exists weak non-uniformity or almost uniformity in the flow properties at the edge of the boundary layer with increase in radius till the inversion radius for the upstream influence location. In such cases, the fluid present at the edge of the boundary layer, at any station downstream of the swallowing location, for any radius lower than the inversion radius, is the one

which has passed through weakly curved portion of the standing shock. However, variation in the edge parameters beyond the inversion radius should be attributed to growth of the boundary layer within the HEL. In such cases, no swallowing takes place before the reference upstream influence location and boundary layer remains thinner than the entropy layer. Hence, the fluid which has passed through the strongly curved portion of the bow shock remains at the edge of the boundary layer for radii higher than 'inversion radius'. Thus low Mach number and high temperature at the edge of the boundary layer are inevitable in these cases. Therefore a close examination of Mach number and temperature variations in the shock layer at different stream-wise locations for different bluntness can help to quantitatively predict the inversion radius. It is therefore easy to see that the inversion radius corresponds to the case where the hydrodynamic boundary layer coincides with HEL at the reference upstream influence location. Such description of the 'inversion radius' is helpful to qualitatively predict the same for given ramp angle, freestream conditions and wall conditions.

For any radius higher than the 'inversion radius', entropy layer remains thicker than the boundary layer at all the locations on the plate. Therefore, presence of non-uniform flow from the HEL at the edge of the boundary layer acts as source of vorticity by the virtue of an entropy gradient in accordance with Crocco's theorem. Same sense or direction of the inviscid vorticity in the HEL and the boundary layer based vorticity manage to let the HEL act as the source. Thus the vortical action in the HEL provides additional resistance to the boundary layer against separation which helps to reduce the separation size. However sufficient thickness of the HEL is required above the boundary layer edge to delay the separation to the extent where separation bubble size decreases in comparison with the reference separation bubble size. Therefore the relative thicknesses of the boundary layer and the entropy layer provide a predictive tool to determine the 'inversion radius' for given geometry and freestream conditions while hinting at the existence of an 'equivalent radius'.

7.6 Prediction methodology for "equivalent radius"

Increase in leading edge radius beyond the 'inversion radius' continues to reduce the separation bubble size and at 'equivalent radius' the separation zone size becomes equal to that of the

reference. It had already been noticed that the pressure difference term from equation (7.2) is responsible for the reduction in size of the separation zone. Essentially, increase in leading edge radius increases the pressure at all locations upstream of the compression corner which includes the upstream influence location as well (figure 7.9). In addition to this, the reattachment pressure increases initially with increase in radius till 'inversion radius' and decreases beyond it (figure 7.19). Such counteracting changes in the incipient and reattachment pressures decrease the governing adverse pressure gradient which in turn reduce the length of separation zone after 'inversion radius'. It can also be noticed from figure 7.18 that, there is negligible increase in maximum temperature within the thermal boundary layer as the radius increases beyond the 'inversion radius'. This effect dampens the process of boundary layer thickening with increase in leading edge bluntness. Thus the changes in governing pressure difference and maximum temperature in boundary layer help to justify the relative decrements in separation zone length. But they do not suffice to construct a robust prediction methodology for the'equivalent radius'. Hence underlying flow physics needs to be inspected to develop the prediction methodology for the second critical radius.

Investigations carried out by Holden[8, 42] for SWBLI concluded with discriminating the effect of leading edge bluntness as being "displacement dominated" and 'bluntness dominated'. In view of these terminologies, wall pressure for the reference case is plotted along with the Blast wave theory (BWT) based wall pressure for various leading edge radii [106] in figure 7.25. The over pressure region or upstream favorable pressure region, seen in this figure for sharp leading edge plate, is the above mentioned 'displacement effect' in the presence of strong viscous interaction. Blast wave theory renders similar pressure variation for blunted slabs which is termed as the 'bluntness effect'. Thus figure 7.25 describes the relative strength of displacement and bluntness effects for given freestream and geometric conditions. It is evident from this figure that, the upstream over pressure region given by BWT for leading edge bluntness case widens with increase in leading edge radius. For a particular radius this region extends till the reference upstream influence location.

Pressure variation, shown in figure 7.9, for the blunt leading edge configurations with viscous interaction, must be viewed as the integration of 'displacement' and 'bluntness' effects. Therefore

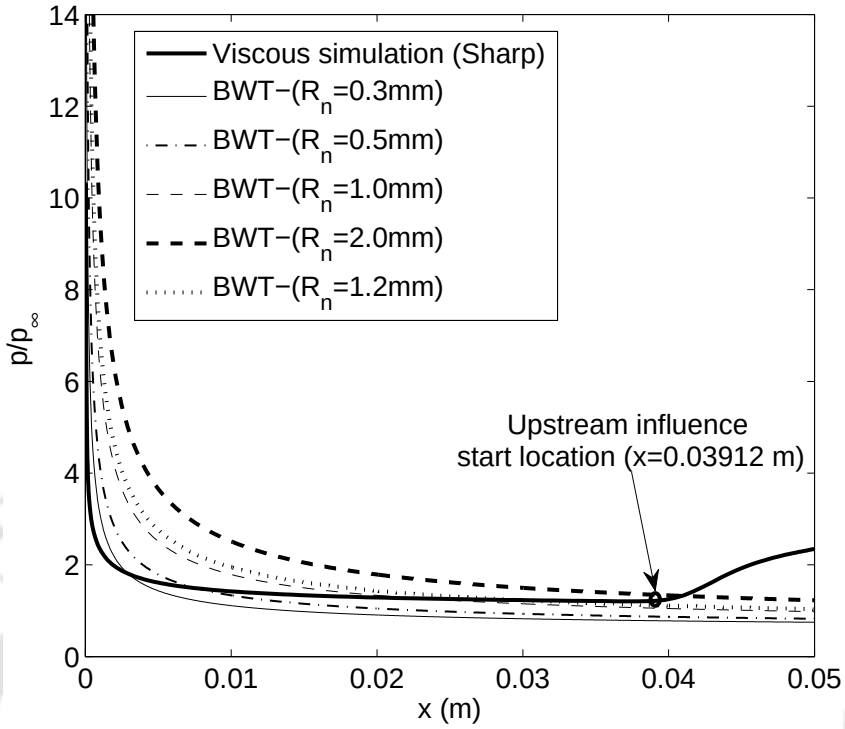

FIGURE 7.25: Comparison of bluntness and viscous interaction based over pressure regions

the integrated favorable pressure gradient tends to reduce the separation bubble size by delaying separation for all radii. However, it is conjectured that the 'entropy layer swallowing' effect counters this reduction till the inversion radius. Nonetheless, it is hypothesized that, for bluntness values greater than the inversion radius, the widened over pressure region in conjunction with the HEL above the boundary layer, decreased governing pressure difference and negligibly increased maximum temperature in the boundary layer provides an integrated effect to decrease the separation bubble size. The critical examination of the wall pressure variation shown in figure 7.9 indicates that the 'over pressure region' saturates well before the reference upstream influence location for sufficiently small radii. It is postulated that the smallest leading edge radius for which no such saturation of the over pressure is observed would correspond to the 'equivalent radius'. The 'equivalent radius' based on this postulate is predicted to be between 1 mm and 1.2 mm for present simulations from figure 7.9. This prediction is in excellent agreement with the numerical simulations shown in figure 7.13. Thus the wall pressure distribution offers a simple and elegant predictive strategy for prediction of the 'equivalent radius'.

7.7 Summary

Ramp induced shock wave and boundary layer interaction has been studied successfully using the in-house high resolution numerical solver. The effect of leading edge bluntness on separation bubble dynamics is investigated using various leading edge radii. Characteristic features of this interaction like boundary layer thickness or sonic height, boundary layer edge Mach number and temperature, entropy layer and pressure difference are evaluated in detail to understand their effect on the separation bubble size. The present studies indicate the existence of two critical radii namely 'inversion radius' and 'equivalent radius' associated with R-SWBLI. The sonic height, wall friction coefficient and boundary layer thickness attain an extremum at the 'inversion radius' which essentially corresponds to maximum separation bubble size. The existence of 'inversion radius' has been conclusively explained through the process of entropy layer swallowing upstream of the reference upstream location. Further increase in radius above the inversion radius has been found to reduce the separation zone size due to prominence of widened upstream over pressure region, presence of HEL above the boundary layer, reduction in downstream adverse pressure gradient and negligible increase in maximum boundary layer temperature. The separation bubble length is observed to decrease monotonically from its maximum at the 'inversion radius' and coincides with that of that of the reference test case at the 'equivalent radius'. The relative thicknesses of the entropy layer and hydrodynamic boundary layer provide a prediction strategy for the 'inversion radius' while the wall pressure distribution can be successfully employed to ascertain the 'equivalent radius' for given geometry and freestream conditions. Current studies indicate that the bluntness greater than 'equivalent radius' can provide 'sufficiently wide' over pressure region and therefore may be implemented to act as separation control mechanism.

Chapter 8

Effect of freestream and wall boundary conditions on critical radii of R-SWBLI

Overview

It has already been noticed that SWBLI changes in the presence of leading edge bluntness. All the characteristic features of this interaction like separation length, separation and reattachment locations, upstream influence etc. are dependent on the degree of bluntness. The major reason for this dependence is the change in upstream over pressure region and interaction of entropy layer with boundary layer with change in leading edge radius. Two critical radii have been observed for this interaction during the previous numerical studies. Freestream Mach number, wall temperature and freestream stagnation enthalpy are the governing parameters for those critical radii for given configuration. Therefore numerical simulations are carried out to understand the effect of these parameters on the magnitude of the critical radii. Entropy layer swallowing by boundary layer and extension of over pressure region are reconsidered for this evaluation. Present studies are found very useful in devising mechanism for estimation of critical radii and as well for incorporating the amendment in the same due to change in governing parameters.

8.1 Background

Considering the inevitable significance of SWBLI in hypersonic flow regime, a passive control technique of leading edge bluntness has been numerically investigated in previous chapter. It

has been observed that, for a given freestream condition, there exist two critical radii viz. inversion radius and equivalent radius. A leading edge radius of size smaller than inversion radius has shown to be offering counter effect of widening the separation zone. Moreover a leading edge radius of size above equivalent radius has been noticed to be reducing the separation zone size below the sharp leading edge case value. Hence it has been concluded that, leading edge bluntness of equivalent radius and above must be considered for the implementation of passive R-SWBLI control technique. In light of existence of two critical radii, it is interesting to investigate the alteration in numerical value of these critical radii at different freestream and wall conditions. Therefore computational investigations need further extension to quantify the change in leading edge bluntness with varying freestream and wall conditions.

8.2 Solver settings and freestream conditions

Simulations are performed for Marini's [23] experimental model with different levels of leading edge bluntness. All the leading edge radii considered in the previous chapter are employed in the present parametric study as well. The variants of freestream conditions considered in the present study are given in table 8.1. These simulations are carried out with higher order spatial accuracy and AUSM+ scheme based convective flux calculation. Steady state results are obtained through implicit time marching. Such implicit time marching has been started with initial CFL of 0.2 and further the CFL has been linearly ramped with iterations to accelerate the convergence. Perfect gas model along with constant value of Prandtl number and Sutherland's viscosity model has been considered to ensure the closdeness of governing equations.

Case	M_∞	Re_∞ m^{-1}	T_∞ K	p_∞ N/m^2	T_w K
1	6	8×10^5	131.7	199.4345	300,400,500
2	6	8×10^5	219.5	406.63	300,400,500
3	5	8×10^5	131.7	239.24	300
4	6	8×10^5	131.7	199.4345	300
5	7	8×10^5	131.7	170.885	300

TABLE 8.1: Freestream and boundary conditions of investigated cases

8.3 Results and discussions

The parametric influence of freestream stagnation enthalpy, wall temperature and freestream Mach number on various critical radii of R-SWBLI are discussed in the subsequent subsections.

8.3.1 Effect of freestream stagnation enthalpy

In order to investigate the influence freestream stagnation enthalpy on critical radii of R-SWBLI, two freestream total enthalpy conditions have been considered. A flowfield with freestream enthalpy corresponding to stagnation temperature of 1080 K, which is referred as low enthalpy conditions (Case 1), and an other flowfield of 1800 K total temperature, referred as high enthalpy condition (Case 2), are considered for this study. The simulations are carried out for all leading edge radii cases with these two freestream conditions. Earlier studies of R-SWBLI with sharp leading edge geometry have showed that, the separation bubble size and extent of upstream influence decrease with increase in freestream stagnation enthalpy. Therefore the objective of present study is to understand the effect of same on separation bubble dynamics for blunt leading edge geometry. It has been observed that, the presence of leading edge bluntness offers increased boundary layer edge static enthalpy for a given freestream total enthalpy. Hence it is interesting to study the combined effect of freestream total enthalpy and leading edge bluntness on downstream R-SWBLI.

The Mach contours of 0.5 mm blunt leading edge domain obtained with two freestream stagnation enthalpies of present considerations are compared in figure 8.1. This figure shows that, the separation zone is wider for low enthalpy freestream as compared to high enthalpy case. This again points towards the observation that has been made with sharp leading edge case. Higher freestream enthalpy seems to be offering more stability to the boundary layer, thus delaying the separation. Figure 8.2 shows normal variation of various flow properties at representative locations for better understanding of separation dynamics in case of 0.5 mm leading edge bluntness. Sharp leading edge case profiles are also been analyzed in figure 8.2 to explore the relative effect of freestream enthalpy on blunt and sharp geometries. All these profile comparisons are performed for a location of 32 mm away from the leading edge, which is the most upstream location of undisturbed boundary layer for all radii of present consideration.

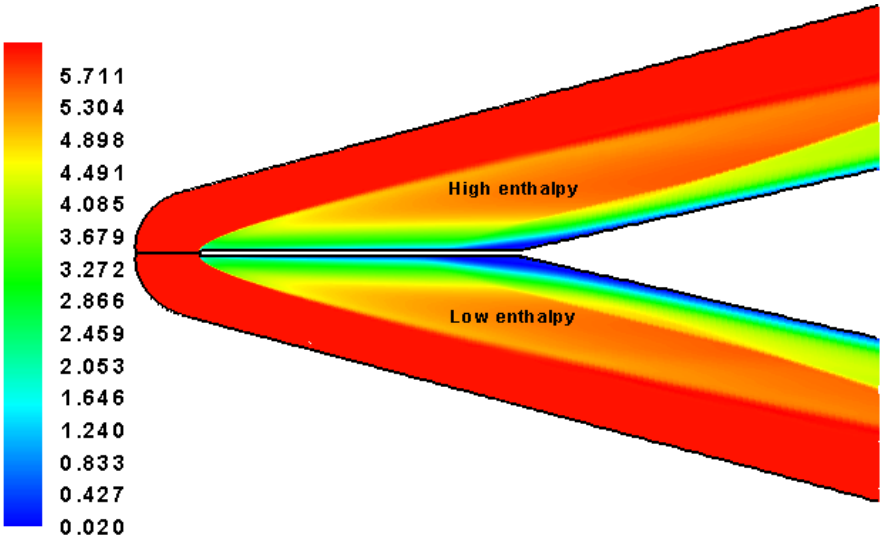

FIGURE 8.1: Comparison of Mach contours 0.5 mm leading edge case for different freestream total enthalpies

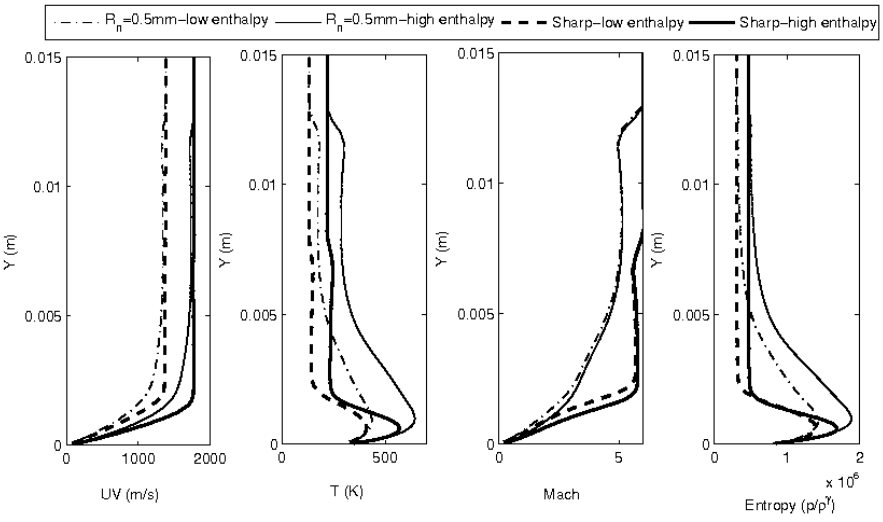

FIGURE 8.2: Comparison of boundary layer profiles for different freestream total enthalpies

The boundary layer profile comparison clearly demonstrates the influence of freestream stagnation enthalpy on both hydrodynamic and thermal boundary layer. The streamwise velocity profiles give qualitative picture of the boundary layer thickness obtained with different stagnation enthalpies. It is very much clear from the velocity and temperature profiles that, thickness of thermal and hydrodynamic boundary layers decrease with increase in stagnation enthalpy for sharp leading edge case. Besides, the temperature values of both inside and outside the boundary layer are observed to be higher for high enthalpy flowfield as compared to low enthalpy flow. Interestingly, maximum temperature in the thermal boundary layer for blunted geometries

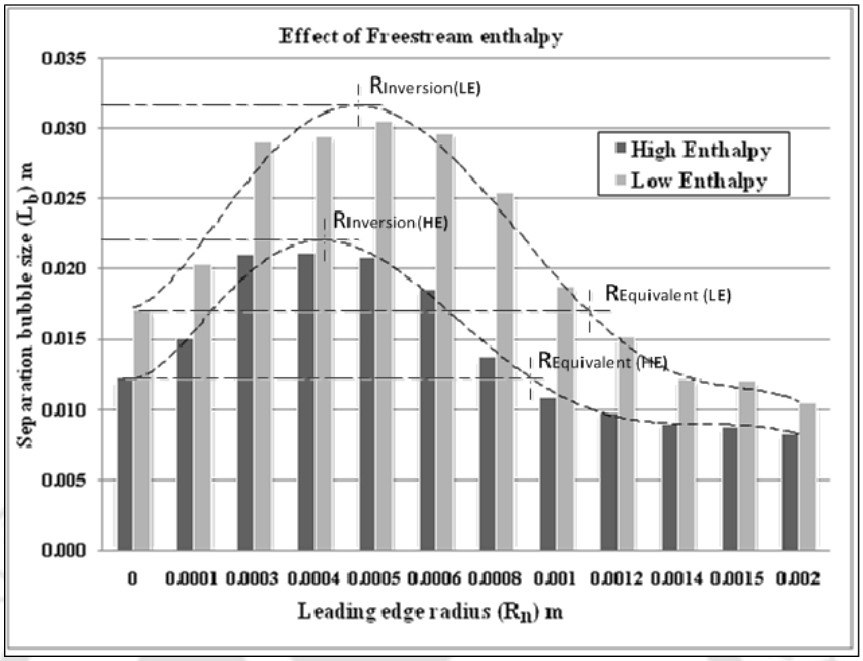

FIGURE 8.3: Effect of freestream total enthalpy on critical radii of R-SWBLI

is higher in comparison with sharp leading edge case for both enthalpies. This difference in maximum temperature of sharp and blunt leading edge cases is more prominent in case of high enthalpy flowfield. The Mach number profile comparison for sharp and bluntness cases clearly displays the significant reduction of inside and edge Mach numbers of the boundary layer with leading edge bluntness. This decrease in Mach number is mainly due to increase in static temperature owing to blunt leading edge. However no significant difference in the Mach profiles of low and high enthalpy flowfields has been noticed in either cases, being same freestream Mach number in both the flowfields. The bluntness based temperature boost also leads to reduction in boundary layer density. In the presence of such low density fluid particles, the boundary layer thickens and separates early.

Separation bubble size obtained for different leading edge radii for two enthalpy conditions are plotted against leading edge radius in figure 8.3. As it has been mentioned earlier, the separation zone widening can be noticed from this figure as well for all the leading edge radii cases with reduction in freestream stagnation enthalpy. Moreover the difference between the separation bubble sizes of higher and lower enthalpy flowfields is observed to be increasing with increase in leading edge radius till a radius just higher than the inversion radius. Beyond

this radius margin, the separation zone sizes of high and low enthalpy flowfield are seen to be approaching close to each other. This observation is more prominent beyond the equivalent radius zone. Interestingly the inversion and equivalent radii are also noticed to be different for two enthalpy cases. The inversion radius for high enthalpy flowfield can be seen to be lower as compared to that of low enthalpy flowfield. The equivalent radius also found to be increased to higher value with reduction in freestream stagnation enthalpy. This observation can again be correlated to boundary layer entropy layer interaction. Since both the freestream have same Mach number, the entropy layer generated for a given degree of bluntness will have almost same structure and size for any stagnation enthalpy. However the boundary layer size at all locations of the forward flat plate is higher for low enthalpy flowstream as compared to high enthalpy. Hence complete swallowing of the entropy layer by the boundary layer would happen with slightly higher leading edge bluntness for lower freestream enthalpy case. This is the reason for the delayed reach of inversion radius in case of low enthalpy freestream. Hence on the same line, equivalent radius also increases in magnitude with decrease in stagnation enthalpy. Therefore increase in freestream total enthalpy effect can be summarized as the lowering of both inversion and equivalent radii for a given flowfield of constant Mach number and for a given flow deflection angle. Therefore the magnitude of leading edge bluntness required for the successful implementation of this passive technique as a R-SWBLI control method reduces with increase in freestream stagnation enthalpy.

8.3.2 Effect of wall temperature

This section deals with the effect of wall temperature on the R-SWBLI in the presence of leading edge bluntness. For this study the wall temperature has been varied from 300-500 K in an interval of 100 K. These wall temperature variation cases have been considered for both the freestream stagnation enthalpy conditions considered in the previous section. The parametric studies of wall temperature effect on R-SWBLI on a sharp leading edge geometry have shown that, the intensity of SWBLI, size of separation zone and upstream influence extent increase with increase in wall temperature. Hence the objective of present study is to understand the wall temperature effect on the R-SWBLI on flat plate-ramp model with non-zero leading edge radius. The flowfied for all the leading edge radii domains have shown the local separation at

the ramp foot region. Separation bubble size obtained from the skin friction distributions of different leading edge radii domains are employed in this study to quantitatively assess the wall temperature effect on R-SWBLIs. The separation and reattachment points of each leading edge radius cases are initially identified from the corresponding skin friction coefficient distributions. Such identified separation and reattachment locations for few selected leading edge cases are compared in figure 8.4. Almost linear shift in both separation and reattachment locations with increase in wall temperature can be seen in this figure. Moreover the separation and reattachment locations are observed to be departing with initial increment in leading edge radius till the first critical radius (inversion radius). Further increase of leading edge radius beyond inversion radius has shown to be allowing these two points to come closer for all wall temperature cases. This in turn leads to separation zone reduction for those leading edge domains. It can be clearly noticed from the comparison of separation bubble sizes plotted against leading edge radius for three wall temperatures in figure 8.5. These comparisons are carried out for high enthalpy flowfield, however the effects are qualitatively same although prominent for low enthalpy flowfield. In figure 8.4, the separation point is observed to be extending beyond the sharp case value at around leading edge radius of 1.2 mm for all wall temperature cases. Where as the upstream shift of reattachment point ahead of the reference sharp case value is obtained for 1.2 mm blunt leading edge domain only when the wall temperature is 300 K. At higher wall temperatures the reattachment points of this domain is still downstream of the reference value. Thus the inversion and equivalent radii increase with increase in wall temperature as displayed in figure 8.5.

The discussed flowfield differences and disparities in critical radii for different wall temperatures can be well understood from boundary layer profiles given in figure 8.6. Here in this figure increase in both hydrodynamic and thermal boundary layer thickness can be noticed with elevation in wall temperature. Such qualitative observation of boundary layer thickness enhancement can again be correlated to boundary layer-entropy layer interaction phenomenon. For a given radius and freestream conditions, the shock layer developed for all the wall temperatures have almost same magnitude. Although the boundary layer contributions of shock layer displacement is present, its effect is not much significant with wall temperature enhancement. Hence the shock structure and higher entropy layer size remain almost same for these wall temperature

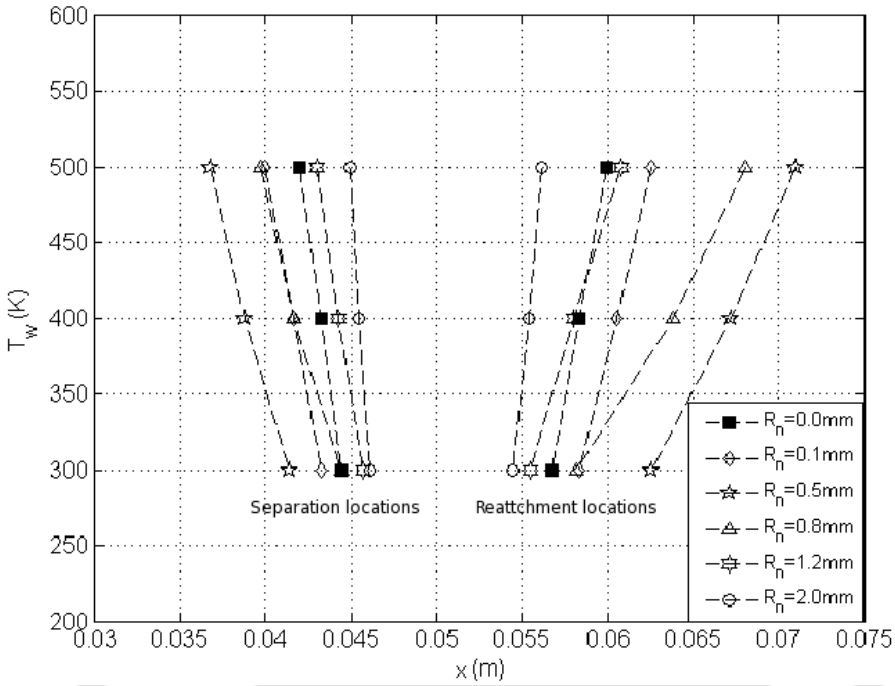

FIGURE 8.4: Comparison of separation and reattachment points under different wall temperature conditions

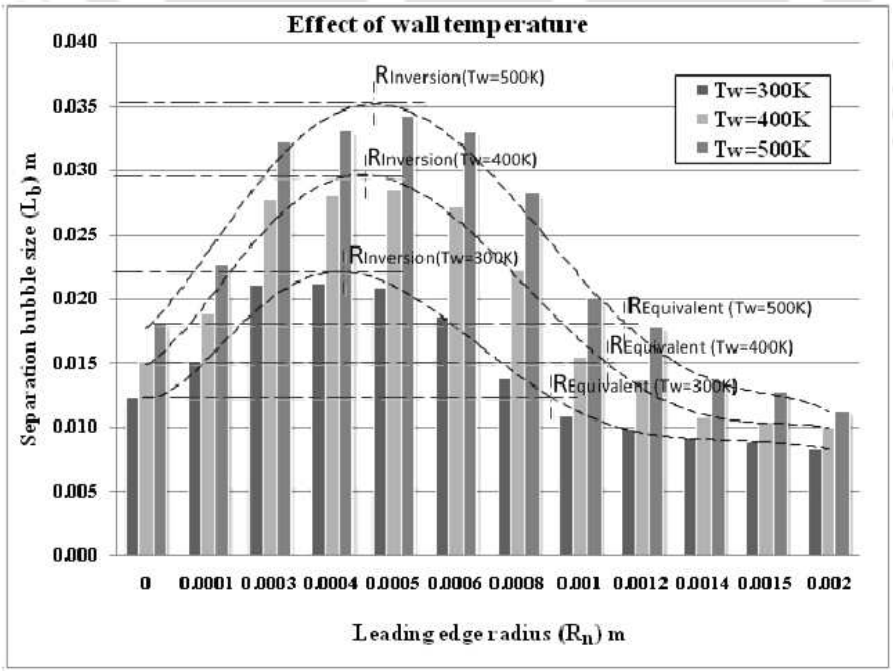

FIGURE 8.5: Effect of wall temperature on critical radii of R-SWBLI

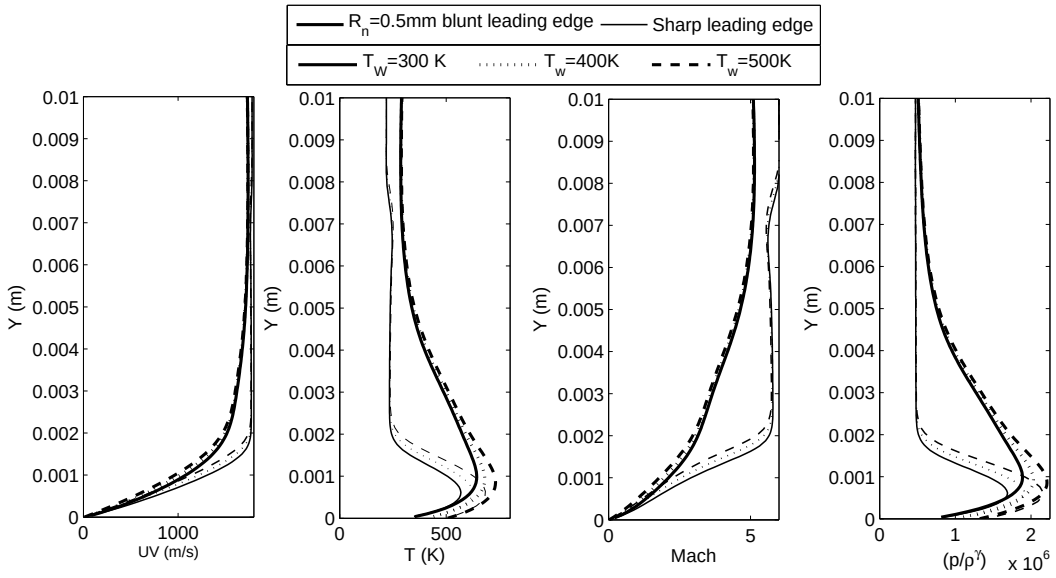

FIGURE 8.6: Comparison of boundary layer profiles of different wall temperature cases

cases. This can be qualitatively read from entropy profiles given in figure 8.6. Therefore in the presence of nearly constant entropy layer, the case having higher boundary layer thickness will swallow more entropy layer as compared to low boundary layer thickness case. For this reason the inversion and equivalent radii are seen to be increasing with increase in wall temperature.

Investigations about the combined effect of wall temperature and stagnation temperature on R-SWBLI based flow separation is also carried out. The parametric studies of freestream enthalpy together with wall temperature for sharp leading edge domains have showed that the wall to freestream total temperature ratio can be treated as a R-SWBLI governing parameter, rather than considering those parameters separately. It has also been observed that the flow structure is same for two freestream conditions upon maintaining a constant T_w/T_0. This flowfield equivalency has been observed for sharp leading edge domain with the combination of high enthalpy flowfield and 500 K wall teperature and low enthalpy freestream with 300 K wall temperature. For these two flowfields the separation bubble size was observed to be very close for sharp leading edge case. Therefore it is interested to seek the possibility of existence of same flowfield equivalence in case of blunt leading edge domains. Therefore, in view of this, all leading edge radii with different freestream enthalpies and three wall temperatures are considered to evaluate the equivalence. The combination of above discussed freestream total enthalpies and wall temperatures give five different wall to total temperature ratios (T_w/T_0), that range from 0.1667 to

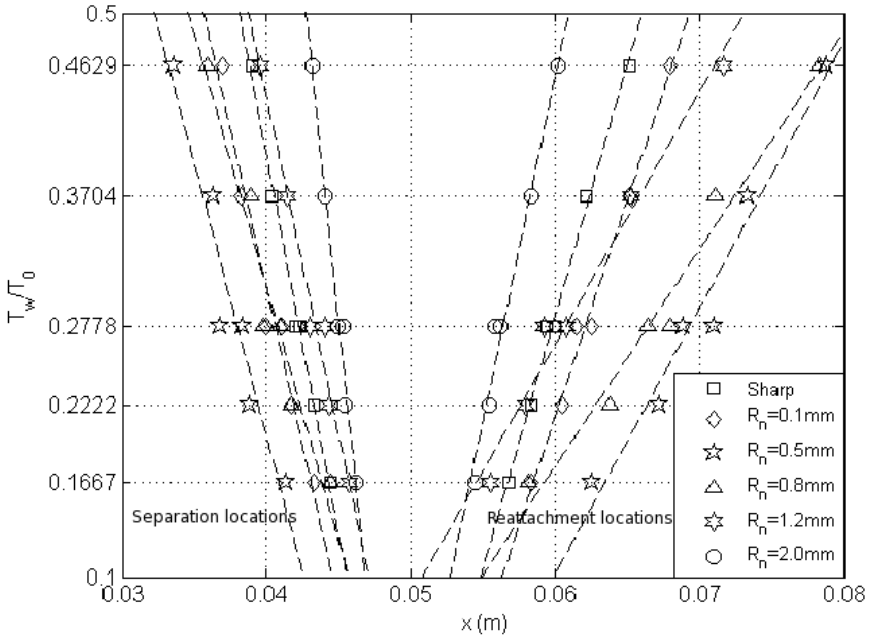

FIGURE 8.7: Comparison of separation and reattachment points under different wall to freestream total temperature ratios

0.462. Simulations are carried out for all these conditions. Separation and reattachment points of few selected leading edge domains are compared in figure 8.7. A nearly linear variation in both separation and reattachment points can be noticed for all the blunt leading radii with increase in T_w/T_0. Moreover the trend lines show continuous upstream shift of separation point while the reattachment point shifts downstream with the initial increment in leading edge radius. However this trend reverses beyond some leading edge radii for all T_w/T_0. The point of reversal depends on the inversion radius of corresponding cases. It can be inferred from this figure that both inversion and equivalent radii shift to higher values with increase in wall to freestream total temperature ratio.

The high enthalpy freestream with wall temperature of 500 K and low enthalpy stream with wall temperature of 300 K result in same T_w/T_0 of 0.2778. Hence the separation bubble sizes obtained with these two cases for all leading edge radii cases are compared in figure 8.8. In this figure the separation bubble size of sharp leading edge domain can be observed as very close for both the flow situations. However as the degree of bluntness increases the separation bubble size of high enthalpy-high wall temperature case over shoots the bubble size of low enthalpy low wall temperature case till inversion radius and onwards decreases. The magnitudes

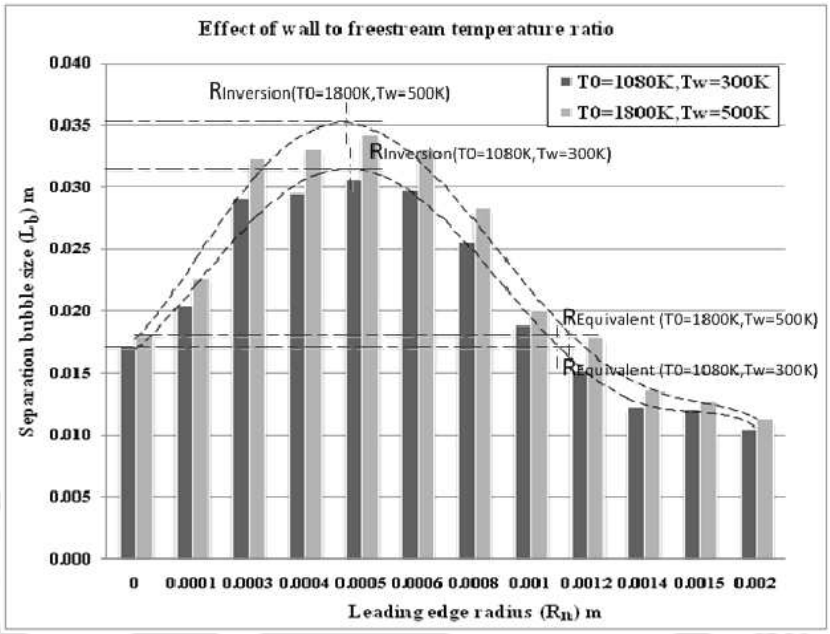

FIGURE 8.8: Effect of wall to freestream total temperature ratio on critical radii of R-SWBLI

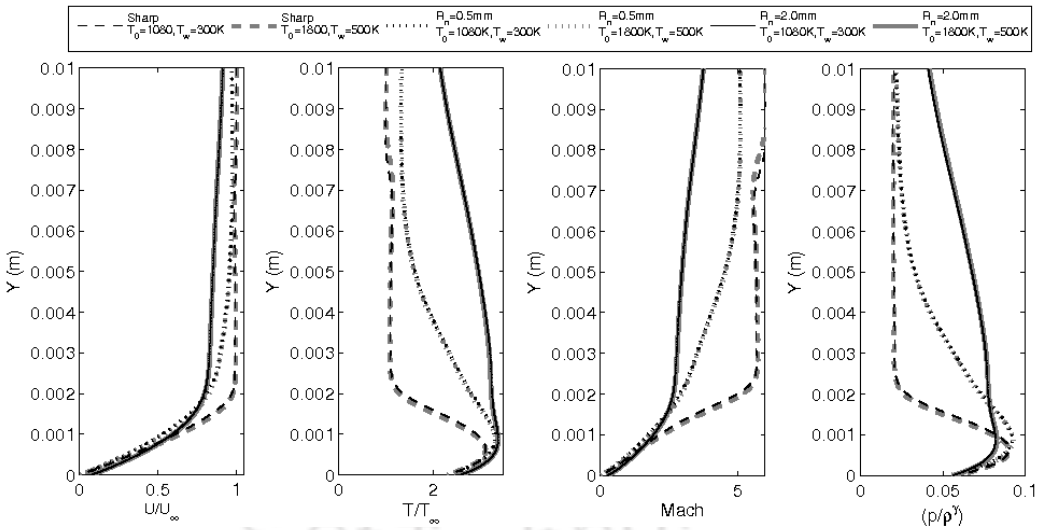

FIGURE 8.9: Comparison of non-dimensional boundary layer profiles of same wall to total temperature ratio cases

of separation bubble sizes observed to be closer for radii above equivalent radius. Therefore it can be summarized from these observations that, the wall temperature effect is more prominent close to the inversion radius, whereas the T_w/T_0 ratio is important for very small and very large leading edge bluntness cases.

Boundary layer profiles of two conditions specified above are analyzed using figure 8.9 for few selected leading edge domains. Interestingly it is observed that the non-dimensional distributions in normal direction at a location 32 mm away from the leading edge are almost same for both this flowfields. This fact points towards the nearly equal nature of boundary layer thickness for blunt and sharp cases. The non-dimensional entropy distribution trend is also the same for both the flowfields at this location. Therefore the reason behind the deviation of separation bubble sizes at inversion radius regime can be attributed to the relative difference in absolute magnitude of entropy swallowed by the boundary layer. Therefore, though both the cases expected to be dealing with same thickness of entropy layer at a given location of boundary layer for a given leading radius, the absolute values of entropy and temperature of swallowed portion of entropy layers are different. Swallowed entropy layer is thus intense for high enthalpy stream. This can be the possible reason for lose of flowfield equivalence at moderate leading edge radii.

8.4 Effect of freestream Mach number

Influence of freestream Mach number on R-SWBLI in the presence of leading edge bluntness are discussed in this section. Investigations about Mach number influence on R-SWBLI for sharp case revealed that separation zone widens with decrease in freestream Mach number. This inverse proportionality of Mach number with separation bubble size has been explained in terms of reduced flowfield inertia. Since low Mach number flow holds low inertia, it separates early as compared to high Mach number flow due to combined effect of adverse pressure gradient and wall friction near the ramp foot. This reasoning was found appropriate for very low streamwise pressure gradient flow (sharp leading edge case). But presence of leading edge offers significant favorable pressure gradient to boundary layer developing over the forward flat plate section, which in turn gives additional stability to the boundary layer. Hence relevance of the earlier proposed reasoning for the blunt leading edge case is the subject of investigation of this section. In view of this, freestream Mach number of 5, 6 and 7 are considered for this study. The remaining freestream properties corresponding to each of these Mach numbers are given in table 8.1. Simulations are carried out for all those conditions employing all the radii mentioned earlier. The steady state results analysed in terms of skin friction distribution proved that the flow separation

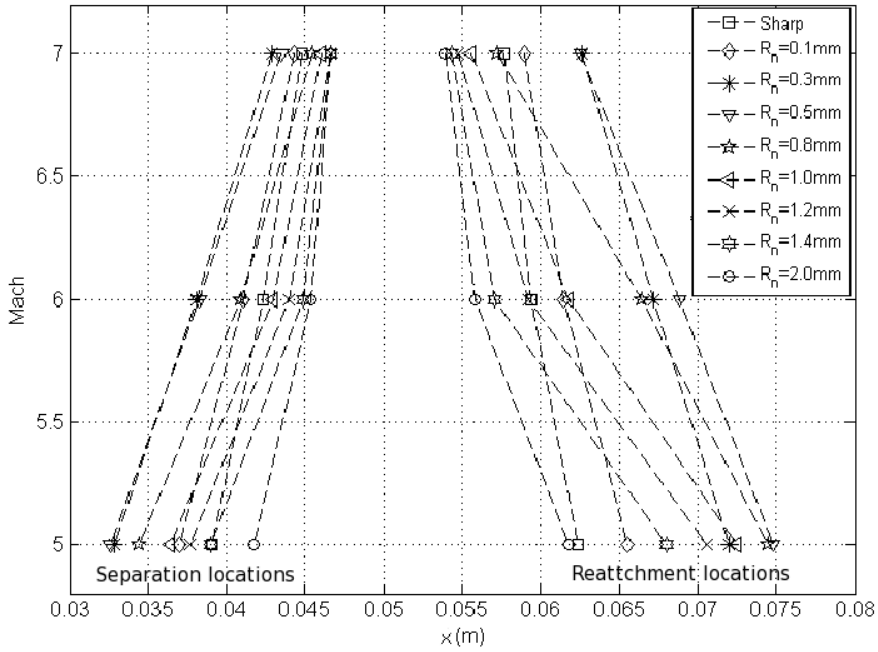

FIGURE 8.10: Comparison of separation and reattachment points under different freestream Mach numbers

presents in all the conditions considered in this study. Further the separation and reattachment points are noted from the skin friction coefficient distributions to quantify the size of separation zones. Thus obtained separation and reattachment locations are compared for few selected leading edge domains in figure 8.10. A nearly linear upstream shift of separation point for a given leading edge case with decrease in freestream Mach number is observed for small leading edge domains. However separation point starts shifting downstream with further increase in leading edge bluntness. Moreover for those leading edge radii the linearity of separation location with Mach number also deteriorates. Apart from this only few domains are showing upstream shift of separation location with reference to separation point of sharp case for Mach 7 flowfield. Similarly the downstream movement of reattachment point from the reference sharp case is also seen to be restricted to very limited number of small leading edge domains for Mach 7 flow. However such cases are more in numbers for Mach 5 and 6 freestreams. This figure hints for the variation of inversion radius with variation in freestream Mach number.

Separation bubble sizes of all blunt domains are further analyzed in figure 8.11 for all three freestream Mach numbers. This separation bubble size comparison provides better insight to the effect of freestream Mach number on R-SWBLI based flow separation of blunt domains. As the

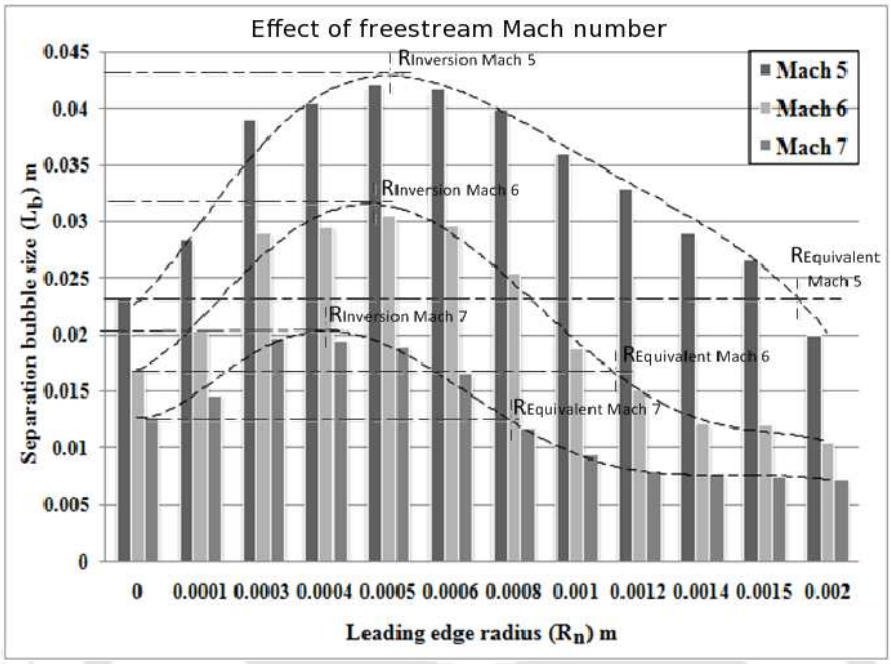

FIGURE 8.11: Effect of freestream Mach number on critical radii of R-SWBLI

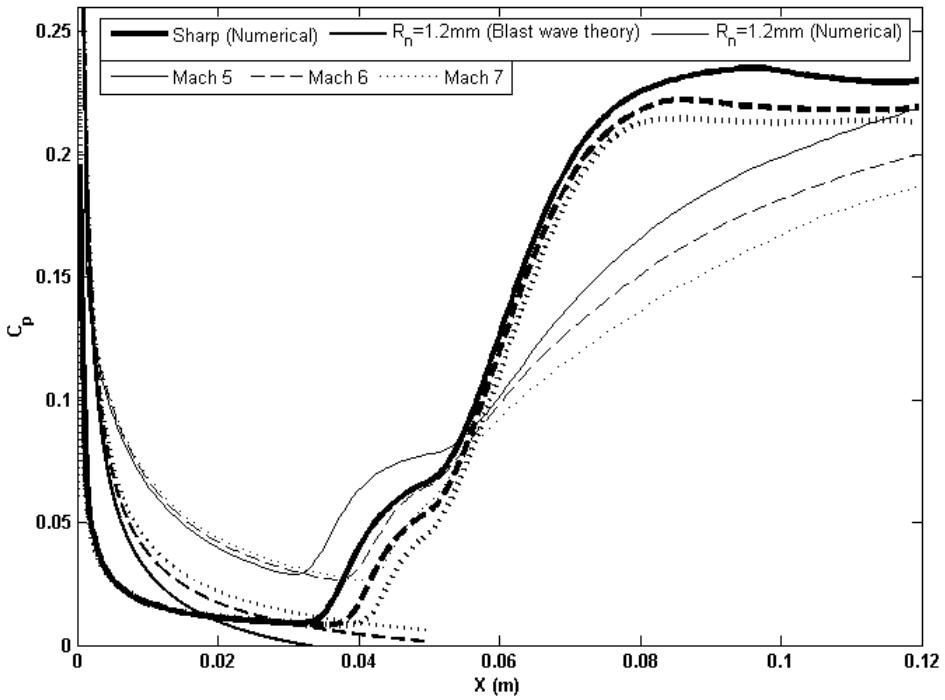

FIGURE 8.12: Comparison of surface pressure distributions to show the effect of freestream Mach number

consequence of above discussed separation and reattachment points shift, the separation bubble size is seen to follow the same trend of initial increase followed by trend reversal and subsequent reduction for all Mach number cases. However the point of trend reversal can observed to be increasing with reduction in freestream Mach number. Magnitude of trend reversal radius (inversion radius) can again be correlated to distinct boundary layer-entropy layer interactions for different freestream Mach number cases. For a given leading edge radius of magnitude less than that of the minimum inversion radius of all these Mach numbers, upstream swallowing of the high entropy layer can be expected for low Mach number stream. Hence requirement of leading edge bluntness for covering the boundary layer with entropy layer increases with decrease in Mach number. This is the reason for inversion radius increment with decrease in freestream Mach number. Nevertheless the increment of equivalent radius with decrease in Mach number is more significant than the same of inversion radius in figure 8.11. The difference between the equivalent radii of two consecutive Mach nuber streams are higher than the difference between the inversion radii of same streams. This prominent nature of equivalent radius enhancement with reduction in freestream Mach number can be explained in terms of surface pressure distributions. Hence, to facilitate that discussion, surface pressure distributions of few selected cases are given in figure 8.12. In this figure, the surface pressure coefficient distributions of sharp leading edge domain is compared with that obtained for 1.2 mm leading edge blunt domain through both numerical simulation and blast wave theory (BWT) [106]. These comparisons are carried out for all three Mach numbers considered in the present study. The reason for the selection of 1.2 mm radius is its closeness towards equivalent radius of all three Mach cases. Here in this figure, the pressure distributions corresponding to blast wave theory are the representatives of bluntness based pressure distributions in the absence of viscous effects. Therefore BWT gives a qualitative measure of bluntness contribution to upstream over pressure region. The numerically obtained pressure distributions of 1.2 mm blunt case represents the combined effect of bluntness and viscous displacement. It can be seen from the figure that the bluntness based over pressure region of BWT is failed to reach the sharp case interaction location for Mach 5 flowfield. However the extension of this over pressure region can be observed to be approaching the basic interaction location with increase in Mach number. For Mach number 7 case, the over pressure region extension is well beyond the basic interaction location. Such extension of over pressure

region gives more stability to the flowfield, which in turn leads to reduction of separation bubble below sharp case value. This is the reason for smaller value of equivalent radius for Mach number 7 flowfield as compared to lower Mach streams. Hence magnitude of critical radii decrease with increase in freestream Mach number.

8.5 Summary

Parametric influences of freestream Mach number, freestream enthalpy and wall temperatures on R-SWBLIs of 15^0 compression ramp model with different degree of leading edge bluntness are studied in this chapter. It is observed that the intensity of R-SWBLI based flow separation increases with increase in wall temperature and decrease in freestream Mach number for all the leading edge radii. Whereas the increase in freestream enthalpy is shown to be delaying the flow separation in all cases. The critical radii of R-SWBLI are observed to be increasing with decrease in freestream Mach number and total enthalpy. However magnitude of critical radii enhancement is noted with increase in wall temperature. Flowfield equivalence is observed for very small and large leading edge radii for two total enthalpy streams, upon maintaining constant T_w/T_0. However this flowfield equivalence is seen to decay for moderate leading edge radii domains. Disparity in entropy layer swallowing and associated upstream boundary layer alterations along with difference in over pressure extensions are identified as the reason for deviation of critical radii for different flow and wall conditions.

Chapter 9

Dimensionality effect on laminar shock wave boundary layer interaction at hypersonic Mach number

Overview

Present investigations focus on the effect of leading edge bluntness on shock wave boundary layer interaction for double cone and double wedge configurations. The concept of leading edge bluntness for controlling the consequences of shock wave boundary layer interactions are visited numerically using second order accurate, finite-volume based 2D-axisymmetric compressible flow solver. This study seeks the differences in the flow physics of SWBLI in case of two dimensional and axisymmetric flowfields which asserts for dimensionality effect on this commonly pursued control technique. In view of this, influence of leading edge bluntness on two SWBLI parameters viz. separation bubble size and surface heatflux distribution have been investigated in this chapter. For the range of radii considered for present studies, it has observed that, the implementation of leading edge bluntness can offer reduction in separation bubble size in comparison with the base case of sharp leading edge case for 2D flowfield beyond a critical value. However enhanced separation zone size has been noticed for axisymmetric flowfields for all radii. Thicker entropy layer and stronger favorable pressure gradient have been accredited for the possibility of separation control in case of 2D flowfields. Further, thin entropy layer due to three dimensional relieving effect and it's swallowing by the boundary layer is attributed for consistently higher separation bubble size in comparison with the base, for all radii, in case of

axisymmetric simulations. The critical radius for trend reversal ('inversion radius') has been observed to be 1 mm for 2D flowfield, whereas, the same for axisymmetric flowfield is observed in between 4 and 5 mm. The 'equivalent radius,' which is the limiting bluntness value beyond which separation bubble size reduces bellow sharp leading edge case is seen to be close to 4 mm for 2D flowfield. However with in the range of present investigated leading edge radii, equivalent radius has not been observed for axisymmetric flowfield. These observations of critical radii have been made for a freestream Mach number of 6. Hence the present analysis about interaction of entropy layer and hydrodynamic boundary layer disproves the leading edge bluntness as the separation control techniques for axisymmetric flowfields which would demand for larger bluntness values. Apart from this, changes in thermal boundary layer in the presence of leading edge bluntness have altered the wall heatflux distribution. Monotonic decrement in local heat flux has been noticed for axisymmetric case while trend inversion has been detected for 2D case with increase in leading edge bluntness. Thus present studies demand for closer inspection of field and surface properties in the presence of leading edge bluntness when implemented for separation control.

9.1 Background

Double cone or double wedge geometries are the commonly considered configurations for understanding SWBLI. Such simplified objects help in simulating and understanding the flow pattern around complex configurations like engine inlet, wing-body junction, control surfaces etc. Supersonic or hypersonic flow encounters adverse pressure gradient due to sudden turning around these compression corners or ramps. Such compression corner induced shock wave boundary layer interactions in 2D flowfields have been extensively studied in the previous chapters. The influence of freestream and geometric parametres on 2D ramp induced SWBLI are revealed through detailed numerical studies. Further studies of SWBLIs with leading edge bluntness showed that, it can be implemented as a passive separation control technique for R-SWBLI. Such studies [8, 15, 16, 17] about the effect of leading edge bluntness on shock wave boundary layer interactions are also available in the open literature. However, all of these reported studies have been conducted for two dimensional configurations. Consequently the study for three dimensional effect in the context of leading edge bluntness as a separation control technique needs

to be initiated. One of the earlier investigation dealing with SWBLI on axisymmetric geometry [15] reports that, the provision of leading edge bluntness always enhances the SWBLI based separation zone on axisymmetric geometries. This observation needs to be re-investigated to understand the disparity between 2D and axisymmetric flowfields. Therefore present research focuses on the investigation of both 2D and axisymmetric flowfields to understand the flowfield alterations in the presence of leading edge bluntness. Efforts are then extended initially to identify the critical radii for two dimensional and axisymmetric cases and onwards to understand the flow physics at those radii. The necessary computations are carried out using in-house CFD solver 'USHAS' for literature reported freestream conditions and geometry [27]. Details about the solver, test conditions and results are given in following sections.

9.2 Solver settings

All the simulations presented in this chapter are performed with higher order spatial accuracy. Among the different convective flux calculation methodologies of USHAS, the AUSM+ scheme has been considered for present studies due to its comparative advantages for high speed flow simulations. Implicit time marching strategy has been employed for all simulations. For all the simulations initial value of CFL is taken as 0.2, which is then linearly ramped with iterations. Air is assumed as perfect gas for all cases.

9.3 Results and discussion

9.3.1 Grid independence study

Solver assessment and grid independence study are initially performed for the test case of Mach 6 flow over a blunted cone-flare configuration at zero degree angle of incidence. Experimental results for this axisymmetric case are available in the open literature [27]. These experiments were carried out in H3 hypersonic wind tunnel of Von Karman Institute. The leading edge bluntness employed for the experimental test model is 3.5 mm. Therefore the same test model and freestream conditions of Mach 6, Reynolds number $8 \times 10^6\ m^{-1}$ and static temperature of

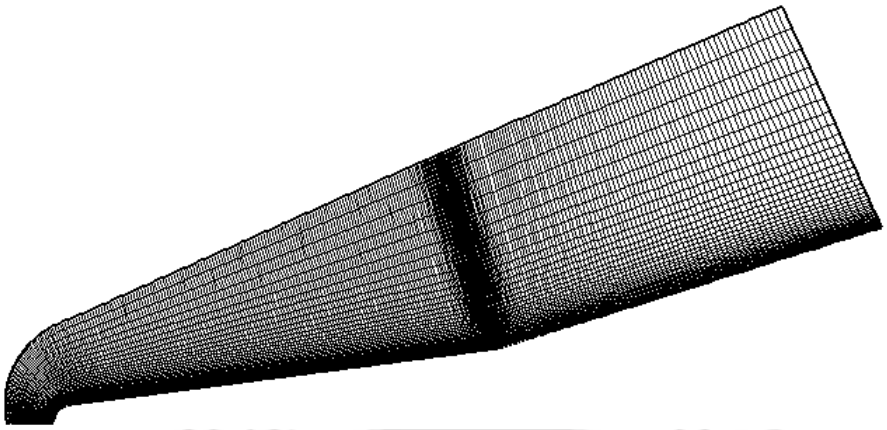

FIGURE 9.1: Grid used for the axisymmetric blunt cone-flare simulation

67.07 K are considered herein. Three meshes viz. 240×40, 480×80 and 600×100 are employed for the grid independence test. Typical mesh used in the present study is shown in figure 9.1. Only half portion of the model is considered for computations to account for the symmetricity of the model about its axis.

Comparison of the experimentally measured surface pressure and wall heat transfer rate with various mesh levels are shown in figure 9.2(a) and figure 9.2(b) respectively. Encouraging match among the experimental and simulated results is evident from this figure for the mesh size of 480×80 and onwards. Hence the basic features of the interaction like upstream influence location, separation point and reattachment point are seen to be correctly captured for the hypersonic flow over blunted cone-flare configuration. Separation bubble size of $L_b = 26.3$ mm, obtained for 480×80 mesh, is in very close agreement with the reported experimental results. Therefore the strategy followed for this mesh can be adopted for subsequent studies. Hence the present study has proved the capability of USHAS for simulating hypersonic shock wave boundary layer interaction in case of axisymmetric configurations. Therefore the same solver settings are used for subsequent investigations.

9.3.2 Flowfield around the sharp leading edge 2D and axisymmetric configurations

The validated solver is then used to investigate the flowfield around the earlier considered test model without bluntness. Hypersonic flow over such sharp geometry has been simulated for the

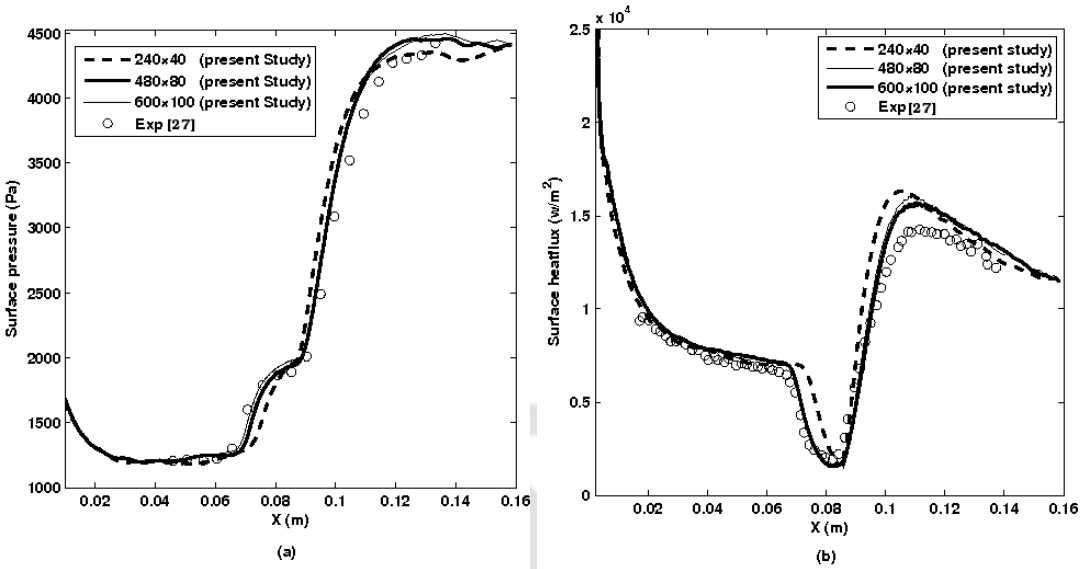

FIGURE 9.2: (a)Surface pressure comparison of hypersonic flow over axisymmetric blunt cone-flare (b) Heatflux comparison of hypersonic flow over axisymmetric blunt cone-flare

same freestream conditions as considered in validation studies. Here the same configuration has been simulated with two dimensional formulation along with axisymmetric one to understand the dimensionality effect on the basic SWBLI parameters without leading edge bluntness.

Typical Mach number contours, for the both the cases, are shown in figure 9.3. This figure clearly segregates the flowfield in three distinct zones viz. pre-separation, separation and post re-attachment. The Mach contour comparison primarily shows the lower first-cone shock angle for axisymmetric case which led to thin shock layer in comparison with the same for 2D case. The three dimensional relieving effect is the reason for this disparity. Therefore the axisymmetric flow experiences lesser deceleration in the pre-separation region across the standing shock as compared to the 2D planar flowfield. Hence the approach Mach number for second compression surface is more in case of axisymmetric double cone model as compared to the double ramp model. Such high speed flow extends the pre-separation zone by downstream shift of upstream influence start location where SWBLI is first experienced. The upstream influence start location is noticed to be 75.4 mm from the leading edge for axisymmetric case while the same is 54 mm from the leading edge for 2D case.

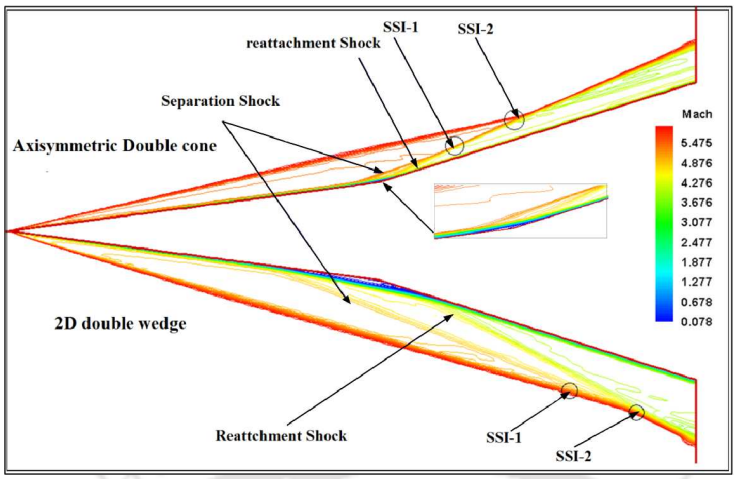

FIGURE 9.3: Comparison of Mach contours of double cone and double ramp with sharp leading edge

Extended pre-separation zone is the sign of decrease in strength of interaction for axisymmetric flow. Separation bubble size of 7.3 mm for axisymmetric case and 40 mm for 2D case reconfirm this observation. Hence the separation zone size is smaller for axisymmetric case for the same freestream and wall conditions. In addition to this, Mach contours also show two triple points in the presence of interaction of shocks in both 2D and axisymmetric cases. The location of these two 'Shock-Shock Interaction (SSI)' points is vital for the flow behavior and wall properties in the post reattachment zone. Out of the two points for axi-symmetric flow, first one (SSI-1) is formed due to the interaction of separation and reattachment shocks, whereas the second one (SSI-2) is formed due to the interaction of shock originated from SSI-1 and the first standing shock. Unlike axisymmetric case, both the SSI points in the 2D flowfield involve the first standing shock. Therefore the flow approaching the second compression surface in either case passes through shocks of different strengths which would lead to dissimilar flowfields and wall properties in post-reattachment zone for the same freestream and wall conditions.

9.3.3 Flowfield around the blunt leading edge 2D and axisymmetric configurations

The same basic geometry is considered herein with leading edge bluntness to understand its effect on SWBLI for 2D and axisymmetric flowfields. Leading edge radii, considered for present studies vary from 0.0 mm (sharp) to 10 mm. Such leading edge bluntness has been introduced for the given test model by keeping same lengths and angles of the compression

surfaces by varying base diameters. The computational domains considered for each of these bluntness radii are meshed in the similar manner as discussed in the validation studies. Hence such mesh independent results are considered for subsequent discussion of SWBLI. The same computational domain is used for both 2D and axisymmetric simulations in case of each leading edge radius.

Mach number contours for two representative leading edge radii, demonstrating the leading edge bluntness effect for 2D and axisymmetric configurations are as shown in figure 9.4. These contours provide better insight about the near wall and far field variations in the computational domain. It had been already noticed that the separation and reattachment shocks interact with first ramp shock separately for sharp leading edge double wedge model in figure 9.3. However for the double wedge model with 1 mm leading edge radius (figure 9.4), the reattachment shock doses not interact with any of the shocks in the domain. Similar situation has been noticed for both separation and reattachment shocks for 2 mm leading edge radius. In case of further increment of leading edge radius to 4 mm and above, the boundary layer edge Mach number decreases to very low supersonic values, thereby the separation and reattachment shocks become weak. Therefore the interaction of these shocks loses its prominence. Apart from the shock-shock interactions, Mach contours of 1 mm leading edge also shows widened separation zone for 2D domain in comparison with the basic sharp leading edge configuration (figure 9.4). However the provision of a higher leading edge radius of 4 mm is seen to be reducing the separation bubble size below the reference sharp leading edge case.

The separation and reattachment shock interactions are clearly present in case of all blunt radii for axisymmetric computations. Mach contours of 1 mm and 4 mm leading edge radii for double cone models as given in figure 9.4 provide evidence of the same. For smaller radii cases both SSI-1 and SSI-2 are well within the computational domain. Therefore their effects would be reflected on the second compression surface. However at higher leading edge radii, the second interaction point may not exist within the present computational domain. This can be inferred from Mach contours for 4 mm blunt double cone model, where the SSI-2 is seen to be occurring very close to the outlet boundary of the flow domain. The major reason for such situation is

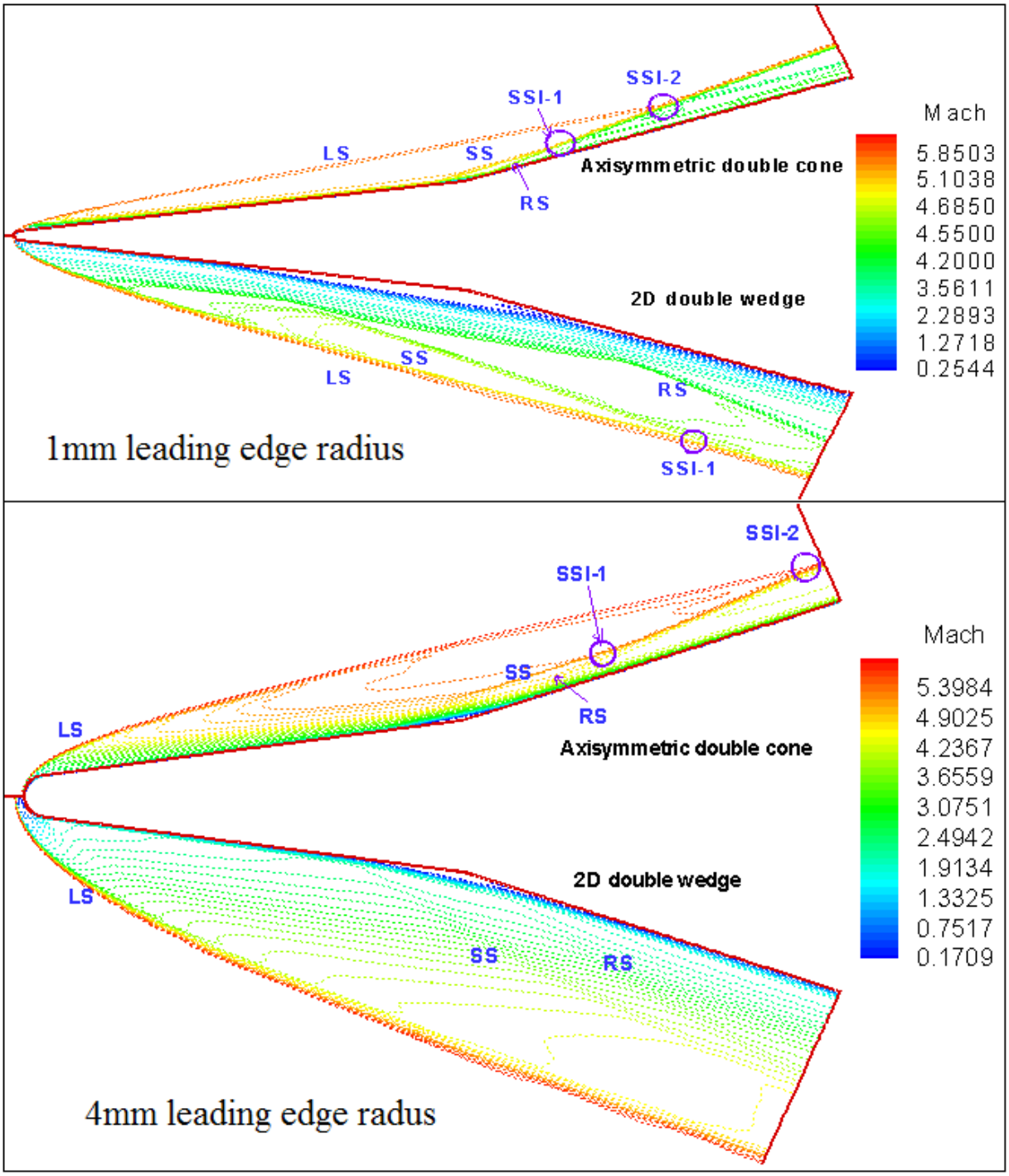

FIGURE 9.4: Comparison of Mach contours of double cone and double ramp with blunt leading edge radii

that, the oblique portion of the standing detached shock has higher angle for higher leading edge radii, which avoids the interaction between the shock generated from first interaction and the standing shock in the computational domain. These disparities in the field interactions associated with different level of leading edge bluntness would induce significant alterations in the second compression surface properties for both two dimensional and axisymmetric flowfields.

9.3.4 Wall property variation for 2D and axisymmetric configurations with leading edge bluntness

This section seeks the variations of surface property distributions associated with different degree of leading edge bluntness. Typical pressure distributions obtained for 2D and axisymmetric models during these investigations are as shown in figure 9.5(a) and 9.5(b) respectively. In either of the cases, pressure can be seen to be decreasing downstream of the leading edge. The region of enhancement of pressure in the distribution, over the reference distribution of sharp leading edge domain, can be referred as over pressure region imposed by the leading edge bluntness. Length of this 'over pressure region' or 'favourable pressure gradient region' depends on the leading edge radius for given freestream conditions. This over pressure region is then followed by a nearly constant pressure region till upstream influence start location where pressure starts raising in the presence of SWBLI. Most of the upstream or first cone portion can be noticed to be the constant pressure region for axisymmetric flow while the same has been replaced by over pressure region for 2D flow. Common noticeable fact in both the figures exists downstream of the upstream influence start location where surface pressure rises across the separation shock and attains a pressure plateau in separation region. Wider separation regions are evident for 2D simulations in comparison with the axisymmetric one for a given leading edge radius. This distribution also displays further rise in the wall pressure downstream of the separation as soon as the flow reattaches on the second ramp surface.

Wall pressure distribution gets altered with degree of bluntness for both 2D and axisymmetric configurations. Increase in leading edge radius is seen to increase the pressure on the forward compression ramp/cone surface mainly due to increase in curved portion of the standing bow shock. However it is more prominent in case of present 2D simulations. Decrease in

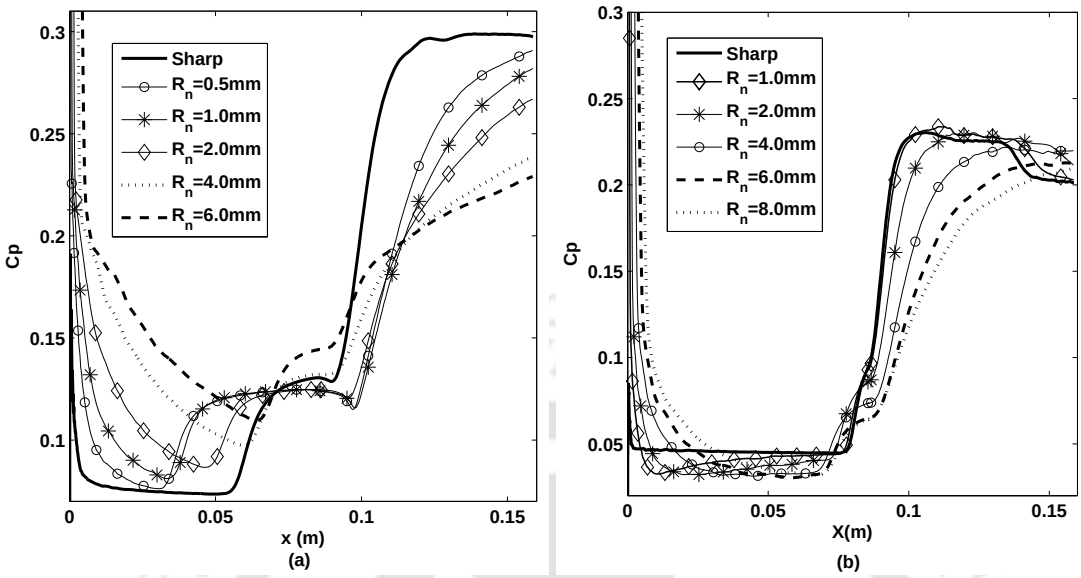

FIGURE 9.5: (a)Surface pressure comparison of hypersonic flow over (a) 2D double ramp and (b) axisymmetric double cone

post-reattachment region pressure can be noted with increase in leading edge radius, for both the simulations. This fact can be attributed to reduced strength of separation and reattachment shocks as observed in earlier section for higher leading edge radii. Moreover the post reattachment pressure values are higher for 2D model as compared to axisymmetric double cone models. It can be reasoned by two ways. Primarily the first compression surface over pressure region is observed to be extending till the interaction zone for most of the 2D cases which make the first ramp as the high pressure region as is unseen in other case. In case of axisymmetric models, the first compression surface pressure is seen to be almost constant and low due to comparatively lower strength of the standing shock. Therefore the subsequent pressure rise across interaction zone is also lower in axisymmetric cases. Secondly the part of the flow that reaches the second cone surface has passed through the weak shocks in axisymmetric flow as compared to equivalent 2D flowfield. Another point to be noted from the pressure distributions of double cone model with sharp and blunt cases till 2 mm radius is that the pressure in the post reattachment region initially attains a maxima and decreases downstream on the second cone surface. The reason behind this pressure drop is the presence of an expansion wave emanating from the SSI-2 which leads to decrease in pressure on the second cone surface. For higher radii, SSI-2 is not present in the domain therefore such decrement in pressure is not noticed. Similar situation has

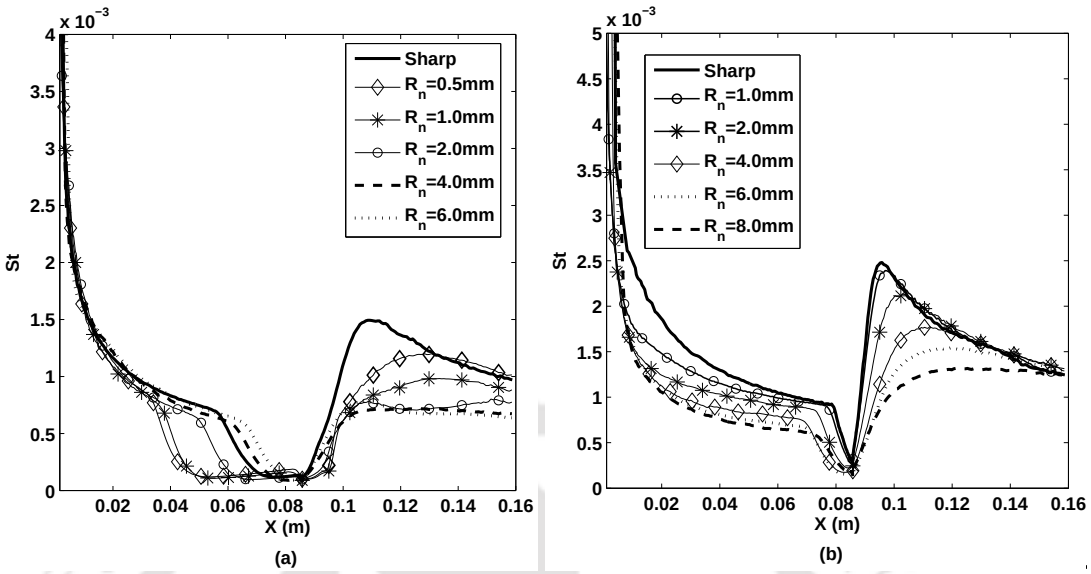

FIGURE 9.6: Stanton number comparison of hypersonic flow over (a) 2D double ramp and (b) axisymmetric double cone

been observed for the 2D flowfield as well.

Computationally obtained non-dimensional wall heat flux in terms of Stanton number is as shown in figure 9.6(a) and 9.6(b), in case of 2D and axisymmetric situations respectively, for various leading edge radii. These comparisons again portray the significant differences in heatflux distributions among those cases. Beside, heatflux decreases monotonically in the streamwise direction for the first compression surface till the upstream influence start location in both the figures for any radii. Beyond which, the heatflux decreases suddenly and the distribution holds V or U shape depending on the size of separation bubble. Most of the double cone cases exhibit V shapes due to narrow separation zone. However U shaped distribution in the separation zone is prominent for 2D situations. Hence these figures reconfirm the earlier observation of wider separation zone for 2D case in comparison with the axisymmetric case from the surface pressure profiles. Variation in the heatflux in the post reattachment region is seen to be similar to that of the pressure and hence can be explained in the same way.

Effect of leading edge radius on wall heat transfer rate in individual cases can be read from figure. 9.6(a) and figure 9.6(b). These distributions show decrement in heatflux at all locations with initial increment of leading edge radii for both 2D and axisymmetric flow fields. Beyond a

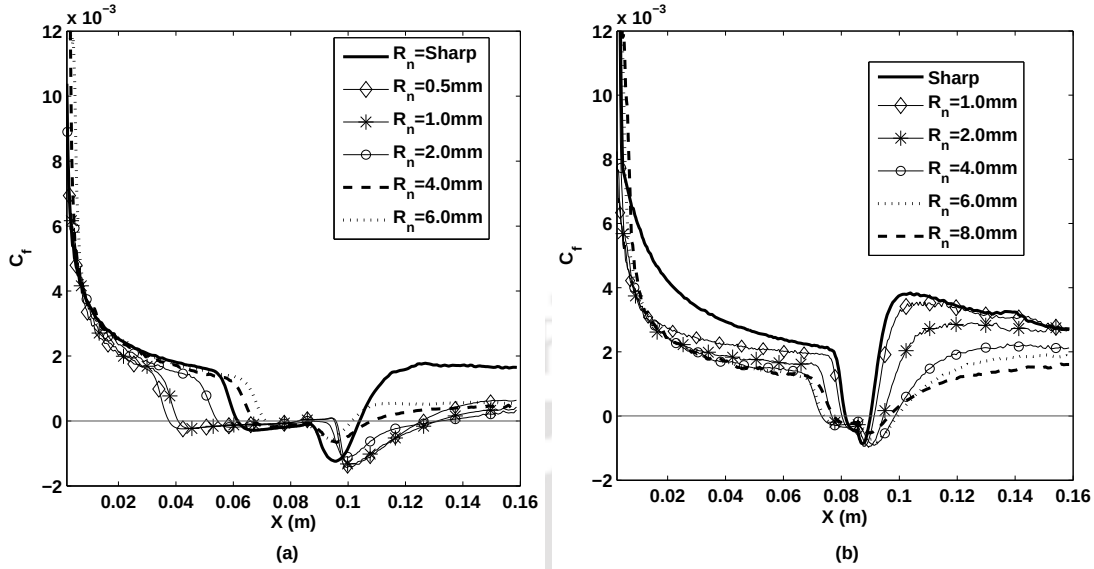

FIGURE 9.7: Skin friction coefficient comparison of hypersonic flow over (a) 2D double ramp and (b) axisymmetric double cone

particular or critical radius, any increment in leading edge radius is observed to enhance the surface heat transfer rates at all stations for 2D cases. However wall heat flux at a particular location continues to decrease with increase in leading edge radius for all radii in case of axisymmetric flow. This difference in first compression surface heatflux distribution, observed with 2D and axisymmetric flowfields, again points towards the difference in basic flow structure in the presence of leading edge bluntness. Beyond the reattachment point, surface heat flux distribution follows the trend as observed in pressure distribution in either cases.

Wall shear distribution can be effectively used for understanding and quantification of separation in the presence of SWBLI. Therefore the skin friction coefficient (C_f) variation along the length with different leading edge radii is shown in figure 9.7(a) and figure 9.7(b) respectively for 2D and axisymmetric simulations. Variation in skin friction coefficient along the compression surfaces, for any radius in any dimensionality, is similar to that of Stanton number and can be reasoned in the same manner. Here, initially the skin friction coefficient at a particular location on the first ramp/cone is seen to be decreasing as the leading edge radius increases. However, unlike heat flux variation, such decrement reverses beyond a particular or critical leading edge radius for both the cases. This trend reversal takes place at different radius for double ramp and

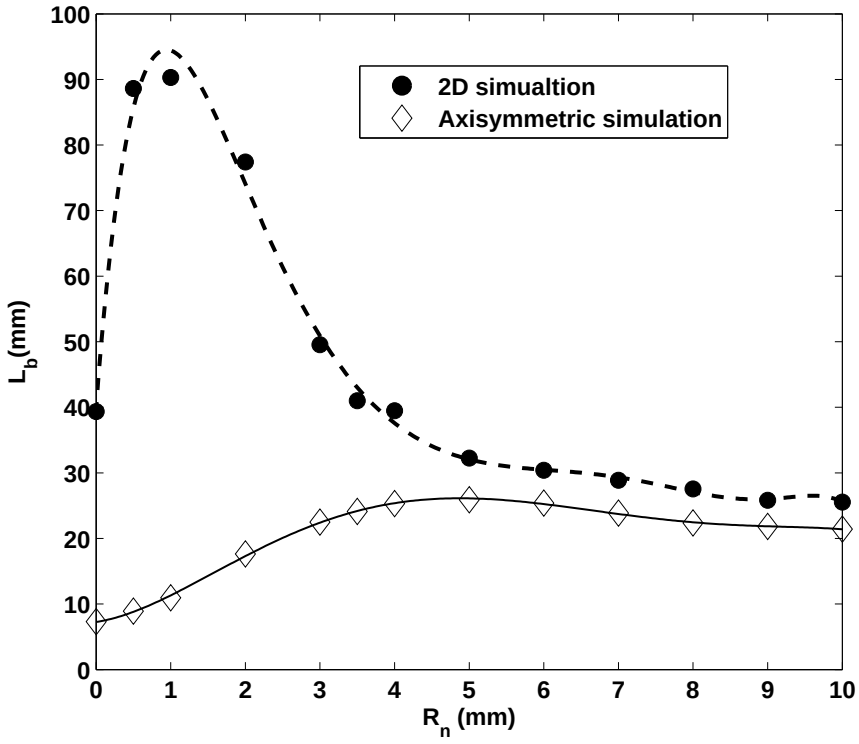

FIGURE 9.8: Variation of separation bubble size with leading edge radii for 2D and axisymmetric flowfields

double cone configurations. Moreover for the range of leading edge considered in the present studies, this reversal is prominent mainly for 2D simulations and takes place at around 1 mm radius. However for the axisymmetric case marginal enhancement in local skin friction has been noticed beyond the critical radius, which is between 4 mm and 5 mm. For all the cases, skin friction coefficient experiences sudden decrement at the upstream influence start location.

Extent of separation or separation bubble size can be evaluated from the above discussed skin friction distribution as the linear distance between separation and reattachment point. For the present study such separation length for different leading edge radii are calculated from the zero cross-over of the skin friction profile. Thus obtained separation bubble sizes plotted against degree of leading edge bluntness are given in figure 9.8 for both the cases. It is clear from this figure that the separation bubble size initially increases with increase in leading edge bluntness for both 2D and axisymmetric simulations. The separation bubble enhancement is very sharp for double ramp case while the same for double cone is gradual. The variation of separation bubble size reverses the trend beyond a certain critical radius in both the cases. For the present

geometric and freestream conditions this trend reversal has been noticed between 0.5 and 1 mm of leading edge radius for 2D case. It is the radius for which trend reversal has been observed for the skin friction coefficient distribution. Beyond this critical radius the separation bubble is seen to be decreasing with further increment in leading edge radius for 2D geometry. However for the axisymmetric test model, the trend reversal critical radius corresponding to maximum separation bubble size has been noted to be around 4 mm which is much greater than the 2D case. In line with this, further enhancement in leading edge radius offers reduction in recirculation zone size but at lower rate in comparison with the variation of the same beyond this critical radius for 2D case. Apart from this, for the range of leading edge radii considered in the present study, the axisymmetric flowfield has not shown separation reduction below the reference sharp leading edge case even with the largest radius of 10 mm. Moreover the separation zone size matches to its reference value for the leading edge bluntness of around 4 mm in case of 2D simulations. Such 'equivalent radius' is also a critical radius since it's the minimum radius beyond which separation control is guaranteed.

9.3.5 Interaction of entropy layer and boundary layer

It has been noticed in the previous sections that the presence of bluntness significantly alters the surface property variations and the flowfield. Such alterations differ for 2D and axisymmetric flowfields. As a result of which, the separation bubble size variation exhibits two distinct critical radii for 2D double ramp geometry. Out of these two, the first one corresponds to trend reversal or maximum separation bubble size and the second is the one beyond which separation bubble size shrinks below the reference case. The first critical radius would be termed here onwards as the 'inversion radius' while the second one as the 'equivalent radius'. In the range of leading edge radius considered for investigations, only 'inversion radius' has been noticed for the axisymmetric flow field. Disparity has also been noticed for the Stanton number distribution in 2D and axisymmetric flowfields. All these inconsistencies should be reasoned out for proposing this passive technique as an SWBLI control measure.

The prime flow alteration that happens with the introduction of even a small leading edge radius is the replacement of attached oblique shock by the detached strong bow shock. A region

of entropy variation forms in the shock layer behind the bow shock as supported by the Croco's theorem. Thus developed entropy layer interacts with the wall based boundary layer over the first compression ramp or cone, thereby affects the downstream shock wave boundary layer interaction zone. Intensity or pattern of entropy layer and boundary layer interaction strongly depends on the leading edge bluntness. In view of this, entropy contours of 4 mm leading edge radius for 2D and axisymmetric cases are compared in figure 9.9. From these contours, it is clear that only a portion of entropy layer which corresponds to strong gradient is responsible for its interaction with the boundary layer. Therefore the entropy layer here onwards would be discriminated in two portions viz. higher entropy layer (HEL) which corresponds to non-uniform entropy region or strong entropy gradient region and low entropy layer (LEL) corresponding to almost uniform entropy region or negligible entropy gradient region. Such distinction upholds the fact that, HEL is comprised of fluid that has passed through the curved portion of the bow shock and LEL is comprised of the flow that has passed through the nearly oblique portion of first compression surface shock. Thus the HEL can be separated from LEL by a dividing stream line. Location of this dividing streamline at the leading edge is calculated herein for 2D and axisymmetric flowfield separately. As seen in the previous chapter and investigations of Borovoi et. al. [29], the higher entropy layer thickness can be taken as bluntness radius value at leading edge region for 2D flowfields. Therefore the downstream HEL can be segregated from LEL by means of a streamline that crosses the detached bow shock at a height equal to twice the leading edge radius from the stagnation line as shown in figure 9.9. However this HEL definition is inadequate for axisymmetric flowfield. This inaccuracy of the above mentioned technique is due to the fact that, shock layer is thinner for axisymmetric case as compared to 2D for both blunt and sharp domains (figure 9.3 and 9.4). Therefore the thickness of HEL at the leading edge of the axisymmetric configuration is certainly lower than twice the leading edge radius due to three dimensional relieving effect. Hence a new concept of defining the HEL for axisymmetric configuration at zero angle of attack is devised in this study.

As per the new methodology, HEL definition is based on the ratio of shock stand-off distance of axisymmetric and 2D flowfield (δ_{axi}/δ_{2D}). Since the shock detachment distance for axisymmetric flow is lower as compared to 2D, the same effect will be reflected in the HEL thickness

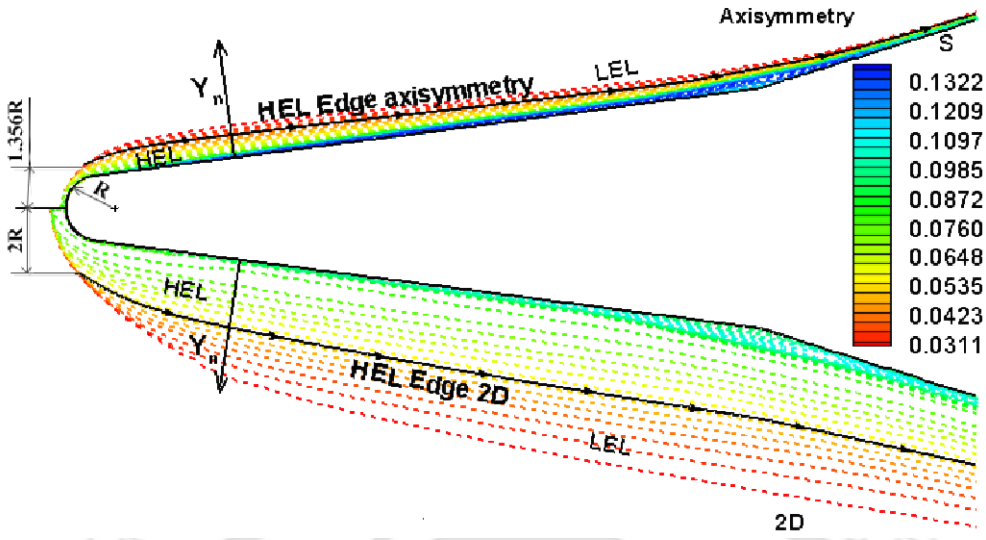

FIGURE 9.9: Comparison of entropy contours of 4mm leading edge radius and definition of high entropy layer

near the leading edge region as well. Therefore the height of HEL near the leading edge is defined as $(1 + (\delta_{axi}/\delta_{2D}))\, R_n$. Here, R_n is the leading edge radius. Following this strategy, HEL-LEL separtion, dowstream of the leading edge can be obtained by considering the dividing stream line that crosses the standing bow shock at a height of $1.356R_n$ from the stagnation line, as shown in figure 9.9. The constant 1.356 has been obtained from present shock stand-off distances. The ratio of shock stand-off distance here can be easily calculated by making use of Billig correlation [1]. The presented HEL definition for both 2D and axisymmetric flowfield can be found to be appropriate from figure 9.9, where most of high entropy field lies within the defined HEL.

Proposed definitions of HEL edge can be used to study its interaction with the boundary layer. In view of this, variation of velocity, parallel to the wall, in the direction normal to it, is used to visualize the boundary layer profile at some specific streamwise locations. Such a boundary layer profile and the variation of entropy along the same normal are given in figure 9.10(a) for 1 mm leading edge radius case of 2D ramp geometry. These profiles are drawn together with the inviscid velocity profiles obtained with 'free-slip' wall boundary condition in order to predict the edge of the boundary layer for the flow with favourable pressure gradient. Hence asymptotic match between inviscid and viscous velocity profiles are considered herein to estimate the local boundary layer thickness. Edge of the HEL is also shown in the same figure to

reconfirm the existence of strong entropy gradient in it. From this figure, it can be noticed that, although boundary layer thickness increases in the streamwise direction, from 0.01 m to 0.03 m from the leading edge, entropy layer thickness increases equally. Moreover entropy layer remains thicker than the boundary layer at both the stations. Further downstream, separated velocity profile can be experienced for this radius at stations 0.05 m and 0.07 m. Hence it is expected to have separation point between 0.03 m and 0.05 m which can be reconfirmed from figure 9.7(a). Relative thicknesses of both the layers also hint for their match between same stations. Such stations are termed as entropy layer swallowing location. Downstream of this station, boundary layer thickness is more than the entropy layer. This phenomenon can also be interpreted as entropy layer getting swallowed by the boundary layer around the SWBLI zone. For the bluntness radii smaller than 1 mm, upstream swallowing has been observed. Necessarily, swallowing of the entropy layer by the boundary layer leads to reduction of density due to ingestion of high temperature fluid. Thereby, boundary layer thickness increases and it becomes separation prone. Moreover, size of the entropy layer increases with degree of leading edge bluntness. Therefore complete swallowing of the entropy layer makes it more susceptible for separation. This reasoning justifies decrease of local skin friction coefficient on the first compression ramp (figure 9.7(a)) and increase in separation bubble size (figure 9.8) with initial increase in leading edge radius.

From the figure 9.10(b), it is clear that, boundary layer remains attached till 0.05 m from the leading edge in case of 4 mm radius double ramp. The velocity profile corresponding to location 0.07 m is expected to be for separated boundary layer since separation takes place around this location (figure 9.7(a)). Apart from this, significant portion of HEL is seen to be passing over the boundary layer for this leading edge bluntness. Thus the entropy layer does not get swallowed by the boundary layer for this case. Such relatively thick entropy layer acts in two ways; having opposite effects on the boundary layer. In one way, ingestion of high temperature fluid tries to thicken the boundary layer and make it separation prone. At the same time the, presence of entropy layer above the boundary layer acts as source of vorticity and provides stabilizing effect. Apart from these two actions, the extended over pressure region which lasts around the interaction zone (figure 9.5(a)) accelerates the flow and provides stabilizing effect by

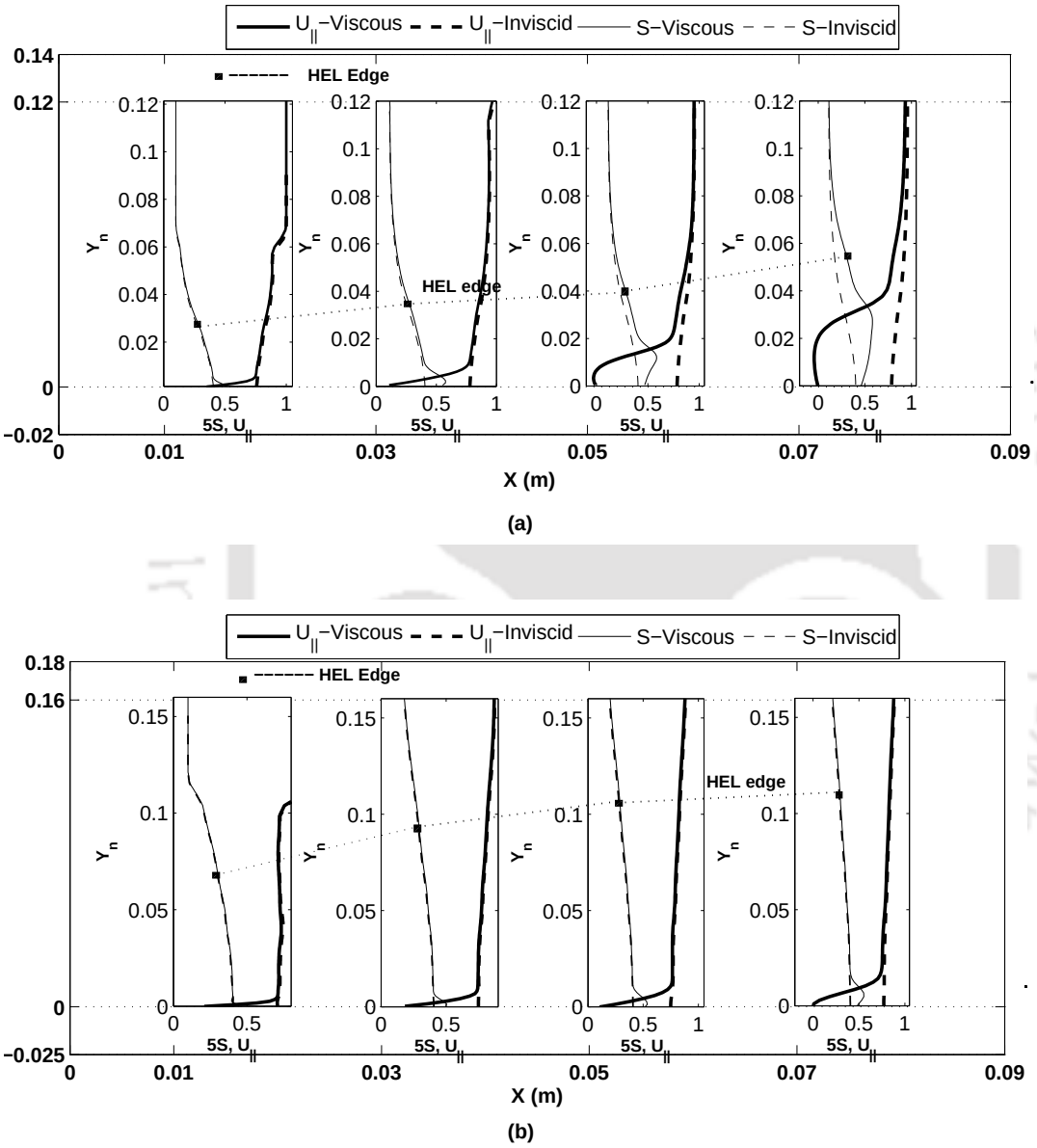

FIGURE 9.10: Comparison of entropy layer and boundary layer interactions for (a) 1 mm leading edge and (b) 4 mm leading edge double ramp model

reducing the driving adverse pressure gradient. Therefore reduction in separation zone size is the integrated effect of these stabilizing and de-stabilizing actions. Hence increase in bluntness beyond the inversion radius increases intensity of favourable effects which further reduce the separation bubble size. This explanation suits to the earlier observation of inversion of skin friction coefficient distribution on first compression ramp (figure 9.7(a)) and decrease of separation bubble size with increase in leading edge radius beyond the inversion radius (figure 9.8). Below inversion radius, only destabilizing effect is present while both the effects are present above the same. Therefore, at the equivalent radius boundary layer becomes equally stable as that of the reference sharp leading edge case so as to give the same separation bubble size. Thus there onwards any increment in the leading edge guarantees reduction in separation zone below the reference one.

In case of axisymmetric flowfield the same dynamics between entropy layer and the boundary layer can be expected. In view of this, results obtained from three representative axisymmetric simulations for leading edge bluntness of 2 mm, 4 mm and 8 mm are considered in figure 9.11(a), 9.11(b) and 9.11(c) respectively. From these figures it is clear that, both boundary layers and shock layers are thinner as compared to respective 2D cases; subsequently the separation bubble sizes are also low in the same comparison. Notable reason for this decrease with the shift from two dimensionality to the axisymmetricity is the reduction in shock stand-off distance due to three dimensional relieving effect. As a result of this, boundary layer and entropy layer thicknesses decrease in comparison with its 2D equivalent. Such thin boundary layers are seen to be attached for all the representative stations and all radii considered in figure 9.11. This fact reconfirms the observation of figure 9.7(b) that flow remains attached for all radii till 0.07 m from the leading edge. Moreover looking at the entropy layer-boundary layer interaction, it can be seen that the entropy layer created due to the detached conical shock is seen to be consistently swallowed by the boundary layer till 4 mm radius. Well upstream swallowing for 2 mm case and swallowing around 0.07 m for 4 mm is clear from figure 9.11. The major reason for the swallowing upstream of the interaction zone is the streamwise thickening of the boundary layer and almost constant thickness of the entropy layer. This fact conflicts the observation from 2D case. Finally figure 9.11(c) for 8 mm leading edge radius shows considerable amount of high

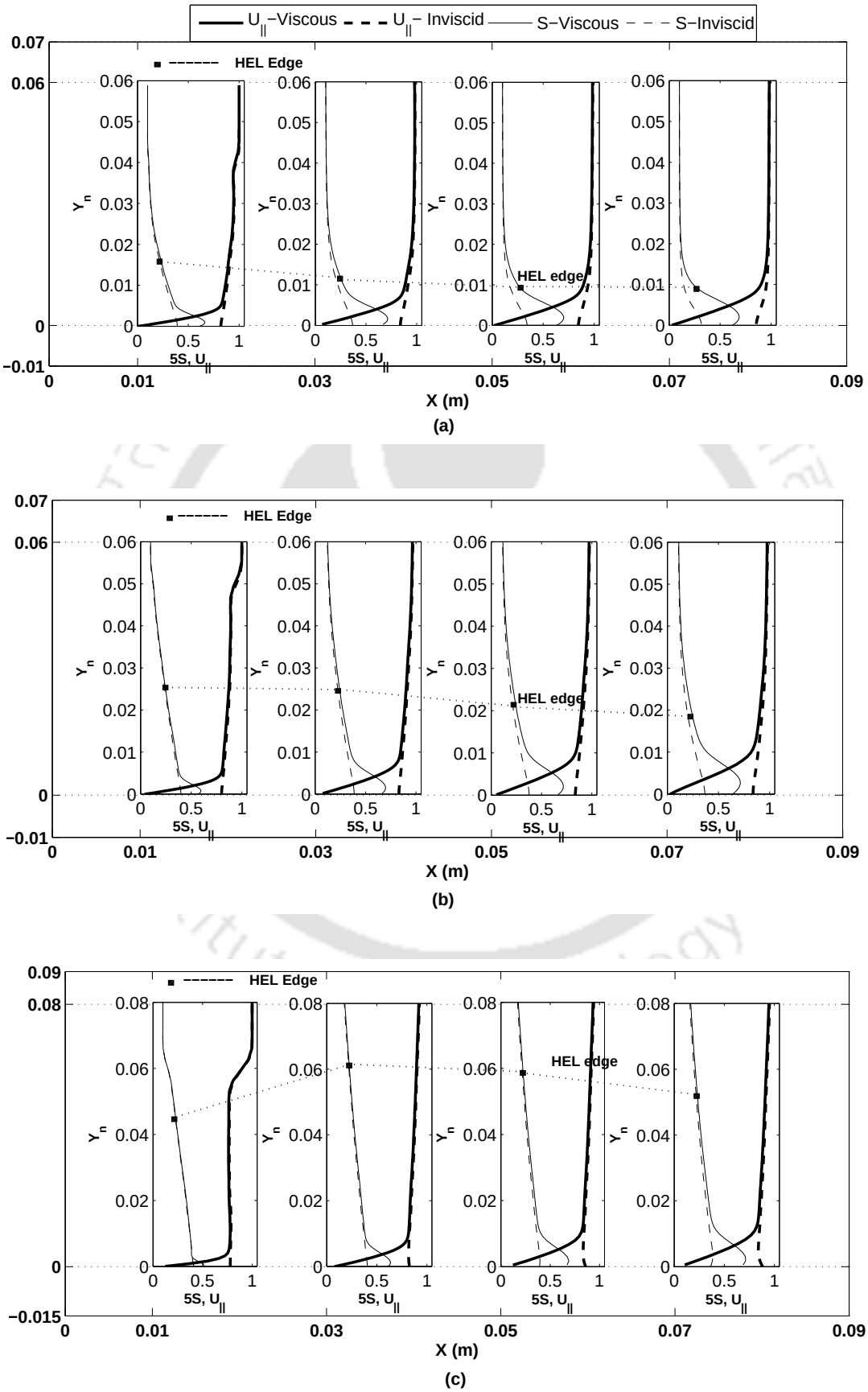

Figure 9.11: Comparison of entropy layer and boundary layer interactions for (a) 2 mm leading edge (b) 4 mm leading edge and (c) 8 mm leading edge double cone model

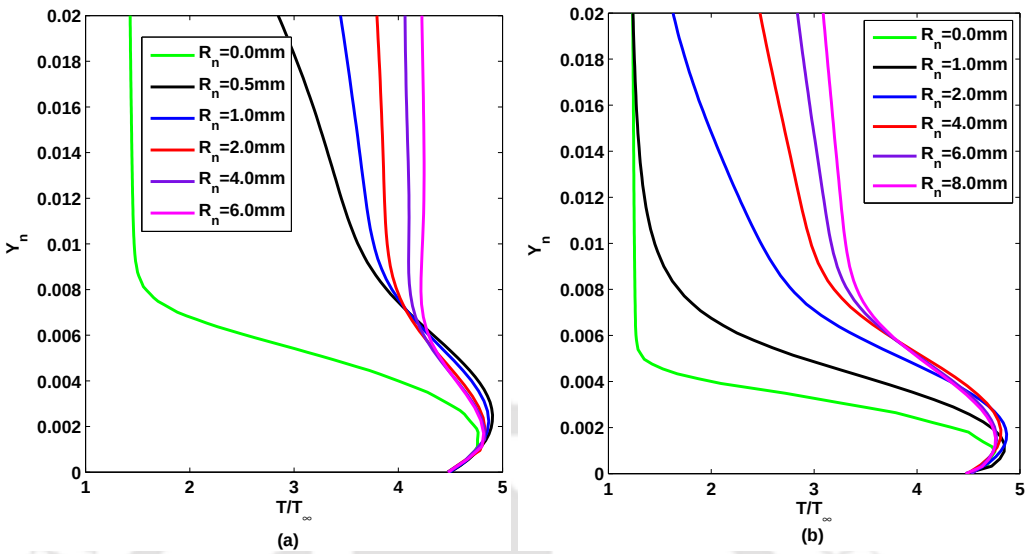

FIGURE 9.12: Comparison of temperature variation for different leading edge radii for (a) 2D and (b) axisymmetric flowfields

entropy layer above the boundary layer. Hence the same inviscid or boundary layer edge vortical effect discussed in case of unswallowed entropy layer for 2D model can be reasoned for the separation zone reduction with increase in leading edge radius beyond the inversion. Such complete covering of boundary layer with entropy layer is also observed for leading edge radius of 6 mm and above. Therefore the critical radius for trend reversal (inversion radius) can be expected for axisymmetric body in between 4 and 5 mm. Therefore, requirement of leading edge bluntness, necessary to provide thicker entropy layer to cover the boundary layer before interaction zone, is seen to be higher than the 2D case for the same freestream conditions. This argument provides the necessary evidence to the observation of higher inversion radius for axisymmetric flowfields than the 2D flowfield (figure 9.8). Although thickened entropy layer is observed with further increase of leading edge radius above 5 mm, the entropy layer thickness enhancement is very nominal in axisymmetric simulations. Apart from that, the extension of over pressure region till interaction location is unseen for any of the leading edge radii under consideration. Hence among the earlier mentioned two boundary layer stabilizing effects, only one is present for axisymmetric flow fields for all the selected radii. Therefore the rate of separation bubble reduction beyond the first critical radius is very less as compared to the double ramp case. This is the major reason for having no equivalent radius for axisymmetric flowfields.

The second noticeable disparity with change in dimensionality is in the Stanton number distribution seen in figure 9.6(a) and figure 9.6(b). Here Stanton number distribution on the first compression ramp is seen to encounter a reversal for 2D configuration while the axisymmetric ones experience monotonic decrease in local Stanton number with increase in leading edge radius. This discrepancy can also be explained through the close observation of thermal boundary layer shown in figure 9.12(a) and 9.12(b) for 2D and axisymmetric cases respectively. For the 2D flowfield, initial increment in leading edge radius increases the maximum temperature in the thermal boundary layer. However, outward shift of the location of maximum temperature with increase in radius at higher rate, decreases the gradient at the wall and in turn the heat flux and Stanton number. Moreover, a particular radius onwards (between 0.5 and 1mm for 2D), maximum temperature in the thermal boundary layer decreases with increase in leading edge radius and its location shifts inwards. It leads to enhancement in local heat flux and hence the Stanton number due to lower rate of decrease of maximum temperature and higher rate of its inward shift with the increase in leading radius. Hence this close observation hints for a thermally critical radius corresponding to Stanton number trend inversion. Similar changes in maximum temperature in the thermal boundary layer are observed for axisymmetric cases with increases in leading edge radius. The initial decrement in local Stanton number can also be reasoned in the same way here as discussed for 2D case. However, in this case unlike 2D flowfield, the local Stanton number does not increase after decrement of maximum temperature in the thermal boundary layer (close to 4 mm). Unchanged or minor inward shift of maximum temperature location should be reasoned for the further decrement of local Stanton number. Nevertheless trend inversion for Stanton number can be expected for the higher radius, beyond the range of present studies, which would marginally shift the location of maximum temperature.

9.4 Summary

The effect of blunt leading edge on SWBLI on a double ramp and double cone models are numerically investigated by employing “USHAS”. Present studies are carried out for hypersonic flow of Mach number 6.0 over the double wedge and double cone configurations having 7.5^0 inclination for first compression surface and 17.5^0 for the second. Strong dimensionality effect

has been observed in these studies with increase in leading edge bluntness. Mach number contours revealed the alterations in the flowfield and in turn the shock-shock interaction pattern with added dimensionality. Close observation of skin friction distribution for the range of radii under consideration showed an increasing trend for separation bubble size till critical leading edge bluntness for both the cases. This inversion radius is found to be 1 mm for 2D configurations and 4 mm for axisymmetric. Swallowing of entropy later by the boundary layer and weak leading edge favourable pressure gradient have been the contributors for separation size enhancement till inversion radius. Enhanced strength of the over pressure region and thickened entropy layer are found responsible for decrement in separation bubble size with increase in bluntness beyond the inversion radius. However the radii under consideration are found to be ineffective to provide the sufficiently strong over pressure region and thick entropy layer so as to reduce the separation size beyond the base value for axisymmetric configurations. Hence the second critical radius or the equivalent radius, which is 4 mm for 2D case, has not been encountered for axisymmetric case. The detailed thermal boundary layer analysis showed that initial increase in leading edge radius decreases the local heat flux for both the cases and this is attributed to outward shift of location of maximum temperature, or increase in thermal boundary layer thickness. An inversion has been noticed here as well when the local heat flux reversed between 0.5 mm and 1 mm for 2D configurations due to inward shift of maximum temperature location in the thermal boundary layer. However such inversion has not been observed for the axisymmetric configurations since local heat flux continued to decrease monotonically due to decrease in maximum temperature in the thermal boundary layer in the range of radii under consideration. Thus, present studies help to assess the proposed leading edge bluntness based separation control technique. This critical assessment cautions the implementation of this separation control technique for axisymmetric configurations which might converge for very large bluntness values. Besides, it has been found comfortable for 2D configurations to reduce the separation bubble size beyond the equivalent radius.

Chapter 10

Conclusions and scope of future work

10.1 Conclusions

Shock wave and boundary layer interaction is one of the potential topics of research in hypersonic flow regime. This phenomenon is the classical example of viscous and inviscid interaction. Understanding of this flow feature is essential since it may lead to flow separation and intensive surface heating. Major victim of such interactions are ramp like shapes which are very common in the design of space vehicles and engine inlets. In view of this importance, shock wave boundary layer interaction has been investigated through numerical simulations during present studies.

Development of an accurate hypersonic flow solver has been the foremost objective for proposed studies about the shock wave boundary layer interaction. An in-house compressible flow Navier-Stokes solver (USHAS) has been developed to achieve the set goals. Following are the conclusions from this development.

1. An unstructured finite volume compressible flow solver has been successfully developed and validated. This solver holds second order accuracy using the strategy proposed by Barth and Jespersen [70] through the implementation of Venkatakrishnan's limiter. Present solver has the facility of two gas models viz. perfect gas and equilibrium flow. Both the methodologies namely implicit and explicit are considered for time marching while developing the in-house solver. Provision of seven convective flux schemes is one of the vital features of USHAS.

2. Numerical assessment of convective flux computation schemes for the simulation of high speed flows has been carried out using the literature reported experimental and numerical test cases. These studies have shown that, Roe and AUSM family schemes are the most accurate flux schemes among the available schemes of present solver. However Roe scheme has been found to be unstable for high Mach number flow simulations. The most dissipative scheme Rusanov has seen to offer maximum stability. The performance of Van-Leer and HLLE schemes, in terms of accuracy and stability, lies in between AUSM and Rusanov. This study has also pointed out the chance of further improvement of performance of these upwind schemes in terms of stability and accuracy through proper blending of the flux formulae of different schemes.

The validated and verified in-house solver, USHAS, is then implemented for R-SWBLI studies. It has been noticed that limited number of findings are reported about the effect of Mach number and freestream stagnation enthalpy on the interaction. Experimental pressure measurements were considered for estimation of separation bubble size. Therefore proper quantification of such estimates is found essential for precise understanding of the interaction. Apart from this, doubts had also been raised by some authors about the measurements in the post reattachment region during the experimental studies for bluntness based separation control technique. In view of these limitations, R-SWBLI studies are conducted for literature reported test conditions and following conclusions are drawn.

1. Nedham's correlation for prediction of upstream influence start location is found suitable only for well separated flow. Therefore this pressure measurement based empirical relation is doubted for its implementation closer to the incipient angle.
2. Increase in freestream stagnation enthalpy and Mach number reduce the separation bubble size owing to increase in inertia of the flow. Contrarily, increment in ramp angle or wall temperature induces early separation. Increase in adverse pressure gradient is the reason for former case while thickening of the boundary is for the later.
3. Increase in wall temperature introduces adverse effect on the interaction while increase in total temperature stabilizes it. Thus the effect a temperature is counteracting to the effect of other. Therefore wall to total temperature ratio is the governing parameter of R-SWBLI.

4. Simulations with limited range of leading edge of radius, for the experimental conditions and configurations of Coet el. al., [16] confirmed the usefulness of this passive technique for separation zone reduction. These simulations have also showed that the flow can experience turbulent reattachment in the presence of SWBLI. This conclusion is based on the noticed disparity between experimental and simulation results in the post reattachment region. Such doubt has been raised by the Coet el. al. while present investigations reassert the same.

Thus obtained numerical data for range of hypersonic Mach numbers, wall temperatures, ramp angles and freestream stagnation enthalpies are considered for modifications in existing R-SWBLI correlations. The interesting findings from this analysis are mentioned below.

1. The literature reported correlations for upstream influence, separation bubble size, peak heat flux separation pressure and plateau pressure do not exhibit linearity for variation in governing parameters of SWBLI. Most of these widely accepted correlations do not account for the wall to total temperature ratio.

2. Modifications are suggested in three correlations viz. Nedham and Stollary's correlation [3] for extent of upstream influence, Nedham's correlation [20] for separation bubble size and Hung and Barnett's correlation [56] for peak heat flux. The suggested modifications in these correlations are found satisfactory due to attained linearity for wider range of freestream and wall conditions

Effect of leading edge bluntness has been guaranteed for reduction in separation bubble size by many researchers. However, very few finding make thoughtful comment about the proposed passive control technique. Besides, diversity has been noticed for the justification of this cautious remark. This limitation has provided impetus for investigations for large range of leading edge bluntness to access its usefulness in separation bubble reduction. Following are the major conclusions from these studies.

1. Two critical leading edge radii exist for a given freestream and wall conditions. First critical radius, termed as inversion radius, belongs to maximum separation size. The second

critical radius, defined as equivalent radius, is the minimum radius beyond which separation reduction can be expected beyond the reference separation bubble size of sharp leading edge case.

2. Interaction of entropy layer and boundary layer is the major reason for existence of these critical radii. New definition of high entropy layer (HEL) has been proposed herewith as the layer below the streamline passing through a point on bow shock which splits it two parts viz. strongly curved portion and weakly curved portion.
3. Close inspection of the shock layer revealed that the inversion radius corresponds to a radius for which entropy layer gets swallowed by the boundary layer at the reference upstream influence station. Therefore, ingestion of high temperature HEL gas inflates the boundary layer and makes it separation prone. Thus any leading edge bluntness till the inversion radius enlarges the separation bubble size.
4. Extension of upstream favourable pressure gradient with increase in radius, beyond the first critical radius, provides sufficient stability to the boundary layer. The inviscid vorticity from the HEL above the boundary layer assist this over pressure region for the stability to the extent that the separation size becomes equal to the separation bubble size of reference sharp leading edge at equivalent radius.
5. Separation control is certain if the leading edge bluntness is more than the equivalent radius corresponding to the wall and freestream conditions.

Effect of various governing parameters has been analysed on the magnitude of the critical radii. These explorations have led the following conclusions.

1. Both the critical radii increase in magnitude with increase wall temperature and decrease in freestream Mach number. Increased boundary layer thickness in either cases demand for thicker entropy layer to get covered. Enhancement in leading edge radius for the required increment in entropy layer justifies the influence of wall temperature and Mach number on the critical radii.
2. Increased freestream stagnation enthalpy essentially reduces the boundary layer thickness and thus demands for lower critical radii which can cover the boundary layer.

3. The wall to total temperature ratio is not the governing parameter for critical radii. The absolute magnitude of entropy swallowed by the boundary layer controls the SWBLI. Therefore the variation of this magnitude, for the same temperature ratio, disturbs the equivalence.

Studies are extended for dimensionality effect about the leading edge effect on SWBLI. Literature reported axi-symmetric configurations and its two dimensional equivalent are simulated for the same freestream conditions for this work out. Following are highlights of these investigations.

1. Strong dimensionality effect has been observed during the comparative study of 2D and axisymmetric SWBLIs. Two dimensional separation bubble is larger in size in comparison with its axi-symmetric counterpart for any leading edge bluntness. Higher Mach number in the shock layer owing to three dimensional reliving effect is credited for this reduction.

2. Inversion radius has been noticed in both the dimensionalities. Magnitude of its in 2D case is lower than the axisymmetric case. Equivalent radius is present only for the two dimensional SWBLI. Thus blunt leading edge based separation bubble reduction would be expected at very large radii for axisymmetric configurations. Hence it is not advisable to consider the same as a separation control technique for axisymmetric flowfields.

3. Detailed examination of the shock layer showed that thin shock layer and hence thin entropy layer is the major reason for higher magnitude inversion radius for axisymmetric case. Well upstream saturation of the over pressure region has been marked for the non-occurrence of equivalent radius in the axisymmetric simulations.

4. A critical radius has been encountered for wall heat transfer rate in case of 2D simulations. Enhancement in local surface heating rate for the first compression surface has been noticed beyond this radius. Moreover reduction in local heat transfer rate has been noticed for all the radii under consideration in case of axisymmetric configurations.

10.2 Scope of future work

Present studies are found useful for understanding the SWBLI phenomenon. However these investigations have posed various questions about this interaction which can compose the future work in this area.

1. Only low enthalpy hypersonic flows are considered in the present study. Perfect gas model of USHAS is implemented for such situations. However, the real gas effects may contribute significantly to the phenomenon of R-SWBLI in high enthalpy flows. In light of this, presently encountered governing parameter, wall to free stream total temperature ratio (T_w/T_0), need to be assessed for such high enthalpy flows to examine its scaling nature.
2. The modifications suggested for the correlation of upstream influence extent contains the specific heat ratio γ. However its role in the correlation has not been critically assessed. Additional studies shall be performed with different gases thus with different γ to ensure proper scaling of this parameter in the correlation for upstream influence extent. The modified separation bubble size correlation does not contain γ term. Hence, in the light of sufficient number of numerical investigations with varying γ value, the presently proposed separation bubble size correlation may be modified with γ scaling. Such incorporation of proper γ scaling may widen the range of applicability of the present correlation to even high enthalpy flows and also for wide range of gases. Effort may also be extended to incorporate additional scaling parameters for ramp angle, wall temperature and γ in the separation and plateau pressure correlations to enhance their prediction capability.
3. The extension of in-house developed solver to three dimensional N-S solver is an immediate possible extension of the present work. Such solver extension may facilitate the investigation about the three dimensional effect of shock wave boundary layer interactions. The incorporation of reacting flow models to the solver may help in analysing the real gas effects on R-SWBLI. Different flux blending schemes can be introduced into the solver to improve the balance between accuracy and stability of the solver in high speed flow simulations. Although the solver has been implicitised, there is still further scope of improving the computational efficiency of the solver, by means of parallelisation. Such distributed computing is very essential for the simulation of highly complicated 3D flows in hypersonic regime.

4. Investigations for three dimensional SWBLI and turbulence based studies would provide a new dimension to the scope of present studies. Understanding about the interaction of turbulent boundary layer and shock is also a possible goal for future.
5. Incorporation of active techniques alone or together with the passive SWBLI control technique may contribute in suppressing the R-SWBLI based separation zone. Active techniques like boundary layer bleeding, freestream energy addition etc. may be investigated in this regard. Such active techniques must be assessed in terms of their viability in real time implementation and other design constraints.
6. The present research dealt with only steady state SWBLIs. However there is immense scope for investigating the unsteadiness involved in the SWBLI phenomenon. Flowfield turbulence is the main source of such unsteadiness. Hence the present laminar studies can be further extended to turbulent flows to understand unsteadiness involved in the SWBLIs.

Appendix A

Formulations of Convective flux schemes

TABLE A.1: Formulations of different convective flux schemes employed in the present solver

Scheme	Flux formula	Terms
	Interface flux, $H_{I_\perp} = {H_I}^+ + {H_I}^-$	${M_L}^+ = \begin{cases} M_L, & \text{if, } M_L \geq 1 \\ \frac{1}{4}(M_L+1)^2 & \text{if, } \lvert M_L \rvert < 1 \\ 0 & \text{if, } M_L \leq -1 \end{cases}$
Van-Leer	${H_I}^+ = H_{I_\perp},\ {H_I}^- = 0$ if, $M_\perp \geq 1$	
FVM	${H_I}^- = H_{I_\perp},\ {H_I}^+ = 0$ if, $M_\perp \geq -1$	
Van Leer B [86]	$H_{I\perp} = H_I^+ + {H_I}^-$ if, $-1 < M_\perp < 1$	

Continued on next page

Table A.1 – *Continued from previous page*

Scheme	Flux formula	Terms
Van-Leer FVM Van Leer B [86]	$H_{I_\perp} = \begin{bmatrix} \rho u_\perp \\ \rho u u_\perp + p n_x \\ \rho v u_\perp + p n_y \\ (\rho e + p) u_\perp \end{bmatrix}$	$M_R{}^- = \begin{cases} 0 & \text{if, } M_R \geq 1 \\ \frac{1}{4}(M_R+1)^2 & \text{if, } \lvert M_R \rvert < 1 \\ M_R & \text{if, } M_R \leq -1 \end{cases}$ $M_{\perp L} = \frac{u_{\perp L}}{c_L}, \;\; M_{\perp R} = \frac{u_{\perp R}}{c_R}$ $f^+_{mass} = +\rho_L c_L \frac{(M_L+1)^2}{4}$ $f^-_{mass} = -\rho_R c_R \frac{(M_R-1)^2}{4}$
	$H_I^\pm = \begin{bmatrix} \text{if } \lvert M_\perp \rvert < 1 \\ {f_{mass}}^\pm \\ {f_{mass}}^\pm \left[u + n_x \left(-u_\perp \pm 2c\right)/\gamma\right] \\ {f_{mass}}^\pm \left[v + n_y \left(-u_\perp \pm 2c\right)/\gamma\right] \\ {f_{energy}}^\pm \end{bmatrix}$	$f^\pm_{energy} = f^\pm_{mass} \left\{ \frac{[(\gamma-1)u_\perp \pm 2c]^2}{2(\gamma^2-1)} + \frac{u^2+v^2-u_\perp^2}{2} \right\}_{L/R}$
	Interface flux,	

Continued on next page

Table A.1 – *Continued from previous page*

Scheme	Flux formula	Terms
AUSM-delta Hybrid Liou, M.S [90]	$H_{I_\perp} = (M_n)_{I+\frac{1}{2}} \begin{bmatrix} \rho c \\ \rho c u \\ \rho c v \\ (\rho e + p)c \end{bmatrix}_{L/R} + \begin{bmatrix} 0 \\ p n_x \\ p n_y \\ 0 \end{bmatrix}_{I+\frac{1}{2}}$ where $(M_n)_{I+\frac{1}{2}} = {M_L}^+ + {M_R}^-$ $(p)_{I+\frac{1}{2}} = {p_L}^+ + {p_R}^-$ $(M_n)_{I+\frac{1}{2}} = {M_L}^+ + {M_R}^-$ $(\cdot)_{L/R} = \begin{cases} (\cdot)_L & \text{if, } M_{n_{I+\frac{1}{2}}} \geq 0 \\ (\cdot)_R & Otherwise \end{cases}$ Interface flux,	$p_L^+ = \begin{cases} p_L & \text{if, } M_L \geq +1 \\ \frac{p_L}{4}(M_L+1)^2(2-M_L) & \text{if, } \lvert M_L \rvert < 1 \\ 0 & \text{if, } M_L \leq -1 \end{cases}$ $p_R^- = \begin{cases} 0 & \text{if, } M_R \geq +1 \\ \frac{p_R}{4}(M_R-1)^2(2+M_R) & \text{if, } \lvert M_R \rvert < 1 \\ p_R & \text{if, } M_R \leq -1 \end{cases}$ To avoid zero advection Mach number $(M_n)_{I+\frac{1}{2}}$ is modified in AUSM-delta as, $\lvert M_{n_{I+\frac{1}{2}}} \rvert = \begin{cases} \lvert M_{n_{I+\frac{1}{2}}} \rvert & \text{if, } \lvert M_{n_{I+\frac{1}{2}}} \rvert > \delta \\ \frac{{M_n}^2_{I+\frac{1}{2}} + \delta^2}{2\delta} & \text{if, } \lvert M_{n_{I+\frac{1}{2}}} \rvert \leq \delta \end{cases}$

Continued on next page

Table A.1 – *Continued from previous page*

Scheme	Flux formula	Terms
AUSM + Hybrid Liou, M.S [91]	$H_{I_\perp} = m_{I+\frac{1}{2}}{}^{+}(C)_{I+\frac{1}{2}} \begin{bmatrix} \rho c \\ \rho cu \\ \rho cv \\ (\rho e+p)c \end{bmatrix}_L$ $+m_{I+\frac{1}{2}}{}^{-}(C)_{I+\frac{1}{2}} \begin{bmatrix} \rho c \\ \rho cu \\ \rho cv \\ (\rho e+p)c \end{bmatrix}_R + \begin{bmatrix} 0 \\ pn_x \\ pn_y \\ 0 \end{bmatrix}_{I+\frac{1}{2}}$ $m_{I+\frac{1}{2}} = M_L{}^{+} + M_R{}^{-} \qquad c_{I+\frac{1}{2}} = \sqrt{c_L c_R}$ $m^{\pm}_{I+\frac{1}{2}} = \frac{1}{2}\left(m_{I+\frac{1}{2}} + \lvert m_{I+\frac{1}{2}}\rvert\right)$	$M^{\pm}_{L/R} = \begin{cases} \frac{1}{2}\left(M_{L/R} \pm +\lvert M_{L/R}\rvert\right) & \text{if, } \lvert M_{L/R} > 1 \\ \pm\frac{1}{2}\left(M_{L/R} \pm 1\right)^2 \pm \beta\left({M_{L/R}}^2 - 1\right)^2 & \\ & \text{Otherwise} \end{cases}$ where, $-\frac{1}{6} \le \beta \le \frac{1}{2}$ $p_{I+\frac{1}{2}} = p_L{}^{+} + p_R{}^{-}$ $p_{L/R} = \begin{cases} \frac{1}{2}\left(1 \pm sign(M_{L/R})\right) & \text{if, } \lvert M_{L/R} \ge 1 \\ \frac{1}{4}\left(M_{L/R} \pm 1\right)^2\left(2 \mp M_{L/R}\right) \pm \alpha M_{L/R} & \\ \times\left(M^2_{L/R} - 1\right)^2 & \text{Otherwise} \end{cases}$ where $-\frac{2}{4} \le \alpha \le \frac{3}{16}$

Continued on next page

Table A.1 – *Continued from previous page*

Scheme	Flux formula	Terms
AUSMPW Hybrid Hong Kim K et al. [92]	Interface flux, $H_{I_\perp} = \bar{M}_L^+ c_{\frac{1}{2}} \phi_L + \bar{M}_R^- c_{\frac{1}{2}} \phi_R + (P_L^+|_{\alpha=\frac{3}{16}} P_L + P_R^-|_{\alpha=\frac{3}{16}} P_R)$ $\phi = \begin{bmatrix} \rho \\ \rho u \\ \rho v \\ \rho H \end{bmatrix}, P = \begin{bmatrix} 0 \\ pnx \\ pny \\ 0 \end{bmatrix}$ $m_{\frac{1}{2}} = M_L^+ + M_R^-$	(i) for $m_{\frac{1}{2}} \geq 0$, $\bar{M}_L^+ = M_L^+|_{\beta=\frac{1}{8}} + M_R^-|_{\beta=\frac{1}{8}} - M_R^-|_{\beta=\frac{1}{8}} \times w \cdot (1 + f_R) + (f_L M_L^+|_{\beta=\frac{1}{8}} + f_R M_R^-|_{\beta=\frac{1}{8}})$ $\bar{M}_R^- = M_R^-|_{\beta=\frac{1}{8}} \times w \cdot (1 + f_R)$, (ii) for$m_{\frac{1}{2}} < 0$, $\bar{M}_L^+ = M_L^+|_{\beta=\frac{1}{8}} \times w \cdot (1 + f_L)$, $\bar{M}_R^- = M_L^+|_{\beta=\frac{1}{8}} + M_R^-|_{\beta=\frac{1}{8}} - M_L^+|_{\beta=\frac{1}{8}} \times w \cdot (1 + f_L) + (f_L M_L^+|_{\beta=\frac{1}{8}} + f_R M_R^-|_{\beta=\frac{1}{8}})$ The split Mach number and pressure of AUSMPW at a cell interface are the same as those of AUSM+
HLLE FDM Einfeldt,B [89]	Interface flux, $H_{I_\perp} = \frac{H_{I_L} b_{I+\frac{1}{2}}{}^+ - H_{I_R} b_{I+\frac{1}{2}}{}^-}{b_{I+\frac{1}{2}}{}^+ - b_{I+\frac{1}{2}}{}^-}$	$\bar{c} = \sqrt{(\gamma - 1)\left(\bar{H} - \frac{\bar{q}^2}{2}\right)}$
HLLE FDM Einfeldt,B [89]	$H_{L/R} = \begin{bmatrix} \rho u_\perp \\ \rho u u_\perp + p n_x \\ \rho v u_\perp + p n_y \\ (\rho e + p) u_\perp \end{bmatrix}_{L/R}$	$\bar{H} = \frac{H_L \sqrt{\rho_L} + H_R \sqrt{\rho_R}}{\sqrt{\rho_L} + \sqrt{\rho_R}}$ $\bar{V} = \bar{u} n_x + \bar{v} n_y$

Continued on next page

Table A.1 – *Continued from previous page*

Scheme	Flux formula	Terms
	$b_{I+\frac{1}{2}}{}^{+} = max\left(\bar{V}+\bar{c},\ V_R+c_R,\ 0\right)$ $b_{I+\frac{1}{2}}{}^{-} = min\left(\bar{V}-\bar{c},\ V_L-c_L,\ 0\right)$	$\bar{u} = \frac{u_L\sqrt{\rho_L}+u_R\sqrt{\rho_R}}{\sqrt{\rho_L}+\sqrt{\rho_R}},\ \ \bar{v} = \frac{v_L\sqrt{\rho_L}+v_R\sqrt{\rho_R}}{\sqrt{\rho_L}+\sqrt{\rho_R}}$
Rusanov FDM Rusanov V. V [88]	Interface flux, $H_{I_\perp} = \frac{1}{2}(H_{I_L}+H_{I_R}) - \frac{1}{2}S^{+}(U_R-U_L)$ $H_{L/R} = \begin{bmatrix} \rho u_\perp \\ \rho u u_\perp + p n_x \\ \rho v u_\perp + p n_y \\ (\rho e + p)u_\perp \end{bmatrix}_{L/R}$	$S^{+} = max\left(V_L+S_L, V_L-S_L, S_L, V_R+S_R V_R-S_R, S_R\right)$ S_L and S_R can be calculated either from equation given below or can be approximated as correspounding sonic velocity at left and right of the face $S = \sqrt{\lambda_0 2+\beta},\ \lambda_0 = u n_x + v n_y$ $\beta =$ pseudo-compressibility parameter
Roe FDM Roe P L [87]	Interface flux, $H_{I_\perp} = \frac{1}{2}\left[(H_{I_L}+H_{I_R}) - \lvert A_{Roe}\rvert_{I+\frac{1}{2}}(U_R-U_L)\right]$	$\lvert A_{Roe}\rvert_{I+\frac{1}{2}}(U_R-U_L) = \lvert\Delta\vec{F_1}\rvert + \lvert\Delta\vec{F_{2,3,4}}\rvert + \lvert\Delta\vec{F_5}\rvert$
Roe FDM Roe P L [87]	$H_{L/R} = \begin{bmatrix} \rho u_\perp \\ \rho u u_\perp + p n_x \\ \rho v u_\perp + p n_y \\ (\rho e + p)u_\perp \end{bmatrix}_{L/R}$	$\lvert\Delta\vec{F_1}\rvert = \lvert\tilde{V}-\tilde{c}\rvert\left(\frac{\Delta p - \tilde{\rho}\tilde{c}\Delta V}{2c^2}\right)\begin{bmatrix} 1 \\ \tilde{u}-\tilde{c}n_x \\ \tilde{v}-\tilde{c}n_y \\ \tilde{H}-\tilde{c}\tilde{V} \end{bmatrix}$

Continued on next page

Table A.1 – *Continued from previous page*

Scheme	Flux formula	Terms
	$\bar{\rho} = \sqrt{\rho_L \rho_R}$ $\bar{u} = \frac{u_L\sqrt{\rho_L} + u_R\sqrt{\rho_R}}{\sqrt{\rho_L} + \sqrt{\rho_R}}$ $\bar{v} = \frac{v_L\sqrt{\rho_L} + v_R\sqrt{\rho_R}}{\sqrt{\rho_L} + \sqrt{\rho_R}}$ $\bar{H} = \frac{H_L\sqrt{\rho_L} + H_R\sqrt{\rho_R}}{\sqrt{\rho_L} + \sqrt{\rho_R}}$ $\bar{c} = \sqrt{(\gamma-1)\left(\bar{H} - \frac{\bar{q}^2}{2}\right)}$ $\tilde{V} = \tilde{u}n_x + \tilde{v}n_y$ $\tilde{q}^2 = \tilde{u}^2 + \tilde{v}^2$	$\lvert\Delta\vec{F_{2,3,4}}\rvert = \lvert\tilde{V}\rvert\left(\Delta\rho - \frac{\Delta p}{\tilde{c}^2}\right)\begin{bmatrix}1\\ \tilde{u}\\ \tilde{v}\\ \frac{\tilde{q}^2}{2}\end{bmatrix} +$ $\tilde{\rho}\lvert\tilde{V}\rvert\begin{bmatrix}0\\ \Delta u - \Delta V n_x\\ \Delta v - \Delta V n_y\\ \tilde{u}\Delta u + \tilde{v}\Delta v - \tilde{V}\Delta v\end{bmatrix}$ $\lvert\Delta\vec{F_5}\rvert = \lvert\tilde{V} + \tilde{c}\rvert\left(\frac{\Delta p + \tilde{\rho}\tilde{c}\Delta V}{2\tilde{c}^2}\right)\begin{bmatrix}1\\ \tilde{u} + \tilde{c}n_x\\ \tilde{v} + \tilde{c}n_y\\ \tilde{H} + \tilde{c}\tilde{V}\end{bmatrix}$

Appendix B

Quasi 1D formulation

Quasi one dimensional flow assumption is applicable for flows in which the area is changing only as a fuction of flow direction, thereby maintaining one dimensionality at any section. Such quasi one dimensional inviscid flow governing compressible Euler equations can be expressed in a vector form as,

$$\frac{\partial AU}{\partial t} + \frac{\partial E}{\partial x} - S = 0 \tag{B.1}$$

where A is the cross sectional area as a function of x i.e., $A = A(x)$.

$$U = \begin{bmatrix} \rho \\ \rho u \\ \rho E \end{bmatrix} \tag{B.2}$$

$$E = \begin{bmatrix} \rho u \\ \rho u^2 + p \\ \rho u(E + \frac{p}{\rho}) \end{bmatrix} \tag{B.3}$$

$$S = \frac{dA}{dx} \begin{bmatrix} 0 \\ p \\ 0 \end{bmatrix} \tag{B.4}$$

These set of equations have been used for the development of quasi-1D solver for the gas model validation. AUSM scheme has been considered for the convective flux calculation for this 1D solver. Time marching has been achieved through the use of simple explicit method. This quasi 1D solver has same algorithm as base solver USHAS.

References

[1] Anderson JD. *Hypersonic and high temperature gas dynamics*. Aiaa, 2000.

[2] Schlichting H and Gersten K. *Boundary-layer theory*. Springer, 2000.

[3] Needham DA and Stollery JL. Boundary-layer separation in hypersonic flow. *AIAA paper*, pages 66–455, 1966.

[4] Chapman DR, Kuehn DM, and Larson HK. Investigation of separated flows in supersonic and subsonic streams with emphasis on the effect of transition. *NACA TN 3869. NACA Rep. 1356*, 1957.

[5] Kuehn DM. Experimental investigation of the pressure rise required for the incipient separation of turbulent boundary layers in two-dimensional supersonic flow. *NASA Memo 1-21-59A, NASA/TIL/6209*, 1959.

[6] Needham DA. A heat-transfer criterion for the detection of incipient separation in hypersonic flow. *AIAA Journal*, 3:781–783, 1965.

[7] Green JE. Interactions between shock waves and turbulent boundary layers. *AProg. Aerosp. Sci*, 11:235–340, 1970.

[8] Holden MS. Boundary-layer displacement and leading-edge bluntness effects on attached and separated laminar boundary layers in a compression corner. part ii: Experimental study. *AIAA Journal*, 9:84–93, 1971.

[9] Hankey WL and Holden MS. Two-dimensional shock wave-boundary layer interactions in high speed rows. *AGARDograph No. 203, Part II*, 1975.

[10] Bloy AW and Georgeff MP. The hypersonic laminar boundary layer near sharp compression and expansion corners. *J Fluid Mech*, 63:431–447, 1974.

[11] Back LH and Cuffel RF. Shock wave/turbulent boundary-layer interactions with and without surface cooling. *AIAA Journal*, 14:526–532, 1976.

[12] Coët MC and Chanetz B. Experiments on shock wave/boundary layer interaction in hypersonic flow. *Rech. Aerosp (English edition)*, 1:61, 1974.

[13] Hayakawa K and Squire LC. The effect of the upstream boundary-layer state on the shock interaction at a compression corner. *Journal of Fluid Mechanics*, 122:369–394, 1982.

[14] Townsend JC. Effects of leading edge bluntness and ramp deflection angle on laminar boundary layer separation in hypersonic flow. *TTN D-3290, NASA*, 1966.

[15] Gray JD. Nose bluntness effects on axisymmetric laminar reattaching flows at mach 19. *TR-67-16, Arnold Engineering Development Center, Tenn*, 1967.

[16] Coet MC, Chanetz B, and Delery JM. Shock-wave boundary layer interaction with entropy layer effect in hypersonic flow. *ONERA, Colloque sur les Ecoulements Hypersoniques,Garchy, France*, 1992.

[17] Neuenhahn T and Olivier H. Influence of the wall temperature and the entropy layer effects on double wedge shock boundary layer interactions. *14th AIAA/AHI Space Planes and Hypersonic Systems and Technologies Conference,AIAA Paper 2006-8136*, 2006.

[18] Mallinson S, Gai S, and Mudford N. The boundary layer on a flat plate in hypervelocity flow. *Aeronautical Journal*, 100:135–141, 1996.

[19] Hakkinen RJ, Greber I, Trilling L, and Abarbanel SS. The interaction of an oblique shock wave with a laminar boundary layer. *NASA Memo 2-18-59 W*, 1959.

[20] Needham DA. Laminar separation in hypersonic flow. *Ph.D. thesis. University of London*, 1965.

[21] Kaufman LG II and Johnson CB. Weak incident shock interactions with mach 8 laminar boundary-layers. *NASA TN D-7835*, 1974.

[22] Holden MS. A study of flow separation in regions of shock wave-boundary layer interaction in hypersonic flow. *AIAA paper*, 78-1198, 1978.

[23] Marini M. Effects of flow and geometry parameters on shock-wave boundary-layer interaction phenomena. *AIAA Paper*, 98-1570, 1998.

[24] Dolling DS. Fifty years of shock-wave/boundary-layer interaction research: what next? *AIAA Journal*, 39:1517–1531, 2001.

[25] Chanetz B. Study of axisymmetric shock waveiboundary layer interaction in hypersonic laminar flow. *ONERA Technical Report TR No. 4214623*, 1995.

[26] Holden MS. Measurements in laminar regions of shock/shock and shock/boundary layer interaction over cylindrical leading edges, cone/cone and hollow cylinder flare configurations for dsmc/navier-stokes code validation. *22nd International Symposium on Rarefied Gas Dynamics, Sydney, Australia, July 9-14*, 2000.

[27] Dieudonne W, Boerrigter HL, and Charbonnier JM. Hypersonic flow on a blunted cone–flare in the vki-h3 mach 6 wind tunnel. *Technical Note TN-193, Von Karman Institute*, 98-1570, 1999.

[28] Tutty OR, Roberts GT, and Schuricht PH. High-speed laminar flow past a fin-body junction. *Journal of Fluid Mechanics*, 737:19–55, 2013.

[29] Borovoy VY, Egorov IV, Skuratov AS, and Struminskaya IV. Two-dimensional shock-wave/boundary-layer interaction in the presence of entropy layer. *AIAA Journal*, 51: 80–93, 2013.

[30] Howarth L. The propogation of small disturbances in a supersonic stream bounded on one side by a parallel subsonic stream. *Proc. Cambridge Phil. Soc*, 44:380–390, 1948.

[31] Lighthill MJ. Reflection at a laminar boundary layer of a weak steady disturbance to a supersonic stream, neglecting viscosity and heat conduction. *Quart.J. Mech. Appl. Math*, 3:303–325, 1950.

[32] Crocco L and Lees L. Mixing theory for the inter-action between dissipative flows and nearly isentropic streams. *Journal of the Aeronautical Sciences*, 19(10):649–676, 1952.

[33] Lighthill MJ. On boundary layers and upstream influence. ii. supersonic flows without separation. *Proc. R. Soc. Lond. A 217*, pages 478–507, 1953.

[34] Stewartson K and Williams PG. Self-induced separation. *Proc. R. Soc.Lond. A 312*, 23: 3181–206, 1969.

[35] Neiland V Ya. Theory of laminar boundary-layer separation in supersonic flow. *Fluid Dynamics*, 4:33–35, 1969.

[36] Neiland V Ya. Asymptotic theory of boundary-layer separation and interaction with supersonic gas flow. *Usp. Mekh. in Russian*, 4:3–62, 1981.

[37] Stewartson K. Multistructured boundary layers on flat plates and related bodies. *Adv. Appl. Mech*, 14(145-239):136, 1974.

[38] Stewartson K. D'alembert's paradox. *SIAM Rev.*, 23:308–343, 1981.

[39] Messiter AF. Boundary-layer interaction theory. *Trans. ASME J. Appl.Mech.*, 50: 1104–1113, 1983.

[40] Rizzetta DP, Burggraf OR, and Richard Jenson. Triple-deck solutions for viscous supersonic and hypersonic flow past corners. *Journal of Fluid Mechanics*, 89:535–552, 1978.

[41] Katzer E. On the length scales of laminar shock/boundary-layer interaction. *J Fluid Mech*, 206:477–496, 1989.

[42] Holden MS. Boundary-layer displacement and leading-edge bluntness effects on attached and separated laminar boundary layers in a compression corner. part i: theoretical study. *AIAA Journal*, 8:2179–2188, 1970.

[43] Sobey I. *Introduction to interactive boundary layer theory*. Oxford University Press., 2000.

[44] Dechaume A, Cousteix J, and Mauss J. An interactive boundary layer model compared to the triple deck theory. *European Journal of Mechanics BFluids*, 24:439–447, 2005.

[45] Inger GR. Scaling of incipient separation in high speed laminar flows. *AIAA Journal*, 33: 178–181, 1995.

[46] Carter JE. Numerical solutions of the supersonic, laminar flow over a two-dimensional compression corner. *Proceedings of the Third International Conference on Numerical Methods in Fluid Mechanics, Lecture Notes in Physics*, 19:69–78, 1973.

[47] MacCormack R and Baldwin B. A numerical method for solving the navier-stokes equations with application to shock-boundary layer interactions. *13th Aerospace Sciences Meeting, AIAA Paper 75-1*, 1975.

[48] Hung CM and MacCormack RW. Numerical solutions of supersonic and hypersonic laminar compression corner flows. *AIAA Journal*, 14:475–481, 1976.

[49] Le Balleur JC, Peyret R, and Viviand H. Numerical studies in high reynolds number aerodynamics. *Computers and Fluids*, 8:1–30, 1980.

[50] Fay JF and Sambamurthi J. Laminar hypersonic flow over a compression corner using the hana code. *AIAA Paper 92-2896*, 1992.

[51] Rudy DH, Thomas JL, Kumar A, Gnoffo PA, and Chakravarthy SR. Computation of laminar hypersonic compression-corner flows. *AIAA journal*, 29(7):1108–1113, 1991.

[52] Grasso F, Leone G, and Delery JM. Validation procedure for the analysis of shock-wave/boundary-layer interaction problems. *AIAA Journal*, 32:1820–1827, 1994.

[53] Grasso F and Marini M. Analysis of hypersonic shock-wave laminar boundary-layer interaction phenomena. *Computers & Fluids*, 25:561–581, 1996.

[54] Leyland P. Shock-wave/boundary layer interactions at hypersonic speed by an implicit navier-stokes solver. *Int. J. of Computational Fluid Dynamics*, 6:71–87, 1996.

[55] Eckert ERG. Engineering relations for friction and heat transfer to surfaces in high velocity flow, 1955.

[56] Hung FT and Barnett DO. Shock wave boundary layer interference heating analysis. *AIAA paper*, 72-0327, 1973.

[57] Marini M. Analysis of hypersonic compression ramp laminar flows under sharp leading edge conditions. *Aerospace Science and Technology*, 5:257–271, 1973.

[58] Davis JP and Sturtevant B. Separation length in high-enthalpy shock/boundary-layer interaction. *Physics of Fluids*, 12:2661–2687, 2000.

[59] Neuenhahn T and Olivier H. Numerical study of wall temperature and entropy layer effects on transitional double wedge shock wave/boundary layer interactions. *Shock Waves*, pages 683–688, 2009.

[60] Savino R and Paterna D. Blunted cone–flare in hypersonic flow. *Computers & Fluids*, 34:859–875, 2005.

[61] Roy CJ, Bartel TJ, Gallis MA, and Payne JL. Dsmc and navier-stokes predictions for hypersonic laminar interacting flows. *AIAA Paper*, 1030:2001, 2001.

[62] Moss JN. Dsmc computations for regions of shock/shock and shock/boundary layer interaction. *AIAA paper*, 1027:2001, 2001.

[63] Gnoffo PA et al. Cfd validation studies for hypersonic flow prediction. *AIAA paper*, 1025: 2001, 2001.

[64] Wright MJ, Sinha K, Olejniczak J, Candler GV, Magruder TD, and Smits AJ. Numerical and experimental investigation of double-cone shock interactions. *AIAA journal*, 38(12): 2268–2276, 2000.

[65] Kato H and Tannehill JC. Computation of hypersonic laminar separated flows using an iterated pns algorithm. *AIAA Paper*, 1028, 2001.

[66] Holden MS, Wadhams TP, Harvey JK, and Candler GV. Comparisons between measurements in regions of laminar shock wave boundary layer interaction in hypersonic flows with navier-stokes and dsmc solutions. Technical report, DTIC Document, 2006.

[67] Knight D, Longo Jé, Drikakis D, Gaitonde D, Lani A, Nompelis I, Reimann B, and Walpot L. Assessment of cfd capability for prediction of hypersonic shock interactions. *Progress in Aerospace Sciences*, 48:8–26, 2012.

[68] Knight D, Yan H, Panaras AG, and Zheltovodov A. Advances in cfd prediction of shock wave turbulent boundary layer interactions. *Progress in Aerospace Sciences*, 39(2):121–184, 2003.

[69] Edwards JR. Numerical simulations of shock/boundary layer interactions using time-dependent modeling techniques: A survey of recent results. *Progress in Aerospace Sciences*, 44(6):447–465, 2008.

[70] Barth TJ and Jespersen D. The design and application of upwind schemes on unstructured meshes. *AIAA Paper*, 89-0366, 1989.

[71] Venkatakrishnan V. On the accuracy of limiters and convergence to steady state solutions. *AIAA Paper*, 93-0880, 1993.

[72] Venkatakrishnan V. Convergence to steady state solutions of the euler equations on unstructured grids with limiters. *Journal of Computational Physics*, 118(1):120–130, 1995.

[73] Blazek J. *Computational Fluid Dynamics: Principles and Applications: Principles and Applications*. Elsevier, 2001.

[74] Poinsot TJ&amp and Lelef SK. Boundary conditions for direct simulations of compressible viscous flows. *Journal of computational physics*, 101(1):104–129, 1992.

[75] Sutherland W. Lii. the viscosity of gases and molecular force. *The London, Edinburgh, and Dublin Philosophical Magazine and Journal of Science*, 36(223):507–531, 1893.

[JC and PH] Tannehill JC and Mugge PH. *Improved Curve Fits for the Thermodynamic Properties of Equilibrium Air Suitable for Numerical Computation Using Time-dependent Or Shock-capturing Methods*. Number v. 2470.

[76] Jameson A, Schmidt W, and Turkel E. Snumerical solution of the euler equations by finite volume methods using runge-kutta time-stepping schemes. *AIAA Paper*, 81, 1981.

[77] Kroll N and Jain RK. Solution of two-dimensional euler equations: Experience with a finite volume code. *NASA STI/Recon Technical Report N*, 88:20572, 1987.

[78] Ganesh N, Shende NV, and Balakrishnan N. R-parameter: A local truncation error based adaptive framework for finite volume compressible flow solvers. *Computers and Fluids*, 38(9):1799–1822, 2009.

[79] Luo H, Baum JD, and Löhner R. A fast, matrix-free implicit method for compressible flows on unstructured grids. *Journal of Computational Physics*, 146(2):664–690, 1998.

[80] Yoon S and Jameson A. Lower-upper symmetric-gauss-seidel method for the euler and navier-stokes equations. *AIAA journal*, 26(9):1025–1026, 1988.

[81] Aftosmis MJ and Berger MJ. Multilevel error estimation and adaptive h-refinement for cartesian meshes with embedded boundaries. *AIAA paper*, 863:2002, 2002.

[82] Klaus A, Hoffmann, and Steve T. Chiang. *Computational Fluid Dynamics*. Engineering Education System, 2000.

[83] Billig FS. Shock-wave shapes around spherical-and cylindrical-nosed bodies. *Journal of Spacecraft and Rockets*, 4(6):822–823, 1967.

[84] Bura RO, Roberts GT, Yao YF, and Sandham ND. Investigation of supersonic/hypersonic shock-wave/boundary-layer interactions (sblis). In *Shock Waves*, pages 695–700. Springer, 2005.

[85] Druguet MC, Candler GV, and Nompelis I. Effects of numerics on navier-stokes computations of hypersonic double-cone flows. *AIAA journal*, 43(3):616–623, 2005.

[86] Van Leer B. Flux-vector splitting for the euler equations. In *Eighth international conference on numerical methods in fluid dynamics*, pages 507–512. Springer, 1982.

[87] Roe PL. Approximate riemann solvers, parameter vectors, and difference schemes. *Journal of computational physics*, 43(2):357–372, 1981.

[88] Rusanov VV. Calculation of interaction of non-steady shock waves with obstacles. *J. Comput. Math. & Phys. USSR*, 1(2):267–279, 1961.

[89] Einfeldt B. On godunov-type methods for gas dynamics. *SIAM Journal on Numerical Analysis*, 25(2):294–318, 1988.

[90] Liou MS and Steffen Jr CJ. A new flux splitting scheme. *Journal of computational physics*, 107(1):23–39, 1993.

[91] Liou MS. A sequel to ausm: Ausm+. *Journal of computational Physics*, 129(2):364–382, 1996.

[92] Hong Kim K, Ho Lee J, and Hyun Rho O. An improvement of ausm schemes by introducing the pressure-based weight functions. *Computers & fluids*, 27(3):311–346, 1998.

[93] DeZeeuw D and Powell KG. An adaptively refined cartesian mesh solver for the euler equations. 1993.

[94] Hornung HG and Robinson ML. Transition from regular to mach reflection of shock waves part 2. the steady-flow criterion. *Journal of Fluid Mechanics*, 123:155–164, 1982.

[95] Ben-Dor G. *Shock wave reflection phenomena*. Springer, 2007.

[96] Azevedo DJ and Liu CS. Engineering approach to the prediction of shock patterns in bounded high-speed flows. *AIAA journal*, 31(1):83–90, 1993.

[97] Vuillon J, Zeitoun D, and Ben-Dor G. Reconsideration of oblique shock wave reflections in steady flows. part 2. numerical investigation. *Journal of Fluid Mechanics*, 301:37–50, 1995.

[98] Kumar A. Numerical analysis of the scramjet-inlet flow field by using two-dimensional navier-stokes equations. *NASA Paper TP-1940*, 1981.

[99] Gustafsson B, Pärt-Enander E, and Sjögreen B. Solving flow equations for high mach numbers on overlapping grids. In *Hypersonic flows for reentry problems*, pages 585–599. Springer, 1991.

[100] Holden MS and Moselle JR. Theoretical and experimental studies of the shock wave-boundary layer interaction on compression surfaces in hypersonic flow. *ARL 70-0002. Aerospace Research Laboratories, Wright-Patterson AFB, OH*, 1970.

[101] Bertram MH and Blackstock TA. Some simple solutions to the problem of predicting boundary-layer self-induced pressures. *NASA TN D-798*, 1961.

[102] Kubota T, Lees L, and Lewis JE. Experimental investigation of supersonic laminar, two-dimensional boundary-layer separation in a compression corner with and without cooling. *AIAA journal*, 6(1):7–14, 1968.

[103] Schulte D, Henckels A, and Neubacher R. Manipulation of shock/boundary-layer interactions in hypersonic inlets. *Journal of Propulsion and Power*, 17(3):585–590, 2001.

[104] White FM and Corfield I. *Viscous fluid flow*, volume 2. McGraw-Hill New York, 1991.

[105] Hayes WD and Probstein RF. Hypersonic flow theory, 1966.

[106] Lukasiewicz J. Blast-hypersonic flow analogy theory and application. *ARS Journal*, 32 (9):1341–1346, 1962.

List of publications

Journals:

1. John B, Kulkarni V and Natarajan G. Shock Wave Boundary Layer interactions in hypersonic flows. *Int. J. Heat Mass transfer*, 70:81-90, 2014.
2. John B and Kulkarni V. Numerical Assessment of Correlations for Shock Wave Boundary Layer Interaction. *Computers & Fluids*, 90:42-50, 2014.
3. John B and Kulkarni V. Effect of leading edge bluntness on the interaction of ramp induced shock wave with laminar boundary layer at hypersonic speed. *Computers & Fluids*,96:177-190, 2014.
4. John B, Sarath G, Kulkarni V and Natarajan G. Performance Comparison of Flux Schemes for Numerical Simulation of High-Speed Inviscid Flows. *Progress in Computational Fluid Dynamics An Int. J.*, 14(2):83-96, 2014.
5. John B and Kulkarni V. Investigation of Energy Deposition Technique for Drag Reduction at Hypersonic Speeds. *Applied Mechanics and Materials*, 367:222-227, 2013.
6. Sahai A, John B and Natarajan G. Effect of Fineness Ratio on Minimum-Drag Shapes in Hypersonic Flows. *Journal of Spacecraft and Rockets*, 51(3):900-907, 2014.

Conferences:

1. John B, Sarath G, Kulkarni V and Natarajan G. Development of unstructured compressible flow solver for hypersonic applications. *IIST Research Scholar's Day, Trivandrum, India*, Dec 16-17, 2011.
2. Sarath G, John B, Kulkarni V and Natarajan G. Investigation of shock stand-off distance at hypersonic Mach numbers. 2^{nd} *National Symposium on Shock Waves, Thanjavur, India*, Feb 27-28, 2012.
3. John B and Kulkarni V. Investigation of Energy Deposition Technique for Drag Reduction at Hypersonic Speeds. 3^{rd} *International Conference on Mechanics, Simulation and Control (ICMSC 2013), Kanyakumari, India*, June, 2013.

4. John B and Kulkarni V. Investigations about the non-dimensional heatflux distribution for laminar hypersonic freestream. 29^{th} *International Symposium on Shockwaves, Madison, WI (USA)*, July 2013.
5. John B and Kulkarni V. Numerical Investigation of Blast Wave-Shock Wave Interaction Caused Unsteady Wave Drag Reduction. 15^{th} *Annual AeSI CFD Symposium, IISC Bangalore, India*, August 2013.
6. John B and Kulkarni V. Development of Unstructured Solver for Hypersonic Aerothermodynamic Simulations (USHAS). *National Conference on Wind Tunnel Testing (NCWT-03), ISRO Trivandrum, India*, August 2013.
7. John B and Kulkarni V. Investigations of shock-boundary layer interaction control methods in laminar hypersonic flow. *International Conference on Computer Aided Engineering, IIT Madras, India*, December 2013.
8. John B and Kulkarni V. Effectiveness Studies of Concentrated Energy Addition Based Drag and Heat Transfer Reduction Technique. *The* 22^{nd} *National and* 11^{th} *International ISHMT-ASME Heat and Mass Transfer Conference, IIT Kharagpur, India*, December 2013.